UNIVERSITÄT DUISBURG ESSEN

Universitätsklinikum Essen

Mesoscopic Whole Organ Imaging using Light Sheet Fluorescence Microscopy

-

From Experimental Systems to Clinical Application

Dissertation

zur Erlangung des Doktorgrades

doctor rerum naturalium

(Dr. rer. nat.)

der Fakultät für Biologie

an der Universität Duisburg-Essen

vorgelegt von: **Simon Frederik Merz, M. Sc.**

geboren in: Melbourne, Australien

Datum der Abgabe: November 2019

Everything you do with the entire heart will bring the best results.

Chinese fortune cookie, presumably referencing to whole organ imaging shortly before submitting manuscript #1 to

Nature Communications

DOI: 10.17185/duepublico/71557
URN: urn:nbn:de:hbz:464-20210607-082953-4

Angaben zur Prüfung

Die der vorliegenden Arbeit zugrunde liegenden Experimente wurden am Institut für Experimentelle Immunologie und Bildgebung der Universität Duisburg-Essen durchgeführt.

1. Gutachter:
Prof. Dr. rer. nat. Matthias Gunzer
Institut für experimentelle Immunologie und Bildgebung
Essen, Deutschland

2. Gutachter:
Prof. Dr. rer. nat. Mirko Trilling
Institut für Virologie
Essen, Deutschland

3. Gutachter:
Andrés Hidalgo Alonso
Spanish National Center for Cardiovascular Research
Madrid, Spanien

Vorsitzende des Prüfungsausschusses:
Prof. Dr. rer. nat. Wiebke Hansen
Institut für Medizinische Mikrobiologie
Essen, Deutschland

Tag der mündlichen Prüfung: 23.03.2020

List of publications and scientific activities

The following scientific articles were published during this thesis. Some of these publications were used in this work and cited accordingly.

List of publications

First author papers

Merz, S.F.*, Korste, S.*, Bornemann, L.*, Michel, L., Stock, P., Squire, A., Soun, C., Engel, D.R., Detzer, J., Lörchner, H., Hermann, D.M., Kamler, M., Klode, J., Hendgen-Cotta, U.B., Rassaf, T., Gunzer, M.# & Totzeck, M.#
* these authors contributed equally
Contemporaneous 3-D characterization of acute and chronic myocardial I/R injury and response.
Nature Communications **10**, 2312 (2019).

Cited as [1].

Si, Y.*, **Merz, S.F.***, Jansen, P.*, Wang, B., Bruderek, K., Altenhoff, P., Mattheis, S., Lang, S., Gunzer, M., Klode, J., Squire, A., Brandau, S.
* these authors contributed equally.
Multi-dimensional imaging provides evidence for downregulation of T cell effector function by MDSC in human cancer tissue
Science Immunology **10**, 2312 (2019).

Cited as [2]

Co-author papers

Grüneboom, A., Hawwari, I., Weidner, D., Culemann, S., Müller, S., Henneberg, S., Brenzel, A., **Merz, S.**, Bornemann, L., Zec, K., Wuelling, M., Kling, L., Hasenberg, M., Voortmann, S., Lang, S., Baum, W., Ohs, A., Kraff, O., Quick, H.H., Jäger, M., Landgraeber, S., Dudda, M., Danuser, R., Stein, J.V., Rohde, M., Gelse, K., Garbe, A.I., Adamczyk, A., Westendorf, A.M., Hoffmann, D., Christiansen, S., Engel, D.R., Vortkamp, A., Krönke, G., Herrmann, M., Kamradt, T., Schett, G., Hasenberg, A. & Gunzer, M.
A network of trans-cortical capillaries as mainstay for blood circulation in long bones.
Nature Metabolism (2019).

Cited as [3].

Schleier, L., Wiendl, M., Heidbreder, K., Binder, M.T., Atreya, R., Rath, T., Becker, E., Schulz-Kuhnt, A., Stahl, A., Schulze, L.L., Ullrich, K., **Merz, S.F.**, Bornemann, L., Gunzer, M., Watson, A.J.M., Neufert, C., Atreya, I., Neurath, M.F. & Zundler, S.
Non-classical monocyte homing to the gut via alpha4beta7 integrin mediates macrophage-dependent intestinal wound healing.
Gut (2019).

Cited as [4].

Jansen, P., Petri, M., **Merz, S.F.**, Brinker, T. J., Schadendorf, D., Stang, A., Stoffels, I. & Klode, J.
The prognostic value of sentinel lymph nodes on distant metastasis-free survival in patients with high-risk squamous cell carcinoma.
Eur J Cancer **111**, 107-115, (2019)

Cited as [5]

Manuscript in preparation/submission

Merz, S.F.*, Jansen, P.*, Ulankiewicz, R, Bornemann, L., Schimming, T., Griewank, K., Cibir, Z., Stoffels, I., Aspelmeier, T., Brandau, S., Schadendorf, D., Hadaschik, E., Ebel, G., Gunzer, M.# & Klode, J.#
Identification and quantification of hidden melanoma metastases in human sentinel lymph nodes using light sheet fluorescence microscopy.
* these authors contributed equally

Cited as [6]

Presentations & tutoring at conferences

Presentations

11/2019, BIOME Graduate College, Cologne
Poster: "Identification and quantification of hidden melanoma metastases in human sentinel lymph nodes using light sheet fluorescence microscopy"

09/2019, Imaris Webinar hosted by Labroots
Oral: "Seeing through the murine heart – quantitative 3-D assessment of myocardial ischemia/reperfusion injury and response"
https://www.labroots.com/ms/webinar/seeing-murine-heart-quantitative-3-D-assessment-myocardial-ischemia-reperfusion-injury-response (on demand free video).

12/2018, 17th Day of Research of the Medical Faculty, Univ. of Duisburg-Essen, Essen
Poster: "Seeing through the murine heart: simultaneous 3-D quantification of myocardial ischemia/reperfusion injury and response"

11/2018, 20th EMBL PhD Symposium of the EMBL Heidelberg, Heidelberg
Oral & Poster: "Quantifying murine myocardial infarction and immune cell infiltration via light sheet fluorescence microscopy"

11/2018, BIOME Graduate College retreat, Cologne
Oral: "Light Sheet Fluorescence Microscopy in Cancer Diagnostics"

09/2018, Imaging the Immune System, Paris
Poster: "Seeing through the murine heart: simultaneous 3-D quantification of myocardial ischemia/reperfusion injury and response"

09/2018, 5th European Congress of Immunology (ECI), Amsterdam

Poster: "Quantifying Murine Myocardial Infarction and Immune Cell Infiltration via Light Sheet Fluorescence Microscopy"

05/2018, 13th ENII EFIS EJI Summer School on Advanced Immunology, Porto Cervo
Oral & Poster: "Sentinel lymph node status determination and immune cell interaction in melanoma using llight sheet microscopy"

11/2017, 16th Day of Research of the Medical Faculty, Univ. of Duisburg-Essen, Essen
Poster: "Sentinel lymph node status in melanoma: light sheet fluorescence guided histology"

11/2017, BIOME Graduate College retreat, Xanthen
Poster: "Sentinel lymph node status in melanoma: light sheet fluorescence guided histology"

Invited tutor for ECi-mediated clearing

03/2018, 2nd UltraMicroscope User Meeting, Essen

12/2017, LaVision BioTec workshop: Edinger Institute, Frankfurt

09/2017, LaVision BioTec workshop: Karolinska Institute, Stockholm

Awards and Grants

Top20 winning image
10/2019 in the Nikon Small World Photomicrography Competition.
Visit https://www.nikonsmallworld.com/people/simon-merz

Image of distinction
12/2018 in the Nikon Small World Photomicrography Competition.
Visit https://www.nikonsmallworld.com/people/simon-merz

Best abstract award
11/2018, at the 20th PhD Symposium "Game Changers - Taking Life Sciences to the next Level" at the EMBL, Heidelberg
"Seeing through the murine heart: simultaneous 3-D assessment of myocardial ischemia/reperfusion injury and response"

Presentation award
11/2018, at the BIOME Graduate College retreat, Cologne
"Light Sheet Fluorescence Microscopy in Cancer Diagnostics"

Poster award
09/2018, at the 5th European Congress of Immunology, Amsterdam
"Quantifying murine myocardial infarction and immune cell infiltration via LSFM"

Travel grants from BioLegend, DGfI, GBM and EFIS/EJI.

Abstract

Cellular interactions and thus organ function and anatomy are inherently of a three-dimensional nature. Knowledge of the cellular distribution patterns in organs in health and disease is key to understand ongoing microscopic processes on a mesoscopic organ-wide scale. However, until recently, no imaging modalities capable of imaging entire organs with cellular resolution were available. Magnetic resonance or ultrasound imaging lack resolution, whereas fluorescence-based imaging approaches typically lack tissue penetration depth. To unlock the mesoscopic scale, tissue clearing can be used to render samples optically transparent, literally allowing to see through entire intact organs. The combination of tissue clearing with specific fluorophore-conjugated antibody labeling and light sheet fluorescence microscopy (LSFM) delivers organ models with cellular resolution.

In this thesis, multiple LSFM-based approaches were developed assessing various organs and models in order to characterize and explore i) anatomical alterations and the early immune response after myocardial infarction in mice, ii) the distribution patterns and role of tumor associated neutrophil granulocytes in head and neck squamous cell carcinoma and iii) the diagnostic potential of LSFM in staging melanoma patients via sentinel lymph node biopsy.

In summary, this showed the vast potential of LSFM to visualize cellular distribution patterns in the context of whole organs and to extract quantitative data from the 3-D space. Furthermore, we showed the applicability of LSFM in answering both clinically and diagnostically relevant questions. In fact, LSFM analysis did not only match to 100% with gold standard histopathology but even allowed one melanoma patient to gain access to therapeutic options, which would have been denied based on gold standard histopathological analysis alone.

Keywords: BALANCE protocol, light sheet fluorescence microscopy, light sheet-guided histology, metastatic melanoma, myocardial infarction, sentinel lymph node, squamous cell carcinoma, tissue clearing, tumor diagnostics, quantitative whole organ imaging

Zusammenfassung

Zelluläre Interaktionen und damit verbundene, übergeordnete Organfunktionen haben zwangsläufig einen dreidimensionalen Charakter. Daher ist die Bestimmung von zellulären Verteilungsmustern innerhalb verschiedener Organe im gesunden wie auch im erkrankten Zustand vonnöten, um lokale zelluläre Vorgänge auf mesoskopischer Organebene zu verstehen. Die technischen Möglichkeiten gesamte Organe mit zellulärer Auflösung darzustellen waren in der Vergangenheit jedoch nicht vorhanden. Magnetresonanztomographie oder Ultraschalluntersuchungen verfügen nicht über die nötige zelluläre Auflösung, während fluoreszenz-basierte Bildgebungsverfahren eine zu geringe Eindringtiefe in Gewebe aufweisen. Um die mesoskopische Ebene zu betrachten, kann nun Gewebsklärung angewandt werden, welche biologische Proben optisch durchsichtig macht. Die Kombination dieses Verfahrens mit gerichteten Färbungen, z.B. durch Fluorophor-gekoppelte Antikörper und der sogenannten Lichtblattfluoreszenzmikroskopie (LSFM) erlaubt die Darstellung von einzelnen Zellen im Kontext intakter Organe.

In dieser Arbeit wurden Verfahren zur mesoskopischen Oganananalyse durch LSFM für verschiedenste Krankheitsmodelle und Organe entwickelt. Hierbei wurden, unter anderem, die anatomischen Veränderungen wie auch die assoziierte frühe Immunantwort nach einem akuten Herzinfarkt charakterisiert. Des Weiteren konnte die Rolle von Tumor assoziierten neutrophilen Granulozyten und deren räumlich lokalisierte Verteilungsmuster in Plattenepithelkarzinomen der Mundregion genauer untersucht werden. Abschließend wurden Wächterlymphknoten von Melanom Patienten mit Hilfe des LSFM Verfahrens analysiert. Hierbei konnte das enorme diagnostische Potenzial der Methode für die postoperative Patienteneinstufung und -therapie klar belegt werden.

Die Ergebnisse unterstreichen die Fähigkeit der LSFM Analyse zelluläre Verteilungsmuster im dreidimensionalen Kontext von Organen präzise zu rekonstruieren und damit quantifierbar zu machen. Darüber hinaus konnte die LSFM sowohl in der Grundlagenforschung als auch zur Beantwortung klinischer oder diagnostischer Fragen erfolgreich eingesetzt werden. Von entscheidender Bedeutung ist hierbei die Tatsache, dass die LSFM Analyse von Wächterlymphknoten nicht nur zu 100% mit dem histologischen Goldstandard übereinstimmte, sondern dass das Verfahren einem

Studienteilnehmer Zugang zu Therapieoptionen ermöglichte, die ihm aufgrund der negativen histologischen Routineuntersuchung verwehrt worden wären.

Schlagwörter: BALANCE Protokoll, Lichtblattfluoreszenzmikroskopie, Melanoma, Wächterlymphknoten, Myokardinfarkt, Plattenepithelkarzinom, Gewebsklärung, Diagnostisches Verfahren, Quantitative Bildgebung in intakten Organen

Table of Contents

Angaben zur Prüfung **3**
List of publications and scientific activities **4**
List of publications 4
Presentations & tutoring at conferences 5
Awards and Grants 6
Abstract **7**
Zusammenfassung **8**
Table of Contents **10**
Table of Figures **13**
Abbreviations **14**
1. Introduction **15**
1.1. The immune system 15
1.1.1. Innate immunity 15
1.1.2. Adaptive immunity 21
1.2. Tumor biology 25
1.2.1. Squamous cell carcinoma 26
1.2.2. Cutaneous melanoma 27
1.2.3. Hallmarks of cancer 28
1.2.4. Cancer staging and treatment: example melanoma 32
1.3. Why and how to look inside an organ – mesoscopic 3-D imaging 35
1.3.1. The problem with scale and penetration depth 35
1.3.2. Key techniques for mesoscopic imaging 36
1.3.3. Potential use of LSFM in clinical diagnostics 41
2. Aim **43**
3. Manuscripts **45**
3.1. Prelude 45
3.1.1. Media and License info manuscript #1 45
3.1.2. Author contributions manuscript #1 46
3.2. M#1: Contemporaneous 3-D characterization of acute and chronic myocardial I/R injury and response 47
3.2.1. Authors & Affiliations 47
3.2.2. Abstract 48

3.2.3. Introduction 49
3.2.4. Results 50
3.2.5. Discussion 64
3.2.6. Methods 66
3.2.7. Data availability 72
3.2.8. References 73
3.2.9. Endnotes 75
3.3. Interlude I 76
3.3.1. Additional info manuscript #2 77
3.3.2. Author contributions manuscript #2 78
3.4. M#2: Multi-dimensional imaging provides evidence for downregulation of T cell effector function by MDSC in human cancer tissue 79
3.4.1. Authors and Affiliations 79
3.4.2. Abstract 80
3.4.3. Introduction 80
3.4.4. Results 83
3.4.5. Discussion 95
3.4.6. Material and methods 99
3.4.7. References 102
3.4.8. Endnotes 104
3.5. Interlude II 106
3.5.1. Media and License info manuscript #3 107
3.5.2. Author contributions manuscript#3 108
3.6. M#3: Identification and quantification of hidden melanoma metastases in human sentinel lymph nodes using light sheet fluorescence microscopy 109
3.6.1. Authors and Affiliations 109
3.6.2. Abstract 110
3.6.3. Introduction 110
3.6.4. Results 112
3.6.5. Discussion 125
3.6.6. Methods 127
3.6.7. References 131
3.6.8. Endnotes 134
3.7. Recapitulation 135
4. Discussion 136

4.1. Technical LSFM restrictions – developments and guidance 136
4.1.1. Fluorescent probe delivery route and associated caveats 136
4.1.2. Sample size 139
4.1.3. Autofluorescence, its attenuation and its use 139
4.1.4. NIR dyes for deep imaging in pigmented tissue 141
4.1.5. Algorithms, quantitative analysis and computational load 142
4.2. Biological and clinical insights due to tissue clearing & LSFM 144
4.2.1. I/R injury assessment in 3-D 144
4.2.2. Neutrophil-rich pockets downregulate local T cell cytotoxic potential in human SCC 147
4.2.3. Diagnostic potential of LSFM in SLN analysis 149
4.3. Outlook 150
4.3.1. BALANCE/LSFM – the future of a research tool 150
4.3.2. Multiplexing to enhance precision 152
4.3.3. LSFM implementation in SLN diagnostics 154
5. Bibliography 157
6. Appendix 167
6.1. Supplementary Material 167
6.1.1. Manuscript #3: LSFM in melanoma diagnostics - Unpublished 167
6.2. Licenses 184
6.2.1. Creative Commons 4.0 184
6.2.2. License for manuscript #2 185
6.3. Personal remarks on multidisciplinary teams 186
6.4. Acknowledgements 187
6.5. Curriculum vitae 189
6.6. Declerations / Erklärungen 192

Table of Figures

Intro Figure 1 Anatomical archimakeup and cellular patterns of a lymph node..... 24

Intro Figure 2 The impact of NA on Rayleigh length (z_R) 37

Intro Figure 3 Principles of light sheet fluorescence microscopy (LSFM) and tissue clearing..... 42

M1: Figure 1 Fluorophore compatible bleaching enables homogenous light sheet fluorescence microscopy (LSFM) in whole murine hearts..... 51

M1: Figure 2 High resolution light-sheet fluorescence microscopy (LSFM) of murine and human tissue. 53

M1: Figure 3 3-D quantification and characterization of ischemia/reperfusion (I/R) injury size using light sheet fluorescence microscopy (LSFM). 55

M1: Figure 4 Correlation of echocardiography, cardiac troponin I (cTNI) plasma levels, triphenyl tetrazolium chloride negative (TTC^{neg}) areas and CD31 negative ($CD31^{neg}$) volumes after 24 h of reperfusion in the same 5 mice... 58

M1: Figure 5 4D analysis of vascular meshwork in basal and infarcted hearts..... 60

M1: Figure 6 Quantifying I/R injury, AAR and $CD31^{curly}$ localization in mice with the left ventricular 17 segment model..... 62

M1: Figure 7 Characterization of immune cell infiltrates into I/R injury..... 63

M2: Figure 1 Intratumoral spatial distribution of granulocytes and T cells 84

M2: Figure 2 Identification and quantification of intratumoral TAN subsets 88

M2: Figure 3 Spatial distribution and interaction of TAN and T cells in situ..... 90

M2: Figure 4 Correlation of TAN phenotypes and TIL effector function 92

M2: Figure 5 Conjugation and functional modulation of TIL by LOX-1^+ TAN provides evidence for PMN-MDSC activity in vivo..... 94

M3: Figure 1 Anatomical and cellular patterns in a human lymph node (LN). 113

M3: Figure 2 Light sheet fluorescence microscopy (LSFM) in melanoma diagnostics. 116

M3: Figure 3 From 2-D to 3-D and back – a capsular nevus in all protocol stages.119

M3: Figure 4 Melanoma metastasis assessment in human SLNs using LSFM. 121

M3: Figure 5 LSFM reveals metastasis missed by the gold standard procedure....124

Abbreviations

2-D. two-dimensional
3-D. three-dimensional
AAR. area at risk
AID. activation-induced deaminase
ARG-1. arginase-1
BALANCE. bleaching-augmented solvent-based non-toxic clearing
BCR. B cell receptor
CD31. platelet endothelial cell adhesion molecule (PECAM-1)
CD66b. CEACAM8, carcinoembryonic antigen-related cell adhesion molecule 8
CSR. class switch recombination
CTLA-4. cytotoxic T-lymphocyte-associated protein-4
DAMPs. damage-associated molecular patterns
DMP. data management plan
ECi. ethyl cinnamate
EORTC. the European Organization for Research and Treatment of Cancer
FFPE. formalin-fixed paraffin-embedded
FOV. field of view
G-CSF. granulocyte colony stimulating factor
GrzB. granzyme b
i.v. intra-venous
I/R injury. ischemia/reperfusion injury
iNTR. intra-tumoral neutrophil-to-T cell ratio
IT. information technology
LOX-1. lectin-like oxidized low-density lipoprotein receptor-1
LSCC. larynx SCC
LSFM. light sheet fluorescence microscopy
Ly6G. lymphocyte antigen 6 complex locus G6D
MHC. major histocompatibility complex
MI. myocardial infarction
MMP9. matrix metallopeptidase 9
MPO. myeloperoxidase
NA. numerical aperture
NETs. neutrophil extracellular traps
NIR. near infrared
NK cells. natural killer cells
OSCC. oropharynx SCC
PD-1. programmed-cell-death-protein-ligand-1
PMN-MDSC. polymorphonuclear myeloid-derived suppressor cell
RI. refractive index
ROS. reactive oxygen species
SCC. squamous cell carcinoma
SHM. somatic hypermutation
SLN. sentinel lymph node
TAN. tumor-associated neutrophils
TCR. T cell receptor
TIL. tumor infiltrating lymphocytes
VEGF. vascular endothelial growth factor

1. Introduction

Within this thesis, organic solvent tissue clearing using ethyl cinnamate (ECi) and light sheet fluorescence microscopy (LSFM) were applied in two published manuscripts to tackle immunological questions in the fields of cardiology[1] and oncology[2]. The studies cover technological advancements and adjustments to answer basic research as well as clinical research questions. Furthermore, the diagnostic potential of the methods was evaluated by visualizing lymph nodes of melanoma patients in the yet unpublished manuscript #3[6]. In this introduction, I will convey background information on the three major themes that interconnect the three manuscripts, namely i) the immune system in its healthy state and the reaction towards sterile inflammation and associated cellular patterns; ii) tumor biology, the importance of specific cellular components of the immune system, and patient staging, and iii) the technology and history behind tissue clearing and LSFM.

1.1. The immune system

The immune system is a complex, interactive network composed of lymphoid organs, versatile, specialized cells termed leukocytes and humoral factors, that together strive to protect the host organism. It is only actively perceived if engaged in fulfilling its purpose, defending the host from external or internal dangers, or if failing to control infection, tumor growth or to discriminate friend from foe, like in autoimmune diseases or allergy. The surveillance of a typical human body (roughly 0.07 m^3) by tiny cells (approx. 1000 μm^3), a difference of $1:10^{14}$ in volume, is not trivial (this is one fill of a bathtub in comparison to the whole Black Sea). To fight on friendly territory requires inspectors, checkpoints, a mobile army, strategy, precision, regulation, and memory. But it also requires speed. In general, the immune system can be distinguished in two parts, the fast and non-specific innate and the slower but trainable and precise adaptive immunity. Both divisions are strongly influenced by each other, granting mutual help and guidance[7].

1.1.1. Innate immunity

The term innate immunity commonly includes physical and chemical barriers as well as semi-specific humoral and cellular components that provide immediate host defence[7-

[9]. Nevertheless, all components are well conserved in jawed vertebrates and some are present in insects and plants as well[8].

Chemical or physical barriers such as pH, specialized keratin rich or mucosal epithelial barriers are important to prevent initial pathogen access. Besides, most of the cellular components of innate immunity consists of myeloid phagocytic cells. These are, amongst others, monocyte-macrophages, neutrophils and mast cells. These leukocytes are also called "professional" phagocytes, recognizing and phagocytosing senescent cells and pathogens via molecular pattern recognizing receptors. In response to infection, they release soluble mediators like histamine, reactive oxygen species (ROS) or lysozyme, creating an inflammatory milieu and recruiting other immune cells to which they present antigens[8]. Antigen presentation is mediated via digestion of either internal (all nucleated cells can do this) or phagocytosed external proteins and subsequent loading of short, linearized amino-acid sequences into the binding grove of major histocompatibility complexes (MHC), which are displayed on the cell surface[10]. Then, T lymphocytes can interact with these peptides, recognizing them with their specific receptors to mediate an adaptive immune response (explained below). These phagocytosing sentinels, like macrophages or dendritic cells, patrol tissue in search of irregularities. For example, a specific subset of immature dendritic cells, called Langerhans cells, patrol epidermis in search of antigens that they later present to other cells of the immune system at checkpoints within the lymphoid organs. They also act in an immunomodulatory manner, producing cytokines and interacting with the adaptive immune response[8]. Other cellular components are natural killer (NK) cells, which have the capacity for non-specific cellular cytotoxicity, being able to effectively kill infected or degenerate host cells[8].

In this thesis, we focused on cellular components of the innate immunity, especially neutrophil granulocytes[2]. We investigated their distribution throughout the murine heart following myocardial infarction, carrying out their ambivalent role as first responders to sterile inflammation[1]. We also investigated neutrophils associated with head and neck tumor and used spatial information to deduce their inhibitory potential towards effector T cells[2]. In general, the idea of a crude and unspecific innate immunity has changed in the past decade and also neutrophils are viewed from a different perspective today, as detailed below[11,12].

1.1.1.1. Neutrophil granulocytes and their role in inflammation and disease

Neutrophils are the most abundant myeloid cell type in human blood, comprising 40-70% of total white blood cells[13]. This stands in contrast to mice, where they compose only 10-25%[12,14]. In circulation, mature neutrophils have an average diameter of 7-10 µm. They are one of the major players during acute inflammation and reduction of their numbers in the blood leads to severe immune deficiency in humans and mice[12].

Neutrophils originate from myeloid precursors residing in the bone marrow. Mature neutrophils either stay in the marrow and can be recruited during inflammation, or leave, forming a cycling pool within the blood and associated organs[14]. In mice, mature neutrophils can be identified by the surface expression of lymphocyte antigen 6 complex locus G6D (Ly6G)[14], which was used as a marker in manuscript #1[1]. Ly6G is a 25 kD protein, part of the Ly6 protein family, and anchored in the plasma membrane[15]. There are reports that hint at a role of Ly6G in neutrophil recruitment[16], but its exact function is still unknown. In humans, neutrophils express, not exclusively, the surface marker CD66b (also known as CEACAM8, carcinoembryonic antigen-related cell adhesion molecule 8), which can be upregulated during activation and might play a role in adhesion[17,18]. CD66b is an Ig-related protein anchored in the plasma membrane and can heterodimerize with other members of the CEACAM family[19].

The half-life time of neutrophils in circulation is heavily debated. Estimates range between hours to days in humans. The difficulty assessing their circulatory time is due to the residence of mature neutrophils in other organs like the marrow, spleen and lung[14,20]. Without inflammation, neutrophils start displaying phosphatidyl serine on their surface and CXCR4 over time, which eventually leads to their elimination[14].

Mature neutrophils can be efficiently recruited to sites of infection in a matter of hours[21,22]. In order to be recruited from the circulation in a targeted manner, neutrophils depend on changes on the surface of the blood vessel-lining endothelium. Once patrolling or tissue-resident sentinels like macrophages, dendritic cells or mast cells encounter tissue damage (characterized by e.g. free adenosine triphosphate, changed collagen structure) or pathogens (lipopolysaccharide, CpG oligodeoxynucleotides) via pattern recognition receptors, they release inflammatory mediators like histamine, cytokines and interleukins. Most mediators act locally, triggering surface changes in neighboring endothelial

cells, which initiates neutrophil recruitment[6]. Others, such as the granulocyte colony stimulating factor (G-CSF) also have systemic effects. G-CSF triggers the acute release of millions of neutrophils from internal stores like the bone marrow into the circulation[23-25].

In general, neutrophil extravasation from the blood to inflamed tissues involves the following steps: tethering, rolling, adhesion, crawling and transmigration[26]. Fast upregulation of P- and E-selectin (also CD62P/E) expression on endothelial cells in response to inflammation leads to the tethering of neutrophils via glycoprotein ligands like P-selectin glycoprotein ligand-1[27,28]. They are slowed down and roll along the "sticky" endothelium, eventually coming to a halt through additional integrin interactions or exiting into the circulation again. Once they halt, they are activated by sensing danger- or pathogen associated molecular patterns and pro-inflammatory cytokines secreted by macrophages within the tissue to unfold their full potential. Active cell migration is initiated and neutrophils crawl to endothelial cell-cell junctions. There, the transmigration through the endothelium and the basement membrane requires the interaction with integrins and junctional proteins, like platelet endothelial cell adhesion molecule-1 (CD31). CD31 is highly expressed by endothelium throughout the body and was used within this thesis as a general marker to visualize blood vessels. However, also neutrophils and T cells express CD31, which they lose during transmigration into tissues or shed upon activation[29,30]. For transmigration, neutrophils may take either a paracellular or transcellular way, with the latter being slower (reviewed here[12]).

Once extravasated, the primed neutrophils follow "end target" chemoattractants, like bacteria-derived *N*-formyl-methionyl-leucyl-phenylalanine or chemokines[12]. In mice, these are CXCL1/2 and 5 whereas the human analogue is CXCL8. CXCL8 can be released from activated epithelium and is sensed by neutrophils via CXCR2[31]. As soon as they arrive at the recruitment site, neutrophils release ROS and specified granules, which contain antimicrobial peptides or enzymes digesting extracellular matrix. They actively clear debris or engage and kill pathogens by phagocytosis or the formation of neutrophil extracellular traps (NETs). NETs are made of nuclear DNA, which is explosively released by dying neutrophils to the outside covering and slowing invaders and marking them for phagocytosis[32]. Exposition of core histones leads to further inflammation progression[33] and is itself highly toxic to host cells, fungi, and bacteria[34]. NETs are further decorated with antimicrobial peptides able to directly kill pathogens. One central effector protein is myeloperoxidase (MPO), which is released and locally synthesizes ROS. Thus, neutrophils

are effectively slowing and killing invaders, but also cause considerable bystander damage in the process due to the unspecific mechanisms at work[12,35].

However, neutrophils cannot just be viewed as rampaging foot soldiers. They act towards resolving inflammation and even healing, too. For example, matrix metallopeptidase 9 (MMP9) is not only associated with transmigration, it also promotes removal of damage-associated molecular patterns (DAMPs) containing intracellular proteins, including actin and tubulin. It also activates vascular endothelial growth factor (VEGF), promoting revascularization of injury sites. The pro-angiogenic role of neutrophils is more and more recognized since it seems to be exploited by various cancer cells[12,36,37].

During inflammation, neutrophils also recruit monocytes, blood-borne precursors of macrophages expressing α4β1 integrin, to inflamed tissue e.g. by promoting endothelial expression of vascular cell adhesion molecule 1[38]. Ultimately, this leads to neutrophil clearance via phagocytosis by macrophages, paving the way for the resolution of inflammation and tissue repair. Phagocytosis of neutrophil debris by macrophages also causes downregulation of IL-23 synthesis and therefore ultimately lowers G-CSF release, reducing mobilization of neutrophils from the bone marrow[12].

Neutrophils have also been shown to regulate adaptive immune responses. In general, neutrophils promote B-cell derived humoral response, releasing CD40 ligand or B-cell activating factors when located in the peri-marginal zone in the spleen. On the other hand, they can suppress cellular immune response carried out by cytotoxic T cells. They have also been associated with the suppression of T cell proliferation and function in acute inflammation (reviewed here[39]). More of their regulatory role, specifically in tumors, is explained below and addressed in one paper of this thesis (Si *et al*, 2019)[2].

In general, this regulatory potential may be due to a high degree of plasticity. The expression of Toll-like receptors and surface integrins can vary, and neutrophils can exert both anti- and pro-inflammatory behaviour[40,41]. It has also been shown that the presence of pathogens can change these phenotypes. To date, it is not entirely clear if indeed separate lineages exist or if neutrophils change their profile over the course of their life cycle, dependent on the ambient conditions[12].

In general, neutrophils are adversely associated with many inflammatory diseases[42]. One prominent example is acute myocardial infarction (MI), where they play an ambivalent role, participating in pathology and resolution[43].

1.1.1.2. Myocardial infarction as a model of sterile inflammation

MI is a disease of the circulatory system accountable for over 9% of all deaths in the EU28 as of 2015. This means, that nearly 97/100.000 EU28 inhabitants die of MI every year[44]. MI occurs if a coronary artery is blocked, which hinders blood flow, thus leading to downstream ischemia of the heart muscle tissue. In a routine clinical procedure, this blockage is typically removed, either enzymatically or during invasive operation. Most frequently used for direct treatment are so called stents, stabilizing and reopening the artery[45]. It is vital to restore oxygen and nutrient supply to the heart muscle tissue as quickly as possible, but in turn, sudden reperfusion also causes further damage to cardiomyocytes. This phenomenon is termed "myocardial reperfusion injury"[46] or "ischemia/reperfusion injury"(I/R injury)[43,47] and gains more relevance with increasing survival rates of the primary infarction due to increasing risk of complications later[45]. An I/R injury mouse model is used in manuscript #1[1].

1.1.1.3. The ambivalent role of neutrophils in MI

The lack of oxygen and nutrients during MI, but also the sudden reperfusion of muscle tissue, leads to cellular damage and thus to a massive release of DAMPs. An example is high-mobility group box 1, typically associated with chromatin, and detection of this DAMP by e.g. neutrophils in the extracellular space is facilitated by pattern recognition receptors like receptor for advanced glycation end products or Toll-like receptors[48-50]. This results in the fast recruitment of neutrophils[49]. Mainly located at the ischemic border zone, they release ROS, causing acute inflammation and ultimately cardiomyocyte death[43]. Importantly, neutrophil production and retention in the bone marrow depends on the time-of-day[51] and at the beginning of the active phase of the organism, neutrophils have a higher capacity to migrate into the myocardium[52]. Consequently, time-of-day of symptom-onset also has an influence on patient survival and infarct size in a clinical setting[53].

However, simply decreasing neutrophil recruitment to the heart, reducing ROS production by blockage of MPO or depleting neutrophils in general[54] has yielded heterogenous results in terms of infarct size and long-term disease development in various animal models (reviewed here[43]). This might be due to protective neutrophil functions associated with inflammation resolution, revascularization[12] and their potential to influence

other cell types towards tissue repair[55]. The importance of neutrophils in patient development post-MI is therefore obvious. Whether the occurrence of different functional phenotypes of neutrophils, also observed in infections[41] or cancer[40], is time, context or lineage dependent remains elusive[43].

1.1.2. Adaptive immunity

The other important half of the immune system of vertebrates is adaptive immunity. It is comprised by T and B lymphocytes as well as subsets of dendritic cells and is characterized by its ability to be trainable in precision and is thus considered to be specific. Here, specificity is derived from highly variable receptors. The potential specificities are 10^8 for T cell receptors (TCR) and 10^{10} for B cell derived antibodies, which is adequate to protect the host from the various pathogens encountered throughout life[7].

Every cell can only carry a receptor of a single specificity, which is determined early in development, before encountering antigens. Both cell types develop from common lymphoid progenitors in the bone marrow. In a developmental phase in either the thymus (T cells) or the bone marrow (B cells), autoreactive clones are negatively selected. After this, naïve cells, i.e. cells that have never met their specific antigen, are released into the circulation and start to patrol the periphery, mainly secondary lymphoid tissues like lymph nodes, tonsils and spleen, in search of their antigen. The effector responses upon antigen recognition are characterized by two stages. First, a presented antigen is recognized, leading to cell priming, activation, massive proliferation and further differentiation. This usually occurs in the lymphoid tissue and is closely connected to observed cellular patterns, which are described in more detail below. These steps to maturity take several days, which is why the initial adaptive reaction is much slower compared to innate immunity. In a second step, the effector response takes place, which is cytotoxic or humoral for T or B cells, respectively. The high specificity of the expanded clones can be preserved in form of long-lived memory cells, that might be reactivated when needed (reviewed here[7]).

In the manuscripts of this thesis, T cells are addressed in their cytotoxic effector role during cancer and both, T and B cells are used to visualize cellular patterns in lymph nodes.

1.1.2.1. T lymphocytes

T cells are characterized by their specific receptor. The TCR forms a complex with non-covalently associated CD3 signaling homo- and heterodimers (CD3$\varepsilon\gamma$, CD3$\varepsilon\delta$, CD3$\zeta\zeta$) crucial for translating external TCR-stimuli into cytosolic signaling pathways, e.g. via recruitment of various proteins[56]. Hence, all T cells are positive for CD3ε, making the molecule a good target for T cell visualization which was utilized in manuscripts #2 and #3. The TCR binds short, linear peptides that are loaded into and presented by MHC on other cells. Depending on the co-expression of either CD4 or CD8, T cells can interact with MHC class II or class I, respectively. MHC class II is mainly restricted to professional antigen-presenting cells, while MHC class I is expressed by all nucleated cells of the body. Hence, CD4+ T cells mostly mediate processes between immune cells, either helping initiate, guide and execute immune responses (helper cells) or regulate and terminate responses, leading to local tolerance (regulatory T cells). On the other hand, CD8+ T cells can scan all nucleated cells of the body for internal pathogens or disease-related changes, e.g. tumor formation.

T cells mature in the thymus. Here, they are positively selected for their ability to bind MHC molecules with intermediate strength, while subsequent negative selection deletes all clones reactive to presented self-antigens. Subsequently, naïve T cells leave the thymus and move constantly within the lymphoid tissue in search for their antigen.

1.1.2.2. B lymphocytes

B cells develop in the bone marrow. Like T cells, they bear a B cell receptor (BCR) on their surface. When they leave the bone marrow, they are naïve and carry a single, unique BCR version. In contrast to T cells, this BCR can detect antigens within the three-dimensional space. Therefore, it can detect proteins in their folded appearance on cell surfaces. Upon contact with their antigen and simultaneous co-stimulation, they can release their BCR into the circulation. These proteins, called “antibodies”, specifically bind a certain epitope which might lead to neutralization of virions or toxins or opsonization of pathogens and tumor cells[57]. The initial response is comprised of relatively low affinity IgM antibodies. Further specialization due to antibody class-switch or affinity-maturation occurs in germinal centers within lymphoid organs (described below).

In general, antibodies are the humoral response of the adaptive immunity. Their ability to bind specific proteins is utilized to research and visualize the abundance and location of target proteins in cells with many techniques, including microscopy.

1.1.2.3. Adaptive reaction to antigens and associated cellular patterns

Adaptive immunity with its highly specific approach faces a caveat: there is a host of B and T cell clones with their individual receptor specificities distributed all over the body, but antigen amounts might be low, and access might be locally restricted. In order to increase the likelihood of matching receptor specificity with antigen, antigen-presenting cells like macrophages or dendritic cells scavenge debris within the body's periphery and subsequently display antigens to T and B cells within the secondary lymphoid organs, namely spleen, tonsils and lymph nodes[7].

Taking the latter as an example, there are clearly defined cellular patterns that help mount a proper adaptive immune response. Various afferent lymphatic vessels carry lymph, which is derived from interstitial fluid, to the so-called draining lymph nodes. Thus, it carries proteins from the periphery into lymphoid organs. Lymph passes the capsule, which isolates the lymph node from surrounding tissue, and enters the lymph node itself. Here, it streams around the cortex with high presence of B and T cells, the paracortex, where mainly T cells are encountered, and the medulla, to eventually leave the node by an efferent lymphatic vessel in the sinus (Intro Figure 1). While passing the afore mentioned zones, antigen is taken up by lining macrophages. Within the cortex, T cells surround B cells which accumulate in roundly shaped primary follicles. Within follicles, follicular dendritic cells present trapped immune complexes on their surface. The complement component C3d-coated, opsonized complexes are bound to the surface of the dendritic cell via complement receptors CR2 and CR3[58]. Thus, the three-dimensional (3-D) protein structure is preserved and B cells are allowed to search for their epitope, the part of an antigen recognized by their BCR (reviewed here[7]).

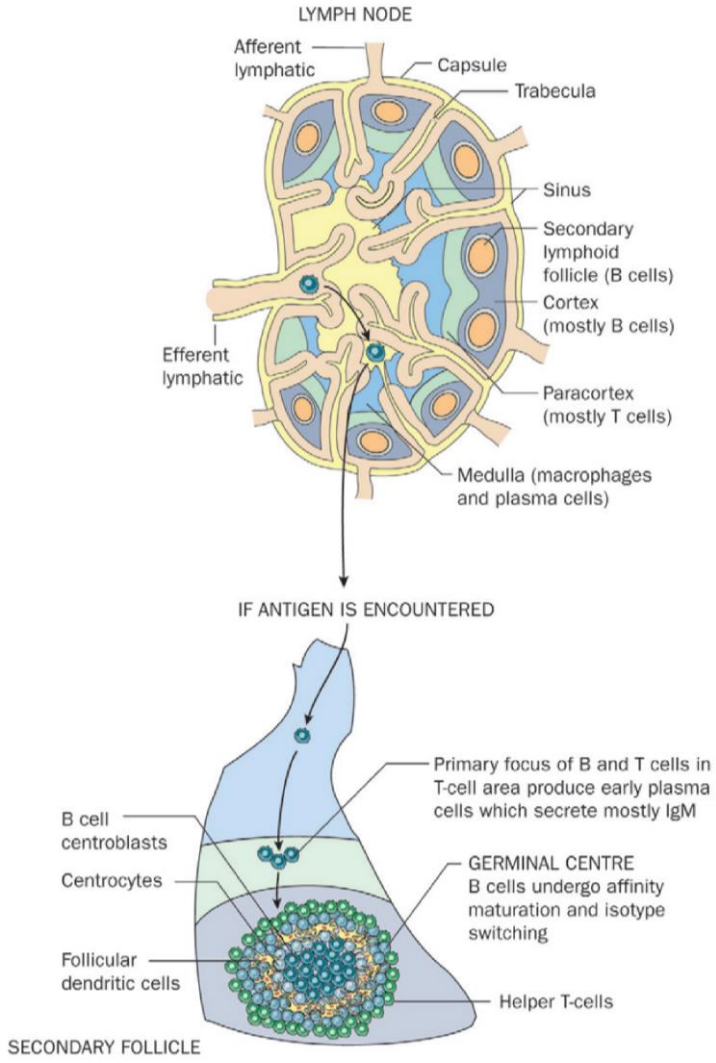

Intro Figure 1 Anatomical architecture and cellular patterns of a lymph node

Top: Schematic cross section of a lymph node showing major architectural and cellular arrangements. Antigen arrives through afferent lymphatics from the periphery.

Bottom: If antigen is encountered by B cells in the cortex, they undergo clonal expansion, forming a germinal center within a lymphoid follicle. These are surrounded by T cells.

Graphic adapted from Parkin *et al.*, Lancet, 2001[7].

If a B cell binds its antigen via its BCR under these circumstances, the BCR-antigen complex is internalized, digested, and different short, linear peptides are loaded upon and presented within MHC class II. These linear fractions of the original protein detected by the B cell can then be recognized by CD4+ T helper cells. Following cytokine release of B cell growth factors, this clone starts to divide. The clonal expansion of cells requires more space, further growing the then called secondary follicle[6] containing a germinal center. T helper cells are recruited into the B cell follicle and line the border of this structure, influencing the internal milieu and help B cells initiate a proper humoral response. In the beginning, an IgM response is mounted (Intro Figure 1).

Within the germinal center, B cells that found their antigen undergo further alterations, aiming at higher antibody affinity via somatic hypermutation (SHM) and changed antibody function via class switch recombination (CSR). In short, both processes are initiated by an enzyme termed activation-induced deaminase (AID. AID deaminates cytosine bases to generate uracils, thereby initiating a DNA repair cascade ultimately leading to

roughly one point mutation per cell division. These mostly cluster within the complementary determining regions of the BCR that facilitate direct antigen contact, which effectively changes the antibodies affinity[59]. Thus, highly efficient neutralizing antibodies e.g. against HIV might accumulate >100 mutations[60]. The same enzymatic activity also contributes to CSR, which is important to orchestrate and tailor the immune response to different dangers in different places (IgG in the blood, IgA in mucosa, IgE against helminths). After switching the class, B cells leave the germinal center baring a high affinity antibody and either become plasma cells, which reside in the medulla of the lymph node and secrete large amounts of antibody, or they differentiate to long-lived memory cells. In manuscript #3[6], we visualized and quantified structural patterns of lymph nodes like primary and secondary follicles and germinal centers within a human lymph node and used them for the relative orientation within the architecture of the organ.

In the case of naïve T cells, simply binding their antigen presented within their target MHC alone is not enough to activate them. Only upon co-stimulation via costimulatory receptors on the surface of activated antigen presenting cells (example: CD40 on B cells, and CD80/86 on APCs), T cells will proliferate and most progeny will be effector cells that can leave the lymphoid tissue and home towards the disease site[61]. CD8+ T cells are also termed cytotoxic killer cells, since post activation, these cells may interact with host cells presenting the T cell's antigen in its MHC class I and can directly release granules filled with molecules designed to kill the target cell. These contain, amongst others, perforin, which inserts transient pores in the plasma membrane through which granzyme b (GrzB) may enter the cell, inducing apoptosis[62-64]. In manuscript #2, effector T cells and capability to kill were identified via staining of GrzB.

1.2. Tumor biology

The word tumor is defined as an abnormal mass of cells that "divide more than they should or do not die when they should"[65]. A tumor may be benign or malignant, with the latter causing cancer[66]. Cancer is the second leading cause of death in the world following cardiovascular diseases, causing 8.9 million and 17.7 million deaths worldwide in 2016, respectively[67]. The word "crab" (Greek: karkinos) itself was introduced by the Greek physician Hippocrates (460-370 B.C.), describing spreading tumors of the skin[68]. Today, the Latin word cancer or "malignancy" are in use. Cancer categories are based on the location

of first appearance. Leukemia, lymphomas and myelomas originate from immune cells in the blood, bone marrow or lymphoid organs while sarcomas summarize cancers beginning within the body, like in bone, fat or connective tissues. Finally, carcinomas, in which the cancers in this thesis reside, are cancers derived from epithelia[66].

In this thesis, squamous cell carcinomas (SCC) from the head and neck region as well as metastases of cutaneous melanoma were investigated.

1.2.1. Squamous cell carcinoma

1.2.1.1. Epidemiology

The common term of "head and neck cancer", as the name suggests, refers to the site of cancer, but not its nature. However, other cancers with mesenchymal or neural origins are much less frequent than SCC[69]. SCC itself, given its epithelial nature, is a very heterogenous cancer with causes and epidemiology of SCCs differing depending on location, like skin[70], esophagus or lung[71]. In general, SSCs collectively cause >300,000 deaths annually worldwide[72]. In manuscript #2 SCCs located at the larynx (LSCC) or the oropharynx (OSCC) were analyzed.

Laryngeal cancer is mostly associated with tobacco and alcohol consumption[69]. Its projected incidence and death toll are 3/100,000 and 1/100,000 inhabitants in the USA in 2019, respectively. This accounts for 0.7% and 0.6% of all cancer diagnoses and deaths. The overall 5-year survival from 2009 to 2015 was 60.3%. Here, health care programs against smoking were successful, causing a steady decline in incidence of -2.4% in the last 10 years (summarized here[73]).

Oral cavity and pharynx cancers are much more common. The estimated incidence 2019 in the USA is 11.3/100,000 and 2.5/100,000 (10,800) deaths. The overall 5-year survival between 2009 and 2015 was 65.3%. Risk is also associated with tobacco and alcohol consumption, but also with human papilloma virus infection (HPV). Interestingly, while tobacco and alcohol-related cases are decreasing, HPV-related cases rise more strongly, resulting in an average increase of cases of 0.8% per year over the last decade[69,74]. With over 370,000 patients in the US in 2016, OSCC is much more prevalent than LSCC with over 96,000 patients at the same time.

1.2.2. Cutaneous melanoma

1.2.2.1. Epidemiology

In 2018, 60,700 people died due to cutaneous melanoma (3% of all cancer deaths), while more than 287,500 new cases were diagnosed worldwide. In Europe specifically, 19 new cases per 100,000 inhabitants are reported by the World Health Organization[75]. Melanoma incidence was increasing by about 3% annually in fair-skinned populations from 1982 to 2011 and is predicted to increase until at least 2022 e.g. in the UK and the USA[76]. In 2017, melanoma had the fifth or sixth highest incidence in males and females in the USA, respectively. Accounting for 72% deaths in the USA, melanoma is the deadliest of all skin-cancers (basal cell and squamous cell skin cancers were excluded)[77]. Risk factors include ultraviolet radiation and subsequent sunburns, indoor tanning, phenotypic characteristics like fair skin or the tendency to freckle. Inherited gene mutations causing melanoma only account for a small proportion of all cases (reviewed here[78]).

1.2.2.2. Origin and markers of melanoma

Melanoma derives from the malignant transformation of melanocytes, which are typically located at the basal layer of epidermis, hair bulb, ears and meninges[79]. There are about 1200 melanocytes per mm^2 skin[80]. The ratio of melanocytes and keratinocytes in the epidermal basal layer is 1:10, but through dendritic processes, one melanocyte is in contact with 30-40 keratinocytes in the epidermal melanin unit[79,80]. Melanocytes are pigment-producing cells, mainly responsible for production of melanin within melanosomes and their cell-to-cell transfer to keratinocytes via their processes. Within the keratinocytes, melanin granules accumulate above the nucleus to protect the DNA from UV radiation. All in all, the amount of melanin in keratinocytes determines the skin color (reviewed here[79]). Interestingly, they normally divide less than twice per year[81].

Due to the origin, most markers used to determine melanoma also stain melanocytes in the skin. Markers used in clinical diagnostics as well as in this thesis are the S100 family and Melan-A. S-100 is a family of proteins expressed in many cells, like glial cells, Schwann cells, melanocytes and dendritic cells. These proteins are therefore associated with a variety of functions including cell motility and growth. S100 staining has a melanoma sensi-

tivity of >89% concerning primary melanoma and >86% concerning metastatic melanoma, at least on formalin-fixed paraffin-embedded (FFPE) sections. However, due to co-expression by other cells, its specificity is <80%. Therefore, other markers are additionally used. Melan-A, also known as melanoma antigen recognized by T cells-1 (MART-1), is a membrane protein of melanocytes, melanoma and retinal pigmented epithelium. It is situated in membranes of the endoplasmic reticulum or Golgi apparatus or membranes surrounding melanosomes. Melan-A is important for the functionality of the premelanosome protein known as Pmel or gp100, which is in turn hypothesized to be important during the polymerization of eumelanin. Melan-A is reported to have a sensitivity of 83-100% and 71-88% for marking primary or metastatic melanoma, respectively. Its melanoma specificity is reported to be >81% (summarized here[82]).

1.2.3. Hallmarks of cancer

The causes and symptoms of cancers are very different, but it is possible to derive some underlying patterns, occurring, at least in part, in all of them. These underlying principles were summarized by Hanahan and Weinberg, 2000, in Cell[83] and updated 2011 in the same journal[84]. They suggest that most cancers acquire, via different mechanisms, the following core hallmarks during their development. Cancers thus i) enable replicative immortality; ii) induce angiogenesis; iii) resist cell death; iv) sustain proliferative signaling; v) evade growth suppressors; and vi) activate invasion and metastasis[83,84]. Especially the latter is of importance in manuscript #3 and described in more detail at the example of melanoma below. Recently proposed arising hallmarks include the capability to i) deregulate cellular energetics towards more effective proliferation; and ii) to avoid immune destruction. Furthermore, two enabling characteristics, namely i) genomic instability and mutation, and ii) tumor-promoting inflammation by innate immune cells help tumors acquire the above mentioned hallmarks[84]. Below, hallmarks important in this thesis are illuminated in the light of the relevant cancer entity.

1.2.3.1. Melanoma and SCC avoid immune cell-mediated destruction

TYPICAL EFFECTOR CELLS

Antitumor effector cells are those that either detect changes in surface expression, like NK cells detecting the absence of MHC class I, or T and B cells, which are able to detect

mutated protein versions either processed or whole, so called neo-antigens[85]. The mutational load of cancers and thus the availability of neo-antigens required to mount a proper adaptive immune response varies between cancer entities. Melanoma exhibits the highest accumulation of mutations and neo-antigens[86] and thus neo-antigen-specific T cell reactivity has been studied extensively[87]. In general, a high density of tumor-infiltrating lymphocytes (TIL) is associated with good prognosis, as shown for SCC[88] and melanoma[89], to only name a few[90]. However, in the tumor microenvironment, T cell responses might be repressed, causing T cell exhaustion[91]. These observations combined are the foundation of modern adjuvant therapies, re-activating and dis-inhibiting the immune system[89].

IMMUNE EVASION AND ESCAPE

Immune-mediated destruction of cancer cells leads to the selection of clones that have mutations protecting against eliciting immune responses. Thus, an inefficient antigen-processing machinery[92] or downregulation of MHC class I can be beneficial to evade T cell mediated cytotoxicity, but enhances NK cell effectiveness[78,85]. Melanoma cells might also secrete VEGF or IL-8, limiting antigen presentation and promoting anti-inflammatory M2 macrophages[93-96]. IL-8 secretion of SCC correlates with poor prognosis as well, with IL-8 effectively recruiting neutrophils[93,94]. In both malignancies, upregulation of suppressor proteins like programmed-cell-death-protein-ligand-1 (PD-L1) on the surface of the tumor cell and PD-1 and cytotoxic T-lymphocyte-associated protein-4 (CTLA-4) on the T cell leads to downregulation of cytotoxic T cell effector functions[78,97]. These interactions are so called immune checkpoints and new therapeutics aim to block them, ultimately disinhibiting the immune system (explained below).

1.2.3.2. Neutrophils causing tumor-promoting inflammation

SUBSETS OF NEUTROPHILS AND PMN-MDSCS

The perspective on neutrophils has changed from mere bystanders to integral contributors in cancer development and progression[98]. The presence of natural killer cells, T cells, B cells, dendritic cells and macrophages[99] has been mentioned above. Also neutrophils are present in various cancers in high amounts, including melanoma, lung, breast and cervical cancers and others, and neutrophil invasion into the tumor is mostly associated with a bad prognosis[98,100-102]. Some studies observed pro-tumor functions (reviewed

here[103]), whereas others reported that tumor-associated neutrophils (TAN) also have antitumor properties[104,105]. Only recently, neutrophil plasticity to certain cues within the tumor microenvironment have been described in mice[106]: while neutrophils exhibited an antitumor phenotype (N1) in the presence of interferon β[107], they exerted pro-tumor functions (N2) in the presence of transforming growth factor β[40]. Adding an additional layer of complexity, the widespread term "polymorphonuclear myeloid-derived suppressor cells" (PMN-MDSCs) is mainly used to describe human myeloid cells carrying out suppressive functions. However, it is argued that PMN-MDSCs are a subset of neutrophils capable of, but not restricted to, T cell suppression[98,108]. As described above, it is not clear whether these neutrophil phenotypes are due to plasticity or different origin. In humans, they can be identified with a large panel of markers[98,109], of which CD66b was used in manuscript #2. Another marker proposed to specifically identify neutrophils with pro-tumor characteristics and used in manuscript #2 is lectin-like oxidized low-density lipoprotein receptor-1 (LOX-1)[110]. In the following, proposed mechanisms of N2 pro-tumor neutrophils are illuminated.

Pro-tumor functions of N2 TAN

One mediator of the pro-tumor phenotype of neutrophils might be upregulation and secretion of CCL17, recruiting CD4+ regulatory T cells to the tumor[111]. CCL17 expression of neutrophils was also found to correlate with inferior prognosis in hepatocellular carcinoma[112]. Arginase-1 (ARG-1) is another protein associated with a tumor-supportive neutrophil phenotype in mice[113] and humans[114]. ARG-1 is thought to deplete arginine in the tumor environment. This ultimately leads to down-regulation of the CD3ζ chain upon T cell activation in an arginine free environment, which results in insufficient cytosolic TCR-signal transmission and T cell suppression[115]. However, ARG-1+ TANs have also been described in the context of good prognosis[116], questioning the sufficiency of ARG-1 activity alone to impair T cell function[98]. MMP9 is also N2 associated, promoting angiogenesis via triggered release of VEGF[117].

1.2.3.3. Invasive growth and metastasis

UNDERLYING HYPOTHESIS

One common hypothesis aiming at explaining the mechanism driving metastasis of epithelial malignancies is the epithelial-mesenchymal transition model[118]. Here, an expression shift in cell-surface proteins that facilitates cell-to-cell or cell-to-extracellular matrix interactions, reorganization of the cytoskeleton and the production of extra-cellular matrix degrading proteins, like MMPs is of importance. This may allow intravasation into deeper tissue layers[94,118].

ASPECTS OF SPACE AND TIME IN MELANOMA METASTASIS

Morbidity and mortality are highest in patients with metastatic disease and thus the prognosis of patients with metastatic disease is poor[119]. But at which step in the development of the malignancy does metastasis occur? Melanoma development is classically described by the Clark model[120]. This assumes a linear development from melanocytes to metastatic melanoma driven by accumulation of genetic mutations[120]. In the model, melanoma metastasizes very late into lymphatics, followed by systemic spread of the disease. However, this view is challenged by epidemiological and experimental observations and might only be true for a subset of melanomas (summarized here[121]).

For example, melanoma recurrence commonly involves distant sites apart from the initial primary tumor site. Interestingly, this recurrence occurs more than 5 years after the initial excision of the primary tumor in about 40% of patients[122]. This is referred to as metastatic dormancy[121,123]. Hypotheses about the underlying mechanisms agree on the statement that disseminated cells have to overcome some barriers encountered in their new environment, delaying metastases expansion[121].

Another challenging phenomenon is that >4% of patients are diagnosed with metastatic melanoma without a known primary tumor[124]. It is hypothesized that melanocytic movement beyond epithelial layers is not a unique feature of malignant cells, but a feature of melanocytes in general[121]. These internal benign melanocytic proliferations are regularly encountered, for example as intracapsular or trabecular nevi within lymph nodes (also in manuscript #3)[6,125,126].

1.2.4. Cancer staging and treatment: example melanoma

Treatments generally evoke benefits for the patients but are also associated with costs and side-effects. Therefore, it is important to categorize the severity of a disease before treatment. The gold standard of melanoma diagnostics is, as in most cancers, histopathological classification and risk assessment[119].

1.2.4.1. Patient staging – access to treatments

Melanoma can be routinely identified by local dermatologists or in specialized hospitals. In a first step, either a biopsy of the potential tumor is taken to confirm its malignant nature in histology, or, in clear cases, a direct wide local excision is carried out, with safety margins of up to 2 cm. In general, patients are staged according to disease severity and their risk of progression. Hereby, the tumor thickness of the primary tumor (T stage, Breslow-index)[127] is measured. Ulceration is incorporated in the T stage as well and is independently associated with poor prognosis[119]. For primary localized melanoma without lymph node involvement, the 5-year relative survival is 98% in stage 1 melanoma[128,129].

Most patients are diagnosed before lymph or distant metastases occur[119]. However, if the analysis reveals heightened metastasis risk (tumor depth exceeding 1 mm or presence of additional risk factors such as young age), the draining lymph node called sentinel lymph node (SLN) of the skin area where the primary tumor was located is identified during operation and excised (SLN biopsy)[119]. This is due to the phenomenon that melanoma mostly metastasizes early into regional lymph nodes before spreading systemically. Lymph node identification is typically achieved by injecting a radioactive or fluorescent small molecule probe peritumorally. The lymphatic drainage carries the probe to the SLN, where it is enriched. During operation, the SLN can thus be identified and surgically removed[130]. Subsequently, the lymph node is processed for FFPE histology and few representative, thin sections are analyzed. The N stage depends on the SLN status. It depends on whether tumor exists within the node or not. It also takes the amount of SLNs or other lymph nodes affected within the same lymph basin into account.

Finally, if there are any distant metastases detected (M stage), the disease severity is highest (stage IV). The average 5-year relative survival rate of melanoma patients with distant metastases is around 23%. With newly available immunomodulatory treatments, the survival rates are increasing rapidly[129].

1.2.4.2. Therapies focusing on immune cell activation

In order to prevent relapse of patients with resectable melanoma, adjuvant treatments are in place. Most modern treatments follow the agenda to (re-) activate the immune system in order to achieve tumor clearance. This technique is called immune checkpoint blockade. In this sense, immune checkpoints are mainly inhibitory signals from the environment to cytotoxic CD8+ T cells.

One example is the reactivation of T cells by the antibody-mediated blockade of CTLA-4 e.g. ipilimumab. CTLA-4 is expressed on T cells and competes with the costimulatory CD28 for its ligand, B7 (CD80/CD86), on antigen presenting cells. CTLA-4 is also reported to induce T cell arrest. Once CTLA-4 is blocked, T cells are readily activated (reviewed here[131]).

Another example is the dis-inhibition of cytotoxic T cell effector function via blockade of the PD-1/PD-L1 pathway. PD-L1, which is expressed by antigen presenting cells, non-lymphoid tissues such as heart and lung but also tumor cells, interacts with PD-1 on T cells as mentioned above. This downregulates T cell activation or counteracts costimulatory CD28 signaling[132]. Disinhibition is achieved by antibodies like nivolumab, binding and blocking PD-1. Furthermore, PD-1 is expressed by other immune cells, like B cells and natural killer cells as well[131].

Treatments with ipilimumab[133], as well as nivolumab[134], have positive effects on both relapse-free survival and overall survival. CTLA-4 blockade has less strong positive effects and is associated with many adverse events, which led to treatment discontinuity in 42.6% of the patients compared to only 9.7% treated with anti-PD1 treatment in a comparative study[134]. The introduction of checkpoint blocker therapy, along with other targeted approaches, has raised the 5-year survival rate for metastatic melanoma from less than 10% to up to 50%. Interestingly, it is still unknown why some patients are resistant against systemic therapy[78].

1.2.4.3. The risk of not being treated – staging difficulties

Although there are good treatment options available today, the disease must first be identified in order to be treated. Future patients might consult their physician for a skin screening. Around 70% of melanomas are correctly diagnosed during a clinical inspection by a dermatologist. This can be enhanced to 90% using dermatoscopy, which leaves 10%

of not reliably detected melanoma cases[78]. On the other hand, there is a tendency towards overdiagnosis[135], leading to unnecessary excisions with no effect on patient survival in general[136].

Secondly, if melanoma is identified within the excised sample during histopathological analysis and the risk for metastasis is high, the SLN is determined during operation[119]. Interestingly, the removal of the SLN itself is not associated with better melanoma-specific survival rates[137]. However, the associated staging is required for the correct planning of follow-up treatment strategies and a more reliable prognosis[119].

At this stage, there might be complications during operation: the lymphatic drainage might be altered, or the expertise of the operator might be low and therefore other lymph nodes might be excised while the true SLN remains within the body. Thus, the patient would not be staged correctly[138,139]. Also, during subsequent FFPE histopathology, only few representative thin sections are considered. The European Organization for Research and Treatment of Cancer (EORTC) provides a protocol that aims to achieve a micro-metastasis detection rate of 25% [140]. Here, a microscopic deposit >0.1 mm is assumed to be relevant, whereas other guidelines advise that any presence of metastases affects the SLN status[141]. Enhancement of existing protocols beyond that margin would come with high additional pathological workload[142]. As a result, current SLN biopsy and staging is associated with high clinical false-negative rates of approximately 10% (3+ year follow-up recurrence of the disease within the same lymph basin)[143]. One reason might be the analysis of only few representative histological slices, leading to technical false-negative findings, thus denying patient access to treatment. Beyond that, recent findings suggest that the exact size of the metastasis within the lymph node correlates negatively with melanoma specific survival of the patients, presenting another prognostic marker[119] that cannot be assessed using two-dimensional (2-D) FFPE representative slices. Therefore, we applied 3-D light sheet fluorescence microscopy combined with tissue clearing to SLNs, determining the exact size and locations of melanoma metastases within human lymph nodes in the unpublished manuscript #3.

1.3. Why and how to look inside an organ – mesoscopic 3-D imaging

The previously described immunological and tumor-associated phenomena all consist of at least 3-D objects and processes. However, most biological and clinical studies and especially routine histopathology rely on the analysis of 2-D thin slices. A multitude of slice generating methods exist, ranging from fresh frozen sections to FFPE histology. Despite the knowledge that what we see in slices is only a tiny excerpt of a sample, a "local reality", the analysis of so called "representative slices" is the gold standard of clinical histopathology to date[140-142]. On the one hand, that may be due to tradition and well-established protocols. On the other hand, science was simply lacking tools to image whole organs with cellular resolution. Already existing procedures to reach a quantitative impression of larger samples lack either localization context (flow cytometry), penetration depth (confocal microscopy), or resolution (computer tomography). Others, like sequential slicing, were connected with a high workload per sample that made incorporation into a routine setting impossible[1]. This changed in the past two decades. The combination of tissue clearing and LSFM features technical advances to overcome problems concerning scale, resolution and tissue penetration depth.

1.3.1. The problem with scale and penetration depth

The scale problem is characterized as follows: visualizing the volume of a single neutrophil of around 10 µm diameter (~400 μm^3) within an entire murine heart[1] with the size of 10 x 6 x 6 mm equals 360 mm^3 is a scale difference of about 1:1,000,000,000. Furthermore, while we strive to obtain information about the distribution of objects that are 10^9-times smaller in volume than the surrounding object, we want to see both at the same time. This is like looking at the blueprints of the entire Pyramid of Cheops (2.6 x 10^6 m^3) and searching for the architects hidden six-pack of beer (~2000 cm^3); or, sticking closer to North Rhine-Westphalia, searching a cup of coffee (350 cm^3) in Oberhausen's Gasometer (347,000 m^3) while viewing it from orbit. No matter if it is the photographer outside the Pyramid of Cheops or the biologist in front of a human lymph node, both need a large field of view (FOV) and a high resolution in order to even hope to achieve what they want to explore.

Another problem is that of penetration depth. To stick to our established comparison: if the photographer manages to bring a camera capable of the above-mentioned criteria and would take an image of the entire pyramid at once, it would only be possible to search the six-pack of refreshments standing outside on the wall. This is simply because visible light does not penetrate stone. The biologist faces the same problem, even though working with biological material. There are methods available that are capable of depicting cells in 3-D with a high resolution[144]. However, even specialized two-photon laser scanning microscopy, which is used for intra-vital imaging, achieves penetration depths a maximum of 1000 µm[145]. Furthermore, these are raster-based techniques. Acquiring a single large optical slice with high resolution can take minutes[146]. Therefore, this is not the technique required to image an entire organ consisting of thousands of optical slices in a diagnostic setup.

1.3.2. Key techniques for mesoscopic imaging

The solution to the problems mentioned above lies in the connection of multiple technologies. In the following, the basics of ultramicroscopy and tissue clearing and how these techniques combined might help revolutionize current histopathology will be explored.

1.3.2.1. Ultramicroscopy or light sheet microscopy

The concept of ultramicroscopy[147], also called light sheet microscopy or selective plane illumination microscopy[148], dates back to Siedentopf and Zsigmondy in 1903[147]. Instead of illuminating a specified region of the sample from below or above, a light sheet was used to illuminate the focal plane perpendicular to the objective. With this, the diffraction limit of the microscope could be broken, the nature of colloids reflecting the light could be described and Zsigmondy received the Nobel prize in chemistry 1925. Where Zsigmondy used sunlight or white light that fell through a slit in a box to form a non-coherent light sheet[149], modern laser technology and optics enhance the performance and robustness of the system. The principle remains the same: a very thin sheet of light created from a point laser by passing a cylindrical lens illuminates one plane in space simultaneously, perpendicular to the objective. This provides us the means to image so called

optical slices, 2-D information obtained without physical but optical sectioning of tissue[149].

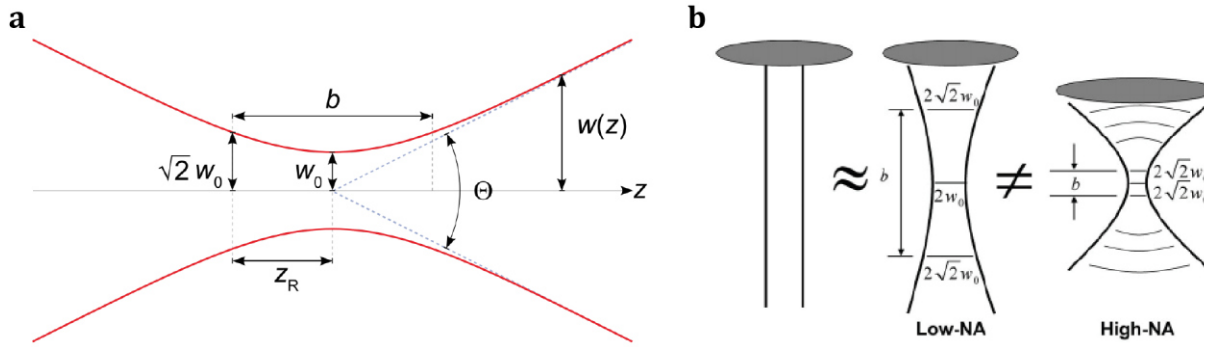

Intro Figure 2 The impact of NA on Rayleigh length (z_R)

(**a**) Physical characteristics of a Gaussian light sheet: total angular spread Θ which correlates with the NA, beam waist w_0, Rayleigh length z_R and dependend confocal parameter *b*, which is 2x z_R. Adapted from Mellisch, 2009[152]. (**b**) Depending on the NA, Θ is larger or smaller, which determines w_0 as well as the length of z_R and *b*. Adapted from Ralston *et al.,* 2006[153].

In summary, this method is perfectly suited for the fast imaging of 3-D samples. Illuminating the whole focal plane of the detecting objective at once while detecting the signal with e.g. a scientific complementary metal-oxide semiconductor camera oriented at a 90° angle. This stands in strong contrast to confocal or multiphoton microscopy, which scan a sample with a focused laser beam pixel by pixel. Furthermore, because of the uncoupling of sample illumination and emission detection, the Z resolution is defined by the product of the point-spread function of both objectives. Therefore, the axial resolution depends on the thickness of the light sheet and thus the numerical aperture (NA) of the lens focusing the light sheet. In theory, the optical slice can thus be ≥ 2x beam waist w_0 of the light sheet (Intro Figure 2a). However, there exists a physical trade-off. In order to create light sheets with a low beam waist (<5 µm,), a high NA is required[150]. Thus, the light's incidence angle (also angular spread, Θ) towards the beam waist is higher and the Rayleigh length z_R, and thus the confocal parameter *b* are shorter. Hence, the light sheet thickness is only low for a very short distance, leading to inhomogeneous image quality (beam waist with high Z resolution and high light intensity vs. outer regions)[151]. Therefore, to acquire homogenous images of larger samples, light sheets are generated with a lower NA, yielding a thickness

between 10-15 µm that stays nearly constant over centimeters (Intro Figure 2b, reviewed here[150]).

However, biological samples are inherently opaque, so light does not travel unperturbed through tissue. It is reflected, rapidly losing intensity in its original directionality.

The underlying reasons are important to understand in order to be able to overcome the problem of penetration depth.

1.3.2.2. Physical background: on scatter, refractive index and opacity

Why is tissue opaque? The answer lies in the physical properties of light and molecules. If light travels through space in the absence of molecules, in the absolute vacuum, it travels at its maximum speed, unobstructed. In comparison, while traveling e.g. in pure water, molecules are in the flight path. Susceptible electrons can absorb the light but re-emit the same wavelength as before nearly instantaneously without energy loss (elastic scatter). While such an interaction takes only about one femtosecond, the light is effectively slowed. The degree depends on the molecular density of the medium but also on the availability of electrons capable of absorbing the specific energy of a wavelength. The deceleration of light within a given medium is correlatively expressed by the refractive index (RI). The RI of water is 1.33. This means that light within vacuum travels 1.33 times faster than within water[150].

In summary, light is always scattered and slowed while travelling through media, but its intensity or directionality is not necessarily altered or reduced. This is true if a medium and thus the occurring scattering is homogeneous. Biological tissues are not. They consist of water (RI = 1.33), fat (RI = 1.45)[150], proteins (RI = 1.50 – 1.58)[154] and more. With such regional differences in the amount of scattering, light is deflected which results in intensity loss.

Thus, the reason for opacity of tissues is the heterogeneity of refractive indices encountered in tissues. Therefore, the key to render tissues transparent lies in homogenizing the refractive index throughout the sample.

1.3.2.3. Towards tissue clearing – principles and protocols

Today, a multitude of approaches exist that aim to clear biological samples. However, the principle behind all of them is the same: to homogenize the refractive index throughout the tissue, allowing light to pass through tissue with minimal loss of intensity or directionality.

WATER BASED CLEARING

One approach is to simply immerse the organ in a water-based solution with a high density of sugars, trying to match the RI of the sample as closely as possible. This works well for very small samples. For larger samples, clearing might take weeks, whereas the sample clarity can be low. Also, the matching solutions are very difficult to handle, viscous and prone to precipitation[150].

Since proteins are the high RI components of a cell, some protocols seek to lower the RI of the tissue towards the RI of water. Here, the entire sample is hyperhydrated. Even hydrophobic protein regions are hydrated by the use of urea[155]. This lowers the high RI of proteins towards the lower RI of water, with an endpoint of approximately 1.38[156]. This is the approximate RI of the cytoplasm of a cell[154]. In other protocols, lipids are often removed using detergents, such as Triton, Tween or SDS. This leads to a loss of protein. Of course, hyperhydration causes the sample to swell. Interestingly, this might even be utilized by so called expansion microscopy, physically enlarging normally small cellular details[157]. Moreover, the high viscosity of the imaging media (due to high density of sugars matching the high RI) and the fragility of the samples can cause problems while imaging or handling the sample. Popular protocols that follow this line of thought, are Sca*l*e[156] and CUBIC[158].

Another well-known procedure is CLARITY[159]. Here, samples are embedded in hydrogel, lipids are removed passively by detergents or actively by electrophoresis, and the RI is matched as described above.

ORGANIC SOLVENT CLEARING

There is also the possibility to remove the component of tissue with the lowest RI, water, and exchange it with something exhibiting a high RI, like organic solvents. First, the sample is dehydrated via ascending concentrations of different alcohols. Thereby, lipids

are solvated, leaving mainly proteins behind (RI = 1.50 – 1.58)[154]. In a second step, more lipids are removed from the sample and the RI of the remaining tissue is matched by an organic solvent that can also be used as imaging solution[150]. Examples for high RI solvents are dibenzyl ether (RI = 1.56)[160] or ECi (RI = 1.558)[161]. Today, many different organic solvent-based methods are available[160,162,163]. All shrink the tissue, which, in case of imaging entire organs with technical size restrictions on the imaging side, is beneficial.

CONCLUSION

There are many ways to achieve sample clarity[150,164]. Available protocols exhibit different strengths and weaknesses. In a general, rough comparison, aqueous buffer-based protocols typically swell the tissue, yielding a good sample clarity. However, the samples are fragile, the handling of the viscous imaging media is difficult and passive clearing approaches take multiple weeks. On the other side, sample clarity is quickly achieved with organic solvents. Due to dehydration, the sample shrinks, enhancing autofluorescence but reducing volume and therefore imaging time. Most organic solvent based approaches utilize toxic chemicals[160,162], but recent advances make use of non-toxic substances instead[1,161]. Throughout this thesis, ECi was used as the refractive index-matching agent[1,2,6].

1.3.2.4. Technological interplay yields cellular information of entire organs

Why did it take so long, until light sheet microscopy and tissue clearing technologies were combined? In 1914, Spalteholz pioneered organic solvent clearing that yielded unprecedented sample clarity of entire organs at the time[165]. He used these insights to further the knowledge of anatomy. Also, ultramicroscopy was theoretically available, as Siedentopf and Zsigmondy published the principle in 1903[147]. However, one key component for the successful combination of the two techniques was still missing, namely artificial fluorescent probes that could mark a specified target or endogenous fluorophores expressed by a genetically modified target cell.

1993, orthogonal-plane fluorescence optical sectioning microscopy was used to image tissue autofluorescence of the inner ear cochlea of the guinea pig[166]. 2004, selective plane illumination microscopy was introduced, imaging green fluorescent protein in naturally transparent Medaka and *Drosophila* embryos[148]. All these techniques hinge on the same

principle: using a light sheet to illuminate an entire optical tissue section perpendicular to the objective (Intro Figure 3a).

Then, in 2007, Dodt and colleagues, imaged optically cleared tissue using light sheet fluorescence microscopy for the first time[163]. While Dodt showed that imaging of both endogenous and artificial fluorescence is possible, clearing samples with organic solvents tends to quench fluorescence of expressed proteins either directly or 3-4 days after clearing[160,161]. This is because fluorescent proteins need to be hydrated in order to be able to absorb and emit light[150]. Therefore, dedicated aqueous buffer-based protocols were developed. Another workaround is to use antibodies conjugated to artificial fluorophores to target modified cells.

Clearing and LSFM was most prominently applied in tackling neuroscientific questions concerning the "connectome", yielding high resolution images of dendrites[163] as well as visualizing differential stainings of single neurons in a large portion of the brain (brainbow technology[167], combined with LSFM[168], and Tetbow[169]). Recently, tissue clearing and LSFM have been utilized to clear and image neuronal projections throughout entire mice[170]. Other exemplary questions concerning human developmental biology[171,172], kidney diseases[161] and bone anatomy[3] have been successfully engaged as well, while samples studied range from organoids[168] and fruit flies[163,168] to human embryos[171].

Within this thesis, organic solvent tissue clearing based on the use of ECi and LSFM was applied in two published manuscripts to address immunological questions in different fields[1,2] (Intro Figure 3b). But what about a step further towards a direct diagnostic clinical application?

1.3.3. Potential use of LSFM in clinical diagnostics

The potential of LSFM in clinical diagnostics is huge. The ability to image large volumes fast with cellular resolution provides unprecedented possibilities compared to the gold standard analysis of representative FFPE slices. LSFM can overcome the restrictions of the FFPE gold standard in predictive power (accuracy) and reproducibility (precision), especially when it comes to sampling errors within the vast volume of human biopsies[173] and the related inability to reconstruct the 3-D nature of structures with diagnostic relevance[174].

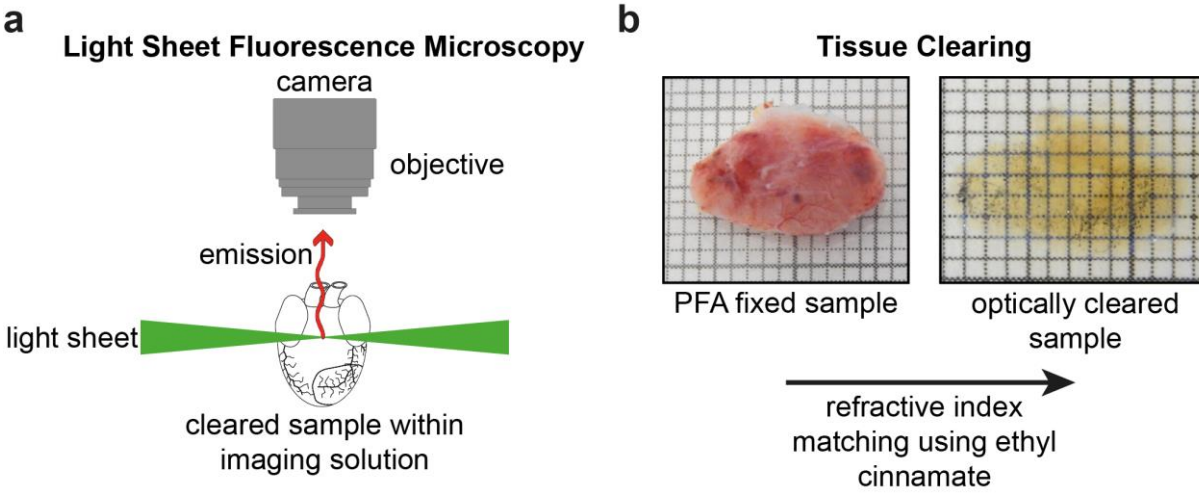

Intro Figure 3 Principles of light sheet fluorescence microscopy (LSFM) and tissue clearing (**a**) Characteristics of LSFM: sample excitation with light sheet perpendicular to the objective. Instead of fluorescence, also reflected light can be measured[147]. Graphic adapted from Merz *et al.*[1] (**b**) Macroscopic optical change of human lymph node before and after refractive index matching. Grid squares equal 1x1 mm.

This also comes with challenges concerning data processing and automated scoring. So far, LSFM has been applied to roughly assess human lymph node status in colorectal cancer[175]. Also, an open-top light sheet microscope was used to analyze fresh prostate and breast biopsies intra-operatively[176]. Fresh tissue was not cleared, therefore intra-operative penetration depth was limited. However, a nearly instantaneous, intra-operative guidance tool providing scanning speeds of 25 sec/cm^2 with tissue penetration depths of 160 µm is much more powerful than producing thin frozen sections, which is the standard procedure. Other human studies involve skin biopsies that can be characterized using autofluorescence alone[177] or the 3-D characterization of the lymphatic system in human bladder tumors[178]. More diagnostically relevant projects are summarized here[179].

At the end of this thesis, we show in an unpublished manuscript that it is possible to analyze human sentinel lymph nodes of melanoma patients before processing them for routine FFPE analysis. This yielded unprecedented insights into human lymph node architecture as well as cellular distribution patterns of both tumor and immune cells. LSFM analysis even provided new treatment options for one melanoma patient, highlighting the diagnostic potential of this methodology.

2. Aim

The biological scale at which cellular interactions and environments are typically characterized is microscopic (µm). Biological processes are entwined, always being in a balanced situation respective to external and internal forces influencing the system. In order to understand the cause and consequence of cellular distribution patterns in health and disease, like organ function or tumor metastasis, respectively, we need to avert our gaze from the sole 2-D slide-based perspective to face the mesoscopic scale (mm) and apply the knowledge to a three-dimensional system architecture.

Therefore, the aim of this thesis was to develop protocols and strategies to visualize immune cell distribution patterns in organs of mice and humans in the context of their surrounding 3-D architecture based on tissue clearing and LSFM. How focused is the neutrophil response following ischemia/reperfusion (I/R) injury within the mouse heart? Do neutrophils invade the I/R injury zone? In the context of squamous cell carcinoma, are neutrophils homogenously distributed if associated with the tumor? Do they influence their local microenvironment in a specific way, especially in terms of other effector cells?

Subsequently, the technical knowledge should be further utilized to explore the potential clinical and diagnostic applications of LSFM in tumor surveillance and patient staging. Is tissue clearing and LSFM analysis compatible with follow-up FFPE histology, being a prerequisite for assessing diagnostically relevant samples? How can multiple anatomical and cellular lymph node features be assessed with only 2 different channels? Is LSFM more efficient in detecting metastases compared to FFPE histology? Is it possible to exactly quantify the metastatic tumor load in a large pigment-rich human biopsy?

To that end, tailored 3-D assessment protocols should be developed featuring i) autofluorescence-attenuation to enable homogenous quantitative imaging in autofluorescent organs, ii) different antibody delivery routes, e.g. intra-venous injection or whole-mount staining in order to have fast readouts in mice and robust tissue penetration in human samples, iii) multiplexing different specific fluorescent signals while using the information about tissue architecture given by homogenized tissue autofluorescence alone, iv) quantitative strategies to determine cell populations, distances and exact volumes, and v) follow-up workflows of gold standard two-dimensional histology.

In the following thesis, I attempt to convey the concept that purely technical advances combined with a differential observation angle cannot only add to already existing

knowledge but can change one's perspective on biological complexity outside the single cell in its entirety. As a result of this change in perspective a wealth of new fundamental discoveries can be made, and new, clinically highly relevant information may be obtained, having the power to change therapeutic decisions.

3. Manuscripts

3.1. Prelude

The first manuscript is about shifting the perspective of researchers studying myocardial infarction in mice from 2-D to 3-D. Fundamental architectural questions, like "How does an entire, uncut mouse heart appear in 3-D?", are followed by more complex ones: How can we assess i) anatomical structure, ii) multiple ischemia/reperfusion parameters and iii) the ensuing early immune response simultaneously in an entire murine heart? What impact does the ischemia/reperfusion injury have on vascularization? How are invading immune cells distributed throughout the heart in response to such an injury? How can we quantify phenomena like this in the 3-D space?
The following work, published 2019 in Nature Communications, provides answers and insights into how tissue clearing and LSFM can be combined with intra-venously (i.v.) injected fluorophore conjugated antibodies to create a fast whole organ multiplex analysis that strives to deliver an overview of ischemia/reperfusion injury and response.

3.1.1. Media and License info manuscript #1

3.1.1.1. Supplementary Material deposit

Supplementary Material including tables, figures, videos, and required legends can be found on the attached CD at the end of this thesis, online or following this QR code to a personal repository. Links may be subject to change.
www.nature.com

Supplenmentary information

[provider: *Sciebo*, Password: MerzThesis]

3.1.1.2. QR codes and hyperlinks

Here, and throughout manuscript #3 I provided scannable QR codes to access supplementary information. Note that QR codes and hyperlinks will take you to the webpage provided by the journal or *Sciebo*. Links may be subject to change.

3.1.1.3. License info

3.1.2. Author contributions manuscript #1

Author contributions for the paper

Contemporaneous 3D characterization of acute and chronic myocardial I/R injury and response

SK: Sebastian Korste; SFM: Simon Frederik Merz; LB: Lea Bornemann

Experimental work

a. Mouse handling/surgery	SK 30%
b. Development of protocol & staining strategy	SK 50%; SFM 50%
c. Sample processing until LSFM	SK 75%; SFM 25%
2. Data acquisition	
i. LSFM	SK 50%; SFM 50%
ii. TTC planimetry	SK 100%
iii. Flow cytometry	SK 100%

Data analysis

1. IMARIS	
i. Vessel tracing	SFM 10%; LB 90%
ii. Thresholdings	SK 10%; SFM 80%; LB 10%
iii. Cell counting	SK 25%; SFM 50%; LB 25%
iv. Volume tracing/measurement	SK 33%; SFM 33%; LB 33%
v. Filament Model	SK 20%; SFM 20%
2. FlowJo	SK 100%
3. ImageJ	SFM 75%; LB 25%
4. Statistics	SK 45%; SFM 10%; LB 45%

Manuscript

1. Figure preparation	SK 15%; SFM 25%; LB 60%
2. Main Text	SK 25%; SFM 25%; LB 25%
3. Supplement preparation (Figure legends etc.)	SK 40%; SFM 40%; LB 20%

Simon F. Merz	Sebastian Korste	Lea Bornemann	Matthias Gunzer	Matthias Totzeck

3.2. M#1: Contemporaneous 3-D characterization of acute and chronic myocardial I/R injury and response

Journal: *Nature Communications*
Received: 4 October 2018, Accepted: 7 May 2019, Published Online: 24 May 2019
DOI: 10.1038/s41467-019-10338-2;
URL: https://www.nature.com/articles/s41467-019-10338-2#Sec22

3.2.1. Authors & Affiliations

Simon F. Merz*[,1,2], Sebastian Korste*[,3], Lea Bornemann*[,1], Lars Michel[3], Pia Stock[3], Anthony Squire[1], Camille Soun[1], Daniel R. Engel[1], Julia Detzer[4], Holger Lörchner[4,5], Dirk M. Hermann[6], Markus Kamler[7], Joachim Klode[2], Ulrike Hendgen-Cotta[3], Tienush Rassaf[3], Matthias Gunzer#[,1] and Matthias Totzeck#[,3]

*These authors contributed equally
#These authors jointly supervised this work

[1]Institute for Experimental Immunology and Imaging, University Hospital Essen, 45147, Essen, Germany
[2] Department of Dermatology, Venerology and Allergology, University Hospital Essen, 45147, Essen, Germany
[3]Department of Cardiology and Vascular Medicine, University Hospital Essen, 45147, Essen, Germany
[4]Max Planck Institute for Heart and Lung Research, Dept. of Cardiac Development and Remodelling, 61231, Bad Nauheim, Germany
[5]German Centre for Cardiovascular Research (DZHK), Partner site Rhine-Main, Frankfurt am Main, Germany
[6]Department of Neurology, University Hospital Essen, 45147, Essen, Germany
[7]Department of Thoracic and Cardiovascular Surgery, University Hospital Essen, 45147, Essen, Germany

Corresponding authors:

Dr. Matthias Totzeck
Department for Cardiology and Vascular Medicine
West German Heart and Vascular Center
Medical Faculty, University Hospital Essen
University Duisburg-Essen
Hufelandstraße 55, 45147 Essen, Germany
Phone:+49 201 723 4818
Fax: +49 201 723 5401
Matthias.Totzeck@uk-essen.de

Prof. Dr. Matthias Gunzer
Institute for Experimental Immunology and Imaging
Medical Faculty, University Hospital Essen
University Duisburg-Essen
Hufelandstraße 55, 45147 Essen, Germany
Phone:+49 201 183 6640
Fax: +49 201 183 6642
Matthias.Gunzer@uni-due.de

3.2.2. Abstract

Cardioprotection by salvage of the infarct-affected myocardium is an unmet yet highly desired therapeutic goal. To develop new dedicated therapies, experimental myocardial ischemia/reperfusion (I/R) injury would require methods to simultaneously characterize extent and localization of the damage and the ensuing inflammatory responses in whole hearts over time. Here we present a three-dimensional, simultaneous quantitative investigation of key I/R injury components by combining bleaching-augmented solvent-based non-toxic clearing (BALANCE) using ethyl cinnamate (ECi) with light sheet fluorescence microscopy. This allows structural analyses of fluorescence-labeled I/R hearts with exceptional detail. We discover and 3-D-quantify distinguishable acute and late vascular I/R damage zones. These contain highly localized and spatially structured neutrophil infiltrates that are modulated upon cardiac healing. Our model demonstrates that these characteristic I/R injury patterns can detect the extent of damage even days after the ischemic index event hence allowing the investigation of long-term recovery and remodeling processes.

3.2.3. Introduction

Restoration of perfusion after acute myocardial infarction is the most frequent and effective medical treatment, but the process may inflict massive ischemia/reperfusion (I/R) injury[1]. A hallmark of I/R injury is the major loss of the vasculature[2] accompanied by impairment of the endothelium. In parallel, I/R results in an extensive inflammatory response[3]. Within minutes, circulating neutrophils are attracted to the affected vasculature where they transmigrate into the damaged tissue with incompletely defined roles in injury progression or protection[4,5]. Macrophages, in turn, exhibit complex functions in cardiac inflammation and injury site repair peaking days after the onset of I/R[6]. A precise spatial identification and characterization of the cellular composition of the injured region reflecting the complex interplay between I/R-signalling and repair mechanisms, therefore, is essential for their breakdown into tractable therapeutic targets[7].

The established tools for the characterization of I/R injury and response assessment have several limitations. This particularly relates to the co-localization of pathophysiological events including inflammation and (re-) vascularization. The mainstay for cardiac injury analysis in animal models is measurement of metabolic activity of cardiomyocytes in serial thick sections using triphenyl tetrazolium chloride (TTC)[8]. However, this does typically not include advanced histological and immuno-histochemical co-assessments and fails to provide an accurate 3-D reconstruction of the affected tissue. To precisely localize and quantify the extent of cardiac damage, a global 3-D-structural analysis of the heart is mandatory. Light sheet fluorescence microscopy (LSFM) has been particularly effective to perform similar analyses and was previously used to image large tissue specimens[9,10], including the heart[11]. Therefore, we hypothesized that LSFM was capable of characterizing myocardial ischemia/reperfusion (I/R) injury in conjunction with significant I/R injury response mechanisms, particularly immune cell infiltration. However, the technique requires high tissue transparency. In murine organs, this can be achieved by complex, often toxic chemical pretreatments, collectively termed clearing[12,13].

We have recently introduced a non-toxic clearing method using ethyl cinnamate (ECi) as the refractive index-matching component[9]. While ECi performed well for murine organs, such as kidney and bone, it suffered, like other approaches, from extremely high tissue autofluorescence of the heart muscle. Until now, this made quantitative LSFM of whole hearts challenging.

Hence, we wished to (i) develop a readily applicable, non-toxic workflow with chemicals and tools that are commercially available, (ii) benchmark this work flow against standard I/R histology techniques in compliance with recent guideline recommendations[14], (iii) quantify I/R injury parameters in 3-D, (iv) assess the long-term impact of I/R injury following days after reperfusion and (v) relate the I/R injury zones to immune response mechanisms.

Here we introduce an ECi-based 3-D myocardial I/R injury assessment workflow, termed BALANCE (Bleaching-Augmented soLvent-bAsed Non-toxic ClEaring), to overcome the limitations of the current analysis tools.

3.2.4. Results

3.2.4.1. BALANCE enables 3-D whole heart imaging and analysis

Central to BALANCE is a peroxide-based bleaching step compatible with antibody-mediated fluorescence labeling in vivo. Bleaching was key to unlock lower wavelength channels for homogenous imaging (M1: Figure 1 and M1: Supplementary Figure 1 a and d). We tested other established protocols[15] for tissue autofluorescence reduction and found BALANCE to be the most suitable for homogenizing tissue autofluorescence fast and throughout the whole heart using our I/R injury protocol workflow (M1: Supplementary Figure 1, Supplementary Table 1 and Supplementary Note 1). Applying BALANCE to our samples, tissue autofluorescence itself could be used to visualize the overall heart muscle structure allowing clear detection of cardiomyocytes and their nuclei (M1: Figure 2 a and b) at much higher optical resolution than previously possible[16,17].

CD31, a surface molecule on endothelial cells, is a potential marker for vascular integrity[18]. Intravital staining with fluorescent anti-CD31 antibodies[9] revealed homogenously labeled vasculature- and heart-structures as shown before[19,20] (M1: Figure 2 a). BALANCE now allowed to combine autofluorescence and CD31 signals to precisely reconstruct prominent but delicate structures such as the aortic valve (M1: Figure 2 c and M1: Supplementary Movie 1). Additionally, we could demonstrate the applicability of our clearing protocol to other murine tissues (e.g. liver, M1: Figure 2 d)[9,21,22] and the human heart (left atrial appendage biopsy, M1: Figure 2 e). Note that BALANCE was designed to maximize the signal quality of intravenous (i.v.)-mediated staining using synthetic fluorophores, allowing cell identification with high precision against a highly autofluorescent background.

However, homogenizing tissue autofluorescence with peroxide may quench endogenously expressed fluorophores (M1: Supplementary Figure 2, Supplementary Note 2).

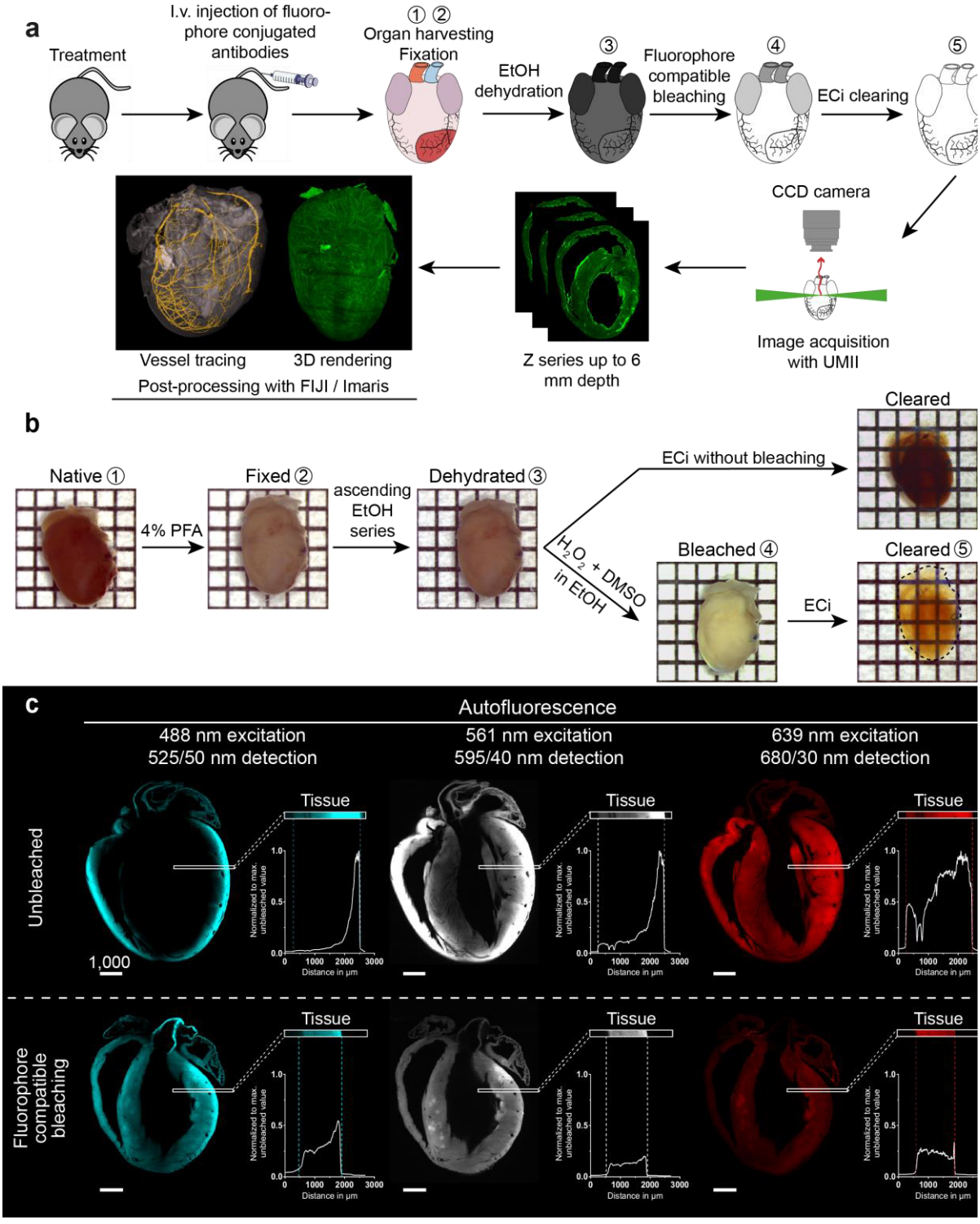

M1: Figure 1 Fluorophore compatible bleaching enables homogenous light sheet fluorescence microscopy (LSFM) in whole murine hearts.

(**a**) Graphical abstract of light sheet guided heart analysis procedure. (**b**) Macroscopic images of murine hearts during protocol steps. In comparison to the non-bleached sample, fluorophore compatible bleaching enhances the clarity of the sample. One square equals 2x2 mm. (**c**) Signal distribution of ethyl cinnamate (ECi)-cleared, unbleached or bleached hearts in LSFM in different channels, single wavelength excitation and filtered detection range given in wavelength/range, detecting autofluorescence. The region of interest (ROI) in the left ventricular wall (LVW) shows high autofluorescence at the edge of unbleached hearts. This peak is lowered, together with an overall lower autofluorescence intensity in bleached hearts. The homogenization of autofluorescence is most prominent in the short wavelength channels, unlocking those for quantitative imaging and general thresholding. Scale bar values in µm. Source data are provided as a Source Data file.

3.2.4.2. Generating infarct and area at risk volumes for I/R analysis

Next, we identified the 3-D-extent of I/R injury in a model of left coronary artery (LCA) I/R. This induced an area of terminated blood supply, which could be restored upon reperfusion (area at risk [AAR])[23]. To precisely define and quantify the AAR, we injected a fluorescein isothiocyanate (FITC)-conjugated albumin solution into the aorta following re-occlusion of the LCA in the excised heart. This led to a clearly detectable AAR as FITC negative ($FITC^{neg}$), hence non-perfused zone (M1: Figure 3 a and b). I/R generated an AAR that comprised around 29% (21-35, median and interquartile range, n=6) of the whole heart (M1: Figure 3 b, M1: Supplementary Movie 2, M1: Supplementary Figure 5 e).

The onset of I/R injury causes not only a deterioration of cardiomyocytes but also neighboring endothelial cells[18]. Therefore, this I/R injury could be identified by complete loss of CD31 signals, termed $CD31^{neg}$, in LSFM images (M1: Figure 3 c). 3-D tracing of $CD31^{neg}$ areas allowed to generate volumetric and quantifiable 3-D infarct-bodies (M1: Figure 3 c, M1: Supplementary Movie 3). These were clearly distinguishable from autofluorescent artifacts showing reduced CD31 signal ($CD31^{dim}$) which were seen in all hearts (M1: Supplementary Figure 3). Figure 3 b and c show a $CD31^{neg}$ to AAR injury of 10%, but the spectrum of small to larger infarction of this model can be visualized as outlined below. Furthermore, 3-D vessel tracing allowed to reconstruct the relation between vessels affected by I/R, the ensuing AAR and the respective size and localization of infarct-bodies

(M1: Figure 3 d). This analysis also demonstrated that vessels occluded during I/R matched the AAR defined by FITC-absence (M1: Supplementary Movie 4).

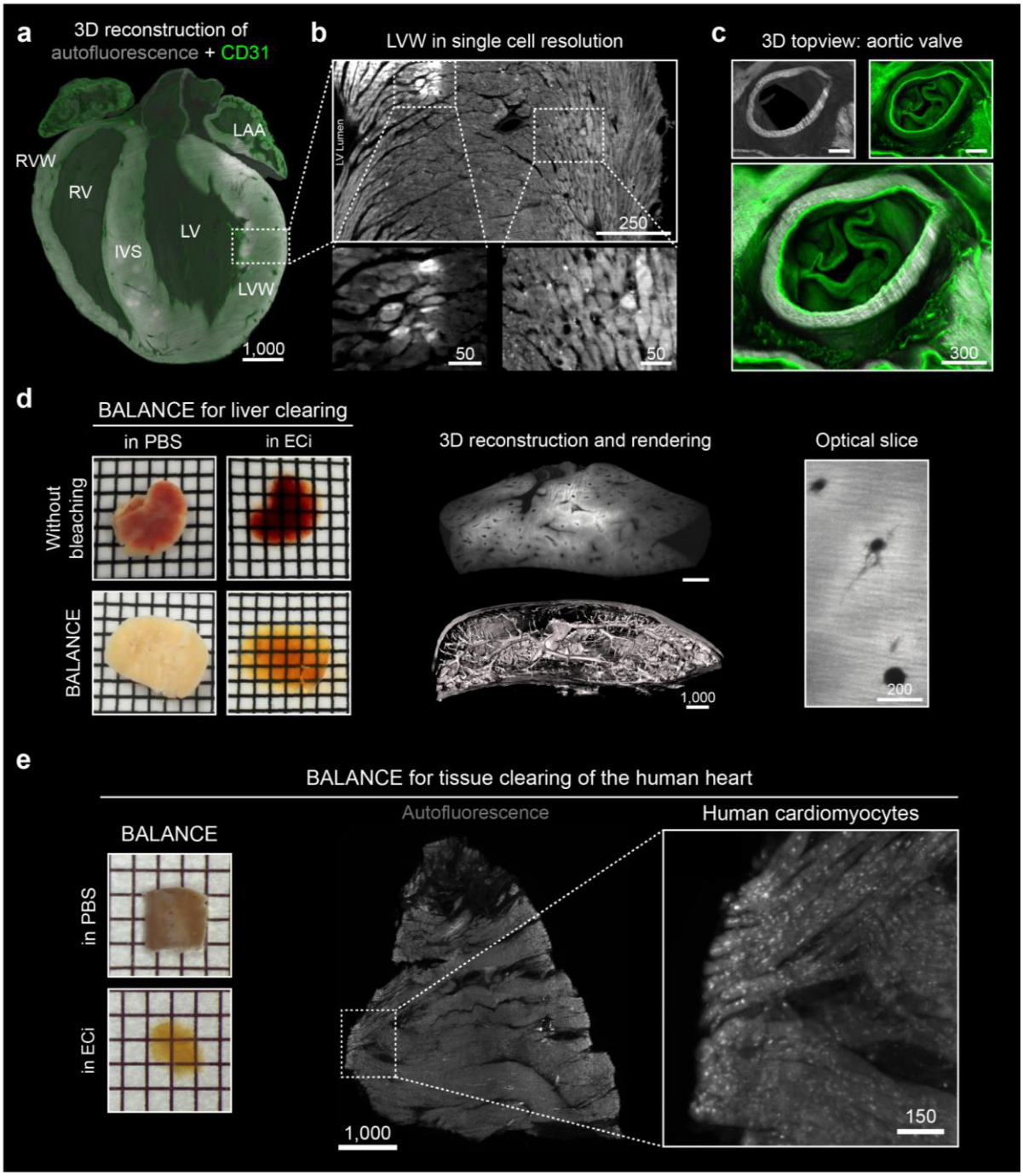

M1: Figure 2 High resolution light-sheet fluorescence microscopy (LSFM) of murine and human tissue.

(**a**) 3-D reconstruction of the inferior (dorsal) half of an ECi-cleared murine heart depicting both CD31 (blood vessels; green) and autofluorescence (total heart tissue; grey) showing distinct heart structures such as right ventricular wall (RVW), right ventricle (RV), intraventricular septum (IVS), left ventricle (LV), left ventricular wall (LVW) and left atrial appendage (LAA). (**b**) Single optical slice obtained by LSFM showing a cross-

section of the LVW (enlarged ROI highlighted in (a)) with cellular detail using autofluorescence (grey) only. Enlargements show that high autofluorescence in restricted regions is of cellular origin (ROI left, different contrast settings) and that the directionality of visualized cardiac cells depends on their respective localization within the muscle (ROI right). Magnification: 8x. (**c**) 3-D reconstruction of the aortic valve in a top-view visualized by autofluorescence (grey) and CD31 (green). Magnification: 4x. (**d**) BALANCE applied to murine liver enhances sample transparency (left) and enables imaging of large tissue samples for quantitative purposes (mid and right). High contrast between vessel lumen and surrounding tissue allows direct rendering of the portal vein system from autofluorescence raw data (mid). (**e**) Left: BALANCE also enables clearing of a human left atrial appendage (LAA) biopsy and enhances sample transparency. Mid: The autofluorescence signal alone gives a structural overview and single cellular resolution (right). Scale bar values in µm. One square on the macroscopic images equals 2x2 mm. (ECi - ethyl cinnamate)

Suppl. Movie 1	Suppl. Movie 2	Suppl. Movie 3	Suppl. Movie 4

3.2.4.3. Benchmarking of CD31-based I/R injury analysis

Histological 2-D approaches using triphenyl tetrazolium chloride (TTC) have been the mainstay for quantifying the degree of I/R injury[24]. Cardiomyocytes with intact mitochondria convert TTC to a red dye, while I/R-affected cells remain unstained (TTC^{neg}). By classical TTC staining of sequential 2-mm slices, we assessed the I/R injury. When we analyzed the same slices by LSFM, we indeed observed $CD31^{neg}$ regions that overlapped with TTC^{neg} areas (M1: Figure 4 and M1: Supplementary Figure 4). While larger vessels appeared to retain CD31 inside the infarcted area, smaller capillaries had completely lost their CD31 signal. The 3-D analysis also demonstrated that TTC overshadowed the fine structural details of I/R damage. In contrast, LSFM of CD31 faithfully reconstructed the complex 3-D structure of the I/R injury-site after 24h without destroying the tissue (M1: Supplementary Figure 4). We correlated $CD31^{neg}$ volumes to standard markers of

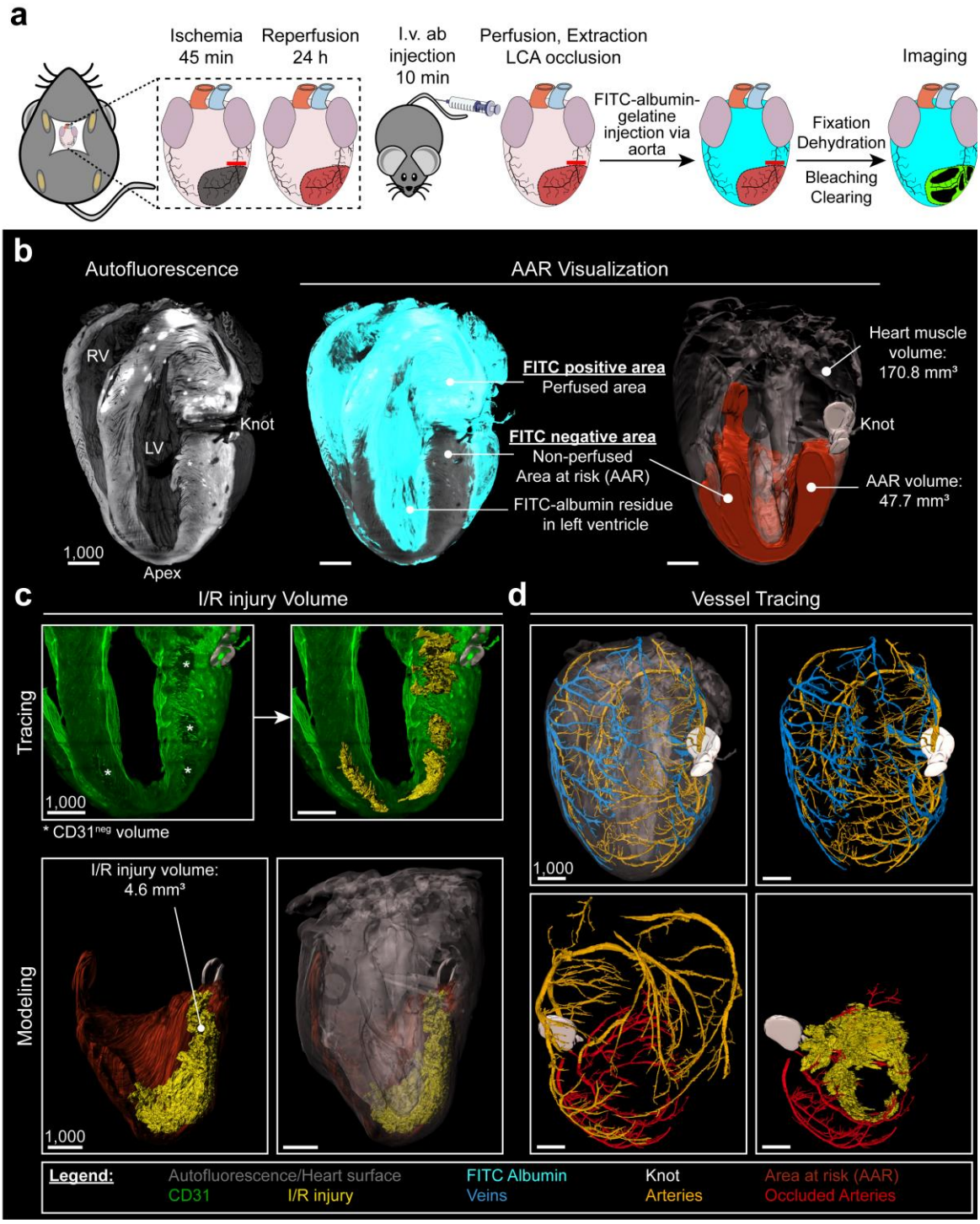

M1: Figure 3 3-D quantification and characterization of ischemia/reperfusion (I/R) injury size using light sheet fluorescence microscopy (LSFM).

(**a**) Workflow for LSFM-guided 3-D analysis of I/R injury. (**b**) Quantification in 3-D; Left: heart model based on autofluorescence (grey) for orientation. Middle: an overlay with the fluorescein isothyocyanate (FITC)-albumin filling (turquoise), all perfused areas are FITC positive ($FITC^{pos}$), whereas non-perfused areas show no FITC signal ($FITC^{neg}$) and

autofluorescence only. Right: traced FITC^{neg} area, building up a volume model for the area at risk (AAR, orange). The traced shape of the knot (white) together with the heart surface (translucent grey) give detailed spatial information and enable volume measurements. (**c**) I/R injury quantification; Top: based on slice by slice tracing of areas negative for CD31 (CD31^{neg}) (white stars, left) a volume model of I/R injury (right) is reconstructed (bright yellow). Bottom: combined 3-D models of I/R injury (yellow), AAR (orange), knot (white; left) and heart surface (right). (**d**) In vivo CD31 labeling and spatial information allow tracing of major arteries (dark yellow) and veins (blue). Together with the visualization of the knot, occlusion of the left coronary artery (LCA) can be confirmed and occluded arteries can be identified (red). Scale bar values in µm.

myocardial damage, such as TTC staining, ejection fraction (EF) reduction and cardiac troponin I (cTNI) release, as recommended tools in experimental studies[14]. We found a highly linear relationship between TTC^{neg} areas, CD31^{neg} volumes (both normalized to single slices as well as total hearts) and EF reduction (M1: Figure 4 a and e). Regions of abnormal left ventricular wall movement were located mostly in mid anterior, mid lateral and mid inferolateral zones, where TTC^{neg} and CD31^{neg} co-localized (M1: Figure 4 c and d). Plasma cTNI levels indicated establishment of infarction, but linearity was not statistically significant for the assessed infarction sizes (M1: Figure 4 f). Of note, infarct size determination by troponin assessment has been rather difficult in both, clinical and experimental environments[14,25]. Finally, a comparison of 3 operators regarding CD31^{neg} volume quantification yielded <15% difference of average values (M1: Figure 4 b). Interestingly, we observed a wide spread of infarct-body sizes relative to the AAR (M1: Supplementary Figure 5). Notably, several zones low on TTC (TTC^{low}), which might be considered I/R injury, were not co-localized with CD31 negativity (M1: Figure 4 and M1: Supplementary Figures 4 and 5).

3.2.4.4. 3-D vascular ultrastructure during I/R injury recovery

The CD31 label allowed to reconstruct the 3-D appearance of the cardiac vasculature in detail. We observed a highly organized capillary network (M1: Figure 5 a). 2-D quantification of vessel densities revealed no significantly different values within the heart muscle, but high variances concerning the field of view in the same heart region (M1: Supplementary Figure 6 a). We observed a variability in directionality of vessels, which seemed

to be linked to localization within the muscle (M1: Supplementary Figure 6 b). In addition, 3-D analysis of the left ventricular wall displayed continuous tracts of capillaries surfacing multiple times in one image, which might explain counting errors in 2-D immuno-histology (M1: Supplementary Figure 6 c). We next employed a filament tracing pipeline[18] to quantify length and complexity of the vasculature in 3-D. In the left ventricular wall, we found a vessel length density (VLD) of 2,946 mm per mm^3 and an interbranch distance (IBD) of 67 µm (median; n=3) reflecting a >2x higher VLD compared to brain (M1: Figure 5 d and e and M1: Supplementary Figure 6 d)[18]. Hence, the blood vessel architecture is a characteristic hallmark of intact cardiac tissue.

Following I/R injury, the heart muscle undergoes a complex and dynamic healing process[26]. To investigate whether such structural alterations were detectable by changes in the expression pattern of CD31, we investigated hearts 24 hours and 5 days following I/R by LSFM (M1: Figure 5 b and c). At day 5 post-I/R, we only found small $CD31^{neg}$ areas throughout the damaged heart when compared with cardiac samples after 24 hours. With special regard to injured regions, we observed shorter, less oriented and more branched vessels within the damaged area at day 5 post-I/R. We termed this zone curly ($CD31^{curly}$) to describe its distinctive morphological features. Compared to healthy myocardium, filament tracing in curly areas revealed a trend for lower VLD (1,771 mm/mm3, median, n=3) and smaller IBD (51 µm, n=3, median) values, which principally confirms the initial observation of a shorter and more complex vascular network at sites of injury (M1: Figure 5 d and e).

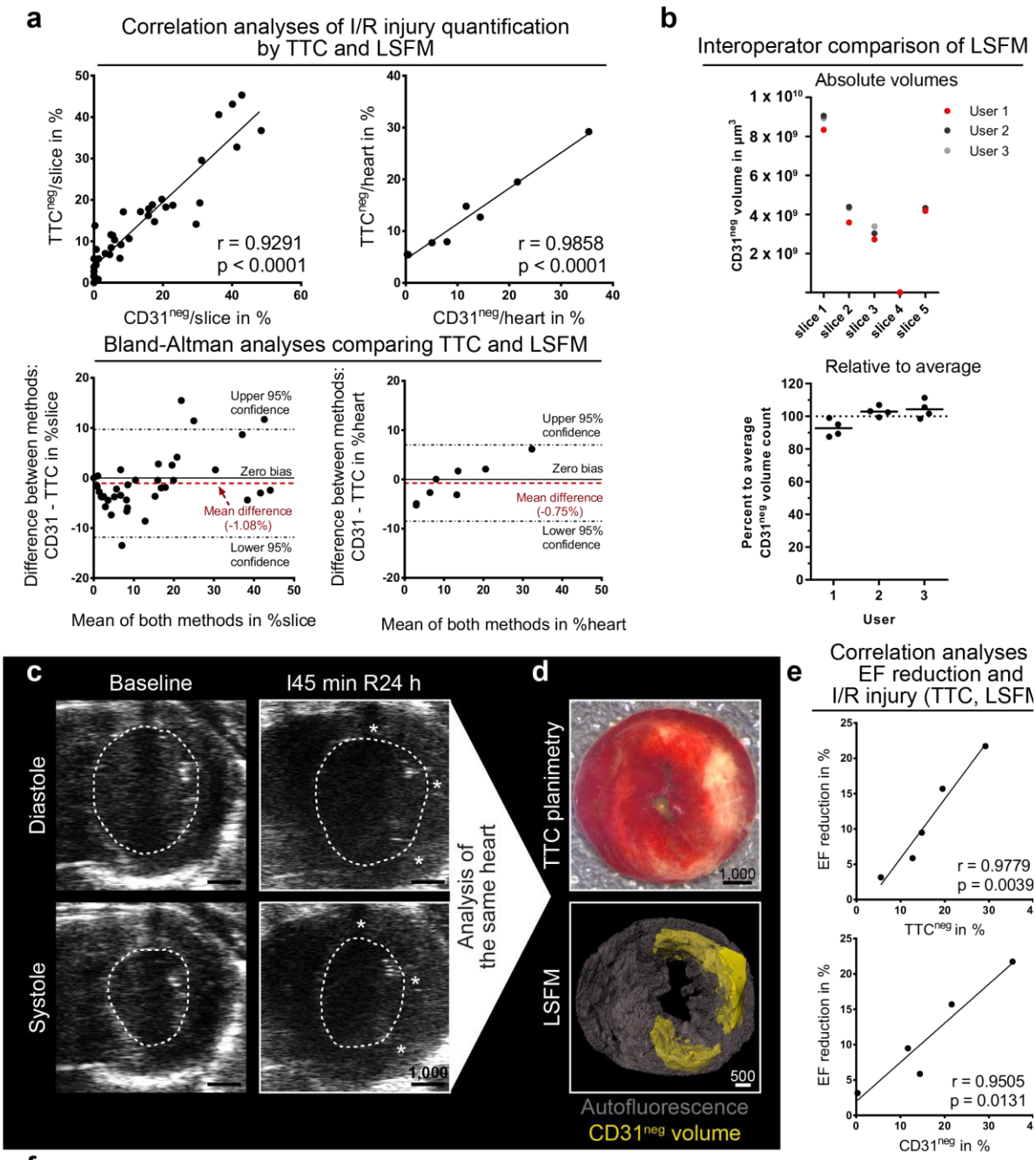

f

Measuring 4 I/R injury parameters in the same animal

Animal	EF reduction in %	TTC^{neg} in %heart	CD31^{neg} in %heart	cTNI in ng/ml
#1	21.73	29.20	35.35	36.61
#2	15.70	19.49	21.58	58.19
#3	9.48	14.80	11.68	1.29
#4	5.86	12.70	14.40	36.49
#5	3.15	5.53	0.31	20.72
mean	11.19	16.34	16.66	30.66
s.d.	6.74	7.84	11.58	18.91

Correlation analyses of cTNI with other parameters assessed

	cTNI
EF reduction	r=0.45 p=0.45
TTC^{neg}	r=0.40 p=0.51
CD31^{neg}	r=0.50 p=0.30

M1: Figure 4 Correlation of echocardiography, cardiac troponin I (cTNI) plasma levels, triphenyl tetrazolium chloride negative (TTC^{neg}) areas and CD31 negative (CD31^{neg}) volumes after 24 h of reperfusion in the same 5 mice.

(**a**) Top panel: Correlation of CD31neg volumes and TTC^{neg} areas per slice (left) and heart (right) of various infarct sizes (left: n=40 slices from 8 hearts; right: n=8 hearts; r- and p-values depicted). Bottom panel: Associated Bland-Altman analyses of $CD31^{neg}$ volumes and TTC^{neg} areas per slice (left, -1.08% mean difference) and per heart (right, -0.75% mean difference) of correlations depicted above (dashed black lines mark 95% confidence intervals, solid black line marks zero bias, red dashed line marks mean difference). (**b**) Inter-operator $CD31^{neg}$ volume quantification variances. (Top) Absolute quantified volume of 3 users in 5 randomly selected slices of different hearts subject to 45 min of ischemia and 24 h of reperfusion. (Bottom) The quantification results per user relative to the average (100%, dashed line) quantified volume (in comparison to left, slice #4 was excluded as no $CD31^{neg}$ volume was measurable). (**c**) Original micrographs of echocardiographic imaging. Dashed lines indicate left ventricular lumen. White stars indicate zones of abnormal left ventricular wall movement. (**d**) Same I/R injury heart as in (c): exemplary TTC staining and subsequent light sheet fluorescence microscopy (LSFM)-based 3-D reconstruction of the same slice. (**e**) Correlation of ejection fraction (EF) reduction with TTC^{neg} areas and $CD31^{neg}$ volumes, respectively, per heart (n=5 hearts; r- and p-values depicted). (f) Left: raw data used for correlation of EF reduction, TTC^{neg} and $CD31^{neg}$ with plasma cTNI levels (value for each animal given, n=5). Right: correlation of absolute cTNI levels with EF reduction, TTC^{neg} and $CD31^{neg}$. Scale bar values in µm. Source data are provided as a Source Data file.

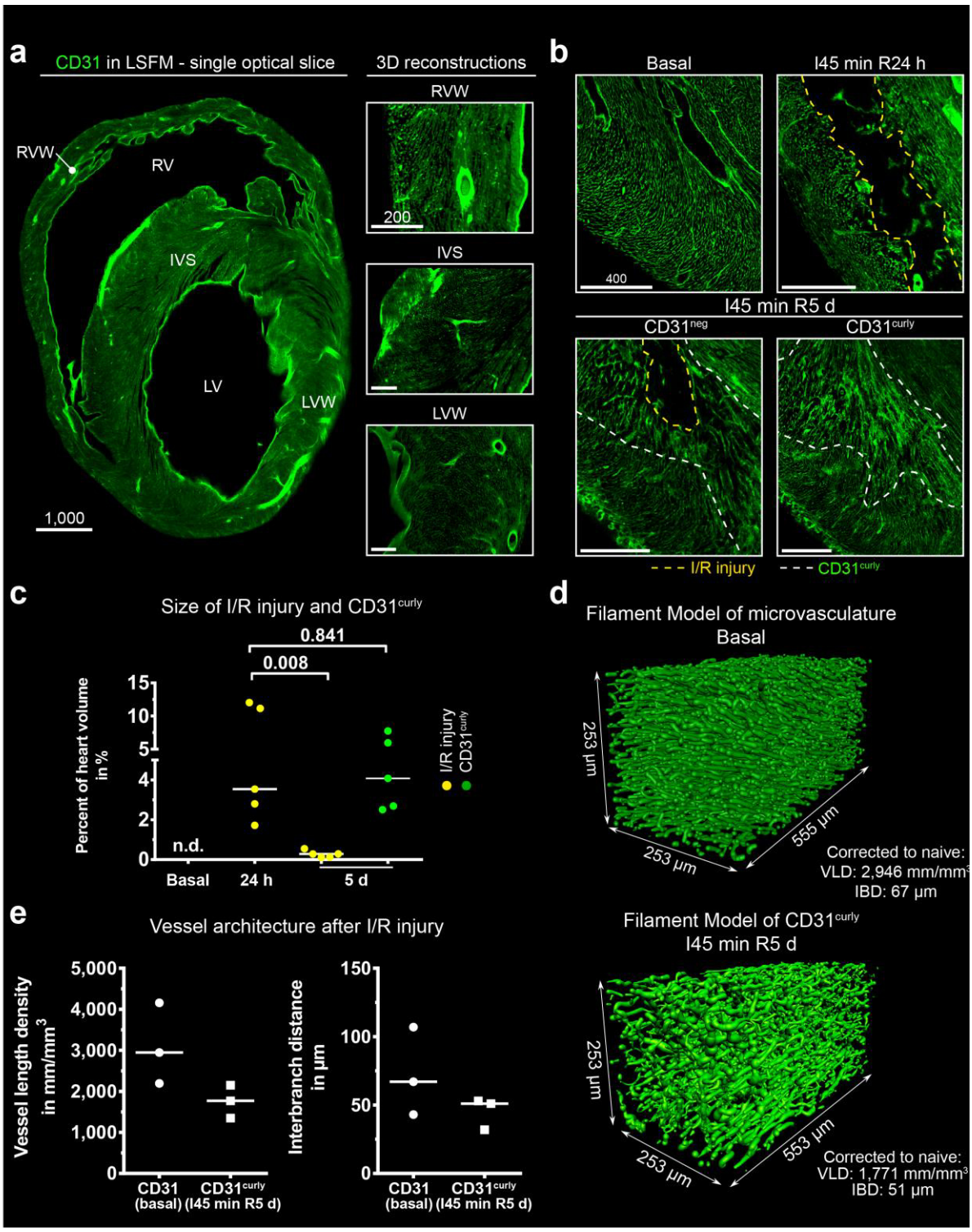

M1: Figure 5 4D analysis of vascular meshwork in basal and infarcted hearts

(**a**) Left: single optical slice through a cleared murine heart depicting CD31 (green). Right: 3-D reconstructions of enlargements, visualizing the microvasculature and its respective directionality. Magnification: 10x. (**b**) Maximum intensity projections (MIPs) comparing CD31 staining in basal, 24 h and 5 d murine hearts. I/R injury is highlighted

with yellow dashed line, CD31 curly ($CD31^{curly}$) region with white dashed lines. Magnification: 6.4 x (basal), 3.2x (24 h), 4x (5 d). (**c**) Quantification of I/R injury and $CD31^{curly}$ volume normalized to heart muscle volume (including appendages and right ventricle (RV)) over time (n=5 hearts; median; two-sided Mann-Whitney test, p-value depicted). (**d**) Filament model of CD31 baseline expression (top) and $CD31^{curly}$ region (bottom). Magnification: 6.4x. (**e**) Vessel length density (VLD, left) and interbranch distance (IBD, right) in baseline and $CD31^{curly}$ regions (ROIs from 3 hearts; median). Scale bar values in µm. Source data are provided as a Source Data file.

To better localize the I/R injury-zones, $CD31^{neg}$ areas were overlaid to a well-known 17-segment heart muscle scheme[27] (M1: Figure 6 a and M1: Supplementary Figure 7). Apical and lateral heart segments were primarily affected (M1: Figure 6 b). After 5d of reperfusion, the detectable I/R injury was largely resolved, with only residual peri-apical $CD31^{neg}$ segments remaining.

The analysis also suggested that $CD31^{curly}$ zones on day 5 co-localized with previous $CD31^{neg}$ I/R regions. Hence, curly zones might serve as a proxy to delineate previous areas of I/R injury, even days after their revascularization (M1: Figures 5 b, c and 6 b).

3.2.4.5. 3-D mapping of immune cells to zones of infarction

To investigate the impact of cardiac tissue injury on inflammatory response mechanisms, we next assessed immune cell infiltration of I/R-affected zones. To this end we localized and quantified neutrophils and macrophages in the infarcted heart after 24 hours and 5 days of reperfusion. In line with previous studies and flow cytometric analyses of injured hearts, we found that Ly6G positive ($Ly6G^{pos}$) neutrophils were most prominent after 24 hours (M1: Figure 7 a-c and M1: Supplementary Movies 5-8). Intriguingly, the localization of neutrophils matched with $CD31^{neg}$ areas, but did partly not overlap with TTC^{neg} zones (M1: Supplementary Figure 8). Neutrophil numbers strongly decreased after 5 days, whereas F4/80 positive ($F4/80^{pos}$) macrophages increased. At 24 hours we found neutrophils to be highly enriched within the AAR and at the rim of infarct bodies (M1: Supplementary Movie 5) indicating neutrophil presence at the border of infarction rather than within the damaged tissue itself (M1: Figure 7 d and M1: Supplementary Movies 7 and 8). Interestingly, at d5, the majority of neutrophils was no longer associated with the border of the residual infarct-body but localized in the $CD31^{curly}$ volume (M1: Figure 7 d,

n=5, and M1: Supplementary Movie 6). At this time, we could also detect F4/80^{pos} macrophages throughout this area (M1: Figure 7 e, n=5). Such a timing of arrival might reflect the ongoing tissue repair mediated by macrophages[26].

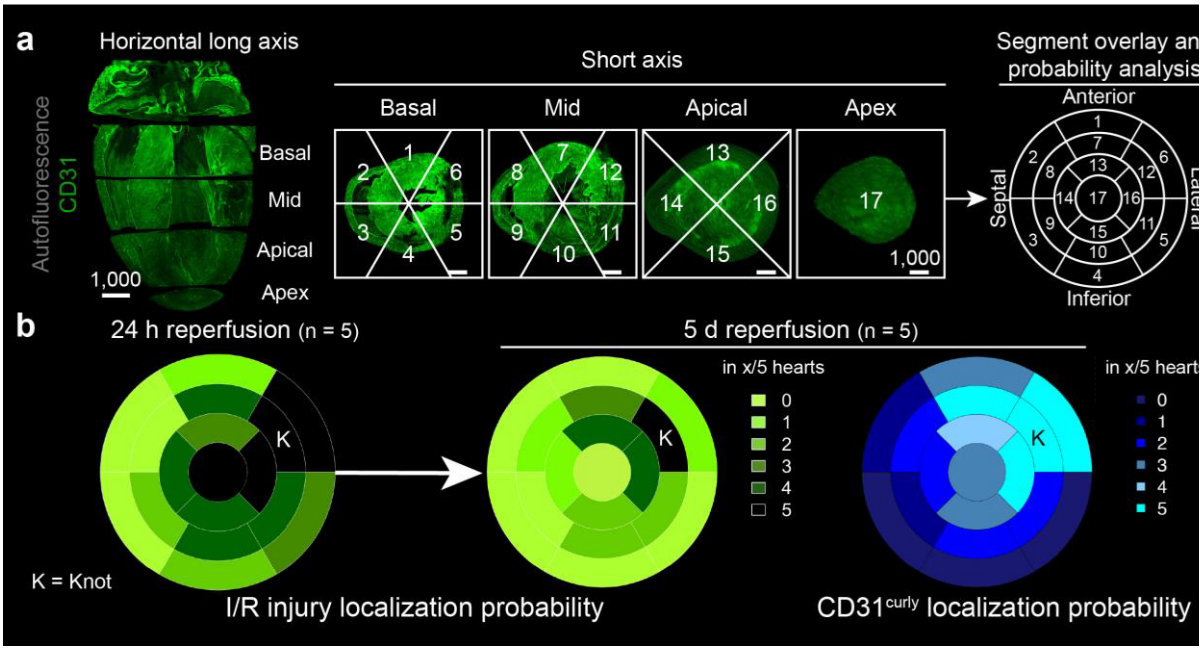

M1: Figure 6 Quantifying I/R injury, AAR and CD31^{curly} localization in mice with the left ventricular 17 segment model.

(**a**) Left: 3-D model of inferior heart half, cut along the horizontal long axis, based on CD31 labelling (green). Four slices are defined: Apex (1), not containing left ventricle (LV) lumen, Apical, Mid and Basal, which are equally spaced with LV lumen. Middle: These slices, viewed from the apex perspective, can be further segmented. The segments do not include the right ventricle. Right: Overlay of the segments viewed from the apex gives a backbone for probability heat-maps. (**b**) The localization probability of I/R injury after 24 h (left) and 5 d (middle) together with CD31^{curly} (right) given in the total amount of hearts affected, represented in heat-maps. K = position of knot in mid anterolateral (segment 12). Scale bar values in µm. Source data are provided as a Source Data file.

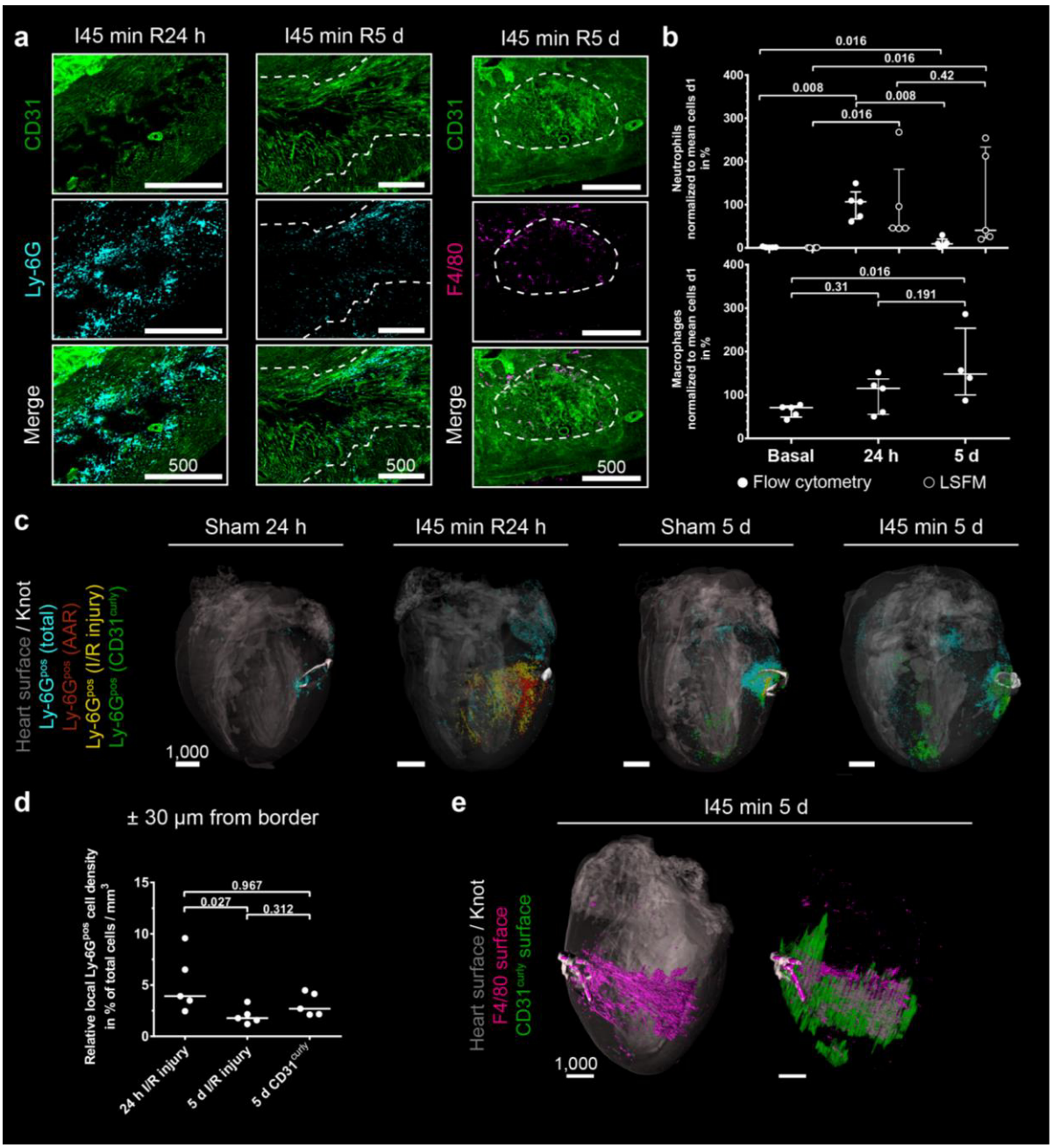

M1: Figure 7 Characterization of immune cell infiltrates into I/R injury.

(**a**) Example maximum intensity projections (MIPs) of Ly6G positive (Ly6G^{pos}) neutrophils after 24 h (left) as well as Ly6G^{pos} neutrophils and F4/80 positive (F4/80^{pos}) macrophages after 5 d (middle; right). Depicted are CD31 (green, top row) and Ly6G (turquoise) or F4/80 (purple) signals (middle row) together with a merge (bottom). Dashed white line marks the border of the CD31^{curly} region. Magnification: 3.2x (24 h), 4x (5 d). (**b**) Immune cell quantities (top neutrophils, bottom macrophages) determined by flow cytometry (white, filled dots) or based on LSFM (white, empty dots) analysis after 24 h and 5 d of reperfusion, as well as under baseline condition (n=4-5; median ± interquar-

tile range; Kruskal-Wallis test with Dunn's correction). (**c**) Representative 3-D visualization of Ly6G^{pos} cell distribution across whole murine hearts. Heart structure (grey,) and knot (white) are shown for orientation. Ly6G^{pos} cell populations are colored in respect to their localization in either AAR (red), I/R injury (yellow), CD31^{curly} (green) or outside the above-mentioned structures (turquoise). (**d**) Relative cell density ± 30 µm from the respective volume border (n=5; median; Kruskal-Wallis test with Dunn's correction). (**e**) 3-D visualization of F4/80^{pos} signals depicted as a surface rendering (purple) in relation to heart surface (left; heart volume in grey) or CD31^{curly} surface (right; CD31^{curly} in green) after 5 d of reperfusion. The knot (white) is visualized for orientation. Scale bar values in µm. This finding was verified in 5 mice. Source data are provided as a Source Data file.

Suppl. Movie 5	Suppl. Movie 6	Suppl. Movie 7	Suppl. Movie 8

3.2.5. Discussion

We developed BALANCE for the fast 3-D characterization of damage- and response-mechanisms in whole heart specimens. The ability to reconstruct the 3-D shape of affected zones might require to re-define the current 2-D-concept of myocardial infarction parameters into Volumes At Risk (VAR)/infarct-bodies to give credit to their real 3-D nature.

The established protocol combines the use of non-toxic reagents, short handling and protocol times, less complexity and superior signal homogenization, required for myocardial I/R analysis and not available from other published clearing methods (Supplementary Table 2). In contrast to iDISCO clearing, ethanol was used for sample dehydration to avoid high methanol toxicity and reduce possible incompatibilities with following histological antibody stainings[10]. Also, long clearing times, e.g. in CUBIC[28] or passive CLARITY[29], were circumvented by the use of non-toxic ECi. BALANCE uses a minimum of hands-on time and procedure steps to circumvent initial adaption difficulties as compared to SWITCH[30]. Most importantly, it homogenizes tissue autofluorescence throughout highly

autofluorescent organs such as the heart, which is not the case in the original ECi protocol[9] (Supplementary Table 1 and 2). With the advent of robotics and artificial intelligence (AI) to automate clearing procedures and data analyses[9], the usability and reliability of clearing methods and staining results will be further improved.

Regarding time and expense of experiments, we compared the conventionally applied methods in the field of I/R injury in the murine heart with our current LSFM-based approach (Supplementary Table 3). The hands-on time of our proposed LSFM procedure is comparable to each of the classical methods[14]. However, none of the currently available approaches, including TTC staining, histology, immuno-histology and flow cytometry provides LSFM-comparable data. LSFM combines spatially resolved I/R injury parameter assessment with cellular quantification and 3-D localization in the same heart. Furthermore, LSFM-based analysis offers, inherent from its 3-D nature, the possibility to reconstruct the fine ultrastructure of the inspected feature such as the blood capillary network. We therefore believe that with our proposed method, the robustness over experiments can be increased. At the same time, combined experimental times needed to carry out all other individual methods in different animals can be significantly reduced by our multiplexing approach. In the near future, computer-based algorithms will further reduce analysis time.

Since our technique can be translated to any I/R injury model, this work opens multiple possibilities for identifying new therapeutic targets. Of note, clinical data on cardioprotection have been largely disappointing[31] and morbidity and mortality for patients with an acute myocardial infarction remain considerably high[32]. Novel approaches are therefore desired to improve the outcome of patients. The underlying pathomechanisms in I/R injury are very complex and include e.g. the interaction of heart cells (cardiomyocytes, endothelium, fibroblasts) with platelets and immune cells finally producing heart cell death. It has recently been concluded that an ideal drug/approach for cardioprotection would target the cardiac vasculature, immune cells and cardiomyocytes[14,31]. Several promising strategies have been forwarded recently including beta-blocking metoprolol [33-35] and immune modulatory drugs[36,37]. A common feature of these approaches is that they target not a single but multiple pathways involved in I/R injury. Metoprolol, e.g., interacts with beta-receptors on cardiomyocytes to reduce myocardial energy consumption while also inhibiting neutrophil-platelet interaction involved in microvascular obstruction[33-35]. With our proposed workflow, we provide a tool for the analysis of conventional I/R injury

in conjunction with the characterization of the vascular injury several days after the initial I/R event. Another problem of previously forwarded potentially cardioprotective therapies appears to be the lack of rigor in experimental studies[14]. To establish rigor in our model, we performed benchmarking. Hence we have conducted correlation analyses of our proposed analysis tool for the CD31^{neg} I/R injury against recently recommended standard approaches for experimental animal studies[14] and show a very good correlation (M1: Figure 4)[7,8,14,23,38]. Of note, instead of using CD31 antibody labelling to stain the vasculature, a lectin-based approach would obtain comparable results, depending on the investigator's choice[39-41].

Remarkably, the vasculature has been largely affected as shown by our study and the vascular injury correlates with tissue damage as assessed by classical methods. It is therefore tempting to speculate that the vasculature could become a primary target for future cardioprotective strategies. Hence, we believe that BALANCE/LSFM might also help to identify additional potential novel therapeutic options for the treatment of I/R injury in the future.

3.2.6. Methods

ANIMALS

All experimental animal procedures were approved by the responsible governmental agency, the Ministry for Environment, Agriculture, Conservation and Consumer Protection of the State of North Rhine-Westphalia (MULNV) and complied with all relevant ethical regulations for animal testing and research. Male C57BL/6JRJ (12±3 weeks of age; Janvier) and Catchup (C57BL/6-Ly6g(tm2621(Cre-tdTomato)Arte); 12±3 weeks of age)[42] mice were held at the local animal house on 12 h/12 h day and night cycle with water and food ad libitum.

HUMAN STUDIES

All human studies were approved by the local ethics committee of the Medical Faculty, University of Duisburg-Essen, Germany (Ethics Approval Nr. 18-8527-BO). The whole procedure was in accordance to the World Medical Association Declaration of Helsinki and conducted in accordance with the relevant ethical regulations. Written informed consent was obtained from all participants. The patients underwent coronary bypass surgery, during which human left atrial appendage (LAA) biopsies were routinely excised. This presented no further harm for the patient.

ISCHEMIA/REPERFUSION (I/R) HEART INJURY

Male C57BL/6JRJ and Catchup mice (12±3 weeks of age) were subjected to a published myocardial I/R in vivo protocol[38]. Briefly, mice were anesthetized by intraperitoneal (i.p.) injection of ketamine (100 mg/kg, CatNo. 9089.01.00, bela-pharma) and xylazin (Rompun 10 mg/kg, CatNo. 6324464.00.00, Ceva Tiergesundheit). They were orally intubated and ventilated throughout the operation procedure, with 0.8 l/min air and 0.2 l/min O2 at a

tidal volume of 250 µl/stroke and a breathing frequency of 140 strokes/min. Anesthesia was maintained during the operation by supplementing 2% isoflurane (Forene, CatNo. 2594.00.00, abbvie). The chest was opened through a left lateral thoracotomy and the left coronary artery (LCA) was ligated. After 45 min of ischemia, reperfusion was allowed for indicated time points. As previously described, different infarct sizes may be created by this method due to differences in mouse physiology[43,44]. Mice were treated with 0.1 mg/kg buprenorphine (Temgesic, CatNo. 997.00.00, Indivior) subcutaneously every 8 h after operation for a total of 72 h. Mice received 1000 IE heparin (CatNo. 27586.00.00, LEO Pharma) i.p. 10 min before the end of the experimental protocol and were killed by cervical dislocation.

For light sheet experiments, mice received intravenous (i.v.) tail vein injections 10 min before sacrifice with 5 µg of each antibody in PBS in a total volume of 150 µl per animal of anti-mouse CD31 (clone: Mec13.3; purified: CatNo. 553369, BD; conjugated with AlexaFluor (AF) 647: CatNo. 102516 BioLegend), Ly6G (clone: 1A8; purified: CatNo. 127602, BioLegend; conjugated with AF647: CatNo. 127610, BioLegend) and/or F4/80 antibody (clone: BM8; purified: CatNo. 123102, BioLegend; conjugated with AF594: CatNo. 123140, BioLegend). In other experiments, respective IgG control antibodies were used (rat IgG2a-AF647, CatNo. 400526, BioLegend; rat IgG2a-AF594, CatNo. 400555, BioLegend) (M1: Supplementary Figure 9). Purified antibodies were conjugated with AF790 using an IgG coupling kit (CatNo. A20189, Thermo Fisher). After sacrifice, mice were perfused blood-free with phosphate-buffered saline (PBS), hearts were excised and subjected to following tissue processing.

To visualize the area at risk (AAR) for light sheet experiments, the heart was placed in ice-cold PBS after perfusion, the aorta was cannulated, the LCA re-occluded and 2% gelatin / 0.2% fluorescein isothyocyanate (FITC)-albumin in PBS (gelatin CatNo. G9391, Sigma Aldrich; FITC-albumin, CatNo. A9771, Sigma Aldrich) was injected via the aorta. After 10 min incubation in ice-cold PBS, hearts were subjected to tissue processing.

For hearts to be analyzed by both light sheet fluorescence microscopy (LSFM) and triphenyl tetrazolium chloride (TTC) staining, freshly excised hearts were cut transversely along the longitudinal axis in 2 mm slices and stained for 5 min at 37 °C with a 1% (w/v) TTC in 0.0774 M Na2HPO4 / 0.0226 M NaH2PO4 in ddH2O solution (Na2HPO4, CatNo. 4984.2, Roth; NaH2PO4, CatNo. S5011, Sigma Aldrich). Subsequently, macroscopic images of the TTC-stained slices were taken with a M80 microscope with an IC80 HD camera at 1.6x – 2.5x magnifications (both Leica) before being subjected to tissue processing. Computer-assisted planimetry was performed in a double blinded fashion using ImageJ software[45].

Mouse plasma was prepared from whole blood taken from inferior vena cava shortly before heart extraction, mixed with 25 IE heparin (CatNo. 27586.00.00, LEO Pharma) and centrifuged 10 min at 3000 x g, 4 °C. Supernatant (plasma) was collected, snap-frozen in liquid N2 and stored at -80 °C until analysis.

Quantification of I/R injury size using TTC staining

I/R injury size was quantified as described before38. Briefly, after PBS perfusion and extraction, the LCA was re-occluded and 1 ml 1% Evans blue dye (CatNo E2129, Sigma Aldrich) in 0.9% NaCl was injected via the aorta to visualize the AAR. The heart is wrapped in clear food wrap and stored at -20 °C for 1 h. The heart is then cut in 2 mm slices orthogonal to the long axis and incubated in a 1% (w/v) TTC solution as described above. Areas of TTC^{neg}, AAR and non-ischemic myocardium were measured using ImageJ[45] by two blinded, independent operators. I/R injury size was expressed as percentage of AAR.

BALANCE PROTOCOL FOR TISSUE CLEARING

Perfused hearts were immersed in 4% paraformaldehyde (w/v, PFA, CatNo. 10195, Morphisto) in PBS for chemical fixation while standing for 4 h at 4 °C in 15 ml tubes. For all following steps, hearts were kept at 4 °C, always agitated, transferred only to pre-cooled solutions in 15 ml tubes and kept protected from light. Following fixation, hearts were dehydrated in an ascending ethanol series in ddH2O (v/v) of 50%, 70% and 100% (CatNo. 9065.2, Roth) for at least 4 h while shaking. Samples can also be stored longer at each step without loss of staining quality.

Subsequently, samples were bleached for 4 h in freshly prepared 5% (v/v) hydrogen peroxide (CatNo. 349887; Sigma Aldrich) and 5% (v/v) dimethyl sulfoxide (CatNo. 4720.3, Roth) in 100% ethanol. Please beware of building pressure during this step. Bleaching was carried out to enhance sample clarity, enabling homogenous imaging in lower wavelength channels while preserving artificial fluorophore fluorescence (M1: Figure 1). After a washing step of at least 4 h in 100% ethanol, samples were warmed to room temperature (RT) for 5 min before transfer into 7 ml pure (99%) ethyl cinnamate (ECi, CatNo. 112372, Sigma Aldrich) in a glass vial for at least 4 h prior to imaging. Samples were kept at RT in the dark until and after imaging.

ADDITIONAL BLEACHING PROTOCOLS TESTED

Further tested bleaching protocols were performed after fixation and washing. Therefore, perfused hearts were immersed in 4% PFA in PBS for chemical fixation while standing for 4 h at 4 °C in 15 ml tubes, as mentioned above. Hearts were washed in 5 ml PBS + 0.01% sodium azide (w/v, Cat. No. K305.1, Roth) over night at room temperature (RT), shaking. Afterwards, hearts were washed again another change of 5 ml PBS + 0.01% sodium azide for 1 h at RT, shaking.

Sudan Black bleaching was performed according to the original publication15. After fixation and washing, hearts were incubated in 0.5% (w/v) Sudan Black B (w/v, Cat. No. 199664, Sigma-Aldrich) in 70% ethanol in ddH2O for 3 h at RT, shaking. After washing 3x in 5ml PBS + 0.01% sodium azide (w/v, Cat. No. K305.1, Roth) for 30 min at RT, shaking, hearts were dehydrated in ascending ethanol series in ddH2O (v/v) of 50%, 70% and 100% for at least 4 h at 4 °C while shaking. Afterwards, hearts were warmed to RT for 5 min before transfer into 7 ml pure (99%) ECi in a glass vial for at least 4 h prior to imaging. Samples were kept at RT in the dark until and after imaging.

Bleaching using heme elution was accomplished as published beforehand[15]. After fixation and washing, hearts were immersed in 50% CUBIC-1 reagent (v/v) in dH2O for 3 h at 37 °C, shaking. CUBIC-1 reagent was prepared according to published protocols[28] and was comprised of 25% Urea (w/w, Cat. No. U5378, Sigma-Aldrich), 25% Quadrol (w/w, Cat. No. 122262, Sigma-Aldrich) and 15% Triton X-100 (w/w, Cat. No. X100, Sigma-Aldrich) in dH2O. Afterwards, hearts were incubated in pure CUBIC-1 reagent over night at 37 °C, shaking and further in another change of CUBIC-1 reagent for 2 d at 37°C, shaking. Following, hearts were dehydrated in ascending ethanol series in ddH2O (v/v) of 50%, 70% and 100% for at least 4 h at 4 °C while shaking. Afterwards, hearts were warmed to RT for 5 min before transfer into 7 ml pure (99%) ECi in a glass vial for at least 4 h prior to imaging. Samples were kept at RT in the dark until and after imaging.

CUBIC CLEARING PROTOCOL

CUBIC clearing protocol was performed as previously described[28]. All following incubation steps were carried out in the dark. After perfusion, hearts were immersed in 4% PFA in PBS for chemical fixation while standing for 4 h at 4 °C in 15 ml tubes, as mentioned above. Hearts were washed in 5 ml PBS + 0.01% sodium azide (w/v, Cat. No. K305.1, Roth)

over night at room temperature (RT), shaking. Afterwards, hearts were washed again another change of 5 ml PBS + 0.01% sodium azide for 1 h at RT, shaking. Afterwards, hearts were immersed in 50% CUBIC-1 reagent (v/v) in dH2O for 3 h at 37 °C, shaking. CUBIC-1 reagent was prepared according to published protocols[28] and was comprised of 25% Urea (w/w, Cat. No. U5378, Sigma-Aldrich), 25% Quadrol (w/w, Cat. No. 122262, Sigma-Aldrich) and 15% Triton X-100 (w/w, Cat. No. X100, Sigma-Aldrich) in dH2O. Following, hearts were incubated in pure CUBIC-1 reagent over night at 37 °C, shaking and further in other changes of CUBIC-1 reagent for 2 d each for a total of 4 d at 37 °C, shaking. Hearts were then washed in three changes of PBS + 0.01% sodium azide for 2 h each at RT, shaking. Next, hearts were immersed in 50% CUBIC-2 reagent (v/v) in PBS for 6 h at 37 °C, shaking. CUBIC-2 reagent was comprised of 25% Urea (w/w), 50% Sucrose (w/w, Cat. No. S7903, Sigma-Aldrich) and 10% Triethanolamine (w/w, Cat. No. 90279, Sigma-Aldrich) in dH2O following establish protocols28. Afterwards, hearts were incubated in pure CUBIC-2 reagent over night at 37 °C, shaking and another change of CUBIC-2 reagent for 24h at 37 °C, shaking. Hearts were imaged in a 50%/50% silicon oil (Cat. No. 175633, Sigma-Aldrich) and mineral oil (Cat. No. M5904, Sigma-Aldrich) mixture.

LIGHT SHEET FLUORESCENCE MICROSCOPY AND IMAGE PROCESSING

Samples were imaged using an Ultramicroscope II and ImSpector software (both LaVision BioTec). The microscope is based on a MVX10 zoom body (Olympus) with a 2x objective and equipped with a Neo sCMOS camera (Andor). For image acquisition, cleared samples were immersed in ECi in a quartz cuvette and excited with light sheets of different wavelengths (488 nm, 561 nm, 639 nm and 785 nm). Following band-pass emission filters (mean nm / spread) were used, depending on the excited fluorophores: 525/50 for FITC; 595/40 for AF594 or autofluorescence; 680/30 for AF647 and 835/70 for AF790. For quantitative imaging, whole hearts were imaged along the longitudinal axis. For image acquisition, hearts were trapped, with the apex and the aorta horizontally aligned, in a commercially available sample holder (LaVision BioTec). To avoid damage or deformation of the sample, ECi-cleared 1% phytagel/ H2O (CatNo: P8169-100G, Sigma Aldrich) blocks were used as buffers between tissue and plastic holder. Hearts were also rotated along the longitudinal axis, so that the knot, which remains in situ, faced downwards. This reduced blockage of excitation or emission light to a minimum. Whole-heart data sets were obtained with 2x total magnification (pixel size of 3.25 µm / pixel x,y, lateral resolution: 6.5 µm in x and y) with 10 µm z spacing between optical planes. Since the camera's chip has 2560 x 2160 pixels, the field of view with this magnification amounts to 8.32 mm x 7.02 mm. It was thereby possible to image a whole mouse heart without multi-positioning, thus avoiding stitching algorithms while simultaneously reducing acquisition times. Sheet width was set to 4200 and numeric aperture to 0.148, resulting in an approximate light sheet thickness of 4 µm in the horizontal focus. Illumination time was 350 ms, with enabled 8x dynamic focus in both left and right laser lines. Total acquisition time of one plane was thus, theoretically, 5.6 s. The vertical thickness of the hearts was generally smaller than 6 mm. This is the limiting factor due to the objective's working distance. Assuming a z stack as deep as 6 mm, this would have resulted in acquisition of 600 images x 4 channels = 2400 images, which would theoretically have taken 3.73 h. However, in our practical experience one murine heart takes 4 - 6 h of acquisition time. For regions of interest (ROIs), magnifications are indicated in the figure legends.

See https://www.lavisionbiotec.com/products/UltraMicroscope/specification.html for zoom factors, corresponding numerical apertures and resolutions. To avoid photobleaching during imaging, the longest wavelength was imaged first.

16bit OME.TIF stacks were converted (ImarisFileConverterx64, Version 9.2.0, BitPlane) into Imaris files (.ims). 3-D reconstruction and subsequent analysis was done using Imaris software (BitPlane). Heart surface (25 µm grain size) and volume was determined using surface creation algorithms. All surface tracings (AAR, $CD31^{neg}$, $CD31^{curly}$, vessels) are based on the contour tracing tool and are carried out manually/semi-automatically. For surface creation, each (vessels), every 5th (CD31 tracings) or 10th (AAR) image was traced. Surfaces were created with maximum resolution (2160 x 2560 pixel) and preserved features, to ensure matching of the traced lines with the surface border. Discrimination of arteries and veins was done by their respective location within the heart muscle and the signal intensity of the CD31 staining (CD31high for arteries, $CD31^{low}$ for veins).
For 2-D vessel counting, 8 slices of the right ventricular wall (RVW), the intraventricular septum (IVS) and the left ventricular wall (LVW) (n=3 mice) were analyzed. For this, capillaries in 8 fields of view of 251.49 µm x 251.49 µm size (not shrinkage corrected) were manually counted and extrapolated to capillaries per mm^2.
Vessel quantification was performed as previously described[18]. Image data were first preprocessed, as a necessary step to reduce noise and improve vessel contrast, before applying a filament tracer model for vessel quantification in the 3-D software package Imaris (BitPlane).
Briefly, image stacks were first preprocessed in the open source software ImageJ[45] by applying a Gaussian smoothing, where a Gaussian sigma of 2 µm was chosen to be less than half the diameter of the smallest vessels. This was followed by a rolling ball background subtraction. In order not to affect the intensity distribution within the vessels themselves, a rolling ball radius of 20 µm was chosen, which was more than twice the diameter of the largest vessel. Any resulting edge artifacts from background variations could be removed during a later thresholding step in Imaris. The contrast of vessels was further enhanced using a python script (vmtkimagevesselenhancement) from the open source Vascular Modelling Toolkit project (VMTK: www.vmtk.org), which performed a multiscale Hessian-based Frangi vesselness filter[46]. The feature-based enhancement filter of Frangi is now a well-established tool for vessel segmentation[47]. In addition to the improved vessel contrast and non-vessel suppression, the Frangi filter also improved the continuity of the vessels by smoothing out inconsistencies in the vessel labeling along the length of the vessels. These preprocessing steps were found to be necessary for the fidelity of tracing smaller vessels when applying the filament-tracing algorithm in Imaris. In particular since, for the tracing of vessels, it was necessary to apply the 'with loops' filament tracing method, which uses an initial simple thresholding for segmenting the vessels. Without smoothing, background subtraction and contrast enhancement, small vessels that were less intense were either inconsistently segmented, due to variations in the background signal, not distinctly segmented when close to larger much brighter vessels, or were not segmented as an integral vessel, but were broken up due to inconsistencies in the labelling efficiency. It should also be noted that one known artifact of the Frangi filter is that it can lead to discontinuities at branching points. In particular, for branching that occurs in a direction orthogonal to the main branch. Although we observed a reduction in the vessel intensity at these points, this effect occurred at a range very close to the branch point, and for our data did not result in any discontinuities in the Imaris tracing. Furthermore, we also observed that the Frangi vessel filter can affect the relative intensities of the vessel branches. Indeed, the intensity of smaller vessels was seen to be enhanced relative to larger vessels. In the Imaris filament tracer, this could influence the evaluation of their relative diameters, due to the use of the simple intensity threshold method for segmentation. Indeed, in general, the application of a simple thresholding segmentation resulted in a relative mismatch in the filament diameters between small low intensity vessels and the

larger brighter vessels, and also resulted in a mismatch for the filament path, calculated from the center lines of the segmented vessels. Therefore, following the construction of the initial filament model, this mismatch was corrected in Imaris with two further processing steps. Firstly, a 're-alignment' of the filament model was performed against the channel corresponding to the Gaussian smoothed and background subtracted vessel data. The same channel was then used to adjust the filament diameters, using an approach based on the relative contrast change across the diameter of the vessels. From the resulting filament model, parameters for the vascular length and branching points could be extracted.

For quantification of CD31 signal intensities over different specimens, single optical planes and MIPs of whole hearts were manually analyzed.

In order to determine the tissue shrinkage occurring during the BALANCE protocol we measured heart slice thickness after heart extraction (naïve, 1.9 mm ± 0.17; mean ± s.d.) and shortly before light sheet imaging (cleared, 1.555 mm ± 0.12; mean ± s.d.) in 3 mice. The slice height was reduced to 82% ± 2% (mean ± s.d.) of their original size. The factor used to correct all displayed volumes throughout the manuscript was therefore 1.22 (1 divided by 0.82) for every spatial dimension. Please note that displayed scale bars are not corrected, since they relate to the real size of the samples imaged within ECi.

Immune cell counts were determined using the spot detection algorithm with an assumed diameter of neutrophils of 7 µm (14 µm z). After assessment of signal distributions in non-stained, basal, I45min R24h and I45min R5d hearts, a threshold was applied for all hearts (4500 - 35000 grey values, M1: Supplementary Figure 9a and b). Localization of detected spots respective to surface borders was measured using the distance transformation extension on desired surfaces. As a result, spot intensity values are replaced by the minimum distance to the border of the transformed surface. The sum of all detected spots within ± 30 µm of the surface borders of infarct bodies and CD31^{curly} regions were normalized to the respective volume and the total amount of cells present in the heart. We used a transgenic mouse line with endogenously labeled neutrophils (Catchup mice[42]) to show that all neutrophils invading the myocardium are labeled using our i.v.-mediated staining approach (M1: Supplementary Figure 2).

For the 17 segment model, clipping planes were introduced in the required locations of the left ventricle (see Cerqueira et al[48]), images of 3-D content per slice were taken and overlaid with a segment grid in Illustrator CC (Adobe). If a segment showed I/R injury/AAR/CD31^{curly}, it was digitally rated as positive. The sum of the counts per segment over all hearts was depicted as heat maps, generated using R software[49].

Due to the diffuse staining pattern of the F4/80 AF790 antibody, spot detection was not feasible, and we rendered the volume of the immune cell localization instead.

Enlargements and other displayed content was processed using ImageJ software[45].

ECHOCARDIOGRAPHIC ASSESSMENT

Mouse echocardiography was conducted using Visualsonics Vevo 2100 Imaging system. After initial anesthesia with 4% isoflurane in 1 L/min O2, mice were placed on a heated plate and anesthesia was maintained with 1.5% isoflurane. A rectal probe was introduced and heart rate, respiratory rate and body temperature were monitored continuously. After hair removal, images of long and short parasternal axis were acquired in M-mode and B-mode. Ejection fraction was calculated using Simpson's method50.

CARDIAC TROPONIN I ELISA

Cardiac troponin I levels were determined from heparin plasma using ultra-sensitive mouse cardiac troponin-I ELISA (CatNo CTNI-1-US, Life Diagnostics) following manufacturer's instructions. To obtain quantifiable results, samples were diluted 1:100 in diluent YD25-1, according to supplier's suggestions. Absorbance values were recorded using a FLUOStar Omega (BMG Labtech).

FLOW CYTOMETRY PROCEDURE AND ANALYSIS

PBS-perfused hearts of mice after 24 h and 5 d of reperfusion as well as under basal conditions, were mechanically minced and incubated in an enzyme solution comprised of 450 U/ml collagenase I (CatNo C0130, Sigma Aldrich), 125 U/ml collagenase XI (CatNo C7657, Sigma Aldrich), 60 U/ml hyaluronidase (CatNo H3506, Sigma Aldrich), 20mM HEPES (CatNo H3375, Sigma Aldrich), 60 U/ml DNase (CatNo D5319, Sigma Aldrich) in PBS for 40 min in a ThermoMixer C (Eppendorf) at 37 °C and 300 rpm. After enzymatic digestion, the solution was filtered through a 40 µm filter and flow-through was centrifuged for 5 min at 4 °C and 350 x g. Supernatant was discarded and cell pellet resuspended in 1.5 ml PBS. 100 µl of this solution per sample was used for staining, while one solution was chosen for fluorescence minus one (FMO) controls. Blocking of FC-receptors was done by adding 2 µl of TruStain fcX (CatNo 101319, BioLegend) and incubating for 20 min on ice in the dark. Samples were washed by adding 100 µl PBS, centrifuging for 5 min at 4 °C and 350 x g, discarding supernatant, and resuspending the cell pellet in 50 µl PBS. Samples were stained by adding 50 µl PBS containing antibodies CD45-AF700 (CatNo 103127, BioLegend), Ly6G-PerCP/Cy5.5 (CatNo 127615, BioLegend), CD11b-BV605 (CatNo 101257, BioLegend) and F4/80-BV421 (CatNo 123137, BioLegend), all at a dilution of 1:200. Incubation was done for 30 min at RT in the dark, with simultaneous dead and alive staining by addition of Zombie NIR dye (1:2000, CatNo 423105, BioLegend). After antibody incubation, samples were washed as before, supernatant was discarded and cell pellet was resuspended in 150 µl FACS-Buffer, comprised of 1% (v/v) fetal bovine serum (CatNo P30-3302, PAN Biotech) and 0.5% bovine serum albumin (CatNo 8076.3, Roth) in PBS. Data was acquired on a BD FACS Aria III (BD Biosciences) and analysis was performed using FlowJo software (Ashland, USA). Gating strategy is shown in M1: Supplementary Figure 9 c.

STATISTICAL ANALYSIS

Statistical analysis was performed using GraphPad Prism 6.0 for Windows (GraphPad Software). Data are given as indicated in the figure legends. Student's t-test or Mann-Whitney U test were performed for comparison of two groups. Kruskal-Wallis or one-way / two-way ANOVA (with or without repeated measures) followed by Dunn's multiple comparisons test or Bonferroni's correction were performed for multiple group comparisons, as indicated. Correlation was performed using lineary regression best-fit and calculating Pearson's correlation coefficient r. Comparison of two methods was done by Bland-Altman analysis. P-values are depicted and a value of $p<0.05$ was considered significant.

3.2.7. Data availability

The datasets generated during and/or analyzed during the current study are available from the corresponding authors upon request.

3.2.8. References

1 Yellon, D. M. & Hausenloy, D. J. Myocardial reperfusion injury. N Engl J Med 357, 1121-1135, doi:10.1056/NEJMra071667 (2007).
2 Robbers, L. F. et al. Magnetic resonance imaging-defined areas of microvascular obstruction after acute myocardial infarction represent microvascular destruction and haemorrhage. Eur Heart J 34, 2346-2353, doi:10.1093/eurheartj/eht100 (2013).
3 Eltzschig, H. K. & Eckle, T. Ischemia and reperfusion--from mechanism to translation. Nat Med 17, 1391-1401, doi:10.1038/nm.2507 (2011).
4 Wang, J. et al. Visualizing the function and fate of neutrophils in sterile injury and repair. Science 358, 111-116, doi:10.1126/science.aam9690 (2017).
5 Neumann, J. et al. Very-late-antigen-4 (VLA-4)-mediated brain invasion by neutrophils leads to interactions with microglia, increased ischemic injury and impaired behavior in experimental stroke. Acta Neuropathol 129, 259-277 (2015).
6 Hulsmans, M. et al. Macrophages Facilitate Electrical Conduction in the Heart. Cell 169, 510-522 e520, doi:10.1016/j.cell.2017.03.050 (2017).
7 Luedike, P. et al. Cardioprotection through S-nitros(yl)ation of macrophage migration inhibitory factor. Circulation 125, 1880-1889, doi:10.1161/CIRCULATIONAHA.111.069104 (2012).
8 Rassaf, T. et al. Circulating nitrite contributes to cardioprotection by remote ischemic preconditioning. Circ Res 114, 1601-1610, doi:10.1161/CIRCRESAHA.114.303822 (2014).
9 Klingberg, A. et al. Fully Automated Evaluation of Total Glomerular Number and Capillary Tuft Size in Nephritic Kidneys Using Lightsheet Microscopy. J Am Soc Nephrol 28, 452-459, doi:10.1681/ASN.2016020232 (2017).
10 Belle, M. et al. Tridimensional Visualization and Analysis of Early Human Development. Cell 169, 161-173 e112, doi:10.1016/j.cell.2017.03.008 (2017).
11 Ding, Y. et al. Light-Sheet Imaging to Elucidate Cardiovascular Injury and Repair. Curr Cardiol Rep 20, 35, doi:10.1007/s11886-018-0979-6 (2018).
12 Richardson, D. S. & Lichtman, J. W. Clarifying tissue clearing. Cell 162, 246-257 (2015).
13 Erturk, A. et al. Three-dimensional imaging of solvent-cleared organs using 3-DISCO. Nat Protoc 7, 1983-1995 (2012).
14 Botker, H. E. et al. Practical guidelines for rigor and reproducibility in preclinical and clinical studies on cardioprotection. Basic Res Cardiol 113, 39, doi:10.1007/s00395-018-0696-8 (2018).
15 Treweek, J. B. et al. Whole-body tissue stabilization and selective extractions via tissue-hydrogel hybrids for high-resolution intact circuit mapping and phenotyping. Nat Protoc 10, 1860-1896, doi:10.1038/nprot.2015.122 (2015).
16 Lee, S. E. et al. Three-dimensional Cardiomyocytes Structure Revealed By Diffusion Tensor Imaging and Its Validation Using a Tissue-Clearing Technique. Sci Rep 8, 6640, doi:10.1038/s41598-018-24622-6 (2018).
17 Fei, P. et al. Cardiac Light-Sheet Fluorescent Microscopy for Multi-Scale and Rapid Imaging of Architecture and Function. Sci Rep 6, 22489, doi:10.1038/srep22489 (2016).
18 Lugo-Hernandez, E. et al. 3-D visualization and quantification of microvessels in the whole ischemic mouse brain using solvent-based clearing and light sheet microscopy. J Cereb Blood Flow Metab 37, 3355-3367, doi:10.1177/0271678X17698970 (2017).
19 Männ, L. et al. CD11c.DTR mice develop a fatal fulminant myocarditis after local or systemic treatment with diphtheria toxin. Eur J Immunol 46, 2028-2042, doi:10.1002/eji.201546245 (2016).
20 Nehrhoff, I., Ripoll, J., Samaniego, R., Desco, M. & Gomez-Gaviro, M. V. Looking inside the heart: a see-through view of the vascular tree. Biomed Opt Express 8, 3110-3118, doi:10.1364/BOE.8.003110 (2017).
21 Zundler, S. et al. Three-Dimensional Cross-Sectional Light-Sheet Microscopy Imaging of the Inflamed Mouse Gut. Gastroenterology 153, 898-900, doi:10.1053/j.gastro.2017.07.022 (2017).
22 Grüneboom, A. et al. A network of trans-cortical capillaries as mainstay for blood circulation in long bones. Nature Metabolism, doi:10.1038/s42255-018-0016-5 (2019).
23 Hendgen-Cotta, U. B. et al. Nitrite reductase activity of myoglobin regulates respiration and cellular viability in myocardial ischemia-reperfusion injury. Proc Natl Acad Sci U S A 105, 10256-10261, doi:10.1073/pnas.0801336105 (2008).
24 Fishbein, M. C. et al. Early phase acute myocardial infarct size quantification: validation of the triphenyl tetrazolium chloride tissue enzyme staining technique. Am Heart J 101, 593-600 (1981).
25 Thygesen, K. et al. Fourth universal definition of myocardial infarction (2018). Eur Heart J 40, 237-269, doi:10.1093/eurheartj/ehy462 (2019).

26 Nahrendorf, M. Myeloid cell contributions to cardiovascular health and disease. Nat Med 24, 711-720, doi:10.1038/s41591-018-0064-0 (2018).
27 Cerqueira, M. D. et al. Standardized myocardial segmentation and nomenclature for tomographic imaging of the heart. A statement for healthcare professionals from the Cardiac Imaging Committee of the Council on Clinical Cardiology of the American Heart Association. Circulation 105, 539-542 (2002).
28 Susaki, E. A. et al. Advanced CUBIC protocols for whole-brain and whole-body clearing and imaging. Nat Protoc 10, 1709-1727, doi:10.1038/nprot.2015.085 (2015).
29 Tomer, R., Ye, L., Hsueh, B. & Deisseroth, K. Advanced CLARITY for rapid and high-resolution imaging of intact tissues. Nat Protoc 9, 1682-1697, doi:10.1038/nprot.2014.123 (2014).
30 Yu, T., Qi, Y., Gong, H., Luo, Q. & Zhu, D. Optical clearing for multiscale biological tissues. J Biophotonics 11, doi:10.1002/jbio.201700187 (2018).
31 Davidson, S. M. et al. Multitarget Strategies to Reduce Myocardial Ischemia/Reperfusion Injury: JACC Review Topic of the Week. J Am Coll Cardiol 73, 89-99, doi:10.1016/j.jacc.2018.09.086 (2019).
32 Szummer, K. et al. Relations between implementation of new treatments and improved outcomes in patients with non-ST-elevation myocardial infarction during the last 20 years: experiences from SWEDEHEART registry 1995 to 2014. Eur Heart J 39, 3766-3776, doi:10.1093/eurheartj/ehy554 (2018).
33 Ibanez, B. et al. Effect of early metoprolol on infarct size in ST-segment-elevation myocardial infarction patients undergoing primary percutaneous coronary intervention: the Effect of Metoprolol in Cardioprotection During an Acute Myocardial Infarction (METOCARD-CNIC) trial. Circulation 128, 1495-1503, doi:10.1161/CIRCULATIONAHA.113.003653 (2013).
34 Garcia-Ruiz, J. M. et al. Impact of the Timing of Metoprolol Administration During STEMI on Infarct Size and Ventricular Function. J Am Coll Cardiol 67, 2093-2104, doi:10.1016/j.jacc.2016.02.050 (2016).
35 Garcia-Prieto, J. et al. Neutrophil stunning by metoprolol reduces infarct size. Nat Commun 8, 14780, doi:10.1038/ncomms14780 (2017).
36 Liberale, L. et al. Post-ischaemic administration of the murine Canakinumab-surrogate antibody improves outcome in experimental stroke. Eur Heart J 39, 3511-3517, doi:10.1093/eurheartj/ehy286 (2018).
37 Gomez, D. et al. Interleukin-1beta has atheroprotective effects in advanced atherosclerotic lesions of mice. Nat Med 24, 1418-1429, doi:10.1038/s41591-018-0124-5 (2018).
38 Totzeck, M., Hendgen-Cotta, U. B., French, B. A. & Rassaf, T. A practical approach to remote ischemic preconditioning and ischemic preconditioning against myocardial ischemia/reperfusion injury. J Biol Methods 3, doi:10.14440/jbm.2016.149 (2016).
39 Nguyen, C. et al. Near-infrared fluorescence imaging of mouse myocardial microvascular endothelium using Cy5.5-lectin conjugate. J Biophotonics 5, 754-767, doi:10.1002/jbio.201100119 (2012).
40 Robertson, R. T. et al. Use of labeled tomato lectin for imaging vasculature structures. Histochem Cell Biol 143, 225-234, doi:10.1007/s00418-014-1301-3 (2015).
41 Laitinen, L. Griffonia simplicifolia lectins bind specifically to endothelial cells and some epithelial cells in mouse tissues. Histochem J 19, 225-234 (1987).
42 Hasenberg, A. et al. Catchup: a mouse model for imaging-based tracking and modulation of neutrophil granulocytes. Nat Methods 12, 445-452, doi:10.1038/nmeth.3322 (2015).
43 Chen, J., Ceholski, D. K., Liang, L., Fish, K. & Hajjar, R. J. Variability in coronary artery anatomy affects consistency of cardiac damage after myocardial infarction in mice. Am J Physiol Heart Circ Physiol 313, H275-H282, doi:10.1152/ajpheart.00127.2017 (2017).
44 Yang, Z., Berr, S. S., Gilson, W. D., Toufektsian, M. C. & French, B. A. Simultaneous evaluation of infarct size and cardiac function in intact mice by contrast-enhanced cardiac magnetic resonance imaging reveals contractile dysfunction in noninfarcted regions early after myocardial infarction. Circulation 109, 1161-1167, doi:10.1161/01.CIR.0000118495.88442.32 (2004).
45 Schneider, C. A., Rasband, W. S. & Eliceiri, K. W. NIH Image to ImageJ: 25 years of image analysis. Nat Methods 9, 671-675 (2012).
46 Frangi, A. F., Niessen, W. J., Vincken, K. L. & Viergever, M. A. Multiscale vessel enhancement filtering. Medical Image Computing and Computer-Assisted Intervention - Miccai'98 1496, 130-137 (1998).
47 Lesage, D., Angelini, E. D., Bloch, I. & Funka-Lea, G. A review of 3-D vessel lumen segmentation techniques: models, features and extraction schemes. Med Image Anal 13, 819-845, doi:10.1016/j.media.2009.07.011 (2009).
48 Cerqueira, M. D. et al. Standardized myocardial segmentation and nomenclature for tomographic imaging of the heart. A statement for healthcare professionals from the Cardiac Imaging Committee of the Council on Clinical Cardiology of the American Heart Association. Circulation 105, 539-542 (2002).
49 R Core Team. R: A Language and Environment for Statistical Computing. (2014).
50 Heinen, A. et al. Echocardiographic Analysis of Cardiac Function after Infarction in Mice: Validation of Single-Plane Long-Axis View Measurements and the Bi-Plane Simpson Method. Ultrasound Med Biol 44, 1544-1555, doi:10.1016/j.ultrasmedbio.2018.03.020 (2018).

3.2.9. Endnotes

ACKNOWLEDGEMENTS

We thank the imaging center Essen (IMCES, https://imces.uk-essen.de) for continuous support of our imaging experiments.

AUTHOR CONTRIBUTIONS

SFM, SK developed the BALANCE protocol and performed the LSFM experiments together with JD. SFM, SK, LB analyzed the data, generated all illustrations as well as schematics and prepared the figures. PS, SK and LM performed mouse surgeries, TTC planimetry, cardiac troponin I and echocardiographic measurements. AS supervised modeling of the vessel system and CS translated results in R software. HL, MK, JK, DRE, DMH, TR, UHC, MT and MG provided supervision. MT and MG conceived of the study and wrote the manuscript together with TR, UHC, SFM, SK and LB.

COMPETING INTEREST

M. Gunzer and J. Klode received general research funding from LaVision BioTec GmbH. Beyond that, the authors declare no competing interests.

3.3. Interlude I

We have seen how LSFM combined with tissue clearing and i.v. injected fluorophore conjugated antibodies can be used as a fast readout process to analyze anatomical and immunological features of an entire mouse heart after ischemia/reperfusion injury simultaneously. We mainly focused on visualizing neutrophils in their role as first responders in an acute sterile inflammation.

Visualizing cellular components of the immune system in entire organs is of course neither restricted to samples from the vascular medicine field nor to murine models. Human samples can also be processed and cleared using the BALANCE protocol (M1 Figure 3). This is relevant in terms of human clinical research. However, the problem with human samples is that they always exhibit a high background fluorescence due to residual blood, making autofluorescence-attenuation, as implemented before[1], a prerequisite for quantitative imaging. Furthermore, whole-mount staining is the required route of fluorophore conjugated antibodies in human samples in contrast to i.v. injections.

What might be the role and distribution pattern of neutrophils in a chronic sterile inflammation, as it presents in solid cancers? In the past, the impact of tumor invading cytotoxic T cells, amongst others, has been comprehensively studied[90,180]. What about other cellular components of the IS, like neutrophils, that are also known to play a crucial role in tumor development?[100] How do other cells influence tumor biology or T cell function? Are there specific patterns to the location of infiltrating immune cells? Can these interactions influence the patient's outcome and maybe also offer new ideas for treatments?

The following paper, published 2019 in *Science Immunology*, focuses on answering those questions in a 3-D space. Especially the role of TAN and their locally restricted interaction with cytotoxic T cells are assessed in human head and neck squamous cell carcinoma[2].

3.3.1. Additional info manuscript #2

3.3.1.1. Supplementary Material deposit

Supplementary Material can be found on the attached CD at the end of this thesis, on the journal webpage or under my personal *Sciebo* repository. Hyperlinks provided might be subject to change. → immunology.sciencemag

Supplenmentary information

[provider: *Sciebo*, Password: MerzThesis]

3.3.1.2. License info

This article was published in the restricted access journal *Science Immunology*. The license acquired allows reprinting and electronic distribution of the accepted manuscript, but not the published version. For more information, see Appendix – 7.2 Licenses.

3.3.2. Author contributions manuscript #2

Author contributions of Simon F. Merz for the published manuscript

Multidimensional imaging provides evidence for down-regulation of T cell effector function by MDSC in human cancer tissue

Conception:	**0%**
Experimental work	
1. Development of clearing method (KT)	75%
2. Development of staining strategy of LSFM samples	75%
3. Sample processing (KT)	15%
4. Data acquisition via LSFM (KT)	10%
5. Developing and performing slide stainings during revision	30%
6. Data acquisition of slides during revision	25%
Data analysis	
1. IMARIS (3-D) tracing and segmentation (KT)	10%
2. Definiens during revision	10%
Revising the manuscript	**10%**

Simon F. Merz	Prof. Matthias Gunzer

KT = knowledge transfer

3.4. M#2: Multi-dimensional imaging provides evidence for down-regulation of T cell effector function by MDSC in human cancer tissue

Journal: *Science Immunology*

Published Online: 18 October 2019

DOI: 10.1126/sciimmunol.aaw9159

URL: https://immunology.sciencemag.org/content/4/40/eaaw9159

3.4.1. Authors and Affiliations

Yu Si[1,2§], Simon F. Merz[3,4§], Philipp Jansen[4§], Baoxiao Wang[1,2], Kirsten Bruderek[1], Petra Altenhoff[1], Stefan Mattheis[1], Stephan Lang[1,5], Matthias Gunzer[3], Joachim Klode[4], Anthony Squire[3], Sven Brandau[1, 5,*]

[1] Department of Otorhinolaryngology, University Duisburg-Essen, University Hospital Essen, Essen, Germany
[2] Department of Otolaryngology, Head and Neck Surgery, Sun Yat-Sen Memorial Hospital, Sun Yat-Sen University, Guangzhou, China
[3] Institute for Experimental Immunology and Imaging, University Hospital Essen, University Duisburg–Essen, Essen, Germany
[4] Department of Dermatology, University Hospital Essen, University Duisburg–Essen, Essen, Germany
[5] German Cancer Consortium (DKTK), Partner Site University Hospital Essen, Essen, Germany
[§] these authors share first authorship

*Corresponding author:

Sven Brandau, PhD
Research Division, Department of Otorhinolaryngology
University of Duisburg-Essen and University Hospital Essen
West German Cancer Center
Hufelandstrasse 55
45122 Essen, Germany
Phone:+49-201-723-3193
Fax: +49-201-723-5196
E-Mail: sven.brandau@uk-essen.de

One Sentence Summary: Intratumoral physical engagement of T cells with immunosuppressive neutrophils is associated with reduced effector function and poor clinical outcome

3.4.2. Abstract

A high intratumoral frequency of neutrophils is associated with poor clinical outcome in most cancer entities. It is hypothesized that immunosuppressive MDSC (myeloid-derived suppressor cell) activity of neutrophils against tumor reactive T cells contributes to this effect. However, direct evidence for such activity in situ is lacking. Here, we utilized whole-mount labeling and clearing, 3-D light sheet microscopy and digital image reconstruction supplemented by 2-D multi-parameter immunofluorescence, for in situ analyses of potential MDSC-T cell interactions in primary human head and neck cancer tissue. We could identify intratumoral hot spots of high PMN-MDSC and T cell colocalization. In these areas, the expression of effector molecules Granzyme B and Ki-67 in T cells was strongly reduced, in particular for T cells that were in close proximity or physically engaged with PMN-MDSC, which expressed LOX-1 and arginase I. Importantly, cancer patients with evidence for strong downregulation of T cell function by PMN-MDSC had significantly impaired survival. In sum, our approach identifies areas of clinically relevant functional interaction between MDSC and T cells in human cancer tissue and may help to inform patient selection in future combination immunotherapies.

3.4.3. Introduction

The tumor microenvironment is a spatially organized landscape with immune cells located in the core of the tumor, its invasive margin or in the surrounding stroma that mainly consists of fibroblastoid mesenchymal cells (1). Different types of infiltrating immune cells have different effects on tumor progression (2) and location-specific effects on disease progression and response to therapy are possible. A strong lymphocytic infiltration is typically associated with good clinical outcome in many different tumor types, including melanoma, breast, bladder, urothelial, ovarian, colorectal, renal, lung and head and neck cancer (HNC) (2-6). Accumulating evidence also indicates a critical role of myeloid cells in the pathophysiology of human cancers. Increased numbers of neutrophil gran-

ulocytes have been observed both in the peripheral blood and in the tumor tissues of patients with different types of cancer (7). In murine studies, it appears that tumor-associated neutrophils (TAN) can exert both, pro-tumor and anti-tumor effects (8). Numerous studies have shown that neutrophils can promote tumor progression by degrading matrix, stimulating tumor cell proliferation, increasing metastasis, and enhancing angiogenesis (9). In addition, immunosuppressive types of neutrophils, termed PMN-MDSC (polymorphonuclear myeloid-derived suppressor cells), have been described in the circulation, with preferential accumulation and co-purification with mononuclear cells in the so-called "low density" (LDN) fraction of the blood (10). In tissues, neutrophils might also contribute to immune suppression and, subsequently, tumor progression in a manner similar to that described for PMN-MDSC (11). However, TAN can also exert anti-tumor functions, such as promoting tumor cell death via their powerful antimicrobial killing machinery or by inducing factors that recruit and activate innate and adaptive immune cells (12, 13).

In recent years, there has been progress in the phenotypic and functional characterization of circulating immunosuppressive neutrophils. Immunosuppressive MDSC activity has been ascribed to activated neutrophils in the LDN fraction of the peripheral blood (14). Lectin-type oxidized LDL receptor-1 (LOX-1) has been suggested as a potential marker for neutrophils with MDSC activity (15). Of note, mature neutrophils contained stronger suppressive MDSC activity as compared to their immature counterparts (16). In contrast to circulating cells, still very little is known about the identity of PMN-MDSC or other subtypes of neutrophils in human cancer tissue. Functional studies on tissue cells depend on the analysis of bulk cell suspensions released from sufficiently large, fresh tissue pieces. Such studies are possible in lung cancer and Singhal *et al* identified a specific subset of TANs in lung cancer of early-stage disease patients. Those APC-like "hybrid neutrophils" exhibited characteristics of both neutrophils and antigen-presenting cells (APCs), expressed HLA-DR, cross-presented antigens, and stimulated T cell activity (17). Furthermore, Condamine *et al* found that 15 - 50% of neutrophils in tumor tissues stained positive for LOX-1. Neutrophils from the peripheral blood and bone-marrow, which expressed LOX-1, were more suppressive compared to their LOX-1- counterparts. However, no functional analysis of LOX-1+ TAN from tissue was performed in that study (15).

The big disadvantage of ex vivo functional analyses of tumor-infiltrating immune cells based on tissue dissociation is the fact that cells can no longer be assigned to their original

localization in either tumor core, stroma or blood vessels. Cells are isolated from only macroscopically evaluated fresh tissue pieces and mechanical processing or enzymatic treatment further modulate the cells of interest. The purity of the preparation can even be further influenced by remaining peripheral blood cells. Hence, the spatial context, e.g. inflamed vs. less infiltrated tissue is lost and functionally relevant physical interactions of cells are disrupted. Thus, cellular interactions restricted to specific tissue regions cannot be assessed.

Histopathological analysis combined with quantitative multi-parameter immunofluorescence imaging allows mapping the spatial distribution of tumor cells and immune cells (18). It also enables a separate analysis of tumor core, margin and stromal areas together with the definition of tumor regions highly or less infiltrated by immune cells. Finally, potential interactions between immune cells, including conjugate formation, can also be quantified. This spatial context and localization of particular immune cell subsets are crucial for understanding their function as well as their role in disease progression and response to therapy in HNC and other types of cancer (2, 6, 19). Moreover, aided by advanced image analysis technologies, the spatial context of tumor and stromal cells can be analyzed at single-cell resolution using rigorous spatial statistics to investigate locally restricted clustering, dispersion and interactions in two or three dimensions (3D) (18).

In our study, we focused on the interaction of TAN and TIL (tumor-infiltrating lymphocytes) in the microenvironment of tumors of the head and neck region. Understanding the role of TAN in the tumor immune microenvironment is important, as TAN are one of the most powerful predictors of poor survival in large pan-cancer analyses (7). Our study explored the possibility that TAN or TAN subsets impair the activity of tumor-infiltrating T cells in situ. To this end, we utilized both, 2D and 3D quantitative multi-parameter immunofluorescence imaging approaches and analysis. We determined the localization of TAN and TIL in the tumor tissue to further define functional subsets of the cells. By this approach, we identified intratumoral hot spots of TAN/TIL interactions. We found evidence of strongly reduced TIL function in such hotspots, especially in regions where the TAN showed a phenotype of PMN-MDSC and physically engaged with TIL. Since the degree of inhibitory TAN/TIL interactions strongly correlated with patient survival, we propose that one mechanism of PMN-MDSC function is the intratumoral inactivation of TIL by direct physical confrontation.

3.4.4. Results

3.4.4.1. Density and intratumoral localization of granulocytes and T cells

Tumor infiltrating immune cells can be localized either in epithelial tumor core areas with direct contact to tumor cells or in stromal regions, which mainly consist of fibroblastoid mesenchymal cells. Segmentation into stromal and tumor core area was performed for each tissue sample, based on training of the image analysis software and pan-cytokeratin staining (M2: Figure 1a). We then used the markers CD66b and CD3 together with tissue segmentation to determine the density of granulocytes and T cells in tumor core and stromal regions, respectively (M2: Figure 1b, c). We found high inter-individual variation of cell densities, with equal T cell densities in both, stroma and tumor regions. In contrast, the density of CD66b+ cells was significantly lower in the tumor core area. 2-D tissue analysis alone is inherently spatially limited and cannot faithfully represent the complex 3-D tissue architecture. In order to overcome this, we established a whole-mount labeling and tissue clearing approach based on 3-D light sheet fluorescence microscopy (20), which permitted the determination of absolute immune cell numbers as well as their 3D distribution. We segmented and quantified stroma and tumor volumes and determined granulocyte and T cell infiltrate densities in both areas (M2: suppl. video 1, M2: Figure 1d, e). Using this novel technical approach, we could quantify the absolute number of CD66b+ and CD3+ cells in human tissue pieces of up to $1cm^3$ size. Quantitative analysis revealed cellular densities of 15.000 to 60.000 granulocytes and T cells per mm3 for most patients analyzed. Interestingly, 3-D absolute cell counts confirmed the reduced density of CD66b+ cells in tumor core areas (M2: Figure 1f).

The application of a 3-D shell model also allowed grouping segmented cells according to their distance from the tumor margin (M2: Figure 1g-h). Density of $CD3^+$ cells was highest at the tumor margin and decreased with distance (M2: Figure 1i). In contrast, $CD66b^+$ cell densities were relatively consistent in tumor surrounding stromal tissue, but also decreased with higher proximity to the tumor core (M2: Figure 1j).

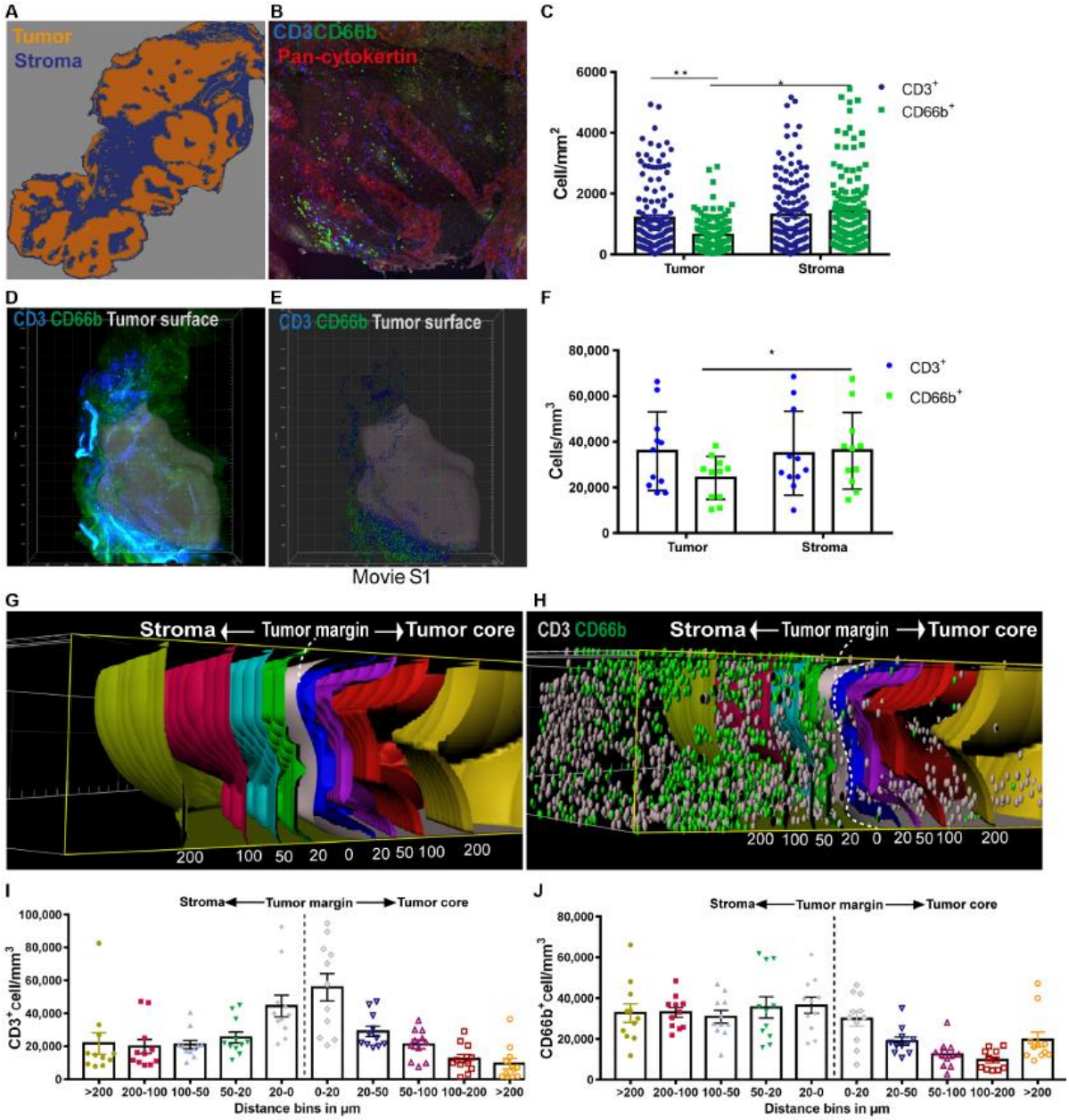

M2: Figure 1 Intratumoral spatial distribution of granulocytes and T cells

Tissue studio composer technology and image-based machine learning (A), pan-cytokeratin staining (B) and the manual tracing wizard of tissue studio were used to define tumor and stroma regions. Multi-parameter immunofluorescence was used to determine the density of CD3 and CD66b cells in 2-D tissue sections (n=137 patients) (C) or whole mount stained 3-D material (n=11) (F) obtained from patients with HNC. Panels D and E represent still images of videos and depict CD3 cells (blue), CD66b cells (green) and tumor surface area. Panel E / video 1 are additionally provided as supplementary material. Using the "split into surface" Spots tool of Imaris, the density of CD3+

and CD66b+ cells within defined distances to the tumor margin was determined (G-I). Paired t-test was used to determine statistical significance.

3.4.4.2. Identification, spatial distribution and clinical relevance of LOX1+ TAN

The myeloid-derived suppressor cell (MDSC) activity of a subtype of polymorphonuclear (PMN) leukocytes in the peripheral blood, now termed PMN-MDSC (21), is well established. For these circulating PMN-MDSC, both CD66b and CD15 have been used as PMN markers and suppressive subsets have been defined by CD10, CD16 and LOX-1 positivity in three independent studies (15, 16, 22). Although LOX-1 has been suggested as a PMN-MDSC marker, very little is known about the phenotype, frequency, localization, activity and clinical relevance of potentially T cell suppressive granulocytic cells in human tumor tissues.

In order to shed more light on this topic, we first characterized tumor-infiltrating leukocytes by flow cytometry applying the markers mentioned above. We found that the majority (90-99%) of CD66b+ neutrophils in the tumor tissues were positive for CD10, CD11b and CD16, a phenotype characteristic for mature neutrophils (M2: Figure 2a,b). Interestingly, and confirming previously reported observation (15), LOX-1 defined two subsets of neutrophils in our cohort of HNC patients. Using multi-color immunofluorescence (M2: Figure 2c) we found the relative proportion of LOX-1+ TAN to vary greatly among patients (M2: Figure 2d; range 4% to 99% and 1% to 97% in tumor and stroma, respectively). Consistent with the reduced overall CD66b+ cell densities reported above, LOX1+CD66b+ cells also had lower densities within tumor core areas compared with stroma (M2: Figure 2e).

The expression of myeloperoxidase (MPO), arginase I and HLA-DR in neutrophils and PMN-MDSC has been associated with their tumor-promoting and T cell suppressive or stimulatory activity, respectively (14, 17, 23). Multi-color immunofluorescence (M2: Figure 2f) revealed that the majority of the CD66b+ cells in both, tumor and stroma, expressed arginase I and MPO, whereas only very few neutrophils (below 20% in most patients) expressed HLA-DR (M2: Figure 2g). While the majority of the LOX-1+ TAN were positive for MPO and immunosuppressive arginase I, these molecules were less frequently expressed in LOX-1-/CD66b+ cells (M2: Figure 2h, i). Nevertheless, HLA-DR-

low/negative and HLA-DR-positive TAN both had substantial expression of LOX-1 and arginase I (M2: suppl. figure S1).

Next, we assessed the clinical relevance of TAN density and localization in two subsets of HNC, namely LSCC and OSCC. Clearly, a high density (above median) of TAN in tumor tissue in both cancer types was significantly associated with reduced overall survival (OS) (M2: Figure S2a, c; see tables S2 and S4 for multivariate analysis). In contrast, high TAN densities in stroma regions did not have a significant effect on OS (M2: Figure S2b, d). Interestingly, a profound prognostic relevance was observed for LOX-1+ TAN density in the tumor core area of LSCC and OSCC patients (M2: Figure 2j, suppl. figure S2e; see table S4 for multivariate analyses). This was in contrast to a moderate and statistically not significant relationship between outcome and LOX-1+ TAN density in the stromal tissue areas (M2: Figure 2k, and M2: suppl. figure S2f). The clinical relevance of TAN and LOX-1 was underscored by the observed correlation of TAN density and LOX-1 expression with lymph node metastasis staging (M2: suppl. figure S2g-h).

3.4.4.3. Quantitative in situ tissue analysis provides evidence for in vivo PMN-MDSC activity

It has been suggested that LOX-1+/CD66b+ cells represent PMN-MDSC (15). However, experimental data on a potential in situ interaction of LOX-1+/CD66b+ cells and T cells in tumor tissues are lacking. Therefore, we embarked on a systematic analysis of TAN and potential PMN-MDSC with T cells in the tumor tissue of patients with HNC.

Using our established 3-D analysis protocol we first delineated potential hot spots of interaction between CD66b+ cells and CD3 cells in defined tissue areas. After quantification of CD66b+ and CD3+ cell densities in both, 2-D and 3-D approaches (M2: Figure 3 a-c) we noted a striking heterogeneous distribution of both cell types. We therefore defined T cell-dominated, TAN-dominated and mixed regions. TAN-dominated regions were defined as areas with a neutrophil/T cell ratio (NTR) >9 (more than 90% neutrophils), T cell dominated with a NTR<0.1 (more than 90% T cells) and mixed regions with a NTR between 0.1 and 9. Mixed regions were the most frequent areas making up 49% of the tumor core area and 54% of the stroma (M2: Figure 3d). Supplementary video 2 and figure 3b show examples for the 3-D reconstruction and color coding of those regions (TAN region = green, T cell region = red, mixed region = yellow).

Next, we determined the exact position and mean nearest neighbor (n-n) distances of CD3 to CD66b cells in entire tissue section of 54 patients. In each instance the n-n distances were normalized by division with the n-n distances for a CSR distribution model, representing theoretical random distribution. We found that the actual relative mean n-n distance had values below 1, which is less than that expected for a CSR distribution, and thus indicates greater proximity and potential functional interaction between the two cellular subsets (M2: Figure 3e). Quantitative analysis of direct CD3-CD66b conjugates revealed on average 5-10% of CD3 and CD66b cells engaged in conjugation (M2: Figure 3f, g). We also measured conjugation with CD66b cells separately for CD4 and CD8 T cell subsets. Both T cell subsets displayed similar conjugation frequencies with neutrophils (mean around 5%, blue symbols in suppl. figures S3a and b).

Since cellular conjugation in tissues is a 3-D process, we validated our data using whole mount labelling of tissue pieces. Video 3 and figure 3h show the identification of unconjugated and conjugated cells in situ after 2-color whole mount staining, ultramicroscope image acquisition, digital conversion and 3-D image reconstruction. The quantification confirmed that indeed 5-10% of CD3 and CD66b cells engaged in conjugates with each other (M2: suppl. figure S4a). While more than 10% of CD3 and CD66b cells formed conjugates close to the tumor margin, the relative percentage of conjugated cells declined to below 5% at distances greater than 200 μm into the tumor core or stromal area (M2: suppl. figure S4b, c). Given the potential role of LOX-1+ TAN in T cell modulation, we next developed a four-color staining protocol (M2: suppl. figure S4d) and indeed found an increased LOX-1 positivity in CD66b+ cells forming conjugates with T cells (M2: Figure 3i). This increased positivity was likewise observed for conjugates with CD4 and CD8 T cell subsets (M2: suppl. figure S3c and d). A plot of the relative CD3 cell density as a function of radial distance around LOX+ TAN and LOX- TAN cells indicates an increased CD3 clustering around TAN cells in general, with a significantly higher degree of clustering around LOX-1+ TAN cells, specifically in the tumor region (M2: Figure 3 j, k). Overall, these data suggest a higher propensity of LOX-1+ TAN to engage with T cells, although an upregulation of LOX-1 as a consequence of conjugate formation cannot be ruled out. Finally, clinical follow-up data supported the potential functional and pathophysiological relevance of TAN-TIL conjugate formation. Patients with a high percentage of CD3 conjugated to LOX-1+ TAN (M2: Figure 3 l, m) or overall TAN (M2: suppl figure S4e, f) in their tumor tissue

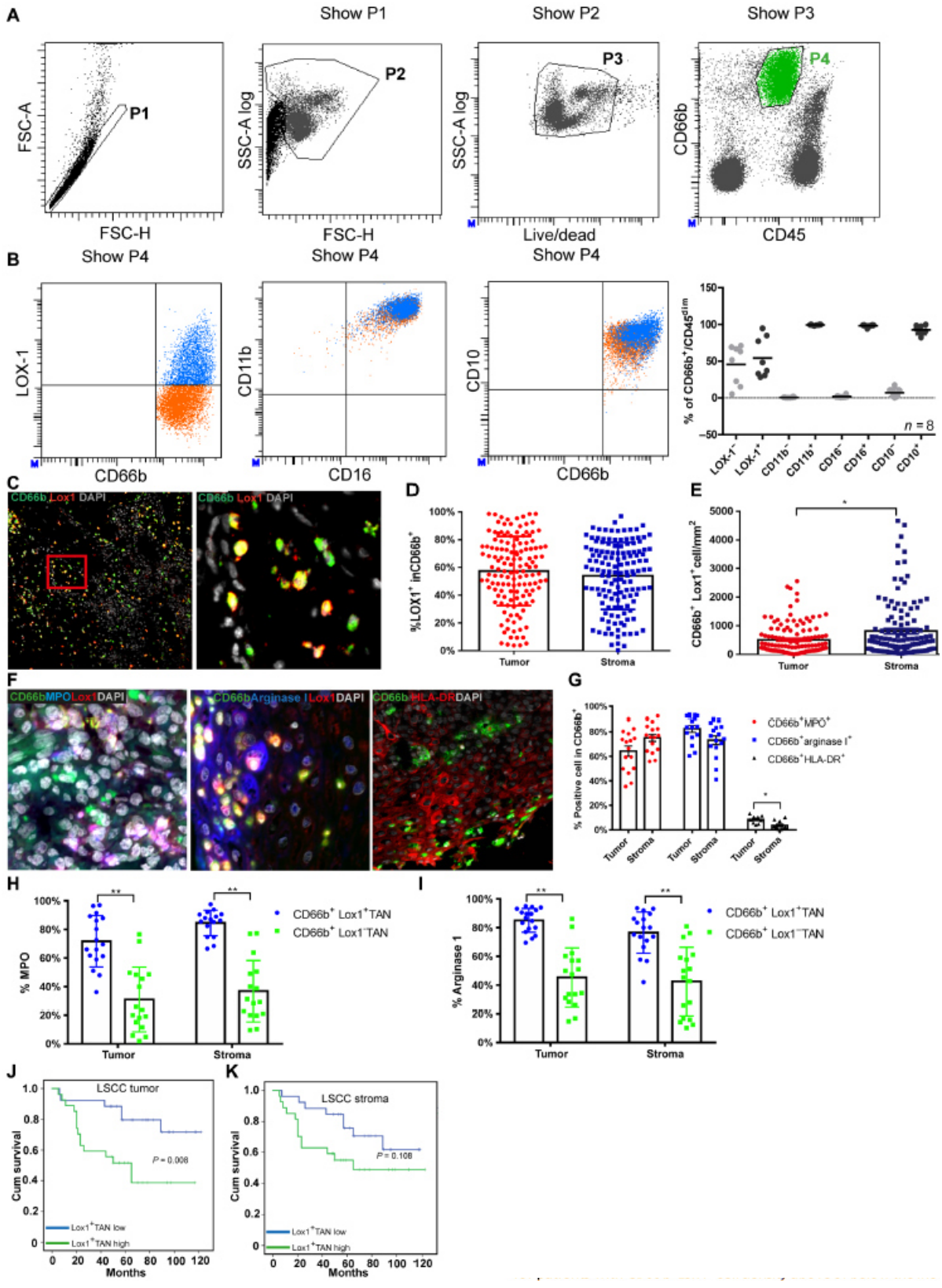

M2: Figure 2 Identification and quantification of intratumoral TAN subsets

TAN (see panel A for gating) isolated from fresh tumor tissue of patients with HNC cancer (n=8) were subjected to flow cytometry and stained for the expression of LOX-1, CD11b, CD16, and CD10 (B). Multi-parameter immunofluorescence in cryosectioned tissue samples (see panel C and F for examples) was used to determine the density of $CD66b^+$ cells expressing LOX-1, MPO, arginase I, or HLA-DR (D, E, G) in tumor and stroma regions, respectively. The percentage of $LOX\text{-}1^+$ and $LOX\text{-}1^-$ TAN expressing MPO (H) and arginase I (I) in tumor and stroma was determined by 3-color immunofluorescence combined with a DAPI counterstain (F). Kaplan-Meier survival curves for overall survival were plotted for patients with $CD66b^+Lox1^+$ cell density above or below the median in tumor and stroma regions (LSCC patients, n= 53). Statistical significance was determined by paired t-test (D-I) or log-rank regression analysis (I).

displayed significantly impaired survival compared to those patients with lower CD3 conjugation. Taken together, these data define and quantify, for the first time, intratumoral areas of substantial TAN-TIL interaction and suggest a functional and clinical relevance of these interactions especially for LOX-1+ TAN.

Data from murine and human ex vivo models suggested downregulation of T cell function by PMN-MDSC. To obtain evidence for this process in human cancer tissue, we performed an in-depth analysis of potential links between CD66b+ cells and expression of GrzB (cytotoxicity, M2: Figure 4a) and Ki-67 (proliferation, M2: Figure 4b) in tumor-infiltrating T cells. Experiments focused on mixed regions, in which frequent interaction of both cell types occurred. In this region, we determined the relative percentage and the density of different subsets of CD66b+ cells, and determined the correlations with the relative percentage and the density of T cells expressing either GrzB or Ki67 (M2: Figure 4c, d). High prevalence of CD66b+ subsets expressing either LOX-1, arginase or MPO negatively correlated with the density or percentage of proliferating and cytotoxic T cells. The strongest negative correlations were found between the density of arginase and LOX-1 expressing TAN and the density of proliferating and cytotoxic T cells in the tumor area (M2: Figure 4c, left part). Correlations in the stromal area were similar but less pronounced, suggesting a stronger modulation of T cell effector function by immunosuppressive CD66b+ cells in the tumor area. Interestingly, the density of HLA-DR+ TAN strongly correlated with the increased prevalence of proliferating and cytotoxic

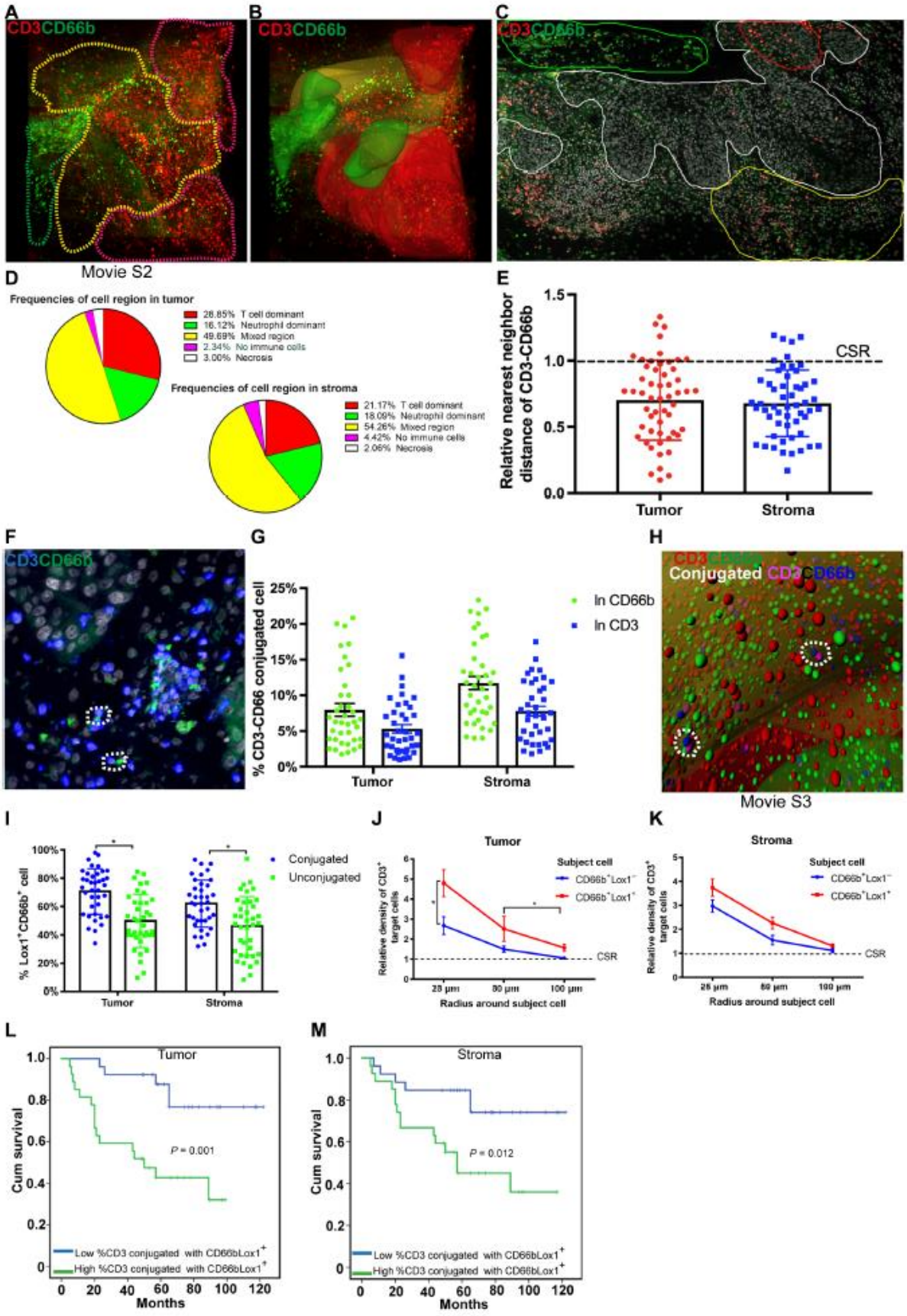

M2: Figure 3 Spatial distribution and interaction of TAN and T cells in situ

T cells (CD3, red) and TAN (CD66b, green) were identified and quantified by whole mount staining (A, B) using Imaris or in cryosections (C) using tissue studio. Neutrophil to T cell ratio (NTR) was determined. Regions with NTR >9 (more than 90% neutrophils, green circle) were defined as "neutrophil dominant", regions with NTR >0.1 (less than 10% neutrophils, red circle) as "T cell dominant" and regions with NTR between 0.1 and 9 as mixed regions (yellow circle) (see video 2 for illustration). White outline in (C) defines the tumor core area and the pie charts in (D) show the relative percentage of the indicated region in tumor and stroma (n=137). Determination of relative nearest neighbor distance from a CSR model (see supplementary methods for details) indicated a non-random distribution and clustering of CD3 and CD66b cells (E). Physical conjugation of CD3 cells with CD66b cells (F-H) and percentage of LOX-1-positivity in conjugated versus unconjugated CD66b+ cells (I) was visualized and quantified (n=53). Video 3 illustrates conjugate analysis after whole mount staining, ultramicroscope image acquisition and 3-D image reconstruction; color code indicates non-conjugated (red/green) or conjugated (violet, blue). Relative density of CD3 target cells as a function of the radial distance around CD66b subject cells was determined in tumor (J) and stroma (K). Here a relative cell density of 1 corresponds to a CSR distribution of cells. The data are indicative of a significantly increased clustering of CD3 cells around LOX-1$^+$ TAN. For (L) and (M) Kaplan-Meier survival curves for overall survival were plotted for LSCC patients (n=53) with the percentage of CD3 conjugated with CD66b$^+$ Lox1$^+$ cells above or below the median. Statistical significance was determined by Log-Rank regression analysis with the level of significance set at $p \leq 0.05$. Cox multivariate regression analysis was performed by adding UICC-TNM stages and the percentage of CD3 conjugated with CD66b$^+$ Lox1 into a model. Differences in both tumor and stroma region remained significantly associated with OS (tumor: HR4.543, P=0.003, stroma: HR 4.007, P=0.005, see supplementary tables 1-4 for details).

and tumor regions, suggesting the possibility of T cell stimulation by this TAN subset (17). Evidence for in situ T cell suppressive activity was underscored by a more detailed analysis of CD66b+ subsets. As shown in figure 4d the density of LOX-1+ cells co-expressing either arginase or MPO strongly correlated with a reduced expression of Ki-67 and GrzB in T cells. Interestingly, this correlation was significantly stronger in the tumor region as

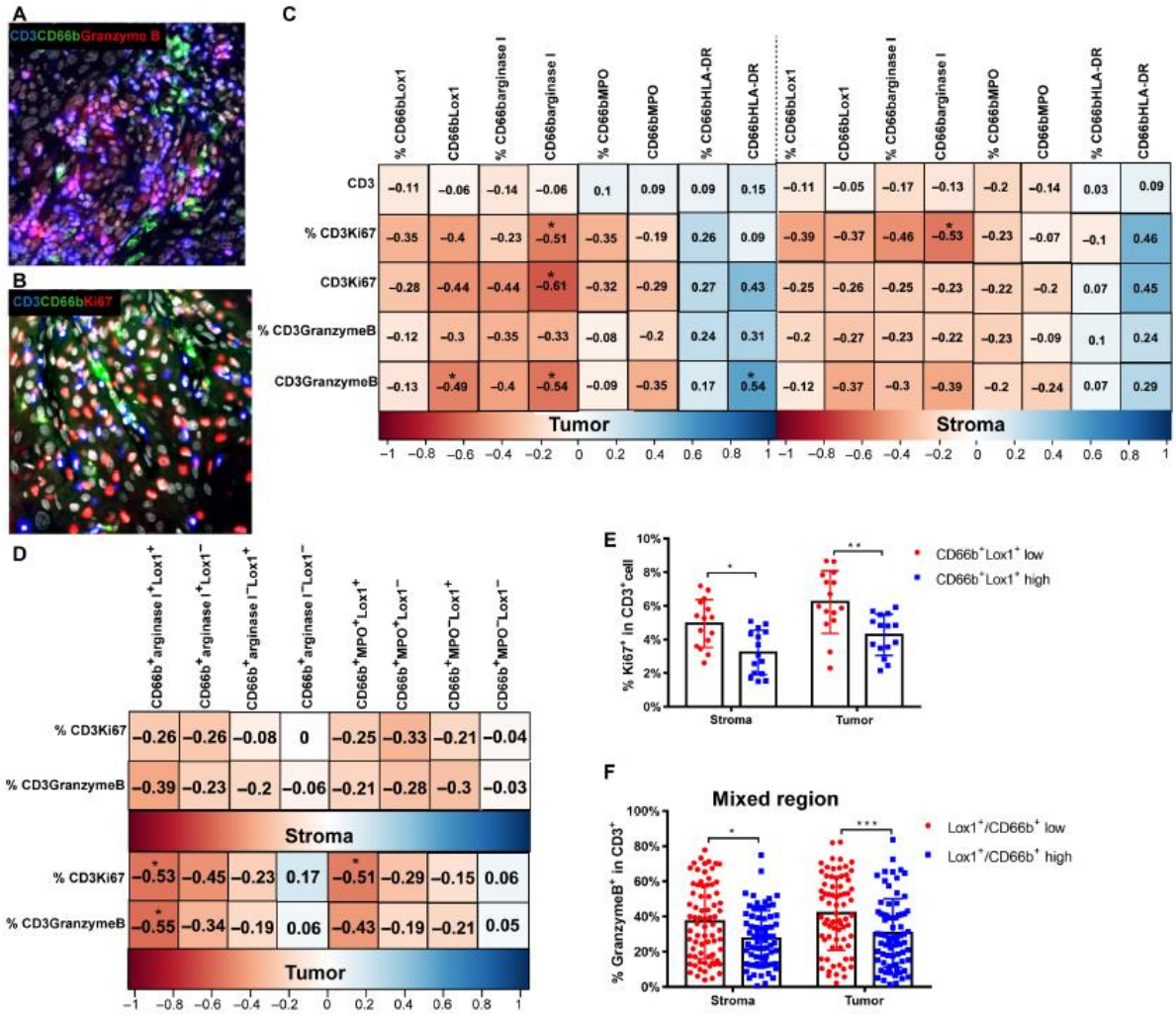

M2: Figure 4 Correlation of TAN phenotypes and TIL effector function

Identification of TIL (CD3) was combined with GrzB (A) and Ki-67 (B) as surrogate markers for T cell functionality. Identification of TAN (CD66b) was combined with LOX-1, Arginase I, MPO and HLA-DR. Density and relative percentage of Ki67 and GrzB expression in T cells was correlated with density and relative percentage of the various TAN subsets (C, D). Heat maps (C, D) show pairwise Pearson´s correlation coefficients of the density and percentage of different phenotype of TAN with total T cells, cytotoxic T cells and proliferating T cells in tumor and stroma, respectively. Color codes indicate positive (blue) or negative (red) correlation. Note the positive correlation of HLA-DR$^+$ TAN with T cell effector function (blue color code). Strongest negative correlations are observed for CD66b$^+$/ArgI$^+$/Lox1$^+$ and T cell effector function in the tumor core area. For (E) and (F) patients were divided into groups with relative percentage of LOX-1$^+$ TAN above (high) or below (low) the median. Percentage of Ki67$^+$ and GrzB$^+$ T cells was determined in the mixed regions of tumor and stroma, respectively. Ki-67 n= 30 patients, GrzB n= 137 patients, t-test.

compared to stroma. Finally, we divided patients into two groups with LOX-1 expression either above or below the median and determined the level of Ki-67/GrzB expression in the mixed region of the tumor tissue (M2: Figure 4e, f). Consistent with previously observed data, T cell effector function was higher in patients with low LOX-1 expression. Separate analysis of CD4 and CD8 T cells showed that proliferation of both T cell subsets was reduced, if the percentage of LOX-1+ TAN was high (M2: suppl. figure S3e and f). As expected, expression of GrzB was mainly restricted to CD8 cells and only smaller numbers of CD4 cells expressed this molecule (suppl. figure S3g and h). Of note, in the presence of higher frequencies of LOX-1+ TAN, GrzB expression in CD8 T cells was substantially reduced, and this reduction was more pronounced in the tumor region. Altogether, these data suggest that LOX-1 could serve as a valuable surface marker to define CD66b+ cells with MDSC activity in human tumor tissues.

It is tempting to speculate that direct contact or close proximity between CD66b+ cells with MDSC activity and T cells is required for the downregulation of T cell effector function. In order to test this hypothesis and further substantiate the modulation of T cells by CD66b+ cells in situ we employed four-color immunofluorescence (M2: Figure 5a-c) and compared the relative percentage of GrzB+ T cells, both conjugated and non-conjugated with CD66b+ cells. In both, 3-D (M2: Figure 5d and video 4) and 2-D analysis (M2: Figure 5e) GrzB expression was significantly reduced, when T cells were engaged in conjugates with CD66b+ cells. This reduction of GrzB positivity was more pronounced in LOX-1+/CD66b+ pairs compared to pairs with LOX-1- TAN (M2: Figure 5f) and was additionally dependent on relative proximity between T cells and CD66b+ cells (M2: Figure 5g, h). If the distance between T cells and the CD66b subject cell reached 100 µm or above, GrzB expression was no longer influenced. Consistent with this finding we observed a higher expression of both Ki-67 and GrzB in tissue regions devoid of CD66b+ cells (T cell dominated, suppl. figure S5a-d). In contrast, both T cell effector molecules were downregulated in regions of T cell to TAN/PMN-MDSC contact (M2: suppl. figure S5 b, d). A separate analysis of CD4 and CD8 T cell showed that Ki-67 expression of both T cell subsets was reduced, if they were in conjugation with CD66b+ cells (M2: suppl. figure S3i, j). In confirmation of total CD3 T cell data, conjugated CD8 cells had dramatically reduced GrzB expression, while the much lower expression of GrzB in CD4 cells was less strongly influenced (M2: Supplementary Figure S3k, l).

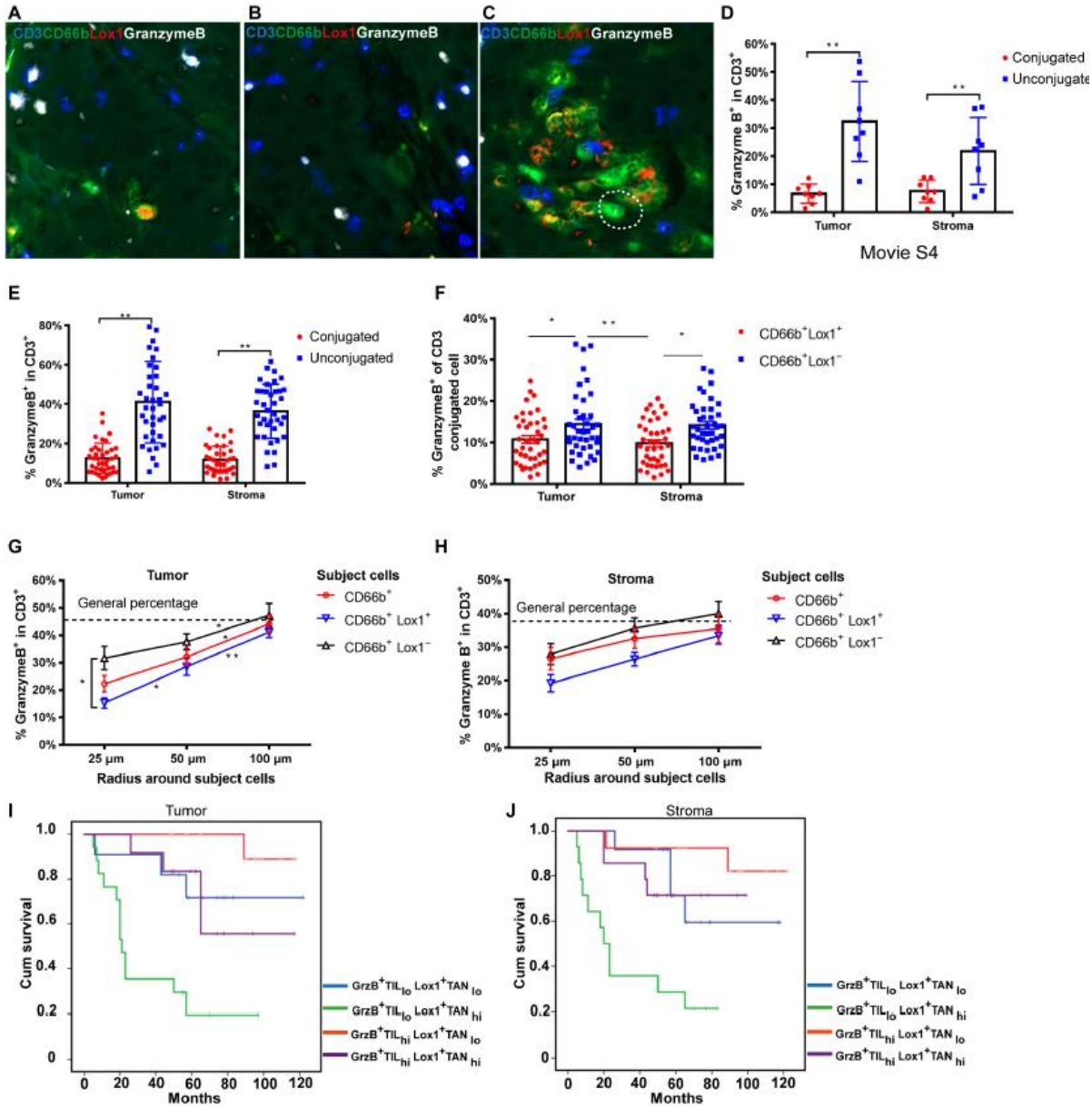

M2: Figure 5 Conjugation and functional modulation of TIL by LOX-1⁺ TAN provides evidence for PMN-MDSC activity in vivo

Four-color immunofluorescence was performed to identify LOX-1⁺/CD66b⁺ cells and CD3⁺/GrzB⁺ cells. Representative stainings are shown for a mixed region (A), a T cell dominated region (B) and a neutrophil dominated region (C). The percentage of GrzB⁺ TIL conjugated or non-conjugated to CD66b⁺ cells (D, E) or conjugated to LOX-1⁺ or LOX-1⁻ CD66b⁺ cells (F) in tumor and stroma are shown for 2-D cryosections (E, F; n= 53 patients) or in 3-D whole mount stained tissue (D; n= 8 patients; video 4 illustrates a 3-D reconstruction of functional TIL modulation). The percentage of Grzb⁺ TIL was also plotted as a function of the radial distance around different CD66b subsets (G, H). The dashed lines indicate the mean percentage of GrzB-positivity for the total tissue

area of all patients in the cohort. Kaplan-Meier survival curves for overall survival were plotted for LSCC patients (n=53) divided into groups according to density of LOX-1$^+$ TAN and GrzB$^+$ TIL being above or below the median. Statistical significance was determined by Log-Rank regression analysis with the level of significance set at $p \leq 0.05$. Cox multivariate regression analysis was performed by adding UICC-TNM stages and the percentage of CD3 conjugated with CD66b$^+$ Lox1 into a model. Low GrzB$^+$ TIL and high LOX-1$^+$ TAN remained significantly associated with OS (tumor: P=0.001, stroma: P=0.01).

To finally test the clinical relevance of the TAN/PMN-MDSC-T cell interaction we combined data on GrzB/CD3 expression with LOX-1/CD66b data and analyzed the correlation with patient follow-up (M2: Figure 5 i, j). Indeed, an extremely poor outcome was recorded for patients with a low frequency of GrzB+ TIL in conjunction with a high frequency of LOX-1+ PMN-MDSC. Collectively, our data support the concept that tumor-associated CD66b+ cells downregulate T cell activity in situ. In agreement with a previous report, which suggested LOX-1 as a PMN-MDSC marker, our data support a higher in situ suppressive capacity of LOX-1+ CD66b+ cells compared with LOX-1- cells. In addition, our data provide evidence that this MDSC activity of LOX1+ CD66b+ cells is more pronounced in the tumor core area compared with stromal regions of the tumor tissue.

3.4.5. Discussion

The impact of the tumor-infiltrating immune cells (the so-called TIME, tumor-immune microenvironment) on the progression of the disease and response to therapy is determined by complex spatial and functional interactions of these cells with other immune cells, but also with tumor cells and mesenchymal cells of the tumor stroma. Understanding this interaction is important for optimization and further development of cancer immunotherapy. Recent techniques, such as high resolution single-cell RNA sequencing, Cytometry by Time of Flight (CyTOF) and multi-parameter flow cytometry have added to this understanding by providing an unprecedented view of the composition and function of immune cells within the TME from bulk tissues. However, because of the nature of the datasets being used, these studies lack important information related to actual cellular proportions, cellular and tissue heterogeneity as well as deeper spatial distribution (24).

Immune cells freshly isolated from tissue pieces for CyTOF or flow cytometry may originate from different regions of the tumor, including tumor core, stromal and necrotic areas and are thus not taking into account the spatial heterogeneity of the malignant tissue (18). Even contamination with circulating blood leukocytes is difficult to exclude, and tissue processing further influences the expression of surface molecules. At the same time, it has become evident that the spatial context of immune cells is critical for tumor development (2, 25). Carstens *et al* defined a 20-µm radius around the cancer cells as enhanced probability of cell–cell contact distance. They found that high infiltration of cytotoxic T cells within this radius of cytokeratin 8-positive cancer cells significantly correlated with prolonged patient survival (26), which indicates that cytotoxic T cells in the direct vicinity of cancer cells may have a more important biological function than more distant cells. Similarly, in an oral squamous cell cancer study, the CD8+ T cell number at the tumor site had a greater effect on overall survival than stromal T cells (27).

In our study, we have profiled a quantitative in situ two-dimensional and three-dimensional tissue analysis that identifies intratumoral hot spots of immunosuppressive neutrophil activity. We found that the overall density of CD66b+ cells was higher in stroma compared to tumor core. Nevertheless, a profound prognostic relevance was observed for CD66b+ and CD66b+ Lox-1+ cell density in the tumor core area but not in the stromal zone. Importantly, the strongest negative correlations were found between arginase I and LOX-1 expressing TAN and proliferating and cytotoxic T cells in the tumor core. These data suggest a higher pathophysiological relevance of TAN-TIL interactions in the tumor core area. We believe that this has important implications for understanding TAN biology, as in most studies that isolate TAN from bulk tissue pieces, the isolated cell suspension is dominated by neutrophils from mesenchymal stromal regions, which appear to have a weaker modulation of T cell effector function.

Recent studies in murine tumor models and cancer patients provided evidence for an important functional role of PMN or PMN-MDSC during tumor progression (16, 28, 29). These studies suggested that TAN might, at least in part, mediate the effects on disease outcome via the regulation of T cell activity. The absence of TAN correlates with increased tumor infiltration and function of activated T cells and led to a T cell–dependent suppression of tumor growth in pancreatic tumors (30). In contrast, HLADR+ TAN, which origi-

nate from immature progenitors, could stimulate and facilitate T cell responses (17). Supporting such a concept, we indeed found positive correlations between HLA-DR expressing TAN and proliferating and cytotoxic T cells in tumor.

Although published studies suggest that TAN with T cell suppressive function (i.e. PMN-MDSC) exist in human tumor tissue, until now, no evidence for such a T cell modulatory interaction of TAN and TIL in situ existed. Tissue section analyses provide the spatial context of single cell interactions within the cancer-microenvironment. Such spatial data has already aided our identification of clinically relevant features that are more powerful than simple cell counts. For example, it was reported that Tregs more proximal to CD8+ T cells are more effective at suppressing anticancer function (27). These and similar studies prompted us to investigate the clustering and expression of functional molecules in T cells and neutrophils in HNC patients with single cell resolution. We used GrzB as a marker of cytotoxic activity and Ki-67 to mark proliferating T cells. While GrzB expression is necessary to demonstrate killing activity, relocalization and mobilization of cytotoxic granules towards the target cells would be required to unequivocally show the active killing process itself (31). However, such studies are mainly limited to in vitro settings and are not feasible in larger series of tissue samples of human tumors. Phosphorylation downstream of T cell receptor signaling is another means to monitor T cell activity and also often used in vitro (32). Again, these events are difficult to assess and quantify in larger series of human tissue samples because of their very transient and time-dependent nature.

Our spatial analyses suggested that clustering effects of TAN and T cells take place in a radius below 100 μm. This range was therefore used for a more rigorous evaluation of clustering behavior. The relative CD3 density was significantly higher within the distance of 25 μm to LOX1+ TAN compared to LOX1- TAN in tumor, which indicates that LOX1+ TAN have a stronger 'local' clustering capacity. However, the significance disappeared with increasing distance, which may indicate that T cell inhibition by LOX1+ TAN is only functional in close proximity, similar to mechanisms described before for Tregs. It is currently unclear, whether this requires direct physical interaction or whether close apposition within diffusive reach of inhibitory molecules is sufficient. Nevertheless, the lack of significant functional difference between LOX1+ TAN and LOX1- TAN in stroma may indicate that localization of LOX1+ TAN within the tumor area may affect their function.

LOX-1 is a class E scavenger receptor that is expressed in macrophages and chondrocytes, as well as in endothelial and smooth muscle cells (33). In our study and in a smaller cohort of 10 patients with HNC and NSCLC (15) a high variance of LOX-1-positivity in TAN was observed. Since LOX-1 is only expressed in a small proportion of circulating neutrophils (15) upregulation of the molecule is expected to take place in the tumor microenvironment. While the full mechanisms of LOX-1 plasticity still have to be elucidated, induction of ER-stress has been suggested to be involved (15, 34). LOX-1+ PMN-MDSC also show elevated production of reactive oxygen species (ROS) and arginase I (15), both of which are suggested as major mechanisms of T cell suppression. We also found a high density of LOX-1+ arginase-I+ TAN, and their presence was most strongly correlated with a reduced expression of cytotoxic GrzB and the proliferation marker Ki67 in closely located T cells. Finally, patients with concomitant high density of LOX-1+ TAN and low density of GrzB+ TIL showed extremely poor survival re-affirming a strong tumor promoting and T cell suppressive function for LOX-1+ TAN.

In our study, whole tissue sections were imaged using an automated microscope operating in tiling mode, followed by automated detection and quantification of CD66b+ cell and TIL in the whole slide images. Despite significant variation in tumor morphology and staining conditions, target structures could be automatically identified resulting in increased objectivity and reproducibility of the analysis.

However, for many approaches a histological three-dimensional imaging of the entire organ is essential to gain a deep understanding of tissue morphology and physiological processes, as well allowing us to address questions that are inaccessible by two-dimensional methods. Therefore, we employed a nondestructive imaging technique for whole organ imaging with precise qualitative and quantitative analysis of functional structures in their natural spatial context (35). A striking heterogeneous distribution of TAN and TIL was noted in 2D tumor sections and in intact 3D tissue architecture. However, only the 3D analysis revealed the existence of TAN dominated, T cell dominated (T cell inflamed) and mixed regions. Mixed regions were the most frequent areas observed and may also be the regions for the interaction of CD66b+ cells with T cells. Importantly, the frequency of GrzB+ TIL and Ki67+ was higher in T cell rich regions compared to the other two regions, in which TAN were present.

Depleting or “re-educating” immunosuppressive myeloid populations has proven to be effective at eliciting antitumor T-cell responses (36-38). In a genetically engineered

pancreatic ductal adenocarcinoma model, the systemic depletion of Gr1+ myeloid cells could increase the infiltration of effector T cells and inhibit tumor growth (39). Host CXCR2 inhibition by genetic ablation prevented neutrophil accumulation in pancreatic tumors and led to a T cell–dependent suppression of tumor growth (30). Therefore, inhibiting neutrophil migration into the tumor may be therapeutic in HNC. However, this is a potentially harmful therapy, as the systemic depletion or inhibition of neutrophils bears the risk of secondary infections. Since we have shown that LOX-1+ TAN have a strong tumor promoting and T cell suppressive function, we propose, that specifically LOX-1+ TAN are a promising therapeutic targets.

Interestingly, whole mount tissue staining also enabled us to assess the density of both cell populations with relative distance to the tumor margin, representing a high-resolution map of tumor infiltrating cells. The highest T cell density was reached within 20 µm off the tumor margin to both sides, and a significant decrease of T cell density in the region of 20–50 µm, followed by a slighter decrease with relative distance from the tumor margin was observed. A similar distribution pattern was noted for CD66b+ cells inside the tumor region, although increased cellular densities were noted in the tumor core area beyond 200 µm from tumor margin. On the contrary, T cell density was the lowest in the tumor core, which may indicate spatial immunosuppression by CD66b+ cells.

In summary, we present here for the first-time detailed data on the local spatial distribution and potential functional interaction of CD66b+ cells and T cells in the microenvironment of a solid tumor. Based on these data "mixed" areas in the tumor core region are especially important hot spots of interaction with high clinical relevance. In addition, we provide the first experimental evidence for a potential downregulation of T cell effector function by LOX-1+ TAN in situ. Our findings suggest that a combination immunotherapy, which concomitantly prevents TAN influx and augments T cell effector function, can be beneficial in head and neck cancer and possibly also in other cancers with a similar TAN-TIL profile.

3.4.6. Material and methods

STUDY DESIGN

It was the aim of this study to obtain evidence for the existence, the phenotype, the localization and the potential clinical relevance of PMN-MDSC in human cancer tissue. To this end, patients with primary HNC and no prior radio- or chemotherapy were included. Inclusion was based on i) tumor type (LSCC or OSCC), ii) provision of informed consent, iii)

availability and quality of obtained tissue, iv) availability of clinical record and follow-up data. Survival data were obtained in a retrospective manner and overall survival was chosen as the primary endpoint. Pseudonymization was applied and during experimentation and data analysis the primary investigator had no access to patient identities. Because of the retrospective and observational nature no prior sample size calculation was performed. Multi-color immunofluorescence was applied on tumor samples after prior establishment of methods and antibody panels on tonsillar tissue.

STUDY SUBJECTS AND COLLECTION OF TISSUE

Tumor tissues from patients with HNC were collected during routine surgery. Patients with prior radiotherapy or chemotherapy, synchronous carcinoma in another location or severe concomitant systemic infectious disease were excluded. UICC/AJCC TNM 7th edition was used to determine HNC stage. Only material from patients with histopathologically proven HNC was included. Treatment strategies (surgery alone, surgery combined by adjuvant radiotherapy or radiochemotherapy, primary radiochemotherapy) were developed by the multidisciplinary tumor board for head and neck cancers, and treatments were conducted according to state-of-the art technique and guidelines in place at the West German Cancer Center. Analysis of tissues was approved by the institutional review board of the Medical faculty of the University Duisburg-Essen and written informed consent was obtained from all patients. In total, material from 74 patients with SCC of the larynx (LSCC) [14 females, 60 males; ages 37-75 years (median 59 years)] and from 112 patients with SCC of the oropharynx (OSCC) [40 females, 72 males; ages 41-78 years (median 61 years) was used in this exploratory and observational study. Survival analysis was performed on patients with a minimum of 36-month follow up.

FLOW CYTOMETRIC ANALYSIS OF TUMOR INFILTRATING CELLS

Unfixed, fresh tumor tissue was digested for 45min with 200µg/mL Dispase (Roche Applied Science, Mannheim, Germany), 200µg/mL Collagen IV and 10µg/mL DNase (both Sigma-Aldrich, Taufkirchen, Germany). Subsequently, digested samples were stained with antibodies CD45 VioGreen (clone 5B1, Miltenyi Biotec, Bergisch Gladbach, Germany) CD66b FITC (clone 80H3, Beckman Coulter, Krefeld, Germany), HLA-DR APC (clone G46-6), CD14 APC-Cy7 (clone MphiP9), CD16 PE-Cy7 (clone 3G8), CD11b APC-Cy7 (clone Mac1, all BD Bioscience , Heidelberg, Germany), CD10 APC (clone HI10a) and LOX-1 PE (clone 15C4, both BioLegend, Koblenz, Germany), followed by a live/dead staining using the fixable viability dye eFluor™ 506 (eBioscience™/ Thermofisher scientific, Darmstadt, Germany). For staining with anti-Arginase I APC (polyclonal sheep, Biotechne, Wiesbaden, Germany) cells were fixed and permeabilized with BD Cytofix/Cytoperm Solution Kit. Stained cells were analyzed with BD FACS Canto II using DIVA 8.01 software (BD Bioscience) or FlowJo10 (LLC, Ashland, Oregon, USA).

WHOLE SLIDE IMMUNOFLUORESCENCE STAINING AND IMAGE ACQUISITION

Surgical material was embedded in Tissue-Tek® O.C.T.™Compound (Sakura Finetek , Staufen, Germany), frozen in liquid nitrogen and stored at -80°C until use .

For fluorescence staining, 5 µm tissue sections were fixed with Cytofix/Cytoperm (BD Biosciences), incubated with the primary antibody overnight at 4°C, followed by secondary antibody. Cell nuclei were stained with DAPI. Combinations of cell detection antibodies as well as reagents used for immunofluorescence analysis are listed in supplementary methods.

After staining multichannel images were acquired on an sCMOS camera (Hamamatsu Orca Flash, 16 bit 4.2 Mp) using an automated Zeiss AxioObserver microscope equipped with

an Apotome for optical sectioning, motorized stage, Colibri LED excitation source (excitation lines: 365nm, 470nm, 555nm and 625nm), and optical filter blocks for the fluorescent labels, DAPI or Alexa 405 (EX G365, BS 395, EM 445/50), FITC (EX 470/40, BS 495, EM 525/50), Alexa 546 (EX 545/25, BS 570, EM 605/70) and Alexa 647 (EX 640/30, BS 660, EM 690/50). All images were acquired using a Carl Zeiss 20X/0.8 NA plan-apochromat objective. For the imaging of whole tissue sections, the microscope was operated in tiling mode, otherwise individual images were acquired in selected regions containing both labelled T cells and neutrophils. Typically, 10 to 20 images were randomly acquired from each patient tissue section.

TISSUE IMAGE SEGMENTATION AND CELL CLASSIFICATION

Using Definiens Tissue Studio® image analysis software (Definiens, Munich, Germany), the multichannel images acquired from whole tissue sections were automatically segmented into tissue regions and cell label classes were identified. Based on cell morphology and pan-cytokeratin staining, the software was trained to initially segment the tissue into 4 tissue classes designated tumor, stroma, necrosis/lumen and background. DAPI staining together with cell detection antibodies were used for nuclei segmentation and cell segmentation and subsequent cell identification.

SPATIAL MAPPING OF CELLS

Following the Tissue Studio batch processing of all patient tissue samples, a csv file containing the patient ID, tissue class, cell label class, cell coordinates, and co-expression parameters for all segmented cells was exported and used in subsequent spatial point pattern analysis. For the analysis of cellular spatial distributions, Spatstat, a R package for spatial point pattern analysis (www.spatstat.org), was used together with an imageJ script for masking tumor and stroma regions.
In general, spatial point patterns for the data were normalized to a corresponding model simulating a Complete Spatial Random (CSR) distribution of cells. Further methodological details on the CSR model, cell cluster analysis and nearest neighbor analysis are provided in supplementary methods.

TISSUE CLEARING AND WHOLE-MOUNT STAINING

The clearing of whole HNC tumor tissue was performed according to Klingberg et al. (20) with some modifications for whole mount labelling. In brief, fresh tumor tissue was first fixed with 4% PFA in PBS at 4°C for 4 hours or overnight, dependent on the tumor size (>1cm3 overnight). All incubations were performed under constant agitation. The tissue was then washed with PBS and permeabilized by incubation in 20% DMSO, 1% TritonX-100, 2.3% glycine in PBS, for 5 days at room temperature. This was followed by blocking with wash-buffer supplemented with 5% normal goat serum (Dianova, Hamburg, Germany) and 10µg/ml sodium-heparin (Ratiopharm, Ulm, Germany), for 1 day at 37°C. Whole tissue samples were then incubated with rabbit anti-human LOX-1 or mouse anti-human Granzyme B at 37°C for 5 days, followed by 4 times 6 hours washing. Incubation with secondary antibodies being either donkey anti-rabbit or donkey anti-mouse, both coupled to Alexa-Flour 546, was performed at 37°C for 3 days. The tissue samples were again washed, as described above, and incubated for 5 days at 37°C with mouse anti-human CD3 Alexa-Flour 647 (BioLegend; Koblenz, Germany) and self-conjugated mouse anti-human CD66b (Beckmann Coulter, Krefeld, Germany) Alexa-Flour 790. Fluorophore conjugation was carried out using an Alexa Fluor 790 antibody labeling kit (A20189, Thermo Fisher, Darmstadt, Germany), following the providers instructions. Afterwards

the tissue samples were washed, dehydrated in a graded ethanol series of 50%, and 70% for 4hours, followed by two further 100% incubations, performed overnight and for 4 hrs respectively. Finally, the samples were cleared by incubation in ECi for 1 day.

IMAGE ACQUISITION AND DATA PROCESSING FOR 3-D TISSUE ANALYSIS

Cleared whole mount stained tumor samples were imaged using a light sheet ultramicroscope (LaVision BioTec Bielefeld, Germany) and multichannel images were acquired for each of the following antigens and fluorescent labels: Lox-1 Alexa 546 , Granzyme B Alexa 546, CD3 Alexa 647 and CD66b Alexa 790. Image stacks were acquired on the Ultramicroscope at a magnification of 6.4 X (pixel resolution 1.0156 microns) using a z-stepping size of 2 microns and employing the dynamic focus function. The 3D rendering of images and subsequent analysis were then performed using Imaris 9.1.2 software (Bitplane, Switzerland). To this end the manual tracing wizard was used to determine the surface and volume of the total tissue, tumor area and stroma area. After background subtraction the absolute number and 3D location of each cell type were obtained using Imaris 'Spots' objects and the 'split into surface' Spots tool. Events double positive for two signals were obtained using the Spots co-localization tool. Spot objects from cells of the same type were defined as co-localized, if they were within 8 µm distance of each other. Spot objects of different cell types were defined as conjugated for a separation distance less than 15 µm. In order to identify the distribution patterns of neutrophils and T cells at different distances from, both inside and outside of the tumor margin, new surface objects were created, whose surfaces were respectively set to the distances 20, 50, 100, and 200 µm from the tumor surface in both directions (tumor and stroma). Then using the "split into surface" Spots tool, the cell density within the volume of each new surface could be derived.

STATISTICAL METHODS

Data were analyzed using GraphPad Prism software. Statistical significance of immunohistochemically quantifications were assessed with Student's t-test, paired t-test or analysis of variance, as appropriate. For the correlation analyses between different phenotype of TAN and T cell distributions, the Pearson's correlation coefficient (r) was calculated. Clinical data were analyzed with the SPSS statistical software version 22. The immune staining results were then correlated with clinical data using univariate and multivariate Cox regression analysis with UICC tumor stage and p16 immunohistochemistry as the confounding factors. Kaplan-Meier survival curves for overall survival were plotted and statistical significance was determined by Log-Rank regression analysis with the level of significance set at $p \leq 0.05$. * indicates $p<0.05$, ** indicates $p<0.005$, *** indicates $p<0.0005$.

3.4.7. References

1. J. Galon, W. H. Fridman, F. Pages, The adaptive immunologic microenvironment in colorectal cancer: a novel perspective. Cancer Res 67, 1883-1886 (2007).
2. W. H. Fridman, F. Pages, C. Sautes-Fridman, J. Galon, The immune contexture in human tumours: impact on clinical outcome. Nat Rev Cancer 12, 298-306 (2012).
3. S. M. Mahmoud, E. C. Paish, D. G. Powe, R. D. Macmillan, M. J. Grainge, A. H. Lee, I. O. Ellis, A. R. Green, Tumor-infiltrating CD8+ lymphocytes predict clinical outcome in breast cancer. J Clin Oncol 29, 1949-1955 (2011).
4. L. Zhang, J. R. Conejo-Garcia, D. Katsaros, P. A. Gimotty, M. Massobrio, G. Regnani, A. Makrigiannakis, H. Gray, K. Schlienger, M. N. Liebman, S. C. Rubin, G. Coukos, Intratumoral T cells, recurrence, and survival in epithelial ovarian cancer. N Engl J Med 348, 203-213 (2003).

5. J. Galon, A. Costes, F. Sanchez-Cabo, A. Kirilovsky, B. Mlecnik, C. Lagorce-Pages, M. Tosolini, M. Camus, A. Berger, P. Wind, F. Zinzindohoue, P. Bruneval, P. H. Cugnenc, Z. Trajanoski, W. H. Fridman, F. Pages, Type, density, and location of immune cells within human colorectal tumors predict clinical outcome. Science 313, 1960-1964 (2006).
6. K. I. Al-Shibli, T. Donnem, S. Al-Saad, M. Persson, R. M. Bremnes, L. T. Busund, Prognostic effect of epithelial and stromal lymphocyte infiltration in non-small cell lung cancer. Clin Cancer Res 14, 5220-5227 (2008).
7. A. J. Gentles, A. M. Newman, C. L. Liu, S. V. Bratman, W. Feng, D. Kim, V. S. Nair, Y. Xu, A. Khuong, C. D. Hoang, M. Diehn, R. B. West, S. K. Plevritis, A. A. Alizadeh, The prognostic landscape of genes and infiltrating immune cells across human cancers. Nat Med 21, 938-945 (2015).
8. S. Brandau, The dichotomy of neutrophil granulocytes in cancer. Semin Cancer Biol 23, 139-140 (2013).
9. A. M. Houghton, The paradox of tumor-associated neutrophils: fueling tumor growth with cytotoxic substances. Cell Cycle 9, 1732-1737 (2010).
10. K. Moses, S. Brandau, Human neutrophils: Their role in cancer and relation to myeloid-derived suppressor cells. Semin Immunol 28, 187-196 (2016).
11. C. A. Dumitru, S. Lang, S. Brandau, Modulation of neutrophil granulocytes in the tumor microenvironment: mechanisms and consequences for tumor progression. Semin Cancer Biol 23, 141-148 (2013).
12. M. van Egmond, J. E. Bakema, Neutrophils as effector cells for antibody-based immunotherapy of cancer. Semin Cancer Biol 23, 190-199 (2013).
13. A. Mantovani, M. A. Cassatella, C. Costantini, S. Jaillon, Neutrophils in the activation and regulation of innate and adaptive immunity. Nat. Rev. Immunol 11, 519-531 (2011).
14. P. C. Rodriguez, M. S. Ernstoff, C. Hernandez, M. Atkins, J. Zabaleta, R. Sierra, A. C. Ochoa, Arginase I-producing myeloid-derived suppressor cells in renal cell carcinoma are a subpopulation of activated granulocytes. Cancer Res 69, 1553-1560 (2009).
15. T. Condamine, G. A. Dominguez, J. I. Youn, A. V. Kossenkov, S. Mony, K. Alicea-Torres, E. Tcyganov, A. Hashimoto, Y. Nefedova, C. Lin, S. Partlova, A. Garfall, D. T. Vogl, X. Xu, S. C. Knight, G. Malietzis, G. H. Lee, E. Eruslanov, S. M. Albelda, X. Wang, J. L. Mehta, M. Bewtra, A. Rustgi, N. Hockstein, R. Witt, G. Masters, B. Nam, D. Smirnov, M. A. Sepulveda, D. I. Gabrilovich, Lectin-type oxidized LDL receptor-1 distinguishes population of human polymorphonuclear myeloid-derived suppressor cells in cancer patients. Sci Immunol 1, (2016).
16. S. Lang, K. Bruderek, C. Kaspar, B. Hoing, O. Kanaan, N. Dominas, T. Hussain, F. Droege, C. Eyth, B. Hadaschik, S. Brandau, Clinical Relevance and Suppressive Capacity of Human Myeloid-Derived Suppressor Cell Subsets. Clin Cancer Res 24, 4834-4844 (2018).
17. S. Singhal, P. S. Bhojnagarwala, S. O'Brien, E. K. Moon, A. L. Garfall, A. S. Rao, J. G. Quatromoni, T. L. Stephen, L. Litzky, C. Deshpande, M. D. Feldman, W. W. Hancock, J. R. Conejo-Garcia, S. M. Albelda, E. B. Eruslanov, Origin and Role of a Subset of Tumor-Associated Neutrophils with Antigen-Presenting Cell Features in Early-Stage Human Lung Cancer. Cancer Cell 30, 120-135 (2016).
18. A. Heindl, S. Nawaz, Y. Yuan, Mapping spatial heterogeneity in the tumor microenvironment: a new era for digital pathology. Lab Invest 95, 377-384 (2015).
19. B. Höing, O. Kanaan, P. Altenhoff, R. Petri, K. Thangavelu, A. Schluter, S. Lang, A. Bankfalvi, S. Brandau, Stromal versus tumoral inflammation differentially contribute to metastasis and poor survival in laryngeal squamous cell carcinoma. Oncotarget 9, 8415-8426 (2018).
20. A. Klingberg, A. Hasenberg, I. Ludwig-Portugall, A. Medyukhina, L. Mann, A. Brenzel, D. R. Engel, M. T. Figge, C. Kurts, M. Gunzer, Fully Automated Evaluation of Total Glomerular Number and Capillary Tuft Size in Nephritic Kidneys Using Lightsheet Microscopy. J Am Soc Nephrol 28, 452-459 (2017).
21. V. Bronte, S. Brandau, S. H. Chen, M. P. Colombo, A. B. Frey, T. F. Greten, S. Mandruzzato, P. J. Murray, A. Ochoa, S. Ostrand-Rosenberg, P. C. Rodriguez, A. Sica, V. Umansky, R. H. Vonderheide, D. I. Gabrilovich, Recommendations for myeloid-derived suppressor cell nomenclature and characterization standards. Nat Commun 7, 12150 (2016).
22. O. Marini, S. Costa, D. Bevilacqua, F. Calzetti, N. Tamassia, C. Spina, D. De Sabata, E. Tinazzi, C. Lunardi, M. T. Scupoli, C. Cavallini, E. Zoratti, I. Tinazzi, A. Marchetta, A. Vassanelli, M. Cantini, G. Gandini, A. Ruzzenente, A. Guglielmi, F. Missale, W. Vermi, C. Tecchio, M. A. Cassatella, P. Scapini, Mature CD10(+) and immature CD10(-) neutrophils present in G-CSF-treated donors display opposite effects on T cells. Blood 129, 1343-1356 (2017).
23. A. L. Rymaszewski, E. Tate, J. P. Yimbesalu, A. E. Gelman, J. A. Jarzembowski, H. Zhang, K. A. Pritchard, Jr., H. G. Vikis, The role of neutrophil myeloperoxidase in models of lung tumor development. Cancers (Basel) 6, 1111-1127 (2014).
24. M. Binnewies, E. W. Roberts, K. Kersten, V. Chan, D. F. Fearon, M. Merad, L. M. Coussens, D. I. Gabrilovich, S. Ostrand-Rosenberg, C. C. Hedrick, R. H. Vonderheide, M. J. Pittet, R. K. Jain, W. Zou, T. K. Howcroft, E. C.

Woodhouse, R. A. Weinberg, M. F. Krummel, Understanding the tumor immune microenvironment (TIME) for effective therapy. Nat Med 24, 541-550 (2018).
25. J. Galon, B. Mlecnik, G. Bindea, H. K. Angell, A. Berger, C. Lagorce, A. Lugli, I. Zlobec, A. Hartmann, C. Bifulco, I. D. Nagtegaal, R. Palmqvist, G. V. Masucci, G. Botti, F. Tatangelo, P. Delrio, M. Maio, L. Laghi, F. Grizzi, M. Asslaber, C. D'Arrigo, F. Vidal-Vanaclocha, E. Zavadova, L. Chouchane, P. S. Ohashi, S. Hafezi-Bakhtiari, B. G. Wouters, M. Roehrl, L. Nguyen, Y. Kawakami, S. Hazama, K. Okuno, S. Ogino, P. Gibbs, P. Waring, N. Sato, T. Torigoe, K. Itoh, P. S. Patel, S. N. Shukla, Y. Wang, S. Kopetz, F. A. Sinicrope, V. Scripcariu, P. A. Ascierto, F. M. Marincola, B. A. Fox, F. Pages, Towards the introduction of the 'Immunoscore' in the classification of malignant tumours. J Pathol 232, 199-209 (2014).
26. J. L. Carstens, P. Correa de Sampaio, D. Yang, S. Barua, H. Wang, A. Rao, J. P. Allison, V. S. LeBleu, R. Kalluri, Spatial computation of intratumoral T cells correlates with survival of patients with pancreatic cancer. Nat Commun 8, 15095 (2017).
27. Z. Feng, D. Bethmann, M. Kappler, C. Ballesteros-Merino, A. Eckert, R. B. Bell, A. Cheng, T. Bui, R. Leidner, W. J. Urba, K. Johnson, C. Hoyt, C. B. Bifulco, J. Bukur, C. Wickenhauser, B. Seliger, B. A. Fox, Multiparametric immune profiling in HPV- oral squamous cell cancer. JCI Insight 2, (2017).
28. Z. G. Fridlender, J. Sun, S. Kim, V. Kapoor, G. Cheng, L. Ling, G. S. Worthen, S. M. Albelda, Polarization of tumor-associated neutrophil phenotype by TGF-beta: "N1" versus "N2" TAN. Cancer Cell 16, 183-194 (2009).
29. S. Trellakis, K. Bruderek, C. A. Dumitru, H. Gholaman, X. Gu, A. Bankfalvi, A. Scherag, J. Hutte, N. Dominas, G. F. Lehnerdt, T. K. Hoffmann, S. Lang, S. Brandau, Polymorphonuclear granulocytes in human head and neck cancer: Enhanced inflammatory activity, modulation by cancer cells and expansion in advanced disease. International Journal of Cancer 129, 2183-2193 (2011).
30. T. Chao, E. E. Furth, R. H. Vonderheide, CXCR2-Dependent Accumulation of Tumor-Associated Neutrophils Regulates T-cell Immunity in Pancreatic Ductal Adenocarcinoma. Cancer Immunol Res 4, 968-982 (2016).
31. V. Bronte, T. Kasic, G. Gri, K. Gallana, G. Borsellino, I. Marigo, L. Battistini, M. Iafrate, T. Prayer-Galetti, F. Pagano, A. Viola, Boosting antitumor responses of T lymphocytes infiltrating human prostate cancers. J Exp Med 201, 1257-1268 (2005).
32. M. Koneru, D. Schaer, N. Monu, A. Ayala, A. B. Frey, Defective proximal TCR signaling inhibits CD8+ tumor-infiltrating lymphocyte lytic function. J Immunol 174, 1830-1840 (2005).
33. A. Taye, A. A. El-Sheikh, Lectin-like oxidized low-density lipoprotein receptor 1 pathways. Eur J Clin Invest 43, 740-745 (2013).
34. J. Nan, Y. F. Xing, B. Hu, J. X. Tang, H. M. Dong, Y. M. He, D. Y. Ruan, Q. J. Ye, J. R. Cai, X. K. Ma, J. Chen, X. R. Cai, Z. X. Lin, X. Y. Wu, X. Li, Endoplasmic reticulum stress induced LOX-1(+) CD15(+) polymorphonuclear myeloid-derived suppressor cells in hepatocellular carcinoma. Immunology 154, 144-155 (2018).
35. A. Feuchtinger, A. Walch, M. Dobosz, Deep tissue imaging: a review from a preclinical cancer research perspective. Histochem Cell Biol 146, 781-806 (2016).
36. L. J. Bayne, G. L. Beatty, N. Jhala, C. E. Clark, A. D. Rhim, B. Z. Stanger, R. H. Vonderheide, Tumor-derived granulocyte-macrophage colony-stimulating factor regulates myeloid inflammation and T cell immunity in pancreatic cancer. Cancer Cell 21, 822-835 (2012).
37. V. T. Phan, X. Wu, J. H. Cheng, R. X. Sheng, A. S. Chung, G. Zhuang, C. Tran, Q. Song, M. Kowanetz, A. Sambrone, M. Tan, Y. G. Meng, E. L. Jackson, F. V. Peale, M. R. Junttila, N. Ferrara, Oncogenic RAS pathway activation promotes resistance to anti-VEGF therapy through G-CSF-induced neutrophil recruitment. Proc Natl Acad Sci U S A 110, 6079-6084 (2013).
38. J. Rodon, M. A. Carducci, J. M. Sepulveda-Sanchez, A. Azaro, E. Calvo, J. Seoane, I. Brana, E. Sicart, I. Gueorguieva, A. L. Cleverly, N. S. Pillay, D. Desaiah, S. T. Estrem, L. Paz-Ares, M. Holdhoff, J. Blakeley, M. M. Lahn, J. Baselga, First-in-human dose study of the novel transforming growth factor-beta receptor I kinase inhibitor LY2157299 monohydrate in patients with advanced cancer and glioma. Clin Cancer Res 21, 553-560 (2015).
39. I. M. Stromnes, J. S. Brockenbrough, K. Izeradjene, M. A. Carlson, C. Cuevas, R. M. Simmons, P. D. Greenberg, S. R. Hingorani, Targeted depletion of an MDSC subset unmasks pancreatic ductal adenocarcinoma to adaptive immunity. Gut 63, 1769-1781 (2014).

3.4.8. Endnotes

ACKNOWLEDGEMENTS

We thank all clinicians of the ENT Department for supporting the retrieval of patient material for this study. We thank Jon Henriksen for help with the multivariate analysis.

FUNDING

Yu Si was supported by the China Scholarship Council and a scholarship from the Medical Faculty of the University of Duisburg-Essen. Sven Brandau, Kirsten Bruderek and Yu Si were supported by European Cooperation in Science and Technology (COST) Action Mye-EUNITER, www.cost.eu and www.mye-euniter.eu. Joachim Klode and Matthias Gunzer were supported by a research grant form LaVision Biotec.

AUTHOR CONTRIBUTIONS

Conceptualization SB; supervision and acquisition of funding MG JK SB; development of methodology YS KB SiMe PJ AS; performance of research YS KB PA; data curation, analysis and visualization YS SiMe BW AS SB; statistical analysis YS SiMe PJ AS BW; provision of resources StMa SL; writing of the manuscript YS AS SB; editing of the manuscript SiMe PJ MG.

COMPETING INTERESTS

J.K and M.G. received research funding from LaVision Biotec, the maker of the light sheet microscope used in this study.

DATA AND MATERIALS AVAILABILITY

All data needed to evaluate the conclusions of the paper are present in the paper and/or the Supplementary Materials.

3.5. Interlude II

In manuscript 2, we learned how assessing distribution patterns of multiple cellular components of the immune system in 3-D in a tumor environment can generate insights into tumor biology and cell-cell interactions. In the future, other methods need to be applied to investigate the mechanisms crucial for TAN-dependent downregulation of cytotoxic T cell function. However, for obtaining an organ wide overview of the immune cells and their cellular microenvironment throughout the tumor, LSFM was decisive.

Study of a primary tumor may also contribute to patient staging, prognosis and access to different treatment options[141]. Another important feature of tumor biology is the ability to form mobile, independent clusters of tumors that can spread throughout the host, a process called metastasis. For therapy success and ultimately patient survival, it is vital to determine whether the tumor is still local, or if it already invaded nearby tissue or eventually other organs as well. To do that, whole-body scans using e.g. positron emission tomography (PET) are useful but lack the resolution to discover tumor clusters smaller than 1 mm[181]. Some cancers, like melanoma, are known to metastasize primarily into the regional draining lymph nodes before spreading systemically via the blood[141]. Therefore, the so-called sentinel lymph node is determined and excised during operation. However, subsequent routine 2-D slice based histopathological analysis is prone to errors due to the vast 3-D space in a human lymph node with diameters ranging from multiple millimeters to centimeters. Furthermore, not only the status of "metastases – yes or no", but also the total metastatic load plays a role in tumor specific survival[141]. In the clinical environment currently no methods exist to 3-D quantify the real tumor burden or analyze multifocal location patterns, a problem being highlighted by van Akkooi *et al*[182]. Additionally, Dewar *et al.* reported that the location of melanoma metastases within the SLN (subcapsular vs. elsewhere) correlated with additional node metastases[183]. Whether the tumor's location within the 3-D architecture of the SLN, like proximity to blood vessels, or its interaction with the local immune system hold any more information or have an impact on disease progression is currently unknown. Reporting microanatomic locations based on 2-D histopathology is difficult and should only occur for the entire SLN[184].

Therefore, in the following unpublished manuscript submitted November 2019, we investigated the application of the above developed LSFM protocols in clinical diagnostics

and patient staging. We report exact tumor volumes in human lymph nodes and report features of the surrounding lymph architecture, e.g. size and amount of B cell follicles and germinal centers per cubic millimeter of lymph tissue. Furthermore, LSFM analysis identified metastases, that would have been missed entirely by routine gold standard histopathological procedure alone.

3.5.1. Media and License info manuscript #3

This manuscript is currently unpublished. Therefore, no license is required. In order to reduce obstacles in the publishing process, please keep contained information confidential. Supplementary material concerning manuscript#3 is attached (6.1.1., p.169). An electronic version of main article, supplementary tables, figures, videos, and required legends are also provided with the attached CD at the end of this thesis and under a *Sciebo* repository. Provided a QR code and hyperlink may be subject to change beyond the reviewing phase of this thesis. Download of the files might be required.
[provider: *Sciebo*, Password: MerzThesis]

Supplenmentary information

3.5.2. Author contributions manuscript#3

Author contributions of Simon F. Merz for the submitted manuscript

Identification and quantification of hidden melanoma metastases in human sentinel lymph nodes using light sheet fluorescence microscopy

Conception:

1. Design of the overall workflow 50%
2. Design of the clearing protocol 80%
3. Data management plan 90%

Experimental work – protocol development

1. Patient acquisition/surgery 0%
2. Development of protocol & staining strategy 75%
3. Sample processing 75%
4. Data acquisition via LSFM 95%

Experimental work – study

1. Patient acquisition/surgery 0%
2. Sample processing 20%
3. Data acquisition via LSFM 95%

Data analysis

1. Conceptions of what to analyze how 90%
2. IMARIS (3-D) tracing and segmentation 75%
3. ImageJ 100%
4. Statistics 50%

Manuscript

1. Concept and initial draft 75%
2. Figure preparation 95%
3. Main Text 50%
4. Supplement preparation (Figure legends, Videos, …) 90%

Simon F. Merz	Prof. Matthias Gunzer

3.6. M#3: Identification and quantification of hidden melanoma metastases in human sentinel lymph nodes using light sheet fluorescence microscopy

Unpublished manuscript. Currently (11.2019) submitted to *Journal of Clinical Oncology*

3.6.1. Authors and Affiliations

Simon F. Merz[1-4,#], Philipp Jansen[2-4,#], Ricarda Ulankiewicz[2-4], Lea Bornemann[1], Tobias Schimming[2-4], Klaus Griewank[2-4], Zülal Cibir[1], Andreas Kraus[1], Ingo Stoffels[2-4], Timo Aspelmeier[5], Sven Brandau[6], Dirk Schadendorf[2-4], Eva Hadaschik[2-4], Gernot Ebel[7], Matthias Gunzer[1,8,§] and Joachim Klode[2-4,§]

#: These authors contributed equally.
§: These authors jointly supervised the work.

[1]Institute for Experimental Immunology and Imaging, University Hospital, University Duisburg–Essen, Essen, Germany
[2-D]epartment of Dermatology, Venerology and Allergology, University Hospital Essen, University of Duisburg-Essen, Essen, Germany
[3]West German Cancer Center, University Duisburg-Essen, 45122 Essen, Germany
[4]German Consortium for Translational Cancer Research, Partner Site University Hospital Essen, Essen, Germany
[5]Institut für Theoretische Physik, Georg-August-Universität Göttingen, Germany
[6]Department of Otorhinolaryngology, University Hospital, University Duisburg-Essen, Essen Germany
[7]LaVision BioTec GmbH, Bielefeld, Germany
[8] Leibniz-Institut für Analytische Wissenschaften - ISAS -e.V., Dortmund, Germany

3.6.2. Abstract

Many cancer guidelines include sentinel lymph node (SLN) staging to identify microscopic metastatic disease. Current SLN analysis of melanoma patients is effective but has the substantial drawback that only a small portion of the node is sampled, while the majority of the tissue is discarded. This might explain the high false-negative rate of current SLN diagnosis in melanoma. We developed an algorithm-enhanced light sheet fluorescence microscopy (LSFM) approach to three-dimensionally reconstruct the entire SLN with single-cell resolution. We comprehensively quantify total tumor volume while simultaneously visualizing cellular and anatomical hallmarks of the associated SLN architecture. In a first-in-human prospective study (21 SLN from 11 melanoma patients), LSFM not only identified all metastases seen histologically but additionally detected metastases not recognized by routine histology. This led to additional therapeutic options for one patient. Our 3-D digital pathology approach can increase sensitivity and accuracy of SLN-metastases detection and potentially alleviate the need for conventional histopathological assessment in the future.

3.6.3. Introduction

According to the World Health Organization, the incidence of melanoma is increasing faster than any other major cancer worldwide. In the United States, melanoma is the fifth most common cancer, posing a substantial health and economic burden[1]. Melanoma metastasizes early into regional lymph nodes[2]. Patient prognosis and survival can be reliably assessed via the sentinel lymph node (SLN) histological status[3,4], which is why SLN excision (SLNE) is a diagnostic procedure recommended by the American Joint Committee on Cancer (AJCC). Current AJCC guidelines emphasize that SLN containing a single malignant melanocyte are defined as a positive, metastatic SLN[5].

Conventional histology of 2-D tissue sections is the currently used gold standard for SLN staging. This approach assesses only a few representative slices of the node, discarding the majority of the tissue[6]. This might be one reason why the reported clinical false-negative rates of SLN diagnosis are high (9 to 44%)[7]. Reliably detecting very few to single metastasizing melanoma cells within the large 3-D volume of an entire lymph node remains a challenge not adequately addressed to date. Aside from the total number of tumor

cells, their position relative to landmark structures within the SLN has also been found to be of prognostic value. Tumor cells positioned in proximity to or breaking through the node capsule are indicative of higher invasive potential and worse prognosis[8-11]. The relevance of other LN structures e.g. B cell follicles, T cell zones or efferent lymphatic vessels for progression of melanoma metastasis remains to be explored in detail.

Despite this knowledge, currently no histological approach exists that would allow analyzing the entire SLN volume in a routine setting. While complete sectioning/analysis of the entire SLN is theoretically possible, the time and cost involved prohibit routine application. Not reliably detecting single or isolated tumor cells in the SLN is a considerable short-coming of current histology protocols, as recent data demonstrate these deposits affect long-term prognosis of melanoma patients[12-14]. Determining the exact size of metastatic deposits is critical as melanoma-specific survival is reduced with increasing SLN tumor burden[5] and microscopic SLN tumor load is a stratification factor for adjuvant treatment[15,16]. These findings highlight the unmet need for a method capable of determining exact tumor volume and location within a SLN.

We and others recently developed clearing techniques to generate optically transparent samples from many different soft and hard tissues of experimental animals[17,18] with subsequent rapid 3-D reconstruction at cellular resolution using light-sheet fluorescence microscopy (LSFM)[19,20]. Recent advances enable the imaging of strongly autofluorescent tissue[21], a highly relevant improvement for skin draining SLN containing pigmented cells. So far, this was an unsolved problem in assessing diagnostically relevant pigmented human samples[22].

Here, we present a method making the entire volume of human SLN amenable to 3-D histological inspection at cellular resolution using optical clearing and immunofluorescence-based LSFM. Our workflow enables whole-mount staining and subsequent identification of anatomical hallmarks of human skin draining LN (capsule, vascularization, immune cells) with embedded pigmented melanoma cells. We demonstrate that algorithm-enhanced LSFM provides a browsable histo-like optical slice library for fast and reliable SLN status determination and tumor environment assessment. Antigen integrity was maintained and our approach was compatible with successive routine FFPE (formalin-fixed, paraffin-embedded) histological assessment. Hence, LSFM results could be correlated with the current gold standard of SLN analysis. As LSFM detected metastases not

found by classical histology, our approach represents a first step towards 3-D digital pathology of clinical samples.

3.6.4. Results

3.6.4.1. Whole mount staining, tissue clearing and LSFM analysis of human SLN and cutaneous melanoma metastases

To make lymph nodes (LN) amenable for 3-D LSFM analysis, the tissue must be optically transparent. We achieved this by modifying a previously described ethyl cinnamate (ECi)-based tissue-clearing protocol[17,21]. A peroxide bleaching step was used to attenuate endogenous autofluorescence and destroy pigments (especially hemoglobin and melanin) that otherwise introduce imaging artefacts. Tissue autofluorescence then enabled visualizing anatomical LN structures. However, we found the display and interpretation of raw LSFM data difficult, especially with the very heterogeneous autofluorescence signals of fat (dark), LN stroma (medium bright) and extremely bright erythrocytes in vessels or tissue (from hemorrhage). The high variance of signal brightness in unprocessed data did not allow all entities to be displayed simultaneously in a single image. Therefore, we developed RAYhance, a multiscale contrast compression algorithm, to display LSFM data as a browsable histo-like stack, similar to 2-D FFPE sections (M3: Supplementary Fig. 1). Following RAYhance processing we could distinguish fatty tissue and the LN capsule from residual LN structures in optical slices simultaneously. Blood vessels were identified by means of erythrocyte enrichment. (M3: Fig. 1a, M3: Supplementary Fig. 1). Autofluorescence was also sufficient to reconstruct an entire LN in 3-D, revealing a complex surface architecture (M3: Fig. 1b, M3: Supplementary Video 1).

To confirm the cellular composition of prominent structural features we established immunofluorescent stainings. Therefore, we adapted previously described whole-mount labeling procedures of murine brain[28] and human embryonic tissues[29]. CD3-expression revealed the T cell zone and germinal centers within the presumed autofluorescence-dim B cell follicles (M3: Fig. 1c). However, simultaneous visualization of the T cell zone with thousands of cells compared to single cells in the germinal centers or surrounding B cell follicles was only possible using RAYhance-processed optical slices

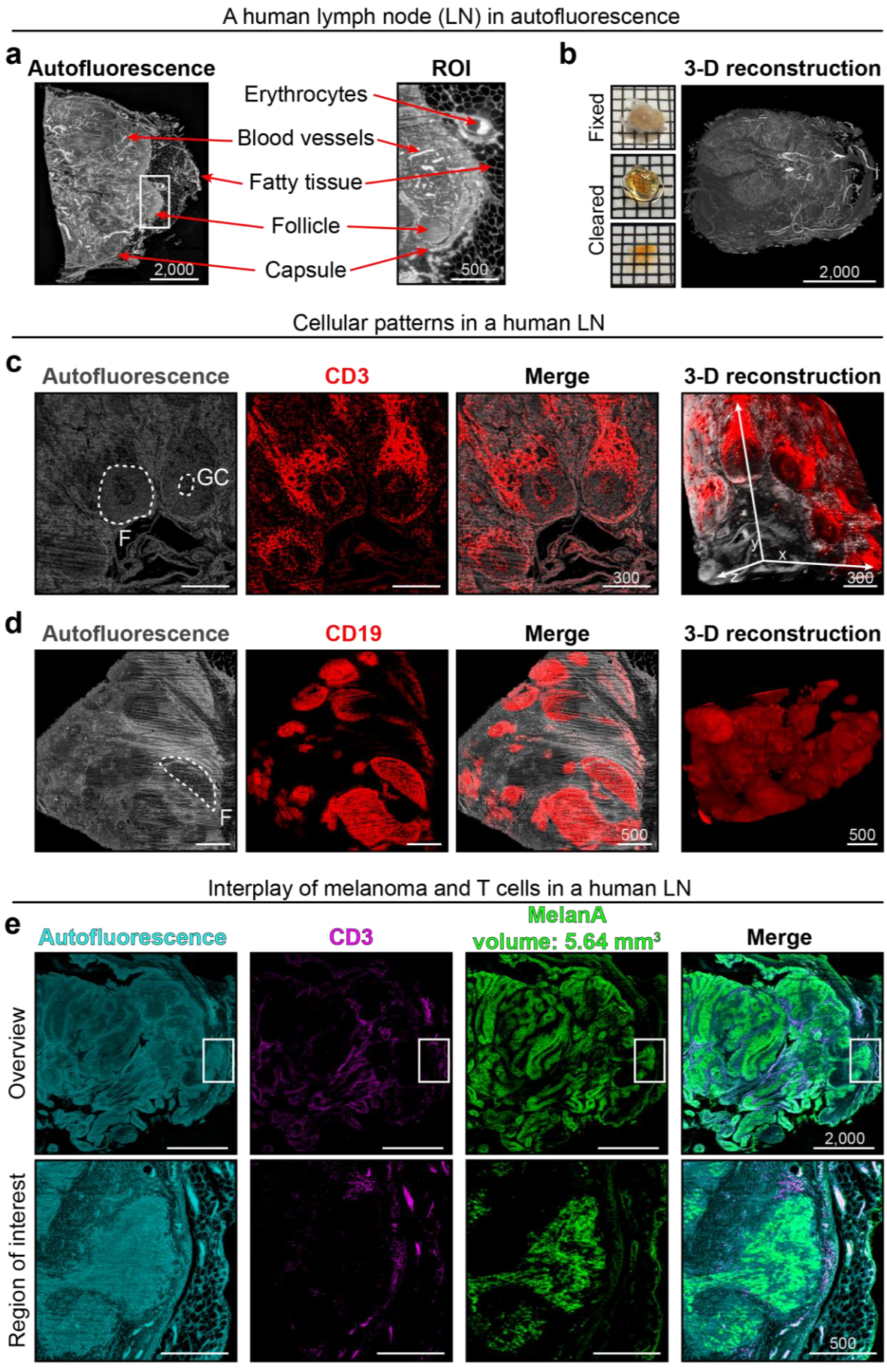

M3: Figure 1 Anatomical and cellular patterns in a human lymph node (LN).

(**a**) Anatomical features of a human LN including position of the capsule, blood vessels or fatty tissue can be derived from the tissue's autofluorescence signal alone. These features are highlighted (red arrows) in the algorithm-enhanced optical LSFM overview slice (left) and the region of interest (ROI, white rectangle; also see M3: Supplementary Figure 1). (**b**) Macroscopic images and a 3-D reconstruction of the same human LN based on autofluorescence (M3: Supplementary Video 1). In order to reveal cellular patterns within a human LN, we applied whole-mount staining prior to clearing. Again, using autofluorescence (gray) alone, follicles (F) and even germinal centers (GC) could be identified. This was confirmed by visualizing anti-CD3 staining (T cells, **c**) and anti-CD19 staining (B cells, **d**). On the right side of each row of LSFM optical slices is a 3-D reconstruction of the data set. (**e**) A melanoma metastasis in a human lymph node revealed by anti-Melan-A staining (green). Anatomical and cellular patterns can be assessed using autofluorescence (cyan) and T cells (magenta), respectively. Region of interest (bottom row) shows Melan-A positive cells surrounded by T cells in close proximity to the capsule (M3: Supplementary Video 2). Scale bar values in µm, squares in macroscopic images 2x2 mm. All optical slices are RAYhance-processed.

(M3: Supplementary Fig. 2). CD19 expression confirmed B cell enrichment in the autofluorescence dim and T cell poor regions (M3: Fig. 1d). In summary, autofluorescence combined with fluorescent immune cell staining was sufficient to portray the overall anatomical structure and major cellular distribution patterns of human LNs (M3: Fig. 1).

Next, we used anti-Melan-A staining, a routinely employed melanocytic marker, to visualize possible metastases within the LN architecture. This approach enabled 3-D quantification of the total volume of Melan-A positive structures and simultaneously demonstrated the interplay of immune cells with Melan-A-expressing elements (M3: Fig. 1e). Here, RAYhance processing permitted the display of single CD3 and Melan-A positive cells (M3: Supplementary Video 2, 3).

3.6.4.2. LSFM analysis is compatible with subsequent routine histology

To exclude that the bleaching, whole-mount and clearing procedure has an impact on the histopathological appearance of human tissue and melanoma markers, we took biop-

sies of the same sample after simple fixation (routine protocol), bleaching and LSFM imaging, respectively. Routine formalin-fixed paraffin-embedded (FFPE) stainings and immunohistochemistry (IHC) were performed on all samples. Importantly, we detected no discernible impact of previous LSFM analyses on the cellular morphology (hematoxylin/eosin staining) or on the staining quality and distribution of the histopathologically relevant melanoma markers Melan-A and S100 in clinical grade FFPE sections (M3: Supplementary Fig. 3). Thus, our approach allows an intra-sample comparison of findings in both, LSFM and subsequent gold standard FFPE histopathological analysis.

3.6.4.3. Integrating LSFM in the routine histopathological analysis of human melanoma SLN

The fact that LSFM analysis did not interfere with classical FFPE analysis allowed us to benchmark the performance of our approach against the routine clinical procedure to analyze SLN of melanoma patients. The goal was to evaluate the applicability of LSFM in diagnostically relevant human tissue. We aimed to test the sensitivity and specificity of LSFM to detect melanoma metastases in SLN. According to the current gold standard, SLN are post-surgically processed for FFPE histopathological analysis of individual representative tissue slices. Hence, resected SLNs were first analyzed by LSFM and then routinely processed for ensuing histopathology (M3: Fig. 2). Of note, during routine slicing of paraffin blocks, gap sections (300 µm – 600 µm) between the relevant FFPE tissue slices are typically discarded and no longer available for later analysis. In contrast, all LSFM samples, once paraffinized, were sequentially cut and non-relevant slices were stored allowing correlation of all possible unique LSFM findings with follow-up histology afterwards (M3: Fig. 2).

With the staining procedure and panel established, we implemented a prospective study assessing the metastatic status of SLN. In total, 21 SLNs of 11 melanoma patients (M3: Supplementary Table 1) were analyzed without prior selection of their location or size (M3: Supplementary Table 2). We cut several SLNs into smaller pieces to i) reduce the processing time before subsequent obligatory histopathological analysis and minimize the delay of patient diagnosis, ii) ensure robust and complete whole mount staining within an acceptable time frame, iii) reduce imaging artifacts from remaining pigmentation. We determined that LSFM sensitivity compared to the gold standard was

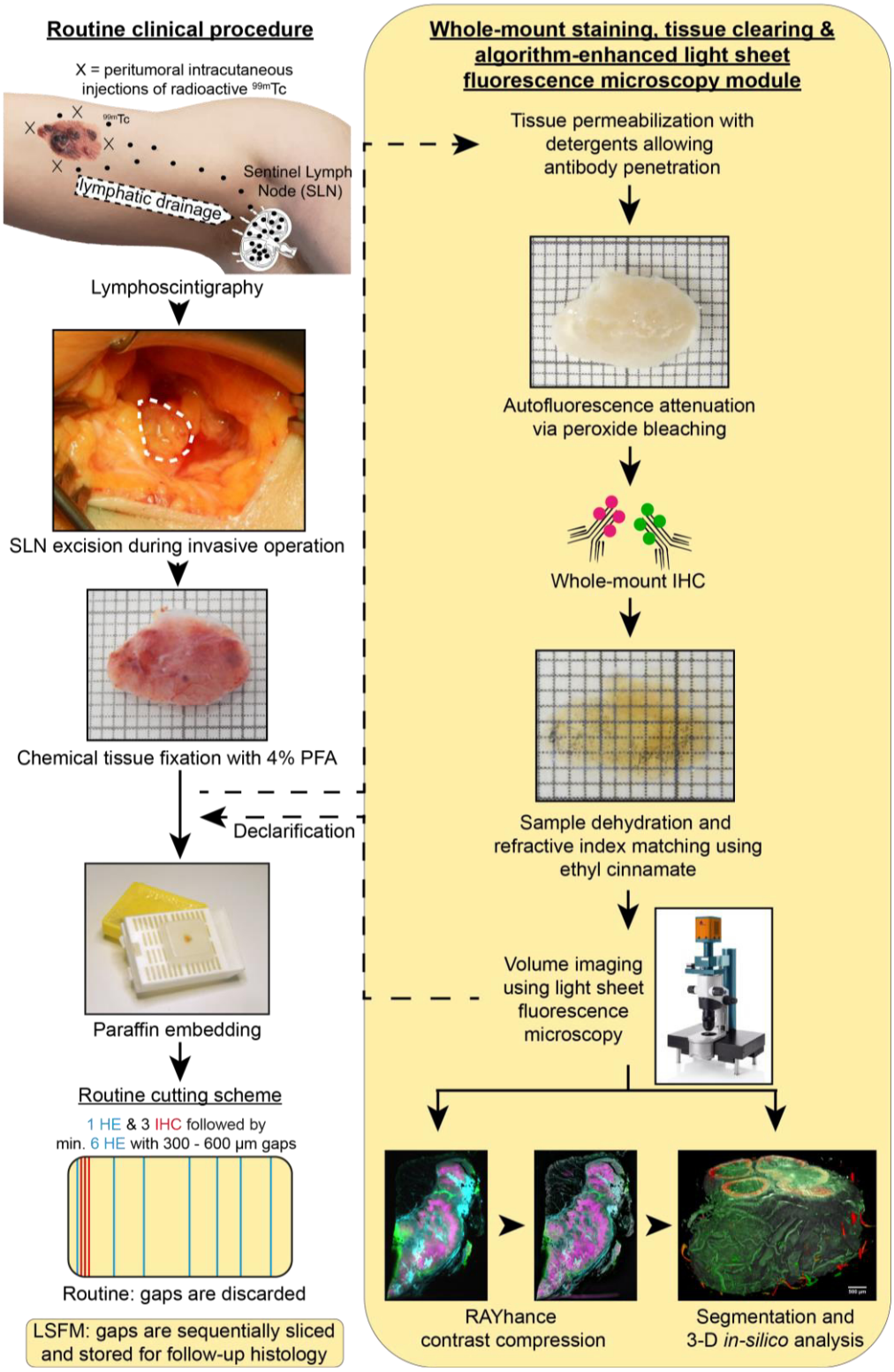

M3: Figure 2 Light sheet fluorescence microscopy (LSFM) in melanoma diagnostics.

Incorporation of LSFM analysis (right yellow column) into the routine clinical diagnostics process to analyze human sentinel lymph nodes of melanoma patients (left column). Lymphoscintigraphy with radioactive technetium (^{99m}Tc) allows the determina-

tion of the local draining lymph node (sentinel lymph node, SLN) of the primary melanoma area. The SLN is excised and post-surgically fixed using formaldehyde (4% PFA). In the fixed state, the SLN is routinely paraffin embedded and sliced for hematoxylin/eosin (HE) staining and immunohistochemistry (IHC). Here, only few representative slices are analyzed for melanoma metastases per sample. To analyze the whole SLN tissue, LSFM analysis was executed after sample fixation with 4% PFA and before performing gold standard histopathological analysis. The SLN was prepared for LSFM analysis using tissue permeabilization, autofluorescence attenuation, whole-mount IHC and tissue clearing by ethyl cinnamate (ECi). Obtained volumetric LSFM data can be algorithm-enhanced and 3-D-segmented for exact volume quantification. After imaging, samples were declarified and transferred back to routine processing. Note that lymph node tissue between the relevant paraffin slices for histopathological analysis (gap sections) are routinely discarded and cannot be considered for SLN status determination. However, in order to validate LSFM findings throughout the entire sample, gap sections were sequentially sliced and stored to allow for follow-up formalin-fixed paraffin-embedded (FFPE) analysis. Squares in the macroscopic LN images are 1x1 mm.

100% and the false negative rate was zero (M3: Supplementary Table 2). Importantly, LSFM was able to identify a metastasis that was not found in the initial routine histopathological assessment (see below).

3.6.4.4. Diagnosis of a capsular nevus in LSFM and histology

In a 1.7 x 1 cm large axillar LN (patient #4), blood residues and pigmentation were successfully bleached before LSFM analysis (M3: Fig. 3a). Three pieces of the node were found positive for intra-capsular Melan-A positive cells and hence suspected to contain a metastasis (M3: Fig. 3b,c). LSFM overview scanning revealed Melan-A positive signals within the LN, while T cell structures remained unperturbed (M3: Fig. 3b, M3: Supplementary Video 4). However, some Melan-A staining artifacts were also encountered. Most prominent was an unspecific accumulation, not correlating with follow-up FFPE IHC, of anti-Melan-A signal at sites of physical manipulation (cutting-edge artifact, CEA, M3: Supplementary Fig. 4). In contrast, a discernible Melan-A background staining was observed by both LSFM and FFPE in fatty tissue (fat artifact, FA in M3: Fig. 3b). Higher magnification LSFM of regions of interest (ROI) showed that i) the localization of the Melan-A positive

cells was intracapsular, ii) the spread of Melan-A positive cells was filamentous and heterogeneous and iii) the associated follicular structure of the LN remained intact (M3: Fig. 3c,d). 3-D segmentation of the total tissue block (96.8 mm^3), the LN capsule used for assessment of the LN tissue volume (70.7 mm^3), the CD3 (35.9 mm^3) and the intracapsular anti-Melan-A (0.24 mm^3) signal did not only allow for volume quantification, but also enabled visualization of the Melan-A positive cells as a sparsely growing intracapsular network, sheathing the round follicular structures (M3: Fig. 3c,d, M3: Supplementary Video 5). Using autofluorescence, we determined the sinus volume of the LN tissue to be 14.5 mm^3. Furthermore, CD3 staining allowed the quantification of cellular and anatomical hallmarks like follicles and germinal centers. In the tissue piece shown in M3: Fig. 3c, we counted 161 follicles with 154 germinal centers, occupying a median volume ± interquartile range (IQR) of $1.7x10^7$ ± $2.1x10^7$ μm^3 and $2.8x10^6$ ± $4.9x10^6$ μm^3, respectively. 124 (77%) of the follicles were secondary follicles, of which 19 (15.3%) contained more than one and up to three germinal centers. Only 37 (23%) were primary follicles. Follicles also differed significantly ($p<0.0001$, Mann-Whitney U-test) in volume with $5.2x10^6$ ± $6.0x10^6$ μm^3 for primary and $2.2x10^7$ ± $2.2x10^7$ μm^3 for secondary follicles (M3: Supplementary Video 6). In total, 7% of the cortex/paracortex tissue (excluding the medulla) consisted of follicles and 17.5% of this space was taken up by germinal centers, demonstrating the power of LSFM to precisely quantify LN functional zones.

Subsequent routine histopathological assessment (M3: Figure 3e) confirmed the Melan-A-expressing cells to be i) intracapsular, ii) of elongated shape with inconspicuous nuclei, iii) next to Melan-A being also positive for the melanocytic marker S100. Based on these findings a benign capsular nevus was diagnosed. This sequence of events showed that LSFM revealed all necessary information required to allow a diagnosis, but also highlights the importance of compatibility and close interplay between 3-D LSFM and routine histology.

3.6.4.5. Identification of melanoma metastases

In another axillar SLN (patient #9), five of twelve pieces were found to be positive for Melan-A (M3: Fig. 4). The signal was primarily enriched directly below the capsule but also extended into the parenchyma. At the borders of the compact, interconnected cell

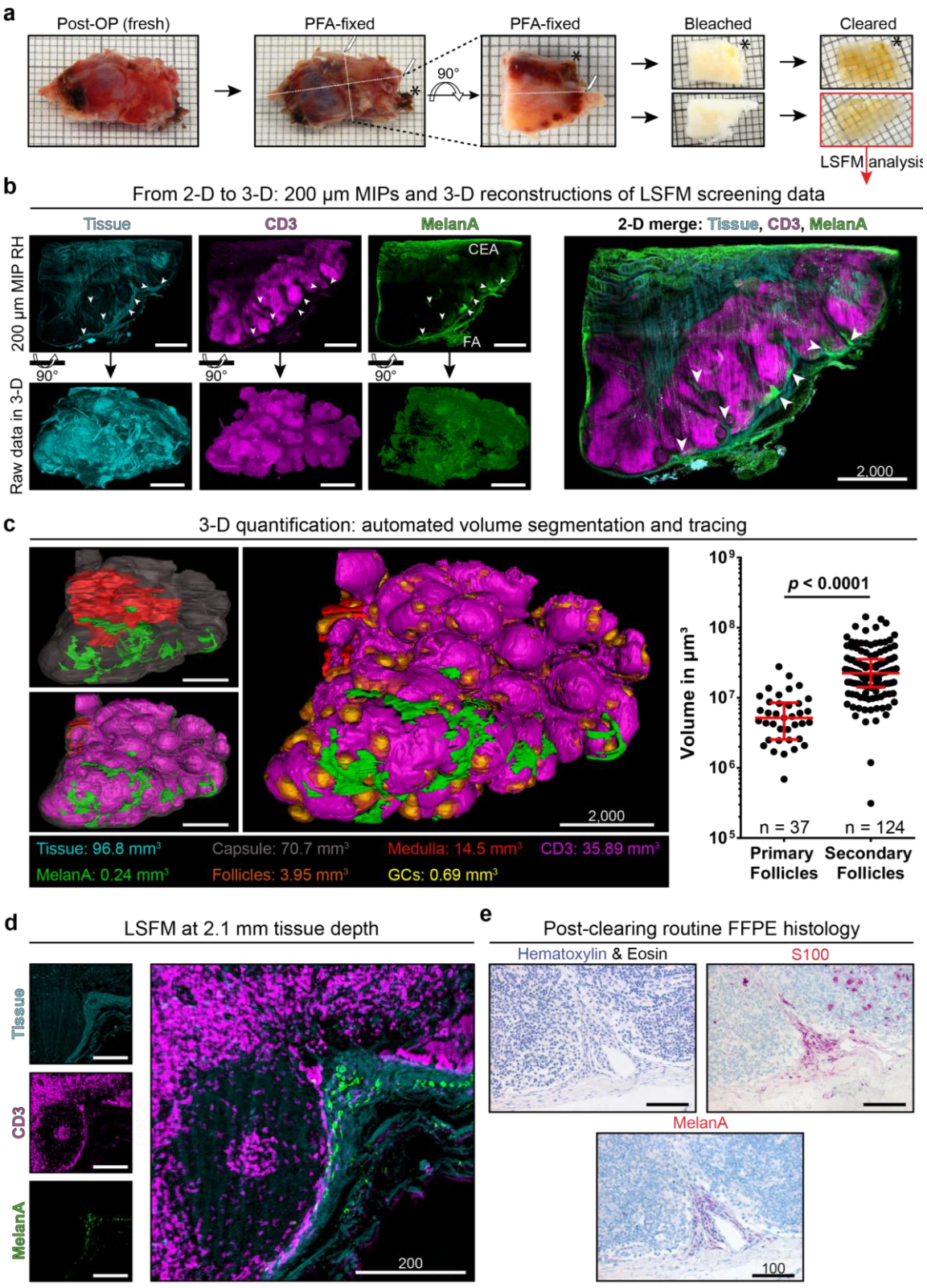

M3: Figure 3 From 2-D to 3-D and back – a capsular nevus in all protocol stages.

(**a**) Macroscopic images of an inguinal human sentinel lymph node (patient #4, S8) at various steps of the protocol. Due to size limitations the sample was cut multiple times

before commencing with the protocol. Dashed lines with a scalpel symbol indicate incisions performed in conformity with the gold standard processing protocol. The black asterisk highlights a pigment-rich region, allowing tracking after bleaching and clearing (in ECi). The lower sample in the clearing panel is shown throughout the analysis process, which is indicated by the red box and arrow downwards. One square equals 1x1 mm. (**b**) Upper panel shows 200 µm maximum intensity projections (MIP) of algorithm-enhanced (RH = RAYhance) fluorescence signal of general tissue autofluorescence (cyan), anti-CD3 (T cells, magenta) and anti-Melan-A (green). Clusters of intracapsular Melan-A signal are highlighted by white arrows. Note that anti-Melan-A staining exhibits artifacts, e.g. cutting-edge artifact (CEA) and fat artifact (FA), which makes rendering the raw signal difficult (M3: Supplementary Figure 4). The lower panel shows the corresponding 3-D reconstructions for every channel (M3: Supplementary Video 4). On the right, a 2-D MIP color merge is depicted. (**c**) 3-D segmentation and quantification of LN tissue within the capsule (gray), T cells (magenta), medulla (red), follicles (orange), germinal centers (GCs, yellow) and Melan-A signal (green) within the capsule (M3: Supplementary Video 5, 6). The right scatter plot displays the size distribution of quantified primary follicles (n = 37), without GCs, and secondary follicles (n = 124), containing one or more GCs, in the shown sample (biological n = 1). The median volume ± interquartile range displayed in red is $5.2x10^6 \pm 6.0x10^6$ µm³ for primary and $2.2x10^7 \pm 2.2x10^7$ µm³ for secondary follicles. p-value ($p < 0.0001$) was calculated using a two-tailed Mann-Whitney U-test. (**d**) One optical slice imaged at 2.1 mm tissue depth with 12.6x magnification. The intracapsular position of the elongated Melan-A positive cells is clearly visible. (**e**) Diagnostically relevant FFPE sections after declarification, paraffination, physical sectioning and routine staining. Anti-S100 and anti-Melan-A antibody signals are visualized in red with a blue nuclear counterstain (Hematoxylin). All scale bar values are given in µm, all optical slices are RAYhance-processed.

mass, multiple single cells and multi-cellular clusters could be identified, like a spray within the LN tissue (M3: Fig. 4b, M3: Supplementary Video 7). It was now possible to 3-D quantify the total Melan-A positive infiltrate. Melan-A positive cells together (in all tissue pieces) occupied a total volume of 5.35 mm³. With respect to the whole lymph node volume of 503 mm³ (excluding all extracapsular fat and tissue), we determined that 1.06% of the entire SLN was enriched with Melan-A positive cells (M3: Fig. 4), information

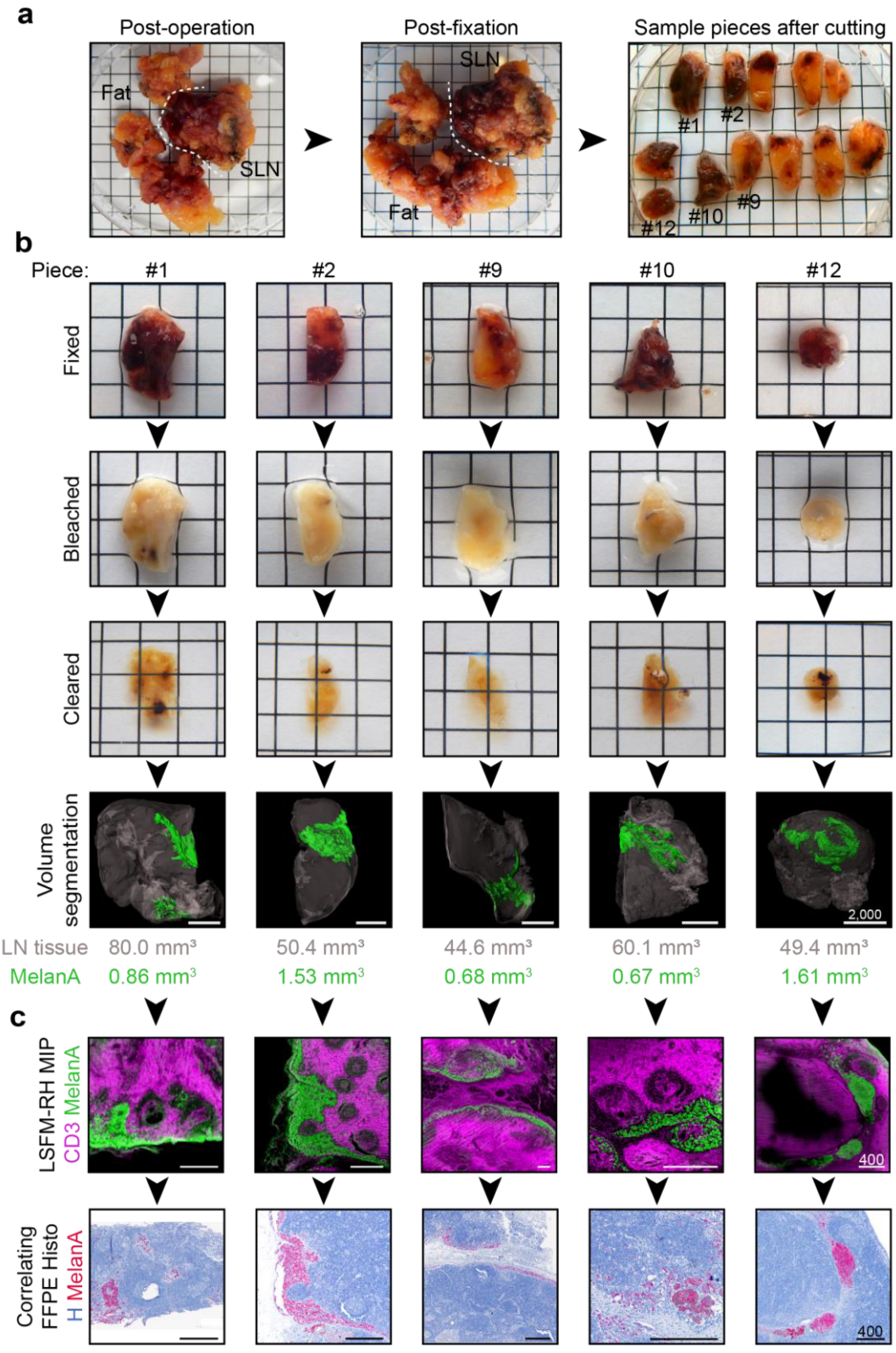

M3: Figure 4 Melanoma metastasis assessment in human SLNs using LSFM.

(**a**) Macroscopic image of an axillar human SLN (patient #9, S18) after operation and fixation. The surrounding fat is cut and processed separately for routine histology. The SLN is cut into twelve smaller pieces, five of which are found to be metastasized. (**b**) From top: Panels of macroscopic images showing the five metastasized SLN pieces, each

one in a column, after fixation, bleaching and clearing (in ECi). Some residual pigmentation can be seen macroscopically. Impact on LSFM imaging see M3: Supplementary Figure 5 and M3: Supplementary Video 8. The LN tissue within the capsule (gray, without surrounding fat) as well as the subcapsular Melan-A signal (green) were volume segmented and quantified (M3: Supplementary Video 7). The total LN tissue volume of all twelve pieces combined amounted to 503 mm^3, the total Melan-A volume to 5.35 mm^3 (1.06%) (**c**) Top: LSFM MIPs of three subsequent RAYhanced (RH) optical slices, showing anti-Melan-A signal (green) and anti-CD3 signal (magenta). Bottom: Correlating FFPE slices of follow-up anti-Melan-A histology (Melan-A = red, Hematoxylin = blue). Squares in macroscopic images are 5x5 mm, scale bar values in µm.

not obtainable from clinical histopathology. Importantly, the distribution patterns of Melan-A positive cells observed in LSFM correlated precisely with subsequent histopathological stainings (M3: Fig. 4c).

Despite performing a peroxide bleaching step, residual pigmentation was present in some tissue pieces. This impacted LSFM imaging with shadow artifacts like stripes or blurriness (M3: Supplementary Note 1). However, despite heavy pigmentation of e.g. piece twelve (M3: Fig. 4b), we were able to completely 3-D quantify the anti-Melan-A signal, highlighting the importance of using infrared laser light (785 nm excitation) for tumor detection. In this LN piece, the association of Melan-A positive cells with a major blood vessel was particularly striking (M3: Supplementary Fig. 5, M3: Supplementary Video 8). Correlative follow-up histology revealed that pigmentation was sometimes, but not always, co-localized with Melan-A positivity (M3: Supplementary Fig. 5).

3.6.4.6. Discovery of hidden metastases

In another inguinal SLN (patient #11) with a total intracapsular volume of 749.3 mm^3, we determined Melan-A positive cells with a total volume of 0.03 mm^3 (0.004%) in 1 of 11 pieces. This volume consisted of two intranodal volumes of 0.013 mm^3 and 0.006 mm^3 and an extracapsular but intravascular volume of 0.011 mm^3. Therefore, each site alone was much larger than the 0.1 mm diameter (0.001 mm^3) measurement considered diagnostically relevant[10,14]. Hence, this would constitute an important stratification factor for further adjuvant treatment.

However, the subsequent routine FFPE histology analysis did not identify a SLN metastasis. Neither Melan-A nor S100 positivity were observed within the SLN of the sections analyzed. The SLN was therefore declared “negative” according to the gold standard histopathological analysis. To further investigate the Melan-A positive signals only observed in LSFM we performed an additional follow-up FFPE histology on preserved gap sections (M3: Fig. 2) of the SLN tissue. Here, we identified Melan-A positive cell clusters confirming the previous LSFM observations (M3: Fig. 5, M3: Supplementary Video 9). As first discovered in the LSFM analysis, small morphologically atypical cells penetrated the lymph node within an afferent lymph vessel. Those cells were distributed within the subcapsular sinus and showed initial infiltration of the parenchyma. Based on the morphology, the cellular distribution and the histopathological staining, this cell accumulation was recognized as a melanoma metastasis. The status of the SLN was subsequently re-evaluated and changed to “positive”. Hence, “LSFM-guided histopathological analysis” enabled identification of a melanoma metastasis in an SLN that would have been classified as “negative” if assessed by conventional histopathology protocols alone. Based on these results, the patient was reassigned to the interdisciplinary melanoma tumor board and was subsequently offered access to adjuvant checkpoint blocker therapy.

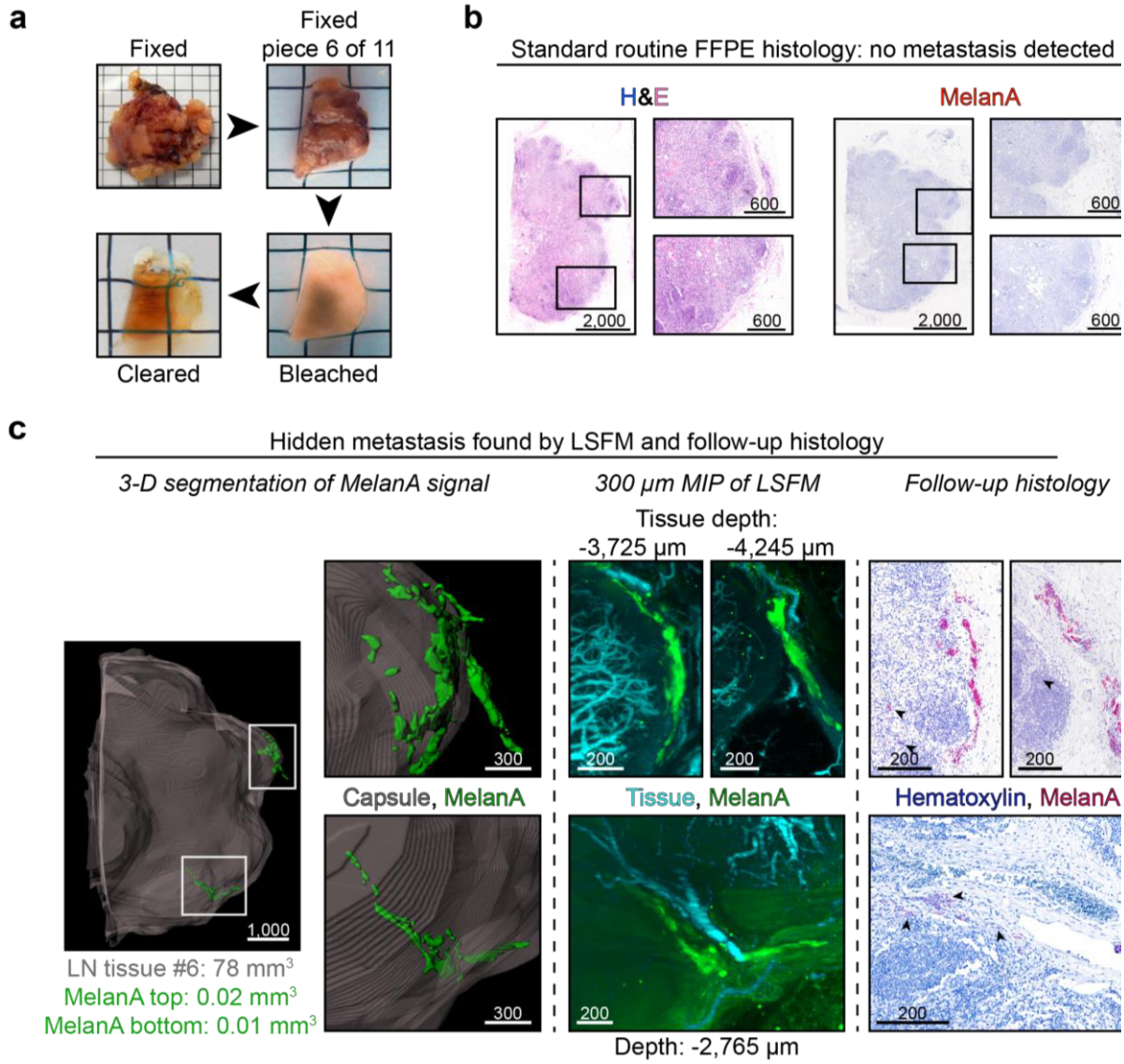

M3: Figure 5 LSFM reveals metastasis missed by the gold standard procedure.

(**a**) Macroscopic images of an inguinal human SLN (patient #11, S21) after operation and piece number six after fixation, bleaching and clearing (in ECi). (**b**) Routine FFPE histology found no Melan-A positive cells within the lymphnode in piece six, nor any other piece of the LN (not shown). Enlargements (black rectangles in overview) correspond to regions of interest from (c). (**c**) Melan-A signal could be detected at two sites (white rectangles) of tissue piece six. Left: Volume segmentation of Melan-A signal (green) and the capsule allowed 3-D quantification. Enlargements of upper and lower Melan-A events can be correlated with both LSFM MIPs (middle) and LSFM-guided follow-up histology (right). Middle: 300 µm maximum intensity projections (MIPs) of tissue autofluorescence (cyan) and Melan-A signal (green). The Melan-A event in the top panel consists of two parts, in total stretching over more than 300 µm in Z. The left part

is located in the sub-capsular sinus (M3: Supplementary Video 9). The right part is outside of the capsule, located within an afferent lymph vessel (see histology). The Melan-A event in the lower panel is closely associated with a blood vessel. Right: Additional LSFM-guided follow-up FFPE IHC stainings against Melan-A (red) confirmed LSFM findings. Black arrows highlight Melan-A positive cells that are easy to miss. In the upper left image, singular parenchymal cells can be identified. Squares in macroscopic images are 5x5 mm, scale bar values in µm.

3.6.5. Discussion

While proven effective, reliable and widely used for decades, histological analysis of the SLN has limitations. As established histopathological protocols merely analyze representative slices[6,8,9,30-32], only a very small portion of the SLN is sampled for histology relative to its volume. Without prior knowledge of tumor cell localization, the SLN is sectioned according to a predetermined cutting scheme (M3: Fig. 2). This regular black-box approach is prone to error allowing small metastases to be missed entirely. When discussing detection of total melanoma volume in SLN, several considerations are important. First, the smallest tumor considered diagnostically relevant in FFPE diagnostics has a diameter of 0.1 mm[10,14]. Assuming an average melanoma cell size of ~20 µm diameter and a spherical volume, such a tumor would contain ~125 cells in 3-D. Second, a small SLN (1 cm diameter) has a volume of $\sim 5.2*10^{11}$ µm^3 while the tumor cell volume would be $\sim 4.2*10^3$ µm^3. Thus, even a small SLN offers $\sim 10^8$ different positions for a single melanocyte or $\sim 10^6$ sites for minimally relevant tumor deposits to be located. Given that melanocytic metastases differ in cellular form (e.g. ellipsoid), complete sequential sectioning of the SLN in 5 µm steps would be mandatory to guarantee not missing a metastasis by conventional histology. As multiple stainings of a single melanoma metastasis are required (e.g. H&E, anti-Melan-A, anti-S100), a melanoma cell may be missed if not present in at least two sequential sections. Hence, ~2,000 serial sections would be necessary to definitively declare a SLN positive or negative. As SLN are often larger, the number of required sections would frequently be substantially higher. Thus, a complete histological analysis of a SLN is not feasible in a routine setting.

Our LSFM approach allows a complete 3-D tumor assessment down to single cells, additionally showing melanocyte interactions with the anatomical and cellular environmental cues of a SLN within reasonable investments of time and expenses. The precise 3-D localization of melanoma metastases with respect to anatomical hallmarks (e.g. blood/lymph vessels, immune cells, LN stroma) could yield important new insights into metastasis formation and biology, impacting prognostic assessment and treatment in the future.

In comparison to routine FFPE histology, which can theoretically be available for histopathological assessment within 2-3 days, our LSFM approach currently still requires 12 additional days until data acquisition is complete (M3: Supplementary Table 3). Therefore, important future challenges address reducing the protocol time. This could be achieved by shortening tissue penetration time of staining molecules by e.g. i) electrostatic fields[33], ii) microwave enhanced diffusion[34,35] or iii) smaller staining molecules, e.g. nanobodies[36] that allow considerably faster diffusion[37]. Furthermore, the development of both, artifact-free antibodies and strong, photobleaching-resistant infrared fluorophores compatible with whole-mount staining, clearing, LSFM and follow-up histology are of high importance. That antibodies can be applied without causing artifacts is demonstrated by the anti-CD3 or anti-CD19 stainings (M3: Fig. 3). The benefits of infrared dyes in whole organ LSFM were demonstrated in a tumor measured despite the illumination and emission shadow of residual pigmentation (M3: Supplementary Fig. 5, M3: Supplementary Video 8), a significant improvement of previous reports investigating human LN[22].

Another problem connected to LSFM (and any in-depth imaging approach) is the size of the resulting data sets that need to be processed and stored[38]. Here, new ways for powerful image compression not impeding data quality need to be developed. Importantly, significant information contained in raw LSFM images can also be obscured when using conventional and strictly linear digital display options for visual inspection that inevitably lead to display saturation in maximal brightness and/or darkness. Therefore, we introduce RAYhance as a multiscale contrast compression algorithm that obeys the characteristics of the human visual system and processes the primary image in several multiscale contrast images. This allows the simultaneous representation of all clinically relevant image entities even if they stem from formerly disparate intensity regions. However, RAYhance, in its current version, being optimally suited to adjust the autofluorescence

channel can only be a starting point. Other signals such as the tumor may need more delicate adjustments to fully represent the biological distribution without creating false positives. New approaches such as artificial intelligence and deep learning may recognize disease-defining features in LSFM data, not discernible to the human eye, yet bearing substantial diagnostic power[39].

Currently, our three channel setup already allows identification of at least seven distinct entities of SLN architecture such as medulla, follicles and germinal centres (M3: Fig. 3). To further improve landmark identification, future developments should overcome current limitations of three colour LSFM. Using more infrared laser lines and more fluorescent dyes between 600-850 nm emission will allow multiplexed analyses. In conjunction with the advent of process automatization, our approach could potentially represent the starting point of a fast, routine stand-alone method of multicolour 3-D tumour analysis in human tissues. It is tempting to speculate that, in the future, pathologists might browse through 3-D data sets of whole tissues in search of conspicuous structures[38] rather than spend hours behind microscope oculars examining thin sections.

The diagnostic potential of the presented approach is strengthened by the fact that in our prospective first-in-human study LSFM not only identified all metastases seen histologically but additionally detected a metastasis not recognized by routine histology. Based on this finding our interdisciplinary tumour board changed their recommendations and this patient was offered an adjuvant systemic therapy with an immune checkpoint inhibitor. Therefore, our procedure already provides a further stratification factor for adjuvant treatment potentially prolonging melanoma specific survival.

However, the application of LSFM-guided histology in diagnostics is not restricted to melanoma patients. Apart from analysing SLN of other cancer types[22], the procedure can also be applied to other diagnostically relevant tissue samples, such as cutaneous metastasis (M3: Supplementary Fig. 3) or any tissue biopsy that fits into a LSFM system[21,22,38]. In conclusion, our workflow can guide and might potentially replace FFPE histopathology as a novel gold standard for SLN staging.

3.6.6. Methods

HUMAN STUDIES - RECRUITMENT OF PATIENTS

This prospective study was approved by the local ethics committee of the Medical Faculty, University Hospital Essen, Germany (17-7420-BO) and registered at the German Clinical

Trials Register (DRKS00015737). Written, informed consent was obtained from all patients before entering the study. Eleven patients, fulfilling the inclusion criteria, with stage Ib or II (AJCC 2009, tumor depth of ≥1.0 mm) malignant melanoma and an age >18 years, who were scheduled to undergo sentinel lymph node excision (SLNE) were included in this ongoing prospective study which started October, 22nd 2018.

Sentinel lymph node excision

SLNE is performed as a standard procedure at the Department of Dermatology, University Hospital Essen, Germany, according to the guidelines of the German Association of Dermatology (Deutsche Dermatologische Gesellschaft, DDG)[23]. Prior to SLNE, lymphoscintigraphy using radioactive technetium was performed and subsequent SLNE was performed either under tumescent local anesthesia or general anesthesia as previously described[24]. Preparation and subsequent excision of all marked lymph nodes was carried out via an incision over the location where a maximum radio-isotype activity could be measured using a mobile manual scintillation probe (C-Trak, Care Wise Medical Products Corporation). Surgery was terminated when no further radioactive foci could be identified in the surgical field. Samples were pseudonymized by the involved medical doctors so that all samples could be processed by non-medical personnel as well.

Whole-mount procedure staining and tissue clearing

Directly after excision, samples were washed in isotonic sodium chloride solution, photographed and chemically fixed using excess volume of 4% PFA in PBS (CatNo: 9143.1, C. Roth) for 24 h at 4 C. After fixation, SLN were macroscopically cut if the smallest dimension (future z in LSFM) exceeded 6 mm, the working distance of the objective. The other two dimensions did not exceed 13 x 11 mm, avoiding multi-positioning and subsequent stitching algorithms while simultaneously reducing acquisition times. The incisions were made according to routine histopathological guidelines. For tissue permeabilization, samples were incubated at room temperature (RT) in 15 ml tubes (CatNo: 188271, Greiner Bio-one) with permeabilization buffer consisting of 20% DMSO (CatNo: 41641, Fluka), 1% TritonX-100 (CatNo: 3051.3, Carl Roth), 2.3 g glycine/100 ml (CatNo: 3908.2, Carl Roth) in Roti®-CELL PBS (CatNo: 9143.1, Carl Roth). During all incubation steps, samples were shaken in 3-D (Model No: 88881002, Thermo Fisher and RS-DS 5, Phoenix Instrument) except when described otherwise. Overhead rotation was avoided to prevent samples from getting stuck and running dry. Afterwards, samples were dehydrated in an ascending ethanol (EtOH) series, consisting of 50% EtOH (1:1 dilution of 100% EtOH, CatNo: 9065.4, Carl Roth, in ddH2O), 70% EtOH (CatNo: T913.2, Carl Roth) and 100% EtOH in 15 ml tubes while at 4°C. Incubation times in 50% EtOH and 70% EtOH were 4 h and 2 h in 100% EtOH.

The bleaching solution was prepared freshly, 10 minutes prior to sample incubation, by diluting 35% H2O2 (CatNo: 349887, Sigma Aldrich) to 7.5% in precooled bleaching solution, consisting of 5% DMSO in 100% EtOH. After 10 minutes, samples were transferred to these tubes, which were only loosely capped and incubated standing upright for 4 h at 4°C. Then, samples were rehydrated by successive incubation in 70% EtOH and 50% EtOH for at least 4 h at 4°C. While in 50% EtOH, the samples were warmed to RT and washed with 15 ml PBS for 30 minutes. Blocking was conducted for at least 30 minutes while shaking in 2 ml blocking solution containing 0.1% saponine (CatNo: 4185.1, Carl Roth), 0.1% Triton X-100, 0.02% NaN3 (CatNo: S2002, Sigma) and 5% donkey serum (CatNo: P30-0101, PAN Biotech) in 1x PBS in amber 2 ml safe-lock tubes (CatNo: 0030120.248,

Eppendorf). Incubation was done in a dry incubator (HERAcell 240i, Thermo Fisher) heated to 37 °C.
Subsequently, the samples were incubated with fluorophore-conjugated antibodies for another 5 d at 37 °C shaking. For the study, the panel was: 2 µg/ml of anti-CD3 AlexaFluor 647 (CatNo: 344826, Clone: SK7, BioLegend) and 10 µg/ml of anti-Melan-A (CatNo: NBP2-46603, NovusBio) which was self-conjugated with AF 790 (coupling kit: CatNo: A20189, Thermo Fisher) according to the manufacturer's manual. Note, that the Melan-A signal was placed in the channel with the longest possible wavelength to ensure a robust detection of Melan-A positive melanoma cells throughout the entire sample, since this was the most important feature for evaluating the clinical applicability of LSFM. In order to be able to compare Melan-A positive cells in the sample in LSFM and follow-up FFPE histology, we applied the same antibody clone (A103) used in local clinical routine diagnostics. For the B cell staining, we used 1 µg/ml anti-CD19 AF647 (CatNo: 302220, Clone: HIB19, BioLegend). After antibody incubation, samples were kept in black 5 ml tubes (CatNo: PE69.1, C. Roth) to protect them from light while being washed twice in 5 ml blocking solution without donkey serum. First, they were incubated for 4 h and then overnight at RT. Samples were then dehydrated in an ascending ethanol series of 50% EtOH, 70% EtOH and 2x 100% EtOH for 4 h at RT in each step. The samples were transferred to brown glass vials (CatNo: 102452 with screw caps CatNo: 102346, Glas-Shop.com) containing pure, fluid ethyl cinnamate (ECi, 99%, CatNo: 112372, Sigma Aldrich) as the refractive index matching agent and incubated for at least 8 h at RT. Tip: Invert samples at least once 2 h before imaging for optimal clarity.

LIGHT SHEET FLUORESCENCE MICROSCOPY (LSFM)
Samples were imaged using an Ultramicroscope II and ImSpector software (both LaVision BioTec). The microscope is based on a MVX10 zoom body (Olympus) with a 2x objective and equipped with a Neo sCMOS camera (Andor). For image acquisition, samples were either screwed or glued (Loctite 408) on a commercially available sample holder. Beware that contact with glue renders the tissue surface milky. If gluing a sample, it should not be imaged from a different angle afterwards. To avoid damage or deformation of the sample if screwing it tight, ECi-cleared 1% phytagel (CatNo: P8169–100G, Sigma Aldrich) in tap water blocks were used as buffers between tissue and plastic holder, from both sides and from below. Samples were placed on the longest cutting edge, with a perpendicular cutting edge facing left, if applicable. This allowed correlation with following histopathology. The cleared samples were then immersed in an ECi-filled quartz cuvette and excited with light sheets of different wavelengths (488, 561, 639 and 785 nm). Depending on the fluorophores, following band-pass emission filters were used (mean nm / spread): 525/50 nm or 595/40 nm for tissue autofluorescence; 680/30 nm for AF647 and 835/70 nm for AF790. For tumor screening, the sample was illuminated from both sides with three light sheets from different angles. Optical slices were taken every 10 µm at a low total magnification between 1.26x-2x, providing a detector resolution of 10.32-6.5 µm, respectively. The NA was set to 0.029, yielding a light sheet thickness of approximately 10 µm at the horizontal focus. During overview imaging, samples were evaluated live noting clarity, LN structure and, if applicable, Melan-A signal position. Regions of interest, e.g. presumably Melan-A positive regions, were subsequently imaged, mostly using a total magnification of 6.4x with a detector resolution of 2.02 µm. Here, acquisition parameters varied depending on size and quality of the region of interest. Sheet width was always at maximum to ensure a homogenous illumination of the sample. Illumination time was set to 350 ms and the total acquisition time of one plane was thus, theoretically, 700 ms. Assuming a z stack

as deep as 6 mm, this would have resulted in the acquisition of 600 images × 3 channels = 1800 images, which would theoretically have taken 21 min. However, in our practical experience including loading the samples, the overview imaging of one sample took 30–40 min. Depending on the number of regions of interest, the additional imaging time per sample ranged from 0-2h. To avoid photobleaching during imaging, the longest wavelength was imaged first. The output was a 16bit OME.TIF stack.
For more information on zoom factors, corresponding numerical apertures and resolutions, please visit: https://www.lavisionbiotec.com/products/UltraMicroscope/specification.html.

Declarification and gold standard formalin-fixed paraffin-embedded (FFPE) histology

After image acquisition, the samples were declarified in a descending ethanol series of 2x 100% EtOH, 1x 70% EtOH and 1x 50% EtOH for 4 h while shaking at RT. Then, samples were transferred into a plastic cassette (CatNo: M491-5, Simport) and stored in PBS. Subsequently, they were routinely paraffinized using a vacuum infiltration tissue processor (Tissue-Tek VIP 6 AI, Sakura). Paraffin embedding was done using a TBS88 (Medite). Sequential slices of 1.5 µm thickness were acquired by cutting the pre-cooled paraffin blocks (HistoStar cooling plate, Thermo Fisher) using a HM340E microtome (Thermo Fisher) with A35 microtome blades (Feather). Slices were transferred to a water bath set to 40°C (CatNo: MH8517, Electrothermal) and mounted on SuperFrost microscope slides (CatNo: 03-0060, R. Langenbrinck). Slides were stored at RT in the dark, while histopathologically relevant slides according to the local guidelines were routinely processed. H&E staining was done using a Ventana HE 600 (Roche) with Hematoxylin (CatNo: 07024282001) and Eosin (CatNo: 06544304001, Ventana). Immunohistochemistry against Melan-A (CatNo: 790-2990) or S100 (CatNo: 790-2914) in red (CatNo: 760-501, all Ventana) was conducted using a BenchMark Ultra (Roche).

Routine staging and follow-up histology

Slides were routinely histopathologically assessed by local histopathologists and patients were staged according to these gold standard findings alone. Histopathologists were only informed of patient's study participation but not about LSFM findings to avoid bias. If live LSFM findings did not match the reported diagnosis, LSFM data were reviewed. If Melan-A positivity could be determined in LSFM only, LSFM-guided FFPE follow-up stainings of stored back-up slides were used to confirm the findings. These were then again assessed by histopathologists. An Aperio At2 (Leica) was used to image FFPE slides.

In-silico 3-D analysis

16bit OME.TIF stacks were converted (ImarisFileConverterx64, Version 9.3.1, BitPlane) into Imaris files (.ims). 3-D reconstruction and subsequent analysis was done using Imaris software (Version 9.3.1, BitPlane). Segmentation of whole tissue including fatty tissue and CD3 positive volume was done using segmentation algorithm on tissue autofluorescence with 20 µm grain size and manual threshold. Segmentations of LN tissue (via LN capsule and/or cutting edges), Melan-A signal, blood vessels, B cell follicles and germinal centers are all based on the contour tracing tool and were carried out manually/semi-automatically. For surface creation of the LN tissue every 10th optical slice (100 µm), for all other surfaces every optical slice was traced. Surfaces were created with maximum resolution (2160 × 2560 pixel) and preserved features to ensure matching of the traced lines with the surface border. Discrimination of B cell follicles was based on T cell absence within the LN stroma.

MULTISCALE CONTRAST COMPRESSION ALGORITHM – RAYHANCE

For a given mean level of brightness the human visual system (HVS) typically is able to discriminate just about 100 different grey levels[25,26]. Therefore we developed RAYhance in order to access the wealth of information hidden in the broad dynamical range of fluorescence microscopy images in one glimpse. It presents slightest contrasts in fine details both in low and high intensity regions simultaneously and keeps strong contrasts under control. Mastering this task provides an image that delivers all structural information at once to the HVS and overcomes the cumbersome and time-consuming task of scanning the entire image by changing the windowing appropriately.

RAYhance modifies the contrast of the input images and its concept of contrast is designed to operate independently of the absolute intensity level of the input image. This allows for processing a whole 3-D-stack of LSFM images without generation of artificial discontinuities in image brightness – the whole 3-D-volume is processed seamlessly along the direction of the light sheet travelling through the specimen.

Each primary image, in our case uncropped 16bit OME.TIF optical slices, is converted in consecutive steps into several multiscale contrast images that obey the characteristics of the HVS as their contrast is given in units of just noticeable differences (JNDs). At each scale-level the JND images undergo non-linear processing of their pixel values that enhances subtle contrasts and decreases high contrasts that are perceivable anyhow. Afterwards, the processed multiscale contrast images are recombined into one grey-level image: the resulting RAYhance-processed image.

RAYhance's algorithm focuses on content and characteristics of the raw image only and thus runs detector independently. The parameters can be tuned to the specific task and, once set, RAYhance works without any user interaction, giving reproducible results even under different intensities of the illuminating laser.

RAYhance is currently available upon request from LaVision BioTec GmbH. In order to use RAYhance, please send your request to goettingen@lavisionbiotec.de.

SHRINKAGE DETERMINATION

Generally, samples were photographed macroscopically after excision, fixation, sectioning (if applied), bleaching (after rehydration) and clearing (before LSFM) in order to keep track of the macroscopically visible pigmentation and the shrinkage per sample/piece. However, not all samples were ideally suited for shrinkage measurement of LN tissue due to e.g. fat enrichment. Using FIJI[27], the area of the samples imaged from directly above was measured using the polygon tracing tool. With the millimeter paper in the background as a reference, the shrinkage per dimension of human LN tissue was determined to be: 5.1% ± 2.4% (arithmetic mean ± SD) from fresh to fixed, 5.9% ± 2.7% from fixed to bleached and another 10.5% ± 1.6% from bleached to cleared. The overall shrinkage from fresh to cleared was 20% ± 5.4% (all N=3). Paraffination of the samples caused further shrinkage compared to the cleared state, which amounted to 18.4% ± 4.6% (N=4).

3.6.7. References

1. Livingstone, E., et al. A first prospective population-based analysis investigating the actual practice of melanoma diagnosis, treatment and follow-up. Eur J Cancer 47, 1977-1989 (2011).

2. Gershenwald, J.E. & Ross, M.I. Sentinel-lymph-node biopsy for cutaneous melanoma. N Engl J Med 364, 1738-1745.
3. Morton, D.L., et al. Sentinel-node biopsy or nodal observation in melanoma. N Engl J Med 355, 1307-1317 (2006).
4. Gershenwald, J.E., et al. Multi-institutional melanoma lymphatic mapping experience: the prognostic value of sentinel lymph node status in 612 stage I or II melanoma patients. J Clin Oncol 17, 976-983 (1999).
5. Gershenwald, J.E., et al. Melanoma staging: Evidence-based changes in the American Joint Committee on Cancer eighth edition cancer staging manual. CA Cancer J Clin 67, 472-492 (2017).
6. Riber-Hansen, R., et al. Treatment influencing down-staging in EORTC Melanoma Group sentinel node histological protocol compared with complete step-sectioning: a national multicentre study. Eur J Cancer 48, 347-352 (2012).
7. Nieweg, O.E. False-negative sentinel node biopsy. Annals of surgical oncology 16, 2089-2091 (2009).
8. Satzger, I., et al. Prognostic significance of histopathological parameters in sentinel nodes of melanoma patients. Histopathology 50, 764-772 (2007).
9. Starz, H., Balda, B.R., Kramer, K.U., Buchels, H. & Wang, H. A micromorphometry-based concept for routine classification of sentinel lymph node metastases and its clinical relevance for patients with melanoma. Cancer 91, 2110-2121 (2001).
10. van Akkooi, A.C., Spatz, A., Eggermont, A.M., Mihm, M. & Cook, M.G. Expert opinion in melanoma: the sentinel node; EORTC Melanoma Group recommendations on practical methodology of the measurement of the microanatomic location of metastases and metastatic tumour burden. Eur J Cancer 45, 2736-2742 (2009).
11. Meier, A., Satzger, I., Volker, B., Kapp, A. & Gutzmer, R. Comparison of classification systems in melanoma sentinel lymph nodes--an analysis of 697 patients from a single center. Cancer 116, 3178-3188.
12. Scheri, R.P., Essner, R., Turner, R.R., Ye, X. & Morton, D.L. Isolated tumor cells in the sentinel node affect long-term prognosis of patients with melanoma. Ann Surg Oncol 14, 2861-2866 (2007).
13. Murali, R., DeSilva, C., McCarthy, S.W., Thompson, J.F. & Scolyer, R.A. Sentinel lymph nodes containing very small (<0.1 mm) deposits of metastatic melanoma cannot be safely regarded as tumor-negative. Ann Surg Oncol 19, 1089-1099 (2012).
14. van der Ploeg, A.P., et al. The prognostic significance of sentinel node tumour burden in melanoma patients: an international, multicenter study of 1539 sentinel node-positive melanoma patients. Eur J Cancer 50, 111-120 (2014).
15. Eggermont, A.M., et al. Prolonged Survival in Stage III Melanoma with Ipilimumab Adjuvant Therapy. N Engl J Med 375, 1845-1855 (2016).
16. Long, G.V., et al. Adjuvant Dabrafenib plus Trametinib in Stage III BRAF-Mutated Melanoma. N Engl J Med 377, 1813-1823 (2017).
17. Klingberg, A., et al. Fully Automated Evaluation of Total Glomerular Number and Capillary Tuft Size in Nephritic Kidneys Using Lightsheet Microscopy. J Am Soc Nephrol 28, 452-459 (2017).
18. Masselink, W., et al. Broad applicability of a streamlined ethyl cinnamate-based clearing procedure. Development 146, dev166884 (2019).
19. Grüneboom, A., et al. A network of trans-cortical capillaries as mainstay for blood circulation in long bones. Nat Metabolism 1, 236-250 (2019).
20. Männ, L., et al. CD11c.DTR mice develop a fatal fulminant myocarditis after local or systemic treatment with diphtheria toxin. Eur J Immunol 46, 2028-2042 (2016).

21. Merz, S.F., et al. Contemporaneous 3-D characterization of acute and chronic myocardial I/R injury and response. Nature Communications 10, 2312 (2019).
22. Nojima, S., et al. CUBIC pathology: three-dimensional imaging for pathological diagnosis. Scientific Reports 7, 9269 (2017).
23. Garbe, C., et al. Evidence-based and interdisciplinary consensus-based German guidelines: systemic medical treatment of melanoma in the adjuvant and palliative setting. Melanoma Res 18, 152-160 (2008).
24. Stoffels, I., et al. Sentinel lymph node excision with or without preoperative hybrid single-photon emission computed tomography/computed tomography (SPECT/CT) in melanoma: study protocol for a multicentric randomized controlled trial. Trials 20, 99 (2019).
25. Wandell, B.A. Foundations of Vision, (Sinauer Associates, 1995).
26. Kalender, W. Computed Tomography, (Publicis Corporate Publishing, 2005).
27. Schindelin, J., et al. Fiji: an open-source platform for biological-image analysis. Nat Meth 9, 676-682 (2012).
28. Renier, N., et al. iDISCO: a simple, rapid method to immunolabel large tissue samples for volume imaging. Cell 159, 896-910 (2014).
29. Belle, M., et al. Tridimensional Visualization and Analysis of Early Human Development. Cell 169, 161-173 e112 (2017).
30. Mitteldorf, C., Bertsch, H.P., Zapf, A., Neumann, C. & Kretschmer, L. Cutting a sentinel lymph node into slices is the optimal first step for examination of sentinel lymph nodes in melanoma patients. Mod Pathol 22, 1622-1627 (2009).
31. Cochran, A.J., et al. The Augsburg Consensus. Techniques of lymphatic mapping, sentinel lymphadenectomy, and completion lymphadenectomy in cutaneous malignancies. Cancer 89, 236-241 (2000).
32. Cook, M.G., et al. An updated European Organisation for Research and Treatment of Cancer (EORTC) protocol for pathological evaluation of sentinel lymph nodes for melanoma. European journal of cancer 114, 1-7 (2019).
33. Lee, E., et al. ACT-PRESTO: Rapid and consistent tissue clearing and labeling method for 3-dimensional (3-D) imaging. Scientific reports 6, 18631-18631 (2016).
34. Katoh, K. Microwave-Assisted Tissue Preparation for Rapid Fixation, Decalcification, Antigen Retrieval, Cryosectioning, and Immunostaining. Int J Cell Biol 2016, 7076910 (2016).
35. Katoh, K., Kano, Y. & Ookawara, S. Microwave irradiation for fixation and immunostaining of endothelial cells in situ. Biotech Histochem 84, 101-108 (2009).
36. Wang, Y., et al. Nanobody-derived nanobiotechnology tool kits for diverse biomedical and biotechnology applications. Int J Nanomedicine 11, 3287-3303 (2016).
37. Gefen, A., Cornelissen, L.H., Gawlitta, D., Bader, D.L. & Oomens, C.W. The free diffusion of macromolecules in tissue-engineered skeletal muscle subjected to large compression strains. J Biomech 41, 845-853 (2008).
38. Poola, P.K., Afzal, M.I., Yoo, Y., Kim, K.H. & Chung, E. Light sheet microscopy for histopathology applications. Biomed Eng Lett 9, 279-291 (2019).
39. Belthangady, C. & Royer, L.A. Applications, promises, and pitfalls of deep learning for fluorescence image reconstruction. Nat Methods (2019).

3.6.8. Endnotes

ACKNOWLEDGEMENTS
We thank the Imaging Center Essen (IMCES, https://imces.uk-essen.de) for continuous support of our imaging experiments. We also express our thanks for the support by Miltenyi Biotec, LaVision BioTec and the Pathology Unit of the University Hospital Essen. Furthermore, we thank S. Rehwald, S. Hendriks of the University Library Duisburg-Essen and S. Beyer and team of the Centre for Information and Media Services, University Duisburg-Essen for their continuous support concerning data management and IT infrastructure, respectively.

AUTHOR CONTRIBUTIONS
These authors contributed equally: SFM, PJ
These authors jointly supervised the work: JK, MG
PJ, JK and IS organized the clinical study, recruited patients and performed surgery. SFM and PJ developed and implemented the workflow and carried out the study supported by RU, AK and LB. SFM did LSFM imaging and in-silico processing, assisted by ZC, LB, RU, PJ. RU was responsible for FFPE sectioning. EH, KG and TS assessed the samples histopathologically. RAYhance/FullView was developed by GE and TA. MG, JK, IS, SB, DS and EH provided supervision. JK, MG and IS conceived of the study and wrote the manuscript together with SFM, PJ, EH, GE and KG. All authors contributed to discussion and correction of the manuscript.

COMPETING INTERESTS
GE is currently employed by LaVision BioTec GmbH, a Miltenyi company. MG and JK received general research funding from LaVision BioTec GmbH. The remaining authors declare no competing interests.

DATA MANAGEMENT
The data management plan can be accessed via DuEPublico. DOI: 10.17185/duepublico/70526.
https://duepublico2.uni-due.de/receive/duepublico_mods_00070526

DATA AVAILABILITY STATEMENT
The datasets generated during and/or analyzed during the current study are available from the corresponding authors upon request.

CODE AVAILABILITY STATEMENT
The Sourcecode of RAYhance cannot be disclosed due to commercial interests. RAYhance is currently available upon request from LaVision BioTec GmbH. In order to use RAYhance, please send your request to goettingen@lavisionbiotec.de.

3.7. Recapitulation

In the above manuscripts[1,2,6], we learned that analysis of cellular distribution patterns within entire organs requires specialized approaches but yields quantitative, meaningful results. On a technical side, we explored how autofluorescence-attenuation, tissue clearing and LSFM together allow homogenous, quantitative imaging throughout the murine heart. The published BALANCE protocol can be applied to assess organ-wide reactions to I/R injury. Here, assessment of myocardial infarction parameters was coupled to the analysis of the distribution patterns of neutrophils in their role as first responders in an acute sterile inflammation[1].

Furthermore, the lessons learned while working with strongly autofluorescent murine tissue also led to effective clearing of bloody and pigmented human biopsy samples ranging from heart to squamous cell carcinoma and entire lymph nodes. The fast i.v. antibody delivery route used in mice had to be replaced with a more time-consuming deep-penetration whole-mount staining approach. This shed light on the specific role of TANs and their inhibitive interaction with T effector cells in a chronic sterile inflammation setting within head and neck squamous cell carcinoma. The findings comprised of neighborhood analyses and the identification of TAN /T cell enriched tumor pockets in the 3-D space highlight the applicability of tissue clearing and LSFM in medical research[2].

Finally, we explored the utility of whole-mount staining, tissue clearing and LSFM in clinical diagnostics. Therefore, we developed a specific staining strategy for human lymph nodes that allowed the simultaneous analysis of i) the tissue architecture, ii) the cellular distribution patterns concerning T cells, B cell follicles and germinal centers, and iii) melanoma metastases and their exact 3-D quantification and localization. The LSFM sensitivity to detect melanoma metastases compared to the gold standard FFPE histology amounted to 100%. Beyond that, one out of eleven patients included in this clinical study only received access to checkpoint blocker therapy due to LSFM analysis and a possible follow-up histology of stored gap sections. The potential impact of tissue clearing and LSFM on the efficiency of clinical pathology, and thus patient treatment and ultimately survival might thus be higher than expected[6].

4. Discussion

4.1. Technical LSFM restrictions – developments and guidance

As shown in this thesis, LSFM in combination with tissue clearing is a powerful tool to analyze tissue samples, even entire organs, with cellular resolution[1,2,6]. New protocols were developed or adapted to allow the analysis of organs of interest. Thereby, the protocols differed in the route fluorescent probes were delivered. While fluorophore conjugated antibodies were i.v. injected into mice[1], human samples underwent whole-mount staining[2,6]. It is important to understand the fundamental differences and caveats of each route in order to utilize both techniques most effectively.

4.1.1. Fluorescent probe delivery route and associated caveats

4.1.1.1. *Intra venous* antibody delivery

Direct injection of conjugated antibodies into the bloodstream of an organism is associated with the benefit that all available targets are stained in their natural state while "blocking and washing", lowering and removing non-specifically bound antibodies is effectively mediated by flowing blood and subsequent perfusion. The delivery to readily accessible targets like endothelium is also very fast, producing robust anti-CD31 staining of the entire heart in less than one minute (data not shown). However, antibodies will not penetrate the intact plasma membrane of a cell and thus only surface markers can be targeted[185]. Moreover, how fast and efficient i.v. injected antibodies can reach and stain target cells in living tissue is not well understood. Concerning immune cells, introduction of a bias towards staining recently extravasated immune cells only should be investigated in different tissues. In pharmacokinetics, models e.g. from Shah *et al.* report that the tissue concentration of monoclonal antibodies linearly correlates with their plasma concentration independent of the time of measurement post dosing[186,187]. The related biodistribution coefficient for murine hearts concerning monoclonal antibodies suggests that the tissue concentration within the heart is about 10% of the plasma concentration[187]. However, these models typically consider minimum post-injection times of hours or days, not minutes (personal correspondence with Prof. Dhaval K. Shah, University of Buffalo,

30.10.2019). In theory, endothelium in the heart is non-fenestrated and in the healthy state larger molecules cross into the tissue via transendothelial channels or via transcytosis. During inflammation, increased permeability leads to enhanced transport of molecules via the paracellular route (reviewed here[188]). Specific information regarding kinetics of antibody transcytosis is sparse and knowledge is mainly based on epithelium, whereas less is known about endothelium[189]. Nevertheless, an exclusive staining of all extravasating immune cells within the total incubation time of 10 min following antibody injection of e.g. anti-Ly6G is unlikely since tissue emigration of a neutrophil may already take >8 min for the fast paracellular route, whereas transcellular emigration takes 20-30 min longer. This is true for healthy tissues and upon macrophage inflammatory protein 2 superfusion[190,191] and might change during inflammation. Moreover, there are reports claiming that anti-CD31 antibodies reduce neutrophil recruitment to inflamed tissues[29] and thus labelling of CD31 and Ly6G simultaneously might slow neutrophil extravasation even further. In manuscript #1, we assessed the capability of anti-Ly6G antibodies (clone 1A8) to stain all neutrophils present in tissues. I.v. labeling of neutrophils that also expressed the endogenous fluorophore tdTomato revealed a perfect overlap of all visible tdTomato+ neutrophils with the anti-Ly6G antibody signal (M1: Supplementary Figure 2c,d). Immune privileged organs like brain, eye and testis represent another restriction of antibody penetration into living tissues[192,193]. Furthermore, longer incubation times of antibodies might lead to adverse events, like inflammation or cell depletion. In the specific case of neutrophils, depletion protocols typically use much higher concentrations of antibodies (>100 µg per animal) and depletion efficiency is typically reviewed after >24 hours (compared to 5 µg/mouse for 10 min for LSFM staining)[194-196].

All in all, i.v. delivery of conjugated antibodies is a fast and reliable way to stain surface markers in non-immune privileged organs, especially the endothelium. Apart from injecting antibodies, injecting small molecule dyes i.v. can achieve staining of e.g. extracellular DNA *in vivo*[197]. Nevertheless, the use of new markers should always be accompanied with comparative analyses of gold-standard methods, like flow-cytometry or 2-D histology as demonstrated in all manuscripts of this thesis.

4.1.1.2. Whole-mount staining

No matter how fast and reliable i.v. antibody delivery is, there are samples that cannot be stained using this technique. Apart from immune privileged sites, this might depend on the experimental setup or the size of the organism of interest. Due to obvious ethical reasons, it is also not possible for human biopsy material. Therefore, labelling agents like fluorophore-conjugated antibodies must be delivered from the outside of the sample while leaving most of the sample intact, in a procedure termed "whole-mount staining". Published protocols incorporate the following principal steps[2,162]: after chemical fixation, the tissue is further permeabilized to allow antibody penetration. The use of detergents like Tween or Triton-X naturally causes loss of lipids but also proteins, and therefore might lower the target density within the tissue[198]. Subsequently, the probe can passively diffuse into the sample. However, depending on the level of antibody concentration, a bright halo might be visible during LSFM analysis, surrounding the tissue. In manuscript #3, instead of an unspecific sample halo due to high antibody clustering before sample entry, an enrichment staining along edges derived from physical sample manipulations was observed. This "cutting edge artifact" was restricted to the anti-Melan-A staining. Tests with other antibody clones against Melan-A revealed that specific clustering at the cutting edges of the tissue is a clone-inherent phenomenon. However, switching clones of detection antibodies against Melan-A might lead to a mismatch with follow-up histology due to differences in specificity. Therefore, cutting edge artifacts were consequently excluded from tracing Melan-A+ cells, although signal intensities matched positive signals. The signal itself was limited to the first 10-20 µm of tissue, making it easily distinguishable from tumor itself (for artifact assessment, see M3: Supplementary Figure 4).

Furthermore, tissue permeabilization and passive antibody diffusion are relatively slow processes taking multiple days to weeks[171] instead of minutes using the i.v. labeling route[1]. Especially in terms of a diagnostic procedure, prolonged processing times minimize its applicability. In turn, routine histopathological analysis may not be faster considering daily routine (M3: Supplementary Table 3). To reduce staining times by avoiding the need for additional incubation with secondary antibodies, mainly primary conjugated antibodies were used in this thesis. In principle, multiple staining rounds are possible and may be necessary due to low signal intensity of a primary antibody or incompatibility amongst multiple primary and secondary antibodies (up to three were used by Si *et al.*)[2].

Additionally, the processing times of the protocols may be lowered by either using smaller probes enhancing diffusion speed[199], like nanobodies[200], or applying active diffusion protocols. The latter comprises the use of specialized microwaves[201] or electrostatic fields[202].

4.1.2. Sample size

The protocol time of whole-mount staining is strongly influenced by the sample size as well. Besides technical restrictions derived from sample holders or the working distance of the objective, the sample size depends on the research question. On the one hand, there is a fast visualization of a small region of interest, e.g. the murine heart, that yields local 3-D information. On the other hand, the system can also be stretched to stain and image neuronal projections throughout an entire mouse[170]. In the latter example, even though the authors already used nanobodies, the probe incubation time was 8 to 9 days for the entire mouse. Furthermore, multi-tile or time-lapse LSFM come with high imaging time and generate immense amounts of data, comparable to CERN output[203]. Therefore, it is advisable to adapt and reduce the sample size to the absolute minimum necessary to answer the research question at hand. In manuscript #3, SLN were cut due to technical restrictions of the imaging system but also to assure robust staining quality of homogenously large samples and to avoid tiling and stitching, that would have introduced another layer of complexity. We were thus able to determine the SLN status and quantify tumor load at the level of single cells. Imaging entire SLN with >1 cm diameter might yield surplus biological information and reduce the handling workload, especially during imaging. However, this comes at a risk of introducing deep imaging artifacts like blurriness or pigmentation shadows (M3: Supplementary Figure 5 and M3: Supplementary Video 8). Moreover, increased sample size might lead to inhomogeneities in staining quality.

4.1.3. Autofluorescence, its attenuation and its use

Tissue autofluorescence and absorption are often related to high contents of hemoglobin or obstructive fluorescent pigments like melanin, respectively[150]. Especially in the 3-D space, sample clarity and signal quality depend strongly on the removal of such obstructions. Furthermore, light absorption of the tissue minimizes tissue penetration depth, which leads to a bright halo surrounding the in comparison highly under-illuminated object (M1 Figure 1c)[1]. Therefore, the reduction of light absorption and homogenization of

autofluorescence throughout the sample are prerequisites for quantitative imaging. Only by use of bleaching, it was possible to image the entire murine heart with its dense muscle tissue (manuscript #1) and assess human biopsies, like SLNs, that cannot be perfused free of blood and might contain further pigments like melanin (manuscript #3).

It is important to bear in mind that tissue bleaching with peroxide, for reduction of imaging artifacts and the enhancement of sample clarity, may cause epitope changes, hindering antibody binding[204]. Therefore, tissue bleaching is only advisable when well titrated and absolutely required. Antigen persistence should always be confirmed by follow-up gold standard histology (M3: Supplementary Figure 3). This was not necessary in the murine heart, since antibodies could bind epitopes in their natural state prior to tissue processing. Whole mount staining of SCC did not require bleaching at all, even though human biopsies are likely to be enriched with erythrocytes. However, tissue bleaching was integral to analyze human SLN that may contain pigmented melanoma. Strict correlation of LSFM findings with histology revealed that at least frequently used markers like Melan-A and S100 survive peroxide bleaching and can be used for gold-standard diagnosis even after initial whole-mount staining and LSFM analysis (M3: Figure 4c). Additionally, peroxide bleaching does not only destroy pigments, it quenches endogenously expressed fluorescent proteins[1], which might be themselves targeted with antibody staining again, recovering signal and shifting it into more appropriate channels (GFP to AF790).

The reduction of sample autofluorescence and absorption in general and even specific destruction of hemoglobin or melanin with peroxide has been described previously[205,206]. The whole-mount protocol iDISCO also utilizes peroxide to destroy pigments and homogenize autofluorescence signals for subsequent analysis with LSFM[162]. In comparison to the iDISCO approach, the published BALANCE protocol is based on less toxic substances, like ethanol instead of methanol, that do not cause incompatibilities of antibodies and their epitopes[171] in subsequent whole-mount staining or histology, as demonstrated in manuscript #3.

As soon as tissue autofluorescence allows for a high signal-to-noise ratio and homogenous imaging, it can also be used to capture local anatomical features, e.g. the structure of the lymph node capsule and blood vessels inside. Obtaining this anatomical information without using additional, specific color channels allows multiplexing of other cellular targets of interest. In manuscript #3, the medulla, the capsule and the total tissue volume including measurements of erythrocyte-filled blood vessels were solely reconstructed

based on tissue autofluorescence (M3: Figure 3). In manuscript #2, the discrimination between tumor and surrounding tissue hinged mainly on autofluorescence. Furthermore, the overall volume measurements of the heart muscle and the observations of cardiomyocyte directionality in manuscript #1 also relied on autofluorescence. Similarly, Abadie *et al.* recently reported the discrimination of different layers of human skin based on autofluorescence alone[177]. Stacks of optical slices depicting autofluorescence provide a label-free overview of the sample, similarly to hematoxylin/eosin staining but lacking information on the nucleus. However, assessment of tissue autofluorescence requires anatomical knowledge and typically does not allow identification of different cell types. One exception are distinctly shaped cardiomyocytes (M1: Figure 2b).

4.1.4. NIR dyes for deep imaging in pigmented tissue

Despite tissue bleaching, residual melanin may cause illumination and emission shadows during LSFM imaging, as shown in manuscript #3. However, since the anti-tumor signal (Melan-A) was measured within the near infrared (NIR) spectrum the detection of the tumor mass within the pigmentation shadow was possible. In general, imaging with shorter wavelengths in the blue spectrum (488 nm) results in more scattering and imaging artifacts compared to longer wavelengths from the red or NIR spectrum (650 – 900 nm). This is because shorter, energy-rich wavelengths are more prone to be absorbed and scattered by molecules much smaller than the actual wavelength (Rayleigh scattering), which limits tissue penetration[150]. Therefore, important signals should be imaged within the NIR window, in which light scatter and absorption occur less frequently, allowing deep tissue imaging[150].

Besides circumventing autofluorescence, scatter and tissue absorption, there is a second reason to image melanoma-related markers in the NIR window. Melanin is typically reported to have a peak in light absorption around 405 nm, with fluorescent characteristics of its oxidated state elicited by 470 nm, while emitting around 540 nm[207,208]. This knowledge is utilized by spectral absorption or fluorescence spectroscopy to quantify melanin content. Interestingly, Huang *et al.* reported that cutaneous melanin is also able to fluoresce after excitation with NIR light of 785 nm wavelength[209]. Using melanin presence alone to detect melanoma in SLNs yielded a 100% sensitivity but only a 48 – 62% specificity in the past[210]. Therefore, melanin fluorescence itself might be considered as a

failsafe in case of strong pigmentation or problems with antibody penetration. On the one hand, melanin fluorescence should be principally quenched using peroxide bleaching and, consequently, a melanin-derived fluorescence signal was absent in non-stained lymph node controls carrying melanoma. However, we cannot exclude that melanin fluorescence in non-quenched pockets with surviving pigmentation is contributing to obtained Melan-A signals in the NIR channel. Importantly, follow-up histology revealed clusters of both pigmented and non-pigmented Melan-A+ cells, and both were detected by LSFM (M3: Supplementary Figure 5). Interestingly, not all pigmented cells were Melan-A+, which might be attributed to the heterogeneity of melanoma metastases[82].

4.1.5. Algorithms, quantitative analysis and computational load

4.1.5.1. Introduction of RAYhance

Even after autofluorescence attenuation, signal heterogeneity of different tissue regions like fat, LN stroma, or bleed-ins with high density of erythrocytes, remains high (M3: Supplementary Figure 1). Thus, a strictly linear digital display might conceal significant information. In order to display multiple entities of different signal intensities within one image, we introduced RAYhance, a multiscale contrast compression algorithm. Using RAYhance, instantaneous and simultaneous examination of LSFM images was possible, even when opened in ordinary image display software. There are published algorithms available, dealing with image heterogeneity, like the "surface extraction algorithm"[176]. Another histopathologically relevant example is the virtual generation of hematoxylin and eosin slides out of a nuclear and a cytoplasmatic staining[211], which has also been implemented for LSFM optical slices[176]. However, solutions applied in research are often in no format for easy introduction into pathology. A pathologist's time is limited, and implementation of different subsequent algorithm modules is not likely to be on their schedule. Furthermore, the background knowledge needed to implement algorithms or to adjust them to specific needs is not commonly distributed. The curriculum of neither biologists nor histopathologists covers information technologies (IT) and programming extensively[203], which is why plug-and-play solutions like RAYhance must be introduced. RAYhance in its current state is not yet ready to be used in routine diagnostics, though. When applied to autofluorescence alone, RAYhance produced extraordinary results and allowed for the simultaneous assessment of all SLN structures. It also allowed automatic

segmentation of tissue volume. However, it also introduced noise in regions where signal is typically absent, such as the imaging medium. Furthermore, RAYhance rendered all small contrasts visible. In channels with specific staining, such as CD3 staining for T cells, RAYhance processing resulted in an increased background of unstained tissue, such as the capsule. This makes 3-D quantification of specific cell types based on simple signal intensity thresholds impossible. The benefit of RAYhance in its current state is the fast and reliable generation of browsable histo-like data sets that do not need further adjustments. Generally, algorithms need to undergo thorough inspection to test their rigor and performance before they can be used as a basis for diagnosis.

This, however, lies in the future. We have established a potential diagnostically relevant workflow and thus also identified its major weak spots. The transfer of the procedure from basic research and method development to a standard of care methodology will have to include automation of sample processing and imaging as well as algorithm development and easy-to-handle image analysis.

4.1.5.2. Quantitative analysis in the 3-D space

LSFM has been used in seminal papers in the past to describe and visualize organs and organisms from a mesoscopic point of view for the first time, often lacking quantification or replication of the underlying data[171] (in this case also due to the rare samples). This highlights that observation and thorough description of biological samples from the mesoscopic perspective alone yields enough fundamental information of the underlying system. Furthermore, software tools for easy 3-D analysis were either not equipped to work with the amounts of data or were not user friendly for a large proportion of biologists[203]. In this thesis, as well as in the above-mentioned paper by Belle *et al.* published in the beginning of 2017 in Cell, the software IMARIS (Bitplane) was used to visualize, segment and quantify all datasets. The in total 24 new IMARIS releases and major updates between November 2014 and the end of 2019 emphasize the tremendous need to update existing code previously focused on confocal microscopy in order to meet the arising need of LSFM[212].

Nevertheless, only a few segmentations, like the overall heart muscle or tissue volume, were performed with automatic surface generation algorithms alone. Counting neutrophils in the heart muscle was done using the IMARIS spot function based on a manually

determined intensity threshold. However, this algorithm underestimates the amount of cells present in high density clusters where discrimination between cells is not easily achieved and resolution (6.5 µm in screening mode) as well as image depth (equals the light sheet thickness of approximately 12.5 µm for most cases) are too low or high, respectively. The use of higher magnification would solve the local counting problem, while simultaneously yielding a smaller FOV which introduces the need for tiling, causing more photobleaching and requiring even more algorithm-based applications, such as stitching.

Thus, most objects were segmented manually, using simple 3-D tracing and contour tools. While producing a high accuracy, manual tracing introduces operator variability (M1: Figure 4b). Furthermore, it is a tedious and time-consuming job, with man-hours ranging from 15 min (e.g. rough capsular surface, M3: Figure 3c) and days (follicles and germinal centers) to multiple weeks (vessel tree segmentation, M1: Figure 3d) per sample. Therefore, we are currently engaged in the development of algorithms based on artificial intelligence or machine learning to identify structures of interest, like follicles, lymph node capsule or Melan-A+ cells. Here, using RAYhanced datasets for analysis may represent an advantage due to the reduction of image variability in increasing tissue depth and between samples. However, training these algorithms also takes substantial time and expertise. Furthermore, IT infrastructure must be equipped to handle and process big imaging data, considering that 500 GB per patient, as mentioned in the data management plan (DMP) of manuscript #3 (see https://duepublico2.uni-due.de/receive/duepublico_mods_00070526), is likely to be expected when screening human SLNs. This involves high tech server structures[203] with high end software-compatible graphics cards to be able to extract meaningful, quantitative information from these huge data sets. It also clarifies that projects need to be carefully planned and DMPs need to be devised to i) keep track of data, ii) decide when to delete or archive data, iii) identify bottlenecks in processing power and dataflow, and iv) meet all regulations regarding data protection.

4.2. Biological and clinical insights due to tissue clearing & LSFM

4.2.1. I/R injury assessment in 3-D

The published BALANCE protocol allows monitoring of organ wide consequences following ischemia/reperfusion (I/R) injury. It is designed to make strongly autofluorescent

and/or pigmented and thus highly absorbing tissues[150] amenable for quantitative LSFM[1]. Analysis of I/R injury in the murine heart demonstrated its applicability, but BALANCE is not restricted to that organ specifically. As shown in manuscript #1, murine liver or even human heart biopsies can be processed alike (M1: Figure 2). This broad applicability is combined with the fast i.v. antibody delivery route in mice, qualifying the protocol for routine high throughput analysis.

4.2.1.1. Interpretation of CD31 negativity

In manuscript #1, CD31 was used as an established endothelial marker[213]. However, other cells like neutrophils or T cells may also express CD31. Interestingly, neutrophils lose CD31 positivity once extravasated[29] while CD31 on T cells is cleaved upon activation[30]. Yet, CD31 expression of immune cells seems to be weaker than of the endothelium, explaining why no CD31 expression on single cells except to continuous filamentous endothelial structures was observed.

In the paper, CD31 negativity after 24 hours of reperfusion was used to quantify the I/R injury. But what does CD31 negativity mean exactly? One interpretation would be that CD31 might be lost during the ischemic impact and subsequent inflammation of the epithelium. In fact, there are reports supporting this view, showing that endothelial CD31 is rearranged and staining becomes weaker during inflammation in response to IFN-gamma[214] and TNF-alpha[215]. However, Hernandez *et al.* showed that ischemia in the brain is associated with microvascular loss by filling vessels with a non-specific marker. They reported reduced vessel densities, hinting to either vessel obstruction, collapse or loss rather than marker loss[216]. Furthermore, the reported selective "survival" of larger vessels compared to loss of micro vessels could be confirmed in the heart muscle (M1: Supplementary Figure 3a).

After 5 days of reperfusion, vessel branching complexity, meaning the frequency of branches, was enhanced (CD31 curly) and the vessel length density was reduced (M1: Figure 5). This observation, restricted to the borders of the much smaller CD31-negative areas, hints at tissue neovascularization and thus supports the theory that CD31 negativity after 24 hours of reperfusion is associated with loss rather than obstruction or collapse of micro vasculature. Typically, the cardiac vascular network is highly structured, accom-

panying elongated cardiomyocytes[217]. However, after 5 days of reperfusion, the directionality of "curly" vessels is no longer in conformation with the surrounding intact myocardium. Hence, the vascularization pattern is changed. This is most likely due to cardiomyocyte death and enhanced myofibroblast presence starting from 4 days after insult[49].

All in all, CD31 negativity should be interpreted as a marker for an area in which bloodflow is still obstructed through the loss or collapse of endothelial cells. This coincides with local ischemia and tissue damage. Consequently, CD31 negativity correlates with the established TTC redox assay as well as physiological heart function parameters like ejection fraction (M1: Figure 4). Interestingly, tracing of CD31+ arteries also allowed visualization of different reactions of microvasculature after I/R injury. While perfusion of both, the dorsal and ventral side of the heart muscle below the occluding knot was restricted, only the ventral side exhibited CD31 negativity (M1: Figure 3). Only BALANCE/LSFM allows the identification of such important differences within the same heart, enabling follow-up and characterization of underlying mechanisms between these two different zones.

4.2.1.2. Increasing experimental rigor through multiplexing

Assessment of myocardial infarction parameters (AAR, I/R injury, remote zone) is typically achieved by tetrazolium chloride redox assay on crude, 2 mm thick slices, which still allows determination of immune cell location on thin sections by further processing. Since working with 2-D slices yields only an excerpt of the situation, quantitative analysis of immune cells within the entire heart is typically done using flow cytometry. This in turn leads to a complete loss of the localization context. Overall, the analysis of the impact a certain drug has on both, myocardial infarction parameters and immune cell quantity and localization requires at least two separate animal cohorts (M1: Supplementary Table 3). Besides an overall reduction in time and expense, using the BALANCE/LSFM approach, fast quantitative analysis of all these parameters is possible, which contributes to experimental rigor and reproducibility[218]. Intra-individual comparisons are possible and the overall need for animals is reduced, which additionally serves the 3R principle[219,220].

4.2.2. Neutrophil-rich pockets downregulate local T cell cytotoxic potential in human SCC

As mentioned above, quantitative flow cytometric analyses of tissues lose complex spatial information and do only provide indirect information about immune cell functionality. To assess cellular effector function capability, tumor tissue is typically digested, cells are purified and subsequent *in vitro* analyses like killing assays are performed. However, the microenvironmental cellular context is lost, which is comprised of cellular interactions or regional cellular accumulations (reviewed here[221]). Also, the attribution of cells to larger but functionally different zones of the tumor tissue like the marginal zone, the tumor core or blood vessels, cannot be made. However, the spatial context of different immune cell subsets is crucial to understand their intra-tumoral function as well as their role in disease progression and related prognosis[221-223]. As an example, there is evidence that CD8+ T cell density within tumor tissue of oral SCC has a stronger positive effect on overall survival compared to T cell density of the surrounding stroma[224]. Furthermore, this study also showed that accumulation of FoxP3+ T regulatory cells within 30 µm from a CD8+ T cell in both tumor and stroma was associated with significantly reduced overall survival. In contrast, the FoxP3+:CD8+ ratio was not. However, mapping of the immune landscape was only possible using high-resolution microscopy on 2-D slices so far[221,224]. Consequently, application of tissue clearing and LSFM to human tumors now allow 3-D mapping of immune cells throughout large biopsy samples *in situ*. Therefore, in manuscript #2, tissue clearing and LSFM analysis was instrumental to uncover differentially dominated or mixed tumor areas referring to TAN or TIL presence in human tumors. Close proximity of TAN+ for CD66b, LOX-1 and arginase-I with cytotoxic T cells was coincidental with lowered expression of GrzB and Ki67 of TIL in human SCC[2].

In humans, TIL presence in tumors is typically associated with positive prognosis[222,223,225] while enhanced presence of TAN is a negative predictor in many cancers [98,226] despite their established anti-tumor functions[105,227]. Along these lines, the intra-tumoral CD66b-positive neutrophil-to-CD8-positive T cell ratio (iNTR) alone is proposed as a prognostic factor in non-small cell lung cancer, with a high iNTR being associated with higher relapse rates and lowered overall survival[228]. Furthermore, it has been described that LOX-1 might be a marker for immunosuppressive PMN-MDSCs, not being expressed

by neutrophils derived from peripheral blood of healthy patients but present in 5-15% of neutrophils in circulation derived from cancer patients. LOX-1+ neutrophils have an immunosuppressive MDSC phenotype and are enriched (15-50% of neutrophils) in tumor tissues[229]. Arginase-I+ neutrophils have also been described to be immunosuppressive, but it is questionable whether ARG-1 expression alone conveys an immunosuppressive phenotype[98]. Importantly, the description of immunosuppressive N2 TAN is mainly derived from research focusing on mice, while research focusing on the immunosuppressive functions of PMN-MDSCs in humans is typically restricted to the analysis of different fractions of the peripheral blood[229,230]. The findings in manuscript #2 therefore allow rare insights into local cellular hotspots and potential interactions of tumor associated immune cells within the human tumor microenvironment. Here, CD3 density within 25 µm from CD66b+ LOX-1+ neutrophils was significantly higher compared to LOX-1 negative cells, suggesting a higher clustering efficiency. Moreover, the presence of CD66b+ and CD66b+ LOX-1+ neutrophils in the tumor core was confirmed to correlate with poor prognosis in OSCC and LSCC. This was in contrast to the elevated presence of cytotoxic GrzB+ proliferating (Ki67+) T cells, which was associated with high overall survival. Furthermore, T cells in close proximity to LOX-1+ arginase-I+ TANs exhibited lower expression of Ki67 and Grzb, suggesting a local downregulation of T cell function. A lack of activation-markers like Grzb has been also previously described to hint towards immunological ignorance, a state in which T cells become unable to respond properly to tumor[221,231].

However, a caveat of tissue clearing is its inherent end-point nature. As a trade-off for sample clarity, the sample must be fixed prior to processing. Therefore, direct evidence for impaired cytotoxic T cell function cannot be gathered by staining fixed tissue. T cell effector function is characterized by mobilization and exocytosis of cytotoxic granules, releasing their contents which in the end leads to tumor cell death[232]. This active process might only be shown either *ex-vivo*, loosing microenvironmental cues, or by using intravital microscopy, as discussed below.

Nonetheless, the proximity-dependent decrease of proliferation-associated markers like Ki67 argue in favor of a TAN dependent suppression of, at least, T cell proliferation. It is known that cytotoxic T cells can proliferate in the tumor microenvironment. Proliferation might be impaired during T cell exhaustion or via other cells of the tumor environment including tumor cells, tumor-associated macrophages or regulatory T cells[233-235]. Of note, a positive correlation of APC-like HLADR+ TAN with TIL proliferation could also be

confirmed, highlighting the ambivalent character of different TAN subsets in the tumor environment[236].

4.2.3. Diagnostic potential of LSFM in SLN analysis

In manuscript #3, we showed the capability of tissue clearing and LSFM in precisely describing and quantifying metastases in human lymph nodes, which has a vast potential to improve precision of patient staging. It is known that the tumor burden correlates negatively with melanoma-specific survival[141]. The burden is typically assessed in one dimension, measuring the diameter of the largest tumor accumulation within the available slices. In 2009, van Akkooi and colleagues proclaimed that the ideal way to analyze SLN metastatic load would be in 3-D. However, such methods would be associated with high inter-observer spread and complicated calculations, referring to sequential 2-D sectioning and analysis[182]. Thus, the LSFM approach described in manuscript #3 represents a long-craved tool to exactly assess 3-D tumor spread within SLN, quantify volumetric extend as well as determine location and size of multiple metastatic foci. Furthermore, it yields detailed biological information on the cellular environment and local LN architecture, such as proximity to important anatomical structures. Rigorous follow-up will thus allow the search for new predictive markers that might enhance prognosis accuracy. One known example is the tumor position relative to the capsule. Here, tumors with different microanatomical locations than subcapsular clustering were associated with 22% non-sentinel node involvement, while subcapsular metastases were not associated with non-sentinel node involvement at all[183]. The location context, along with the possible identification of diverse other diseases like lymphoma are reasons why the SLN should not be dissociated to be merely analyzed via PCR or flow cytometry to detect melanoma cells.

Besides quantification and localization of metastases, LSFM analysis revealed metastases not detected by gold standard FFPE histopathology, thus underlining the potential of this procedure in identifying patients with smaller metastases. However, in contrast to the location and size as important prognostic factors, the clinical relevance of sub-micro metastases <0.1 mm is debated due to the risk of overtreatment[237]. On the one hand, the American Joined Committee on Cancer announced 2017, that there is no unequivocal evidence that a lower size cutoff for staging-irrelevant metastasis exists[141]. On the other hand, patients with small metastasis foci in their SLN between 0.01-0.2 mm (which would

be part of stage III, since N stage is >0) had a similar 10-year melanoma specific survival than patients of stage IB (without any detectable metastases), with 96% and 94%, respectively. Nevertheless, the three metastatic foci of the patient missed by routine histopathology exhibited volumes of 0.013, 0.011 and 0.006 mm^3 and thus cannot be considered sub-micro metastases (M3: Figure 5). As a reference, the volume of a sphere with 0.1 mm diameter is 0.0005 mm^3 and the volume of a cube with 0.1 mm edge length is 0.001 mm^3. The difference between detection efficiency of current gold-standard histology and debated relevance of sub-micro metastases is therefore quite large and associated false-negative patient diagnosis by routine histopathology could be consequently circumvented.

Thereupon, it is obvious that LSFM analysis would indeed lower the technical false-negative rate of SLN analysis, allowing more patients access to potentially life-prolonging therapy. However, it is interesting to speculate whether this higher overall discovery rate of metastases in SLN would also impact melanoma-specific survival rates. It seems logical that by identification and treatment of patients that would have not been considered for therapy otherwise, undetected disease progression would be hindered. However, Welch *et al*.[135] reported that the introduction of skin-screening programs also led to a steady increase in identified primary melanomas without affecting melanoma specific mortality (1986-2001). One interpretation of this phenomenon could be that a strong increase in melanoma incidence was met with an equally strong rise in treatment quality, preventing an increase of disease-related mortality. However, this seems to be unlikely over a long period of time. Another explanation could be prolonged periods of disease dormancy, so that an effect on mortality would only be visible after multiple decades. Whether LSFM analysis has a more profound impact on disease development and mortality in times of checkpoint blockade can therefore only be determined in the future.

4.3. Outlook

4.3.1. BALANCE/LSFM – the future of a research tool

4.3.1.1. Establishment of additional markers for mice and man

In terms of methods, more flexibility is always better. Therefore, one of the first goals should be the establishment of cell death markers like phosphatidylserine[238] that would

directly facilitate the identification of "true" tissue damage compared to indirect I/R injury measurement via CD31 negativity. The visualization of other immune cells like macrophages or T cells, even in the context of other adverse myocardial events, such as myocarditis, would be helpful. Furthermore, the restriction of i.v.-mediated antibody delivery to stain surface markers might be eventually overcome using newly evolving concepts like TransMabs. These antibodies are able to penetrate living cell membranes and can thus target intracellular proteins[185,239]. Furthermore, small molecule markers to stain extracellular DNA etc. could be injected i.v., circumventing the uncertainty of sufficient tissue penetration depth[197]. Since unsuccessful translation of therapeutics is thought to be due to mouse studies[43], BALANCE/LSFM can also be used to understand the effects of therapies on the immune cells localization within human biopsies.

4.3.1.2. Investigating the nature of CD31 negativity after I/R injury

The BALANCE/LSFM approach is the perfect tool to investigate different aspects of I/R injury. To determine the nature of CD31 negativity, filling experiments using unspecific tracers such as FITC-albumin[216] or lectins would give us an idea if vessels are open or collapsed. Furthermore, the assessment of CD31 negativity over time would be important to closely characterize and possibly elucidate the nature of the phenomenon. We know that after 24 hours of reperfusion, CD31 negativity is much larger compared to 5 days after reperfusion. But what about the onset of reperfusion? Preliminary results suggest that the initial CD31 negative volume 5 min post reperfusion nearly equals the area at risk (data not shown). This can be interpreted in a way that the microvasculature is either completely blocked or collapsed and opens only after a certain amount of time. Interestingly, this might also be linked to the "no-reflow" phenomenon, which is defined as inadequate myocardial perfusion without angiographic evidence of mechanical vessel obstruction[240]. Amongst others, I/R injury may lead to no-reflow through different mechanisms. One example is the theory that blockage of capillaries occurs due to leukocyte plugging (reviewed here[241]). Leukocyte blockage of capillaries should also be quantifiable using the BALANCE/LSFM approach.

4.3.1.3. Altering neutrophil recruitment kinetics

Initial neutrophil surge into recently ischemic tissue is adverse but so is the depletion of neutrophils[43]. Too many neutrophils at once cause irreversible bystander damage while neutrophil absence is associated with impaired resolution of inflammation, adverse remodeling and decreased cardiac function[43,55]. Corticosteroids have even been connected with rupture due to insufficient healing[242]. Therefore, strategies that limit neutrophil extravasation but do not completely exclude entry might be successful in reducing infarct severity. Indeed, blocking E/P selectin reduced severity of stroke in nonhuman primates[243] and a clinical trial of the P selectin antagonist inclacumab including 544 patients revealed significant reduction of myocardial damage following percutaneous coronary intervention in 2016[244]. It would be interesting to validate these findings using BALANCE/LSFM and analyze potential changes in neutrophil distribution patterns.

4.3.2. Multiplexing to enhance precision

The data published in manuscript #2 strongly hint towards immunosuppressive properties of TAN. However, there are various marker-associated problems that enhance the difficulty of data interpretation.

4.3.2.1. Marker-associated problems

In general, Ki-67 has been established as a proliferation marker over decades. Although it is known that its functions during cell cycle are diverse, the exact mechanisms of action are not well understood. Nevertheless, it is established that KI-67+ cells belong to an actively dividing pool[245,246].

In humans, it is difficult to determine the sole biomarker to identify neutrophils. Although CD66b expression is commonly used as a marker to quantify neutrophils in flow cytometry or tissues[101,228], CD66b expression is not exclusive for neutrophils as eosinophils express CD66b as well. However, the significant findings of manuscript #2 were related to LOX-1 co-expression. Importantly, LOX-1 expression in PMNs was not reported to be elevated in eosinophil-associated diseases like eosinophilic colitis, and no enrichment of eosinophils was found in LOX-1+ or LOX-1- PMN populations, respectively[110].

Another issue is that CD3+GrzB+ cells are not necessarily cytotoxic CD8+ T effector cells. In the circulating pool, there are also CD4+ T cells that are expressing granzyme B and a strong increase of GrzB expression was demonstrated under differentiation stimuli towards T regulatory 1 cells *in vitro*[247]. In manuscript #2, a small fraction of CD4+ cells was also found to be GrzB+ and, interestingly, CD66b+LOX-1+ TAN presence and conjugation downregulated both Ki67 and GrzB expression in CD4+ as well as CD8+ T cells (M2: Figure S3).

In both cases mentioned above, the availability of more markers per slide would increase precision, e.g. Siglec-8 for eosinophils. With the advent of multiplexing strategies that allow assessment of >30 markers on a single tissue slice, like the CODEX system[248], in-depth analysis of the immunological tumor microenvironment should be possible. However, this will also increase the level of complexity of data interpretation, highlighting the need for automatic parameter assessment. In the case of 3-D LSFM analysis, the restriction to currently 3-4 channels is even more limiting and multiplexing strategies have to be identified in the future.

4.3.2.2. Showing T cell effector function in 3-D samples

GrzB expression alone is demonstrating the potential of an effector cell to kill target cells, but the process of granule release and subsequent target cell death alone validates effector function.

Therefore, assessment of CD8+ T cell effector function in fixed samples can only be indirect. One way to tackle this problem using fixed samples would be staining of tumor cells, CD8+ T cells, CD66b+ LOX-1+ neutrophils together with a marker for apoptosis. In its simplest form, this could be a DNA marker, allowing determination of chromatin condensation. Using multiplex enhanced LSFM analysis, the rate of apoptotic tumor cells in the vicinity of CD8+ T cells could be determined and compared between dominated CD8+ T cell regions and mixed regions. With high-resolution microscopy on cleared tissue, also conjugation events of CD8+ T cells with tumor cells in the different immunological compartments would be possible. These interactions could be followed up by correlative slice-based histology or electron microscopy, visualizing recruitment of granules. All in all, this would characterize the situation in more detail, adding to the indirect evidence for cytotoxic T cell function.

Another challenging approach without destroying the tumor microenvironment by e.g. dissociation could be to incubate a fresh human biopsy *ex vivo*, staining T cells, tumor cells in addition to non-cell permeable DNA dye to perform *in situ* microscopy, assessing live killing rates of T cells within small FOVs of the entire sample. Subsequently, the tissue samples could be analyzed using LSFM microscopy and killing rates assessed by intravital microscopy could be correlated with LSFM findings. However, such complex approaches are typically not feasible for larger cohort studies.

4.3.2.3. Towards new therapies

In general, neutrophils have proven to be a valuable target for mediation of enhanced anti-tumor T cell responses. Hence, different approaches aim on either completely removing neutrophils from the system by antibody-mediated depletion[194] or the prevention of neutrophil migration into the tumor[249]. However, neutrophil depletion or impairment of neutrophil migration is potentially harmful considering secondary infections[12]. Therefore, identification of specific markers associated with a pro-tumor TAN phenotype like LOX-1[110] might pave the way to selective inhibition of negatively associated TAN functions while keeping positive effects and host-defense intact.

4.3.3. LSFM implementation in SLN diagnostics

So far, we have developed a workflow comprised of tissue clearing, LSFM and RAYhance that allowed robust analysis of diagnostic human samples[6]. For translation of LSFM to routine clinical diagnostics, additional steps in protocol development must be made.

4.3.3.1. Marker dependency and protocol speed

LSFM analysis and tumor detection efficiency are only as good as the specificity and sensitivity of the tumor detection marker in use. To be clear, if Melan-A-based LSFM results obtained with the same antibody clone are correlated with follow-up Melan-A FFPE histology, the technical false negative rate of the histological assessment can still be determined, and the aim of the study can be reached. However, since melanoma and especially melanoma metastases display a high degree of heterogeneity, multiplexing strate-

gies need to be established enabling the use of multiple melanoma markers simultaneously. The Melan-A antibody used in this study is reported to have a detection sensitivity of melanoma metastases of around 71-88%. Melan-A staining is also not exclusively specific for melanoma. Therefore, a combination with other antibodies e.g. detecting S100 proteins, might yield a more robust result (summarized by Weinstein *et al.*[82]).

Furthermore, in order to process samples fast and reliably, the different steps of the whole-mount protocol need to be automated (M3: Supplementary Table 3). This could save up to 20 minutes of handling time per sample and 32 hours of overall processing time considering the entire LSFM module. During this process, sample quality might be monitored using ultrasound time-of-flight analysis, which might further reduce excess incubation times while assuring robust sample dehydration and clearing[250]. With added process automation and speed for both wet-lab and *in silico* processes, LSFM might be implemented in routine diagnostic procedures someday.

4.3.3.2. LSFM SLN analysis might provide access to adjuvant therapies

The study itself with a planned participant number of 130 melanoma patients will have to continue to elucidate the exact potential of LSFM analysis to reduce technical false-negative rates. If this histological false-negative rate is indeed 10-20% as our preliminary results and other studies suggest[251], LSFM analysis might be the desired tool to drastically lower overall clinical false-negative rates of SLN analysis in melanoma as well, which are reported to be between 5-20%[143,252,253]. To clarify, a clinical false-negative finding is a patient with a negative SLN that develops metastases in the same lymph basin, whereas histological (technical) false-negative findings are SLNs that are deemed negative due to insufficient node analysis but contain unnoticed metastases. Nevertheless, lower technical false-negative rates would allow the treatment of patients otherwise excluded from therapy.

Beyond melanoma, it is to be expected that analysis of SLN in other cancer entities will also reduce technical false-negative rates. Analysis of these biopsies will most likely be associated with less optical interference due to the absence of melanin in tumors, and a higher tumor detection efficiency and specificity due to availability of better markers. Consequently, the developed protocol should be applied to other cancer entities, which rely on SLN biopsies as a gold standard for staging like breast cancer[254], head and neck

cancer[255] or colorectal cancer[256], to only name a few. This would demonstrate broad applicability and therapeutic benefit of multiple patient cohorts. Thus, LSFM-based SLN analysis might be recognized by clinicians as a new tool improving patient care and, subsequently, the procedure might be established as a standard of care in clinics.

5. Bibliography

1. Merz, S.F., *et al.* Contemporaneous 3D characterization of acute and chronic myocardial I/R injury and response. *Nature Communications* **10**, 2312 (2019).
2. Si, Y., *et al.* Multidimensional imaging provides evidence for down-regulation of T cell effector function by MDSC in human cancer tissue. *Science Immunology* **4**, eaaw9159 (2019).
3. Grüneboom, A., *et al.* A network of trans-cortical capillaries as mainstay for blood circulation in long bones. *Nature Metabolism* (2019).
4. Schleier, L., *et al.* Non-classical monocyte homing to the gut via alpha4beta7 integrin mediates macrophage-dependent intestinal wound healing. *Gut* (2019).
5. Jansen, P., *et al.* The prognostic value of sentinel lymph nodes on distant metastasis-free survival in patients with high-risk squamous cell carcinoma. *Eur J Cancer* **111**, 107-115 (2019).
6. Merz, S.F., Jansen, P.*, Ulankiewicz, R, Bornemann, L., Schimming, T., Griewank, K., Cibir, Z., Stoffels, I., Aspelmeier, T., Brandau, S., Schadendorf, D., Hadaschik, E., Ebel, G., Gunzer, M., Klode, J. In preparation: Identification and quantification of hidden melanoma metastases in human sen-tinel lymph nodes using light sheet fluorescence microscopy.
7. Parkin, J. & Cohen, B. An overview of the immune system. *The Lancet* **357**, 1777-1789 (2001).
8. Riera Romo, M., Pérez-Martínez, D. & Castillo Ferrer, C. Innate immunity in vertebrates: an overview. *Immunology* **148**, 125-139 (2016).
9. Medzhitov, R. & Janeway, C. Innate Immunity. *New England Journal of Medicine* **343**, 338-344 (2000).
10. Neefjes, J., Jongsma, M.L., Paul, P. & Bakke, O. Towards a systems understanding of MHC class I and MHC class II antigen presentation. *Nat Rev Immunol* **11**, 823-836 (2011).
11. Netea, M.G. Training innate immunity: the changing concept of immunological memory in innate host defence. *European Journal of Clinical Investigation* **43**, 881-884 (2013).
12. Kolaczkowska, E. & Kubes, P. Neutrophil recruitment and function in health and inflammation. *Nature Reviews Immunology* **13**, 159-175 (2013).
13. Actor, J.K. 2 - Cells and Organs of the Immune System. in *Elsevier's Integrated Review Immunology and Microbiology (Second Edition)* (ed. Actor, J.K.) 7-16 (W.B. Saunders, Philadelphia, 2012). Available from: http://www.sciencedirect.com/science/article/pii/B9780323074476000028
14. Hidalgo, A., Chilvers, E.R., Summers, C. & Koenderman, L. The Neutrophil Life Cycle. *Trends in Immunology* **40**, 584-597 (2019).
15. Lee, P.Y., Wang, J.-X., Parisini, E., Dascher, C.C. & Nigrovic, P.A. Ly6 family proteins in neutrophil biology. *Journal of Leukocyte Biology* **94**, 585-594 (2013).
16. Wang, J.-X., *et al.* Ly6G ligation blocks recruitment of neutrophils via a β2-integrin–dependent mechanism. *Blood* **120**, 1489-1498 (2012).
17. Torsteinsdóttir, Arvidson, Hällgren & Håkansson. Enhanced Expression of Integrins and CD66b on Peripheral Blood Neutrophils and Eosinophils in Patients with Rheumatoid Arthritis, and the Effect of Glucocorticoids. *Scandinavian Journal of Immunology* **50**, 433-439 (1999).
18. Skubitz, K.M., Campbell, K.D. & Skubitz, A.P. CD66a, CD66b, CD66c, and CD66d each independently stimulate neutrophils. *J Leukoc Biol* **60**, 106-117 (1996).
19. Bonsor, D.A., Günther, S., Beadenkopf, R., Beckett, D. & Sundberg, E.J. Diverse oligomeric states of CEACAM IgV domains. *Proceedings of the National Academy of Sciences of the United States of America* **112**, 13561-13566 (2015).
20. Casanova-Acebes, M., *et al.* Neutrophils instruct homeostatic and pathological states in naive tissues. *The Journal of experimental medicine* **215**, 2778-2795 (2018).
21. Brazil, T.J., *et al.* Kinetics of pulmonary neutrophil recruitment and clearance in a natural and spontaneously resolving model of airway inflammation. *Clin Exp Allergy* **35**, 854-865 (2005).
22. Summers, C., *et al.* Neutrophil kinetics in health and disease. *Trends in Immunology* **31**, 318-324 (2010).
23. Lieschke, G.J., *et al.* Mice lacking granulocyte colony-stimulating factor have chronic neutropenia, granulocyte and macrophage progenitor cell deficiency, and impaired neutrophil mobilization. *Blood* **84**, 1737-1746 (1994).
24. Stark, M.A., *et al.* Phagocytosis of apoptotic neutrophils regulates granulopoiesis via IL-23 and IL-17. *Immunity* **22**, 285-294 (2005).
25. Köhler, A., *et al.* G-CSF-mediated thrombopoietin release triggers neutrophil motility and mobilization from bone marrow via induction of Cxcr2 ligands. *Blood* **117**, 4349-4357 (2011).

26. Ley, K., Laudanna, C., Cybulsky, M.I. & Nourshargh, S. Getting to the site of inflammation: the leukocyte adhesion cascade updated. *Nat Rev Immunol* **7**, 678-689 (2007).
27. Guyer, D.A.*, et al.* P-selectin glycoprotein ligand-1 (PSGL-1) is a ligand for L-selectin in neutrophil aggregation. *Blood* **88**, 2415-2421 (1996).
28. Barthel, S.R., Gavino, J.D., Descheny, L. & Dimitroff, C.J. Targeting selectins and selectin ligands in inflammation and cancer. *Expert Opin Ther Targets* **11**, 1473-1491 (2007).
29. Christofidou-Solomidou, M., Nakada, M.T., Williams, J., Muller, W.A. & DeLisser, H.M. Neutrophil platelet endothelial cell adhesion molecule-1 participates in neutrophil recruitment at inflammatory sites and is down-regulated after leukocyte extravasation. *J Immunol* **158**, 4872-4878 (1997).
30. Fornasa, G.*, et al.* TCR stimulation drives cleavage and shedding of the ITIM receptor CD31. *J Immunol* **184**, 5485-5492 (2010).
31. Williams, M.R., Azcutia, V., Newton, G., Alcaide, P. & Luscinskas, F.W. Emerging mechanisms of neutrophil recruitment across endothelium. *Trends Immunol* **32**, 461-469 (2011).
32. Brinkmann, V.*, et al.* Neutrophil extracellular traps kill bacteria. *Science* **303**, 1532-1535 (2004).
33. Silk, E., Zhao, H., Weng, H. & Ma, D. The role of extracellular histone in organ injury. *Cell Death Dis* **8**, e2812 (2017).
34. Singh, R.K.*, et al.* Excess histone levels mediate cytotoxicity via multiple mechanisms. *Cell Cycle* **9**, 4236-4244 (2010).
35. Chen, G.Y. & Nuñez, G. Sterile inflammation: sensing and reacting to damage. *Nature Reviews Immunology* **10**, 826-837 (2010).
36. Jablonska, J., Leschner, S., Westphal, K., Lienenklaus, S. & Weiss, S. Neutrophils responsive to endogenous IFN-beta regulate tumor angiogenesis and growth in a mouse tumor model. *The Journal of clinical investigation* **120**, 1151-1164 (2010).
37. Seignez, C. & Phillipson, M. The multitasking neutrophils and their involvement in angiogenesis. *Curr Opin Hematol* **24**, 3-8 (2017).
38. Kong, D.-H., Kim, Y.K., Kim, M.R., Jang, J.H. & Lee, S. Emerging Roles of Vascular Cell Adhesion Molecule-1 (VCAM-1) in Immunological Disorders and Cancer. *International journal of molecular sciences* **19**, 1057 (2018).
39. Hampton, H.R. & Chtanova, T. The lymph node neutrophil. *Seminars in Immunology* **28**, 129-136 (2016).
40. Fridlender, Z.G.*, et al.* Polarization of tumor-associated neutrophil phenotype by TGF-beta: "N1" versus "N2" TAN. *Cancer Cell* **16**, 183-194 (2009).
41. Tsuda, Y.*, et al.* Three different neutrophil subsets exhibited in mice with different susceptibilities to infection by methicillin-resistant Staphylococcus aureus. *Immunity* **21**, 215-226 (2004).
42. Wang, J. Neutrophils in tissue injury and repair. *Cell Tissue Res* **371**, 531-539 (2018).
43. Puhl, S.-L. & Steffens, S. Neutrophils in Post-myocardial Infarction Inflammation: Damage vs. Resolution? *Front Cardiovasc Med* **6**, 25-25 (2019).
44. Eurostat. Statistics Explained - Cardiovascular disease statistics. 2018. Last accessed: 15.10.2019. Available from: https://ec.europa.eu/eurostat/statistics-explained/pdfscache/37359.pdf
45. Reed, G.W., Rossi, J.E. & Cannon, C.P. Acute myocardial infarction. *The Lancet* **389**, 197-210 (2017).
46. Frohlich, G.M., Meier, P., White, S.K., Yellon, D.M. & Hausenloy, D.J. Myocardial reperfusion injury: looking beyond primary PCI. *Eur Heart J* **34**, 1714-1722 (2013).
47. Totzeck, M., Hendgen-Cotta, U.B., French, B.A. & Rassaf, T. A practical approach to remote ischemic preconditioning and ischemic preconditioning against myocardial ischemia/reperfusion injury. *J Biol Methods* **3**(2016).
48. Vinten-Johansen, J. Involvement of neutrophils in the pathogenesis of lethal myocardial reperfusion injury. *Cardiovascular Research* **61**, 481-497 (2004).
49. Prabhu, S.D. & Frangogiannis, N.G. The Biological Basis for Cardiac Repair After Myocardial Infarction: From Inflammation to Fibrosis. *Circ Res* **119**, 91-112 (2016).
50. Land, W.G. The Role of Damage-Associated Molecular Patterns (DAMPs) in Human Diseases: Part II: DAMPs as diagnostics, prognostics and therapeutics in clinical medicine. *Sultan Qaboos Univ Med J* **15**, e157-e170 (2015).
51. Casanova-Acebes, M.*, et al.* Rhythmic modulation of the hematopoietic niche through neutrophil clearance. *Cell* **153**, 1025-1035 (2013).
52. Schloss, M.J.*, et al.* The time-of-day of myocardial infarction onset affects healing through oscillations in cardiac neutrophil recruitment. *EMBO Mol Med* **8**, 937-948 (2016).

53. Suarez-Barrientos, A.*, et al.* Circadian variations of infarct size in acute myocardial infarction. *Heart* **97**, 970-976 (2011).
54. Jolly, S.R.*, et al.* Reduction of myocardial infarct size by neutrophil depletion: effect of duration of occlusion. *Am Heart J* **112**, 682-690 (1986).
55. Horckmans, M.*, et al.* Neutrophils orchestrate post-myocardial infarction healing by polarizing macrophages towards a reparative phenotype. *Eur Heart J* **38**, 187-197 (2017).
56. Ngoenkam, J., Schamel, W.W. & Pongcharoen, S. Selected signalling proteins recruited to the T-cell receptor-CD3 complex. *Immunology* **153**, 42-50 (2018).
57. Forthal, D.N. Functions of Antibodies. *Microbiol Spectr* **2**, 1-17 (2014).
58. Heesters, B.A., Myers, R.C. & Carroll, M.C. Follicular dendritic cells: dynamic antigen libraries. *Nature Reviews Immunology* **14**, 495 (2014).
59. Methot, S.P. & Di Noia, J.M. Chapter Two - Molecular Mechanisms of Somatic Hypermutation and Class Switch Recombination. in *Advances in Immunology*, Vol. 133 (ed. Alt, F.W.) 37-87 (Academic Press, 2017). Available from: http://www.sciencedirect.com/science/article/pii/S0065277616300530
60. Klein, F.*, et al.* Somatic Mutations of the Immunoglobulin Framework Are Generally Required for Broad and Potent HIV-1 Neutralization. *Cell* **153**, 126-138 (2013).
61. Sallusto, F., Lenig, D., Forster, R., Lipp, M. & Lanzavecchia, A. Two subsets of memory T lymphocytes with distinct homing potentials and effector functions. *Nature* **401**, 708-712 (1999).
62. Lopez, J.A.*, et al.* Perforin forms transient pores on the target cell plasma membrane to facilitate rapid access of granzymes during killer cell attack. *Blood* **121**, 2659-2668 (2013).
63. Halle, S., Halle, O. & Förster, R. Mechanisms and Dynamics of T Cell-Mediated Cytotoxicity In Vivo. *Trends in Immunology* **38**, 432-443 (2017).
64. Rousalova, I. & Krepela, E. Granzyme B-induced apoptosis in cancer cells and its regulation (review). *Int J Oncol* **37**, 1361-1378 (2010).
65. National Cancer Institute. NCI Dictionary - Tumor. Last accessed: 23.10.2019. Available from: https://www.cancer.gov/publications/dictionaries/cancer-terms/def/tumor
66. National Cancer Institute. NCI Dictionary - Cancer. Last accessed: 23.10.2019. Available from: https://www.cancer.gov/publications/dictionaries/cancer-terms/def/cancer
67. Hannah Ritchie, M.R. Our World in Data. Causes of Death. 2018. Last accessed: 23.10.2019. Available from: https://ourworldindata.org/causes-of-death
68. A, S. History of Cancer, Ancient and Modern Treatment Methods. *Journal of Cancer Science & Therapy* (2009).
69. Cohen, N., Fedewa, S. & Chen, A.Y. Epidemiology and Demographics of the Head and Neck Cancer Population. *Oral and Maxillofacial Surgery Clinics of North America* **30**, 381-395 (2018).
70. Davis, J. & Bordeaux, J. Squamous Cell Carcinoma. *JAMA Dermatology* **149**, 1448-1448 (2013).
71. Janes, S.M. & Watt, F.M. New roles for integrins in squamous-cell carcinoma. *Nat Rev Cancer* **6**, 175-183 (2006).
72. Wang, N.J.*, et al.* Loss-of-function mutations in Notch receptors in cutaneous and lung squamous cell carcinoma. *Proceedings of the National Academy of Sciences* **108**, 17761-17766 (2011).
73. National Cancer Institute - Surveillance, Epidemiology, and End Results Program. Cancer Stat Facts: Laryngeal Cancer. Last accessed: 22.10.2019. Available from: https://seer.cancer.gov/statfacts/html/laryn.html
74. National Cancer Institute - Surveillance, Epidemiology, and End Results Program. Cancer Stat Facts: Oral Cavity and Pharynx Cancer. Last accessed: 22.10.2019. Available from: https://seer.cancer.gov/statfacts/html/oralcav.html
75. WHO. CANCER TODAY. 2018. Last accessed: 18.10.2019. Available from: http://gco.iarc.fr/today/
76. Whiteman, D.C., Green, A.C. & Olsen, C.M. The Growing Burden of Invasive Melanoma: Projections of Incidence Rates and Numbers of New Cases in Six Susceptible Populations through 2031. *J Invest Dermatol* **136**, 1161-1171 (2016).
77. Siegel, R.L., Miller, K.D. & Jemal, A. Cancer statistics, 2017. *CA: A Cancer Journal for Clinicians* **67**, 7-30 (2017).
78. Schadendorf, D.*, et al.* Melanoma. *Lancet* **392**, 971-984 (2018).
79. Cichorek, M., Wachulska, M., Stasiewicz, A. & Tymińska, A. Skin melanocytes: biology and development. *Postepy Dermatol Alergol* **30**, 30-41 (2013).
80. Fitzpatrick, T.B. & Breathnach, A.S. [THE EPIDERMAL MELANIN UNIT SYSTEM]. *Dermatol Wochenschr* **147**, 481-489 (1963).

81. Jimbow, K., Roth, S.I., Fitzpatrick, T.B. & Szabo, G. Mitotic activity in non-neoplastic melanocytes in vivo as determined by histochemical, autoradiographic, and electron microscope studies. *J Cell Biol* **66**, 663-670 (1975).
82. Weinstein, D., Leininger, J., Hamby, C. & Safai, B. Diagnostic and prognostic biomarkers in melanoma. *J Clin Aesthet Dermatol* **7**, 13-24 (2014).
83. Hanahan, D. & Weinberg, R.A. The Hallmarks of Cancer. *Cell* **100**, 57-70 (2000).
84. Hanahan, D. & Weinberg, Robert A. Hallmarks of Cancer: The Next Generation. *Cell* **144**, 646-674 (2011).
85. Passarelli, A., Mannavola, F., Stucci, L.S., Tucci, M. & Silvestris, F. Immune system and melanoma biology: a balance between immunosurveillance and immune escape. *Oncotarget* **8**, 106132-106142 (2017).
86. Alexandrov, L.B.*, et al.* Signatures of mutational processes in human cancer. *Nature* **500**, 415-421 (2013).
87. Schumacher, T.N. & Schreiber, R.D. Neoantigens in cancer immunotherapy. *Science* **348**, 69 (2015).
88. Al-Shibli, K.I.*, et al.* Prognostic Effect of Epithelial and Stromal Lymphocyte Infiltration in Non–Small Cell Lung Cancer. *Clinical Cancer Research* **14**, 5220 (2008).
89. Lee, N., Zakka, L.R., Mihm, M.C. & Schatton, T. Tumour-infiltrating lymphocytes in melanoma prognosis and cancer immunotherapy. *Pathology* **48**, 177-187 (2016).
90. Geukes Foppen, M.H., Donia, M., Svane, I.M. & Haanen, J.B.A.G. Tumor-infiltrating lymphocytes for the treatment of metastatic cancer. *Mol Oncol* **9**, 1918-1935 (2015).
91. Davoodzadeh Gholami, M.*, et al.* Exhaustion of T lymphocytes in the tumor microenvironment: Significance and effective mechanisms. *Cellular Immunology* **322**, 1-14 (2017).
92. Maeurer, M.J.*, et al.* Tumor escape from immune recognition: lethal recurrent melanoma in a patient associated with downregulation of the peptide transporter protein TAP-1 and loss of expression of the immunodominant MART-1/Melan-A antigen. *J Clin Invest* **98**, 1633-1641 (1996).
93. Fujita, Y.*, et al.* Prognostic significance of interleukin-8 and CD163-positive cell-infiltration in tumor tissues in patients with oral squamous cell carcinoma. *PLoS One* **9**, e110378 (2014).
94. Sasahira, T. & Kirita, T. Hallmarks of Cancer-Related Newly Prognostic Factors of Oral Squamous Cell Carcinoma. *International journal of molecular sciences* **19**, 2413 (2018).
95. Failli, A., Legitimo, A., Orsini, G., Romanini, A. & Consolini, R. Numerical defect of circulating dendritic cell subsets and defective dendritic cell generation from monocytes of patients with advanced melanoma. *Cancer Lett* **337**, 184-192 (2013).
96. Hussein, M.R. Dendritic cells and melanoma tumorigenesis: an insight. *Cancer Biol Ther* **4**, 501-505 (2005).
97. Garcia-Diaz, A.*, et al.* Interferon Receptor Signaling Pathways Regulating PD-L1 and PD-L2 Expression. *Cell Rep* **19**, 1189-1201 (2017).
98. Shaul, M.E. & Fridlender, Z.G. Tumour-associated neutrophils in patients with cancer. *Nature Reviews Clinical Oncology* **16**, 601-620 (2019).
99. Gajewski, T.F., Schreiber, H. & Fu, Y.X. Innate and adaptive immune cells in the tumor microenvironment. *Nat Immunol* **14**, 1014-1022 (2013).
100. Shen, M.*, et al.* Tumor-associated neutrophils as a new prognostic factor in cancer: a systematic review and meta-analysis. *PLoS One* **9**, e98259 (2014).
101. Carus, A., Ladekarl, M., Hager, H., Nedergaard, B.S. & Donskov, F. Tumour-associated CD66b+ neutrophil count is an independent prognostic factor for recurrence in localised cervical cancer. *Br J Cancer* **108**, 2116-2122 (2013).
102. Rao, H.L.*, et al.* Increased intratumoral neutrophil in colorectal carcinomas correlates closely with malignant phenotype and predicts patients' adverse prognosis. *PLoS One* **7**, e30806 (2012).
103. Coffelt, S.B., Wellenstein, M.D. & de Visser, K.E. Neutrophils in cancer: neutral no more. *Nat Rev Cancer* **16**, 431-446 (2016).
104. Granot, Z.*, et al.* Tumor entrained neutrophils inhibit seeding in the premetastatic lung. *Cancer Cell* **20**, 300-314 (2011).
105. Gerrard, T.L., Cohen, D.J. & Kaplan, A.M. Human neutrophil-mediated cytotoxicity to tumor cells. *J Natl Cancer Inst* **66**, 483-488 (1981).
106. Sionov, R.V., Fridlender, Z.G. & Granot, Z. The Multifaceted Roles Neutrophils Play in the Tumor Microenvironment. *Cancer Microenviron* **8**, 125-158 (2015).
107. Andzinski, L.*, et al.* Type I IFNs induce anti-tumor polarization of tumor associated neutrophils in mice and human. *Int J Cancer* **138**, 1982-1993 (2016).

108. Brandau, S., Moses, K. & Lang, S. The kinship of neutrophils and granulocytic myeloid-derived suppressor cells in cancer: cousins, siblings or twins? *Semin Cancer Biol* **23**, 171-182 (2013).
109. Damuzzo, V.*, et al.* Complexity and challenges in defining myeloid-derived suppressor cells. *Cytometry B Clin Cytom* **88**, 77-91 (2015).
110. Condamine, T.*, et al.* Lectin-type oxidized LDL receptor-1 distinguishes population of human polymorphonuclear myeloid-derived suppressor cells in cancer patients. *Sci Immunol* **1**(2016).
111. Mishalian, I.*, et al.* Neutrophils recruit regulatory T-cells into tumors via secretion of CCL17--a new mechanism of impaired antitumor immunity. *Int J Cancer* **135**, 1178-1186 (2014).
112. Zhou, S.L.*, et al.* Tumor-Associated Neutrophils Recruit Macrophages and T-Regulatory Cells to Promote Progression of Hepatocellular Carcinoma and Resistance to Sorafenib. *Gastroenterology* **150**, 1646-1658.e1617 (2016).
113. Munder, M.*, et al.* Suppression of T-cell functions by human granulocyte arginase. *Blood* **108**, 1627-1634 (2006).
114. Lang, S.*, et al.* Clinical Relevance and Suppressive Capacity of Human Myeloid-Derived Suppressor Cell Subsets. *Clin Cancer Res* **24**, 4834-4844 (2018).
115. Munder, M.*, et al.* Suppression of T-cell functions by human granulocyte arginase. *Blood* **108**, 1627-1634 (2006).
116. Berry, R.S.*, et al.* High levels of tumor-associated neutrophils are associated with improved overall survival in patients with stage II colorectal cancer. *PLoS One* **12**, e0188799 (2017).
117. Dumitru, C.A., Fechner, M.K., Hoffmann, T.K., Lang, S. & Brandau, S. A novel p38-MAPK signaling axis modulates neutrophil biology in head and neck cancer. *J Leukoc Biol* **91**, 591-598 (2012).
118. Kalluri, R. & Weinberg, R.A. The basics of epithelial-mesenchymal transition. *The Journal of clinical investigation* **119**, 1420-1428 (2009).
119. Gershenwald, J.E.*, et al.* Melanoma staging: Evidence-based changes in the American Joint Committee on Cancer eighth edition cancer staging manual. *CA Cancer J Clin* **67**, 472-492 (2017).
120. Clark, W.H.*, et al.* A study of tumor progression: The precursor lesions of superficial spreading and nodular melanoma. *Human Pathology* **15**, 1147-1165 (1984).
121. Damsky, W.E., Theodosakis, N. & Bosenberg, M. Melanoma metastasis: new concepts and evolving paradigms. *Oncogene* **33**, 2413-2422 (2014).
122. Balch, C.M.*, et al.* Final version of 2009 AJCC melanoma staging and classification. *J Clin Oncol* **27**, 6199-6206 (2009).
123. Ossowski, L. & Aguirre-Ghiso, J.A. Dormancy of metastatic melanoma. *Pigment Cell Melanoma Res* **23**, 41-56 (2010).
124. Reintgen, D.S., McCarty, K.S., Woodard, B., Cox, E. & Seigler, H.F. Metastatic malignant melanoma with an unknown primary. *Surg Gynecol Obstet* **156**, 335-340 (1983).
125. Bautista, N.C., Cohen, S. & Anders, K.H. Benign melanocytic nevus cells in axillary lymph nodes. A prospective incidence and immunohistochemical study with literature review. *Am J Clin Pathol* **102**, 102-108 (1994).
126. McCarthy, S.W., Palmer, A.A., Bale, P.M. & Hirst, E. Naevus cells in lymph nodes. *Pathology* **6**, 351-358 (1974).
127. Breslow, A. Thickness, cross-sectional areas and depth of invasion in the prognosis of cutaneous melanoma. *Ann Surg* **172**, 902-908 (1970).
128. Miller, K.D.*, et al.* Cancer treatment and survivorship statistics, 2016. *CA Cancer J Clin* **66**, 271-289 (2016).
129. American Cancer Society. Survival Rates for Melanoma Skin Cancer. Patients diagnosed 2008 - 20014. Last accessed: 21.10.2019. Available from: https://www.cancer.org/cancer/melanoma-skin-cancer/detection-diagnosis-staging/survival-rates-for-melanoma-skin-cancer-by-stage.html
130. Stoffels, I.*, et al.* Sentinel lymph node excision with or without preoperative hybrid single-photon emission computed tomography/computed tomography (SPECT/CT) in melanoma: study protocol for a multicentric randomized controlled trial. *Trials* **20**, 99 (2019).
131. Postow, M.A., Callahan, M.K. & Wolchok, J.D. Immune Checkpoint Blockade in Cancer Therapy. *Journal of clinical oncology : official journal of the American Society of Clinical Oncology* **33**, 1974-1982 (2015).
132. Freeman, G.J.*, et al.* Engagement of the PD-1 immunoinhibitory receptor by a novel B7 family member leads to negative regulation of lymphocyte activation. *J Exp Med* **192**, 1027-1034 (2000).

133. Eggermont, A.M., *et al.* Prolonged Survival in Stage III Melanoma with Ipilimumab Adjuvant Therapy. *N Engl J Med* **375**, 1845-1855 (2016).
134. Weber, J., *et al.* Adjuvant Nivolumab versus Ipilimumab in Resected Stage III or IV Melanoma. *New England Journal of Medicine* **377**, 1824-1835 (2017).
135. Welch, H.G., Woloshin, S. & Schwartz, L.M. Skin biopsy rates and incidence of melanoma: population based ecological study. *Bmj* **331**, 481 (2005).
136. Stang, A., Jockel, K.H. & Heidinger, O. Skin cancer rates in North Rhine-Westphalia, Germany before and after the introduction of the nationwide skin cancer screening program (2000-2015). *Eur J Epidemiol* **33**, 303-312 (2018).
137. Morton, D.L., *et al.* Final trial report of sentinel-node biopsy versus nodal observation in melanoma. *N Engl J Med* **370**, 599-609 (2014).
138. Morton, D.L., *et al.* Sentinel node biopsy for early-stage melanoma: Accuracy and morbidity in MSLT-I, an international multicenter trial. *Annals of Surgery* **242**, 302-313 (2005).
139. Garbe, C., *et al.* Diagnosis and treatment of melanoma. European consensus-based interdisciplinary guideline – Update 2016. *European Journal of Cancer* **63**, 201-217 (2016).
140. Chakera, A.H., *et al.* EANM-EORTC general recommendations for sentinel node diagnostics in melanoma. *Eur J Nucl Med Mol Imaging* **36**, 1713-1742 (2009).
141. Gershenwald, J.E., *et al.* Melanoma staging: Evidence-based changes in the American Joint Committee on Cancer eighth edition cancer staging manual. *CA Cancer J Clin* **67**, 472-492 (2017).
142. Melanoma Focus. The Current Role of Sentinel Lymph Node Biopsy in the Management of Cutaneous Melanoma – a UK Consensus Statement. 2018. Last accessed: 21.10.2019. Available from: https://melanomafocus.com/wp-content/uploads/2019/01/SNB-Consensus-Final-1.pdf
143. Nieweg, O.E. False-Negative Sentinel Node Biopsy. *Annals of Surgical Oncology* **16**, 2089-2091 (2009).
144. Furia, L., Pelicci, P. & Faretta, M. Confocal microscopy for high-resolution and high-content analysis of the cell cycle. *Curr Protoc Cytom* **70**, 7.42.41-14 (2014).
145. Theer, P., Hasan, M.T. & Denk, W. Two-photon imaging to a depth of 1000 microm in living brains by use of a Ti:Al2O3 regenerative amplifier. *Opt Lett* **28**, 1022-1024 (2003).
146. Helmchen, F. & Denk, W. Deep tissue two-photon microscopy. *Nature Methods* **2**, 932-940 (2005).
147. Siedentopf, H. & Zsigmondy, R. Über Sichtbarmachung und Größenbestimmung ultramikroskopischer Teilchen, mit besonderer Anwendung auf Goldrubingläser. *Annalen der Physik 10*, 1-39 (1903).
148. Huisken, J., Swoger, J., Del Bene, F., Wittbrodt, J. & Stelzer, E.H. Optical sectioning deep inside live embryos by selective plane illumination microscopy. *Science* **305**, 1007-1009 (2004).
149. Schroer, U. UltraMicroscope is the most successful commercial light sheet system for high impact publications. *UltraMicroscope: Applications & Literature*, 1-8 (2017).
150. Richardson, Douglas S. & Lichtman, Jeff W. Clarifying Tissue Clearing. *Cell* **162**, 246-257 (2015).
151. Power, R.M. & Huisken, J. A guide to light-sheet fluorescence microscopy for multiscale imaging. *Nature Methods* **14**, 360-373 (2017).
152. Mellish, B. Wikipedia. Rayleigh length. Last accessed: 12.11.2019. Available from: https://en.wikipedia.org/wiki/Rayleigh_length#/media/File:GaussianBeamWaist.svg
153. Ralston, T.S., Marks, D.L., Carney, P.S. & Boppart, S.A. Inverse scattering for optical coherence tomography. *J. Opt. Soc. Am. A* **23**, 1027-1037 (2006).
154. Liang, X.J., Liu, A.Q., Lim, C.S., Ayi, T.C. & Yap, P.H. Determining refractive index of single living cell using an integrated microchip. *Sensors and Actuators A: Physical* **133**, 349-354 (2007).
155. Hua, L., Zhou, R., Thirumalai, D. & Berne, B.J. Urea denaturation by stronger dispersion interactions with proteins than water implies a 2-stage unfolding. *Proceedings of the National Academy of Sciences of the United States of America* **105**, 16928-16933 (2008).
156. Hama, H., *et al.* Scale: a chemical approach for fluorescence imaging and reconstruction of transparent mouse brain. *Nature neuroscience* **14**, 1481-1488 (2011).
157. Chen, F., Tillberg, P.W. & Boyden, E.S. Expansion microscopy. *Science* **347**, 543-548 (2015).
158. Susaki, Etsuo A. & Ueda, Hiroki R. Whole-body and Whole-Organ Clearing and Imaging Techniques with Single-Cell Resolution: Toward Organism-Level Systems Biology in Mammals. *Cell Chemical Biology* **23**, 137-157 (2016).

159. Chung, K.*, et al.* Structural and molecular interrogation of intact biological systems. *Nature* **497**, 332-337 (2013).
160. Erturk, A.*, et al.* Three-dimensional imaging of solvent-cleared organs using 3DISCO. *Nature protocols* **7**, 1983-1995 (2012).
161. Klingberg, A.*, et al.* Fully Automated Evaluation of Total Glomerular Number and Capillary Tuft Size in Nephritic Kidneys Using Lightsheet Microscopy. *J Am Soc Nephrol* **28**, 452-459 (2017).
162. Renier, N.*, et al.* iDISCO: a simple, rapid method to immunolabel large tissue samples for volume imaging. *Cell* **159**, 896-910 (2014).
163. Dodt, H.U.*, et al.* Ultramicroscopy: three-dimensional visualization of neuronal networks in the whole mouse brain. *Nat Methods* **4**, 331-336 (2007).
164. Costa, E.C., Silva, D.N., Moreira, A.F. & Correia, I.J. Optical clearing methods: An overview of the techniques used for the imaging of 3D spheroids. *Biotechnology and Bioengineering* **116**, 2742-2763 (2019).
165. Spalteholz. Über das Durchsichtigmachen von menschlichen und tierischen Präparaten und seine theoretischen Bedingungen: Nebst Anhang: Über Knochenfärbung. *Leipzig: Hirzel* (1914).
166. Voie, A.H., Burns, D.H. & Spelman, F.A. Orthogonal-plane fluorescence optical sectioning: three-dimensional imaging of macroscopic biological specimens. *J Microsc* **170**, 229-236 (1993).
167. Livet, J.*, et al.* Transgenic strategies for combinatorial expression of fluorescent proteins in the nervous system. *Nature* **450**, 56-62 (2007).
168. Masselink, W.*, et al.* Broad applicability of a streamlined ethyl cinnamate-based clearing procedure. *Development (Cambridge, England)* **146**(2019).
169. Sakaguchi, R., Leiwe, M.N. & Imai, T. Bright multicolor labeling of neuronal circuits with fluorescent proteins and chemical tags. *Elife* **7**(2018).
170. Cai, R.*, et al.* Panoptic imaging of transparent mice reveals whole-body neuronal projections and skull-meninges connections. *Nature neuroscience* **22**, 317-327 (2019).
171. Belle, M.*, et al.* Tridimensional Visualization and Analysis of Early Human Development. *Cell* **169**, 161-173 e112 (2017).
172. Puelles, V.G.*, et al.* Novel 3D analysis using optical tissue clearing documents the evolution of murine rapidly progressive glomerulonephritis. *Kidney Int* **96**, 505-516 (2019).
173. Bedossa, P., Dargere, D. & Paradis, V. Sampling variability of liver fibrosis in chronic hepatitis C. *Hepatology* **38**, 1449-1457 (2003).
174. Roberts, N.*, et al.* Toward routine use of 3D histopathology as a research tool. *Am J Pathol* **180**, 1835-1842 (2012).
175. Nojima, S.*, et al.* CUBIC pathology: three-dimensional imaging for pathological diagnosis. *Scientific Reports* **7**, 9269 (2017).
176. Glaser, A.K.*, et al.* Light-sheet microscopy for slide-free non-destructive pathology of large clinical specimens. *Nature Biomedical Engineering* **1**, 0084 (2017).
177. Abadie, S.*, et al.* 3D imaging of cleared human skin biopsies using light-sheet microscopy: A new way to visualize in-depth skin structure. *Skin Res Technol* **24**, 294-303 (2018).
178. Tanaka, N.*, et al.* Mapping of the three-dimensional lymphatic microvasculature in bladder tumours using light-sheet microscopy. *British Journal of Cancer* **118**, 995-999 (2018).
179. Poola, P.K., Afzal, M.I., Yoo, Y., Kim, K.H. & Chung, E. Light sheet microscopy for histopathology applications. *Biomed Eng Lett* **9**, 279-291 (2019).
180. van der Woude, L.L., Gorris, M.A.J., Halilovic, A., Figdor, C.G. & de Vries, I.J.M. Migrating into the Tumor: a Roadmap for T Cells. *Trends Cancer* **3**, 797-808 (2017).
181. Moses, W.W. Fundamental Limits of Spatial Resolution in PET. *Nucl Instrum Methods Phys Res A* **648 Supplement 1**, S236-S240 (2011).
182. van Akkooi, A.C., Spatz, A., Eggermont, A.M., Mihm, M. & Cook, M.G. Expert opinion in melanoma: the sentinel node; EORTC Melanoma Group recommendations on practical methodology of the measurement of the microanatomic location of metastases and metastatic tumour burden. *Eur J Cancer* **45**, 2736-2742 (2009).
183. Dewar, D.J.*, et al.* The microanatomic location of metastatic melanoma in sentinel lymph nodes predicts nonsentinel lymph node involvement. *J Clin Oncol* **22**, 3345-3349 (2004).
184. van Akkooi, A.C.J., Spatz, A., Eggermont, A.M.M., Mihm, M. & Cook, M.G. Expert opinion in melanoma: The sentinel node; EORTC Melanoma Group recommendations on practical methodology of the measurement of the microanatomic location of metastases and metastatic tumour burden. *European Journal of Cancer* **45**, 2736-2742 (2009).
185. Muller, S., Zhao, Y., Brown, T.L., Morgan, A.C. & Kohler, H. TransMabs: cell-penetrating antibodies, the next generation. *Expert Opin Biol Ther* **5**, 237-241 (2005).

186. Li, Z.*, et al.* Influence of molecular size on tissue distribution of antibody fragments. *MAbs* **8**, 113-119 (2016).
187. Shah, D.K. & Betts, A.M. Antibody biodistribution coefficients: inferring tissue concentrations of monoclonal antibodies based on the plasma concentrations in several preclinical species and human. *MAbs* **5**, 297-305 (2013).
188. Aird, W.C. Phenotypic heterogeneity of the endothelium: I. Structure, function, and mechanisms. *Circ Res* **100**, 158-173 (2007).
189. Fung, K.Y.Y., Fairn, G.D. & Lee, W.L. Transcellular vesicular transport in epithelial and endothelial cells: Challenges and opportunities. *Traffic* **19**, 5-18 (2018).
190. Phillipson, M.*, et al.* Intraluminal crawling of neutrophils to emigration sites: a molecularly distinct process from adhesion in the recruitment cascade. *The Journal of experimental medicine* **203**, 2569-2575 (2006).
191. Phillipson, M., Kaur, J., Colarusso, P., Ballantyne, C.M. & Kubes, P. Endothelial domes encapsulate adherent neutrophils and minimize increases in vascular permeability in paracellular and transcellular emigration. *PloS one* **3**, e1649-e1649 (2008).
192. Benhar, I., London, A. & Schwartz, M. The privileged immunity of immune privileged organs: the case of the eye. *Frontiers in immunology* **3**, 296-296 (2012).
193. Diamond, B., Honig, G., Mader, S., Brimberg, L. & Volpe, B.T. Brain-reactive antibodies and disease. *Annu Rev Immunol* **31**, 345-385 (2013).
194. Stromnes, I.M.*, et al.* Targeted depletion of an MDSC subset unmasks pancreatic ductal adenocarcinoma to adaptive immunity. *Gut* **63**, 1769-1781 (2014).
195. Weber, F.C.*, et al.* Neutrophils are required for both the sensitization and elicitation phase of contact hypersensitivity. *The Journal of Experimental Medicine* **212**, 15 (2015).
196. Faget, J.*, et al.* Efficient and specific Ly6G⁺ cell depletion: A change in the current practices toward more relevant functional analyses of neutrophils. *bioRxiv*, 498881 (2018).
197. Tanaka, K.*, et al.* In vivo characterization of neutrophil extracellular traps in various organs of a murine sepsis model. *PLoS One* **9**, e111888 (2014).
198. Jamur, M.C. & Oliver, C. Permeabilization of cell membranes. *Methods Mol Biol* **588**, 63-66 (2010).
199. Gefen, A., Cornelissen, L.H., Gawlitta, D., Bader, D.L. & Oomens, C.W. The free diffusion of macromolecules in tissue-engineered skeletal muscle subjected to large compression strains. *J Biomech* **41**, 845-853 (2008).
200. Wang, Y.*, et al.* Nanobody-derived nanobiotechnology tool kits for diverse biomedical and biotechnology applications. *Int J Nanomedicine* **11**, 3287-3303 (2016).
201. Katoh, K., Kano, Y. & Ookawara, S. Microwave irradiation for fixation and immunostaining of endothelial cells in situ. *Biotech Histochem* **84**, 101-108 (2009).
202. Lee, E.*, et al.* ACT-PRESTO: Rapid and consistent tissue clearing and labeling method for 3-dimensional (3D) imaging. *Scientific reports* **6**, 18631-18631 (2016).
203. Reynaud, E.G., Peychl, J., Huisken, J. & Tomancak, P. Guide to light-sheet microscopy for adventurous biologists. *Nature Methods* **12**, 30 (2014).
204. Ibsen, P.H. The effect of formaldehyde, hydrogen peroxide and genetic detoxification of pertussis toxin on epitope recognition by murine monoclonal antibodies. *Vaccine* **14**, 359-368 (1996).
205. Liu, C.H.*, et al.* Melanin bleaching with dilute hydrogen peroxide: a simple and rapid method. *Appl Immunohistochem Mol Morphol* **21**, 275-279 (2013).
206. Chung, J.-Y.*, et al.* A melanin-bleaching methodology for molecular and histopathological analysis of formalin-fixed paraffin-embedded tissue. *Laboratory Investigation* **96**, 1116-1127 (2016).
207. Fernandes, B., Matamá, T., Guimarães, D., Gomes, A. & Cavaco-Paulo, A. Fluorescent quantification of melanin. *Pigment Cell & Melanoma Research* **29**, 707-712 (2016).
208. Kayatz, P.*, et al.* Oxidation causes melanin fluorescence. *Invest Ophthalmol Vis Sci* **42**, 241-246 (2001).
209. Huang, Z.*, et al.* Cutaneous melanin exhibiting fluorescence emission under near-infrared light excitation. *Journal of Biomedical Optics* **11**, 1-6, 6 (2006).
210. Stoffels, I.*, et al.* Metastatic status of sentinel lymph nodes in melanoma determined noninvasively with multispectral optoacoustic imaging. *Sci Transl Med* **7**, 317ra199 (2015).
211. Giacomelli, M.G.*, et al.* Virtual Hematoxylin and Eosin Transillumination Microscopy Using Epi-Fluorescence Imaging. *PLOS ONE* **11**, e0159337 (2016).

212. Oxford instruments - Imaris. Imaris Versions. Last accessed: 29.10.2019. Available from: https://imaris.oxinst.com/versions
213. Liu, L. & Shi, G.-P. CD31: beyond a marker for endothelial cells. *Cardiovascular Research* **94**, 3-5 (2012).
214. Bujan, J.*, et al.* Modulation of PECAM-1 (CD31) expression in human endothelial cells: effect of IFNgamma and IL-10. *J Vasc Res* **36**, 106-113 (1999).
215. Romer, L.H.*, et al.* IFN-gamma and TNF-alpha induce redistribution of PECAM-1 (CD31) on human endothelial cells. *J Immunol* **154**, 6582-6592 (1995).
216. Lugo-Hernandez, E.*, et al.* 3D visualization and quantification of microvessels in the whole ischemic mouse brain using solvent-based clearing and light sheet microscopy. *Journal of Cerebral Blood Flow & Metabolism* **37**, 3355-3367 (2017).
217. Hsieh, P.C.H., Davis, M.E., Lisowski, L.K. & Lee, R.T. Endothelial-cardiomyocyte interactions in cardiac development and repair. *Annu Rev Physiol* **68**, 51-66 (2006).
218. Botker, H.E.*, et al.* Practical guidelines for rigor and reproducibility in preclinical and clinical studies on cardioprotection. *Basic Res Cardiol* **113**, 39 (2018).
219. Russel, W. & Burch, R. *The principles of humane experimental technique.*, (Wheathampstead (UK): Universities Federation for Animal Welfare, 1959).
220. Tannenbaum, J. & Bennett, B.T. Russell and Burch's 3Rs then and now: the need for clarity in definition and purpose. *J Am Assoc Lab Anim Sci* **54**, 120-132 (2015).
221. Binnewies, M.*, et al.* Understanding the tumor immune microenvironment (TIME) for effective therapy. *Nature medicine* **24**, 541-550 (2018).
222. Fridman, W.H., Pages, F., Sautes-Fridman, C. & Galon, J. The immune contexture in human tumours: impact on clinical outcome. *Nat Rev Cancer* **12**, 298-306 (2012).
223. Al-Shibli, K.I.*, et al.* Prognostic effect of epithelial and stromal lymphocyte infiltration in non-small cell lung cancer. *Clin Cancer Res* **14**, 5220-5227 (2008).
224. Feng, Z.*, et al.* Multiparametric immune profiling in HPV- oral squamous cell cancer. *JCI Insight* **2**, e93652 (2017).
225. Mahmoud, S.M.*, et al.* Tumor-infiltrating CD8+ lymphocytes predict clinical outcome in breast cancer. *J Clin Oncol* **29**, 1949-1955 (2011).
226. Gentles, A.J.*, et al.* The prognostic landscape of genes and infiltrating immune cells across human cancers. *Nat Med* **21**, 938-945 (2015).
227. van Egmond, M. & Bakema, J.E. Neutrophils as effector cells for antibody-based immunotherapy of cancer. *Semin Cancer Biol* **23**, 190-199 (2013).
228. Ilie, M.*, et al.* Predictive clinical outcome of the intratumoral CD66b-positive neutrophil-to-CD8-positive T-cell ratio in patients with resectable nonsmall cell lung cancer. *Cancer* **118**, 1726-1737 (2012).
229. Condamine, T.*, et al.* Lectin-type oxidized LDL receptor-1 distinguishes population of human polymorphonuclear myeloid-derived suppressor cells in cancer patients. *Science immunology* **1**, aaf8943 (2016).
230. Moses, K. & Brandau, S. Human neutrophils: Their role in cancer and relation to myeloid-derived suppressor cells. *Semin Immunol* **28**, 187-196 (2016).
231. Evans, R.A.*, et al.* Lack of immunoediting in murine pancreatic cancer reversed with neoantigen. *JCI Insight* **1**, e88328 (2016).
232. Janeway CA Jr, Travers P & M, W. General properties of armed effector T cells. in *Immunobiology: The Immune System in Health and Disease* (New York: Garland Science, 2001). Available from: https://www.ncbi.nlm.nih.gov/books/NBK27149/
233. Whiteside, T.L. The tumor microenvironment and its role in promoting tumor growth. *Oncogene* **27**, 5904-5912 (2008).
234. Kuss, I., Saito, T., Johnson, J.T. & Whiteside, T.L. Clinical significance of decreased zeta chain expression in peripheral blood lymphocytes of patients with head and neck cancer. *Clin Cancer Res* **5**, 329-334 (1999).
235. Maimela, N.R., Liu, S. & Zhang, Y. Fates of CD8+ T cells in Tumor Microenvironment. *Comput Struct Biotechnol J* **17**, 1-13 (2018).
236. Singhal, S.*, et al.* Origin and Role of a Subset of Tumor-Associated Neutrophils with Antigen-Presenting Cell Features in Early-Stage Human Lung Cancer. *Cancer cell* **30**, 120-135 (2016).
237. van der Ploeg, A.P.*, et al.* Prognosis in patients with sentinel node-positive melanoma is accurately defined by the combined Rotterdam tumor load and Dewar topography criteria. *J Clin Oncol* **29**, 2206-2214 (2011).
238. Nagata, S., Suzuki, J., Segawa, K. & Fujii, T. Exposure of phosphatidylserine on the cell surface. *Cell Death Differ* **23**, 952-961 (2016).

239. Trenevska, I., Li, D. & Banham, A.H. Therapeutic Antibodies against Intracellular Tumor Antigens. *Front Immunol* **8**, 1001 (2017).
240. Ramjane, K., Han, L. & Jin, C. The diagnosis and treatment of the no-reflow phenomenon in patients with myocardial infarction undergoing percutaneous coronary intervention. *Exp Clin Cardiol* **13**, 121-128 (2008).
241. Kalogeris, T., Baines, C.P., Krenz, M. & Korthuis, R.J. Ischemia/Reperfusion. *Compr Physiol* **7**, 113-170 (2016).
242. Dewenter, M., Wagner, M. & El-Armouche, A. LATITUDE-TIMI: is there still hope for anti-inflammatory therapy in acute myocardial infaction? *Journal of Thoracic Disease* **8**, E1047-E1049 (2016).
243. Mocco, J.*, et al.* HuEP5C7 as a humanized monoclonal anti-E/P-selectin neurovascular protective strategy in a blinded placebo-controlled trial of nonhuman primate stroke. *Circ Res* **91**, 907-914 (2002).
244. Stahli, B.E.*, et al.* Effects of the P-Selectin Antagonist Inclacumab on Myocardial Damage After Percutaneous Coronary Intervention According to Timing of Infusion: Insights From the SELECT-ACS Trial. *J Am Heart Assoc* **5**(2016).
245. Sun, X. & Kaufman, P.D. Ki-67: more than a proliferation marker. *Chromosoma* **127**, 175-186 (2018).
246. Scholzen, T. & Gerdes, J. The Ki-67 protein: from the known and the unknown. *J Cell Physiol* **182**, 311-322 (2000).
247. Grossman, W.J.*, et al.* Differential expression of granzymes A and B in human cytotoxic ymphocyte subsets and T regulatory cells. *Blood* **104**, 2840-2848 (2004).
248. Goltsev, Y.*, et al.* Deep Profiling of Mouse Splenic Architecture with CODEX Multiplexed Imaging. *Cell* **174**, 968-981.e915 (2018).
249. Chao, T., Furth, E.E. & Vonderheide, R.H. CXCR2-Dependent Accumulation of Tumor-Associated Neutrophils Regulates T-cell Immunity in Pancreatic Ductal Adenocarcinoma. *Cancer Immunol Res* **4**, 968-982 (2016).
250. Lerch, M.L.*, et al.* Monitoring Dehydration and Clearing in Tissue Processing for High-Quality Clinical Pathology. *Biopreserv Biobank* **17**, 303-311 (2019).
251. Lobo, A.Z.*, et al.* The distribution of microscopic melanoma metastases in sentinel lymph nodes: implications for pathology protocols. *Am J Surg Pathol* **36**, 1841-1848 (2012).
252. van Akkooi, A.C.J.*, et al.* High positive sentinel node identification rate by EORTC melanoma group protocol: Prognostic indicators of metastatic patterns after sentinel node biopsy in melanoma. *European Journal of Cancer* **42**, 372-380 (2006).
253. Manca, G.*, et al.* Sentinel lymph node mapping in melanoma: the issue of false-negative findings. *Clin Nucl Med* **39**, e346-354 (2014).
254. Zahoor, S.*, et al.* Sentinel Lymph Node Biopsy in Breast Cancer: A Clinical Review and Update. *J Breast Cancer* **20**, 217-227 (2017).
255. Sharma, D., Koshy, G., Grover, S. & Sharma, B. Sentinel Lymph Node Biopsy: A new approach in the management of head and neck cancers. *Sultan Qaboos Univ Med J* **17**, e3-e10 (2017).
256. Resch, A. & Langner, C. Lymph node staging in colorectal cancer: old controversies and recent advances. *World J Gastroenterol* **19**, 8515-8526 (2013).
257. Dreyfuss, E. Wired. Want to Make It as a Biologist? Better Learn to Code. 2017. Last accessed: 30.10.2019. Available from: https://www.wired.com/2017/03/biologists-teaching-code-survive/
258. Leonelli, S. The challenges of big data biology. *eLife* **8**, e47381 (2019).

6. Appendix

6.1. Supplementary Material

6.1.1. Manuscript #3: LSFM in melanoma diagnostics - Unpublished

Supplementary material relating to

Identification and quantification of hidden melanoma metastases in human sentinel lymph nodes using light sheet fluorescence microscopy

Simon F. Merz[1-4,#], Philipp Jansen[2-4,#], Ricarda Ulankiewicz[2-4], Lea Bornemann[1], Tobias Schimming[2-4], Klaus Griewank[2-4], Zülal Cibir[1], Andreas Kraus[1], Ingo Stoffels[2-4], Timo Aspelmeier[5], Sven Brandau[6], Dirk Schadendorf[2-4], Eva Hadaschik[2-4], Gernot Ebel[7], Matthias Gunzer[1,8,§], Joachim Klode[2-4,§]

[1]Institute for Experimental Immunology and Imaging, University Hospital, University Duisburg–Essen, Essen, Germany

[2]Department of Dermatology, Venerology and Allergology, University Hospital Essen, University of Duisburg-Essen, Essen, Germany

[3]West German Cancer Center, University Duisburg-Essen, 45122 Essen, Germany

[4]German Consortium for Translational Cancer Research, Partner Site University Hospital Essen, Essen, Germany

[5]Institut für Theoretische Physik, Georg-August-Universität Göttingen, Germany

[6]Department of Otorhinolaryngology, University Hospital, University Duisburg-Essen, Essen Germany

[7]LaVision BioTec GmbH, Bielefeld, Germany

[8] Leibniz-Institut für Analytische Wissenschaften - ISAS -e.V., Dortmund, Germany

#: These authors contributed equally.

§: These authors jointly supervised the work.

Correspondence

Professor Dr. Joachim Klode
University Hospital Essen
Department of Dermatology
Hufelandstraße 55, 45147 Essen,
Germany
Phone.: +49 201 723-1812
Fax: +49 201 723-5424
E-Mail: joachim.klode@uk-essen.de

Professor Dr. Matthias Gunzer
University Hospital Essen
Institute for Experimental Immunology and Imaging
Hufelandstraße 55, 45147 Essen,
Germany
Phone: +49 201 183 6640
Fax: +49 201 183 6642
matthias.gunzer@uni-due.de

Supplementary Table 1: Patient characteristics

Patient (P) with sentinel lymph node (S)	Sex	Age in years	Melanoma tumor depth (TD) in mm	Localization melanoma	Localization sentinel lymph node excision
P1 / S1	f	41	3.74	cheek (L)	cervical (L)
P1 / S2	f	41	3.74	cheek (L)	cervical (R)
P2 / S3	f	67	1.32	thigh (L)	inguinal (L)
P3 / S4	m	69	2.1	chin (R)	submandibular (L)
P3 / S5	m	69	2.1	chin (R)	submandibular (R)
P3 / S6	m	69	2.1	chin (R)	cervical (L)
P4 / S7	f	56	1.6	gluteal (R)	inguinal (R)
P4 / S8	f	56	1.6	gluteal (R)	inguinal (R)
P4 / S9	f	56	1.6	gluteal (R)	inguinal (R)
P5 / S10	m	59	2.2	capillitium (R)	nuchal (R)
P5 / S11	m	59	2.2	capillitium (R)	cervical (R)
P5 / S12	m	59	2.2	capillitium (R)	cervical (R)
P6 / S13	f	51	1.1	scapula (R)	axillar (R)
P6 / S14	f	51	1.1	scapula (R)	axillar (R)
P6 / S15	f	51	1.1	scapula (R)	supraclavicular (R)
P7 / S16	m	61	1.9	neck (R)	cervical (R)
P8 / S17	m	78	2.0	capillitium (R)	cervical (R)
P9 / S18	m	55	7.2	back	axillar (R)
P9 / S19	m	55	7.2	back	axillar (L)
P10 / S20	m	38	1.9	thigh (R)	inguinal (R)
P11 / S21	f	51	1.8	lower leg (L)	inguinal (L)

Abbreviations: m = male; f = female; L = left; R = right

Supplementary Table 2: Tissue statistics and diagnostic results per patient.

Patient	Quantity of SLNs	Tissue sectioning		*Total samples for processing*	Signal positivity detected in pieces/ of total pieces/SLN			Indication in pieces/of total pieces/SLN	
		SLNs cut	*Pieces*		*LSFM and Histo*	*LSFM only*	*Histo only*	*Capsular nevus*	*Tumor*
#1	2	0	0	2	0	0	0	0	0
#2	1	1	4	4	0	0	0	0	0
#3	3	0	0	3	0	0	0	0	0
#4	3	2	10	11	3/6/1	0	0	3/6/1	0
#5	3	1	2	4	0	0	0	0	0
#6	3	3	12	12	0	0	0	0	0
#7	1	1	4	4	0	0	0	0	0
#8	1	0	0	1	0	0	0	0	0
#9	2	2	30	30	5/12/1	0	0	0	5/12/1
#10	1	1	11	11	0	1/11/1	0	0	1/11/1
#11	1	1	23	23	0	0	0	0	0
Sum	**21**	**12**	**96**	**105**	**8/18/2**	**1/11/1**	**0**	**3/6/1**	**6/23/2**

Abbreviations: SLN = sentinel lymph node; LSFM = light sheet fluorescence microscopy; Histo = gold standard routine histopathological assessment

Additional information: SLNs cut: 57%; average pieces per cut SLN: 8; LN per patient: 1.9

Supplementary Table 3: Sample preparation time of SLN analysis and LSFM module for melanoma diagnostics

Block	Procedure	Hands-on time* per sample in minutes	Protocol time# per sample in hours
Routine 1	Formaldehyde fixation	0.5	24
	Sum	**0.5**	**24 = 1d**
Whole mount and tissue clearing	EORTC conform cutting	6	0.1
	Permeabilization	0.5	120
	Dehydration/Bleaching/Rehydration	4	22.5
	Blocking/ whole mount staining	1	120.5
	Wash	1	8
	Dehydration	2	16
	Clearing	1	6
	Sum	**16**	**293.1 = 12.2d**
Imaging & transfer	LSFM imaging	5-40	1-3
	Declarification/Rehydration	3	18
	Sum	**8-43**	**19-21**
Routine 2	Paraffination	1	11
	Embedding, Slicing, Staining	15-30	3
	Sum	**16-31**	**14**

* = Handling time per simple volume change approximately 30 sec., hands-on time LSFM is without imaging time

= minimal protocol time, neglecting overnight incubations, weekends etcetera. In reality, the light sheet approach from post-fixation to rehydration took around 15.5 d. The routine block 1+2 without LSFM and discarding gap sections ideally takes 2 – 3 d in total, yet, in clinical routine, processing times until final histological diagnosis typically reach 10 working days. Preserving the gaps, sequentially cutting the lymph node pieces took another 30 min – 2 h per piece.

Abbreviations: SLN = sentinel lymph node, LSFM = light sheet fluorescence microscopy

Supplementary Figure 1

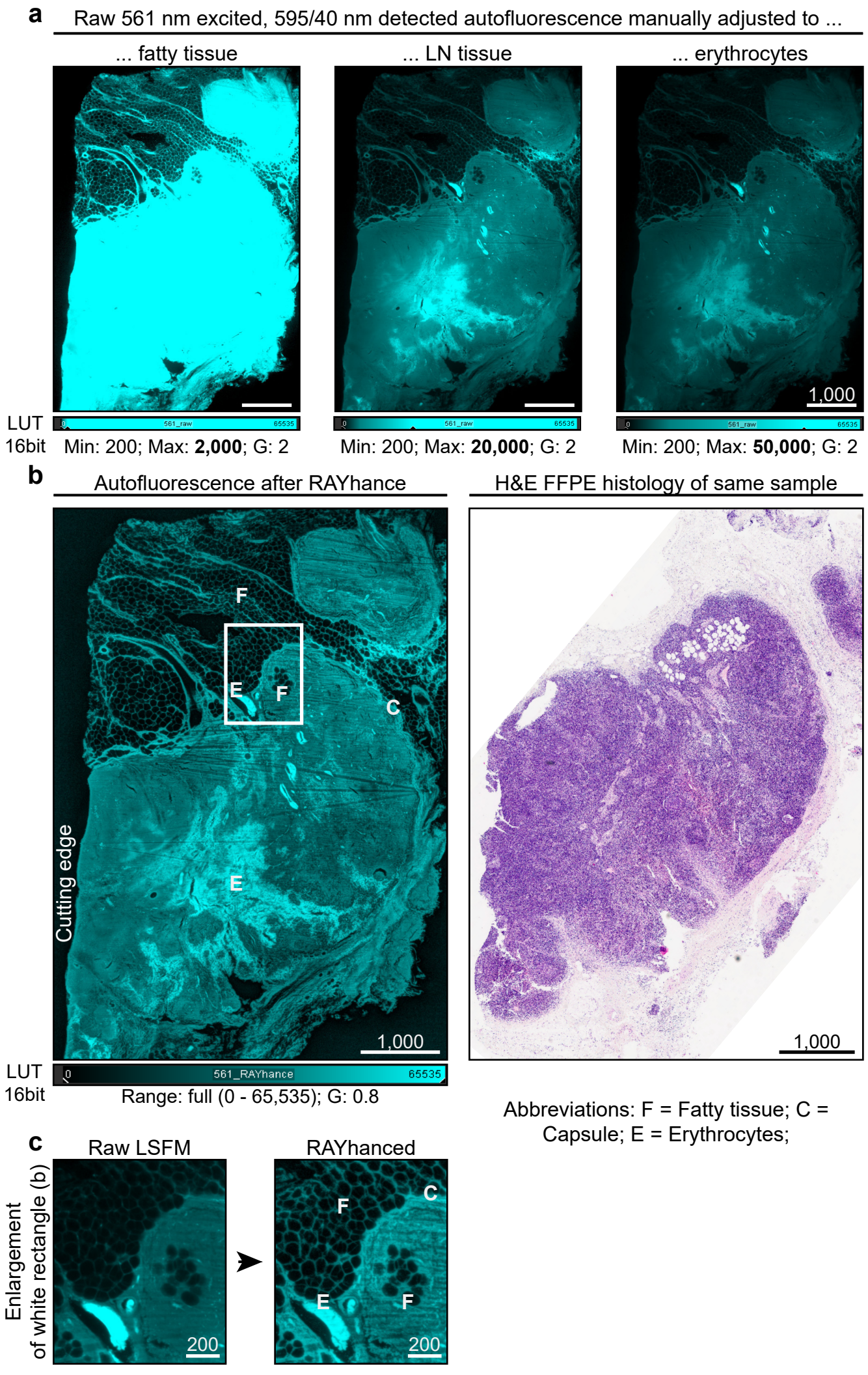

Supplementary Figure 1: Algorithm-enhanced LSFM autofluorescence signal for anatomical sample overview

(**a**) Within one LSFM optical slice based on autofluorescence excited with 561 nm and detected at 595/40 nm, there are immense intrinsic signal intensity differences. While fatty tissue exhibits a low autofluorescence, erythrocytes in vessels or within the tissue (bleedings) have a very high autofluorescence signal, even after bleaching the sample. Therefore, the simultaneous display of all information contained within the data is difficult. (**b**) Using RAYhance, a multiscale contrast compression algorithm, the simultaneous display of all features of the optical slice becomes possible. The obtained data is similar to H&E stainings but lacking morphological information on nuclei. No prior knowledge is needed to handle the data since for display the full 16bit range can be used. (**c**) Enlargement showing raw data and RAYhanced data with fat, LN tissue and an erythrocyte-filled blood vessel in close proximity. Abbreviations: C = capsule, E = erythrocytes, F = fatty tissue. Scale bar values in µm.

Supplementary Figure 2

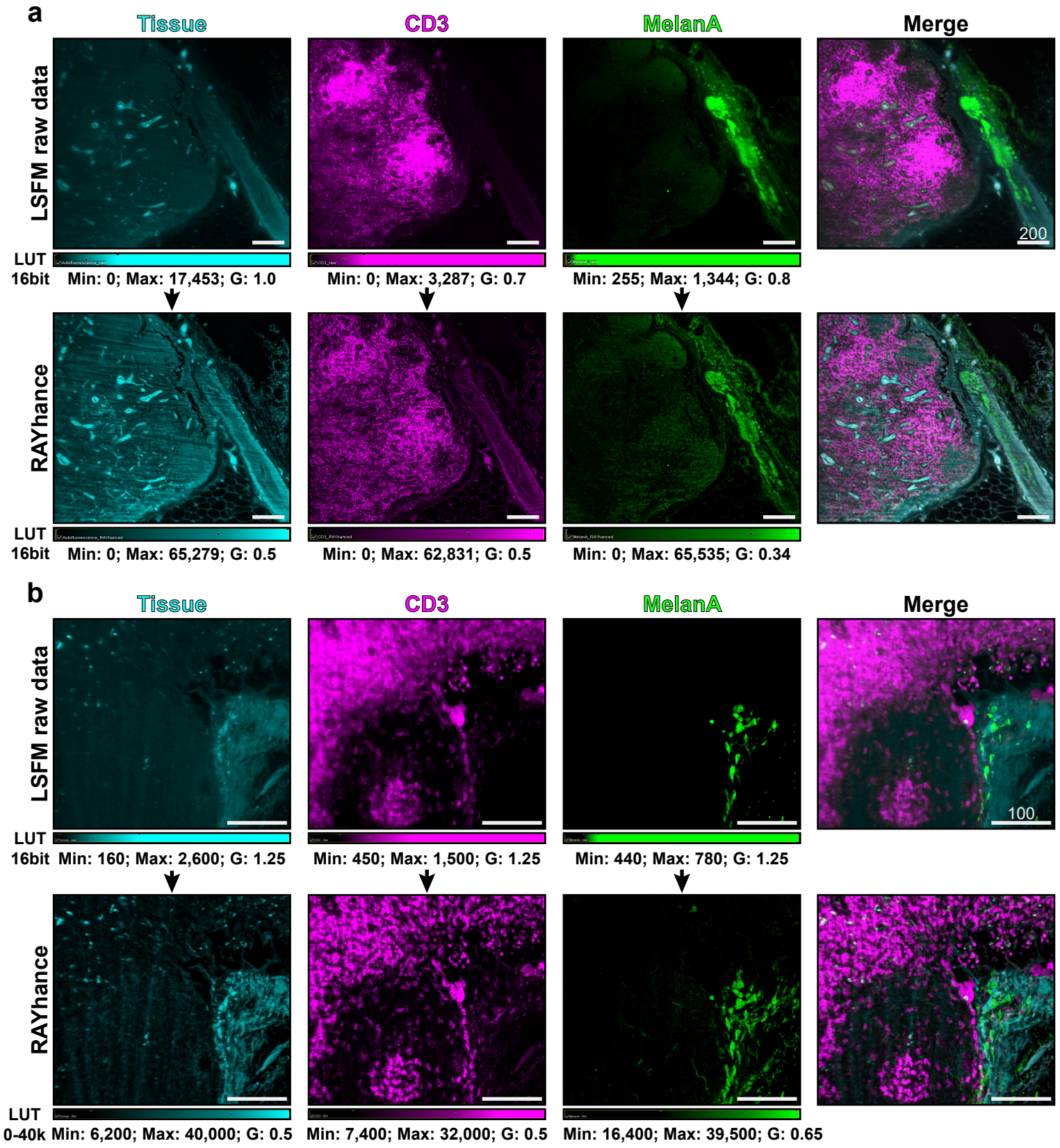

Supplementary Figure 2: RAYhance – a multiscale compression algorithm for simultaneous display of LSFM data with high signal intensity spread

Displayed are two examples of how RAYhance enables easy display of LSFM data: (**a**) the “hidden” metastasis and (**b**) the capsular nevus, Figures 5 and 3, respectively. The upper panel of images are raw data of LSFM optical slices, below are the algorithm-enhanced versions. Specifications of the look up table (LUT) are detailed below the images. Min = lower cut-off - pixels with this value and below are shown as black, Max = upper cut-off - all pixels with this value or above are shown as saturated, G = gamma – defines the linearity of the relationship between actual image intensity values and the brightness of the displayed image (linearity is 1). See also Supplementary Video 3. Scale bars in µm.

Supplementary Figure 3

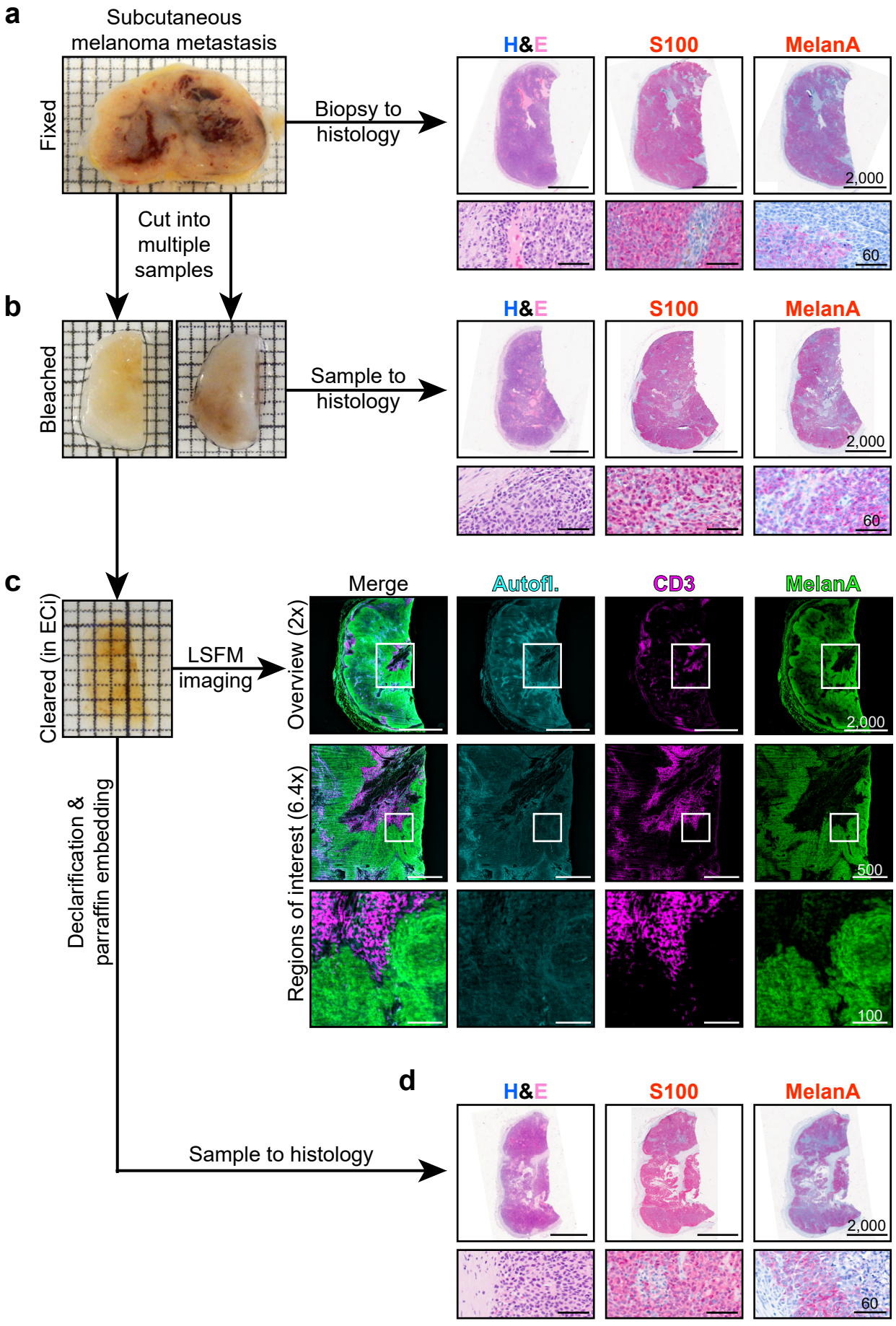

Supplementary Figure 3: LSFM analysis allows subsequent immunohistochemical formalin-fixed paraffin-embedded (FFPE) gold standard stainings

Macroscopic images and correlating H&E and immunohistochemical analysis (anti-S100 red, anti-MelanA red) of the same subcutaneous melanoma metastasis after (**a**) fixation in 4% PFA, (**b**) peroxide-based bleaching and (**d**) staining, clearing and light sheet fluorescence microscopy analysis. (**c**) Algorithm-enhanced LSFM MIPS (three subsequent optical slices) of sample histopathologically processed in (d). Images of the upper row were taken at screening resolution of 2x, enlargements below referring to white rectangles at 6.4x magnification. Tissue autofluorescence (cyan), CD3 (magenta) and tumor marker MelanA (green) are depicted in single channels and as a merge. This staining panel was later used for SLN diagnostic screenings. FFPE slices of the whole-mount stained LSFM sample could be re-stained for MelanA using the same antibody clone (d). Scale bar values in µm, squares in macroscopic images 1x1 mm.

Supplementary Figure 4

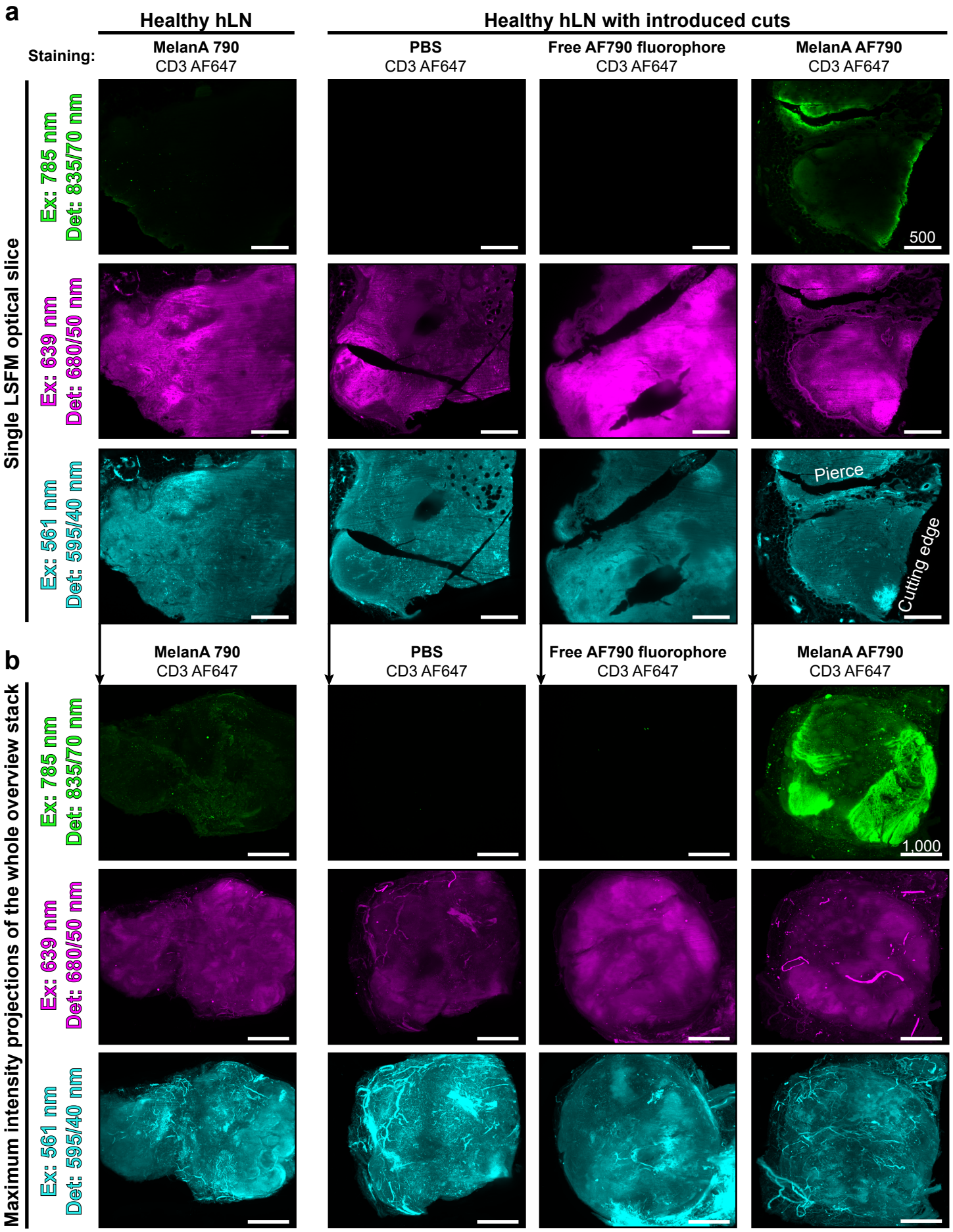

Supplementary Figure 4: Unspecific cutting-edge MelanA artifact

(**a**) From left to right four small healthy human lymph nodes (hLNs) were either used without physical manipulation or sliced (with microtome blade) and pierced (with needle). The uncut LN was stained using the anti-MelanA AF790 (green) and anti-CD3 AF647 (magenta) staining panel, yielding minimal background (upper left). Cut LNs were stained in the MelanA channel (excitation (Ex) 785 nm, detection filter (Det) 835/70 nm), from left to right with PBS, unbound AF790 and normal MelanA AF790. All samples were stained with anti-CD3 AF647. Unspecific anti-MelanA staining accumulated at the cutting edges whereas anti-CD3 staining remained unperturbed. (**b**) Maximum intensity projection (MIP) of the whole sample corresponding to the optical slice shown in (a). Scale bar values in µm.

Supplementary Figure 5

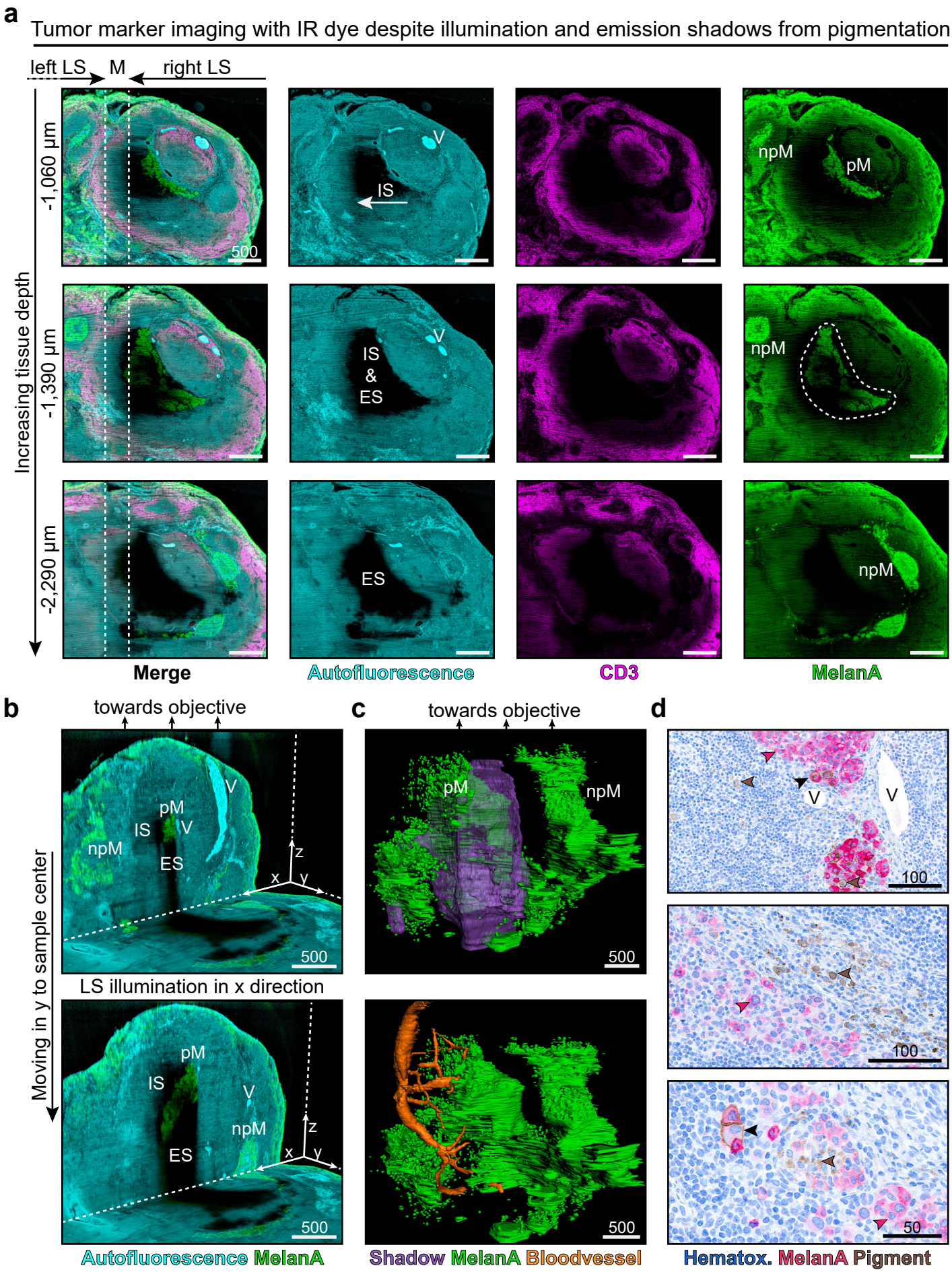

Abbreviations: LS = light sheet, M = merge zone of both LS, IS = illumination shadow, ES = emission shadow, V = vessel, npM/pM = (non-) pigmented MelanA positive cells

Supplementary Figure 5: Infrared (IR) dye enables imaging of tumor through residual pigmentation

Metastasized sample S18-12 showed macroscopic colorization after clearing despite autofluorescence-attenuation protocol. In (**a**), the impact of pigmentation on LSFM imaging is shown. In one row, RAYhanced optical slices of a certain tissue depth are shown, consisting of a merge and the single channels: autofluorescence (cyan), anti-CD3 signal (magenta) and anti-MelanA signal (green). Above the first column, showing, from top to bottom, optical slices of increasing tissue depth, the direction of the incoming light sheets (LS) is noted. The approximate borders of the merge zone (M) are depicted by two dashed white lines. Illumination shadows (IS) in form of stripe artifacts can be seen in all channels. These shadows have their origin at some pigmented MelanA positive cells (pM), while others seem to be non-pigmented (npM). There are no shadow artifacts associated with an erythrocyte-filled major blood vessel (V), showing the efficiency of the bleaching protocol. Deeper within the tissue, the shadow artifact consist of two components, the illumination and the emission shadow (ES). Consequently, there is signal absence in the autofluorescence and the T cell channel (hole). Despite the residual pigmentation blocking emission light it was possible to obtain a weak but contrasted anti-MelanA signal in the blocked zone (white dashed shape, middle row, right image) using an infrared fluorophore. (**b**) Afore described situation shown with optical slicers in three dimensions. (**c**) Segmentations of the anti-MelanA signal (green) the shadow volume (purple) based on the autofluorescence channel and the blood vessel (orange) based on erythrocyte filling. (**d**) The partial retention of pigment observed in LSFM can also be assessed in follow-up FFPE sections showing a high amount of pigmented cells. Most cells are either MelanA positive (red arrow) or contain pigment (brown arrow), but some are also double positive (black arrow). For further explanations, see Supplementary Note 1. Scale bar values in µm.

Supplementary Note 1: LSFM artifacts and their interpretation – concerning tumor detection through residual pigmentation

There are multiple artifacts one can encounter in light sheet fluorescence microscopy (LSFM). Since the samples are three-dimensional, assessing their nature can be quite challenging. Therefore, we describe some of the LSFM background knowledge to be able to interpret the shown datasets.

Sample overviews made with LSFM are typically obtained by illuminating the sample with light sheets (LS) from two sides perpendicular to the objective.

One reason for this is that the sample will always scatter the light, no matter how clear it becomes. Therefore, in general, the illumination (and the emission) signal will be high at the border of the sample and become lower (more scattered) with increasing sample depth. Illuminating the sample from two sides thus enables imaging of thicker samples while homogenizing the signal intensity throughout the sample. However, this means that per optical slice, two images are taken. One from the right and one from the left side. These images can be saved independently, but mostly they are directly fused together in a predefined merge zone. Hence, stripe artifacts (illumination shadow, IS) obtained from illuminating e.g. pigmentation from one side are therefore fading out in the middle of the sample, where the information is blended with the signal obtained from the illumination of the LS from the other side, where there is no corresponding shadow.

If there are multiple shadows (mostly three) originating from one point in the image, the optical slice was illuminated using multiple differentially angled LS from the same side. We use this technique in order to minimize striping artifacts, reducing the shadow of e.g. a small erythrocyte filled vessel. However, this technique will not work when a large cluster of pigmented cells obstructs the light.

Finally, there is the third dimension to consider: observing a shadow can also mean that the region is well illuminated, but the emission light is blocked on its path towards the objective (emission shadow, ES).

Detecting melanoma metastasis even when some pigmentation withstands the bleaching step is of high importance for the clinical application of LSFM. Using infrared fluorophores like AlexaFluor 790 seems to be one solution, since we were able to detect MelanA positive cells that were situated in both, the IS and ES seen in the autofluorescence channel (Supplementary Figure 5, Supplementary Video 8).

Supplementary Video 1: An entire human LN in 3-D based on autofluorescence

An entire human lymph node (LN) reconstructed from 2-D optical LSFM slices imaging tissue autofluorescence only. Imaris' (Bitplane) blend mode was used for reconstruction. Autofluorescence of two channels are shown: i) excitation (Ex) 488 nm and detection filter (Det) 525/50 nm displayed as green and ii) Ex 561 nm, Det 595/40 nm displayed as gray. Display description in upper left corner, scale bar (lower left) displays µm values.

Supplementary Video 2: Interplay of melanoma and T cells in a human LN (hLN)

Example of simultaneously visualizing tissue autofluorescence (cyan), anti-CD3 staining (magenta) and anti-MelanA staining (green). LSFM optical slices have been algorithm-enhanced using RAYhance (RH). Quantification of the tumor volume using automatic segmentation is shown as a green 3-D model. Display description in upper left corner, scale bar (lower left) displays µm values.

Supplementary Video 3: RAYhance for browsable histo-like data stacks

Example of the usage and benefits of the multiscale contrast compression algorithm RAYhance (RH). Tissue autofluorescence (cyan), anti-CD3 staining (magenta) and anti-MelanA staining (green) are shown as LSFM optical slices first as raw data, later as a RAYhance-processed version. Display description in upper left corner, scale bar (lower left) displays µm values. See also Supplementary Figures 1 and 2.

Supplementary Video 4: From 2-D to 3-D – a capsular nevus

Exemplary 3-D data reconstructions created from 2-D LSFM optical slices. White arrows mark intracapsular MelanA positive cells. Both raw and RAYhanced (RH) data are shown. Display description in upper left corner, scale bar (lower left) displays µm values.

Supplementary Video 5: From 3-D to quantification – segmentation of a capsular nevus

Example of how segmentations were used to quantify general tissue volume (including extracapsular fat, cyan), capsule surrounded LN tissue (white/gray), anti-CD3 staining (magenta) and intracapsular anti-MelanA signal (green). Display description in upper left corner, scale bar (lower left) displays µm values.

Supplementary Video 6: Anatomical and cellular LN architecture 3-D quantified

This video highlights the quantitative power of our LSFM approach, only using three channels: tissue autofluorescence, anti-CD3 and anti-MelanA. From these, we derive seven parameters which are: total tissue volume, total LN volume, medulla, total T cells, follicles, germinal centers (GCs) and MelanA volume. Follicles can also be subdivided into primary (without GCs) and secondary (with GCs), which differ significantly in size (Fig. 3). For all information on colors see display description in upper left corner. Scale bar (lower left) displays µm values.

Supplementary Video 7: 3-D quantification of melanoma

Subsequent videos of all five metastasized LN pieces (S18-01 / 02 / 09 / 10 / 12) of patient 9. First, the outline of the capsule and the volume of the LN tissue within is shown (white to gray), then the segmentation of the MelanA positive cells (green). Note that in the video concerning S18-12, a blood vessel (orange) is reconstructed based on erythrocyte-filled vessels. The MelanA positive cells grow in close proximity. Display description in upper left corner, scale bar (lower left) displays µm values.

Supplementary Video 8: Tumor detection through pigmentation

Video explaining nature of the shadow artifacts accompanying residual pigmentation within a lymph node (piece S18-12). It also highlights that the infrared anti-MelanA signal can be detected through pigmentation, whereas other signals are blocked. Segmentation of the shadow (purple) is based on the lack of signal in the autofluorescence channel. Shadow artifacts do not originate from close by erythrocyte-filled vessel (segmentation is orange). For more information, see Supplementary Figure 5 and Supplementary Note 1. Display description in upper left corner, scale bar (lower left) displays µm values.

Supplementary Video 9: LSFM detects “hidden” metastasis

Video featuring a region of interest taken 6.4x magnification showing the upper part of the two MelanA positive events detected in a LN piece that was found negative by gold standard histopathological assessment (Figure 5). Vessels were segmented using Imaris segmentation algorithm. RH = RAYhance. Display description in upper left corner, scale bar (lower left) displays µm values.

6.2. Licenses

6.2.1. Creative Commons 4.0

This license applies to the open access *Nature Communications* paper "". This text is given by the journal (17.09.2019):

I herewith state that except for formatting alterations, no changes concerning the content or context were made to the final submitted manuscript.

6.2.2. License for manuscript #2

Order Completed

Thank you for your order.

This Agreement between Simon Merz ("You") and The American Association for the Advancement of Science ("The American Association for the Advancement of Science") consists of your license details and the terms and conditions provided by The American Association for the Advancement of Science and Copyright Clearance Center.

Your confirmation email will contain your order number for future reference.

printable details

License Number	4693640419990
License date	Oct 21, 2019
Licensed Content Publisher	The American Association for the Advancement of Science
Licensed Content Publication	Science Immunology
Licensed Content Title	Multidimensional imaging provides evidence for down-regulation of T cell effector function by MDSC in human cancer tissue
Licensed Content Author	Yu Si,Simon F. Merz,Philipp Jansen,Baoxiao Wang,Kirsten Bruderek,Petra Altenhoff,Stefan Mattheis,Stephan Lang,Matthias Gunzer,Joachim Klode,Anthony Squire,Sven Brandau
Licensed Content Date	Oct 18, 2019
Licensed Content Volume	4
Licensed Content Issue	40
Volume number	4
Issue number	40
Type of Use	Thesis / Dissertation
Requestor type	Author of the AAAS published paper
Format	Print and electronic
Portion	Full Text
Order reference number	
Title of your thesis / dissertation	PhD thesis
Expected completion date	Dec 2019
Estimated size(pages)	1
Requestor Location	Simon Merz Cranachstr. 75 Essen, NRW 45147 Germany Attn: Simon Merz
Total	0.00 EUR

Note, that permission is only granted for the accepted manuscript version, not the published version, as available online.

6.3. Personal remarks on multidisciplinary teams

If utilizing and implementing new imaging techniques, it is of high importance to recognize the value of multidisciplinary teams, now more than ever. Biological knowledge in a field is acquired over a long period of time and so is detailed knowledge of method development and insights into microscopy. Combining these skill sets in teams assures quick adaptation of existing methodology to the problem at hand. Furthermore, visualization and analysis of large data sets requires expertise, not only in using specialized software, but also in coding, machine learning or artificial intelligence. In my opinion, many researchers still behave like "do it yourself" is the only way one can assure the absolute correctness of projects. This also explains headlines of articles like: "Want to make it as a biologist? Better learn to code"[257]. However, this mostly leads to unnecessary pluralism, like different names for the same thing or special methods or codes in different labs, hindering comparability[258]. Also, researchers who are meant to work on a project alone are frequently overwhelmed by the detailed knowledge their projects require in multiple fields, which adds to the always existing pressure to publish. The attitude that "it is just another method" leads to technological errors, loss of time and motivation. Of course, there are tumor researchers that can code and have a huge background in both microscopy and image analysis. Most likely, however, these skills are not combined. This applies not only to microscopy but also to big data science and science in general. Researchers from many fields (data scientists, physicists and philosophers) are required to go forward in biology.

Therefore, I was honored to work side-by-side with so many enthusiastic people, to share knowledge and to advance science. It is this collaborative atmosphere that is often lacking in biology. Science is all about progress. And progress is most easily achieved when working together, being open-minded and attentive to other fields and influences apart from one's own.

6.4. Acknowledgements

During the last 3 years, I had the pleasure to interact with many people impacting my social and professional perspective. Here, I would like to thank all of them, discussing data, contributing to cooperative projects and lending a hand in times of need. This is especially true for the IMCES, the Department of Cardiology and Vascular Medicine, the Department of Otorhinolaryngology and the Department of Dermatology, Venerology and Allergology as well as LaVision BioTec and Miltenyi Biotec. Nevertheless, I would like to express my gratitude to some persons in particular. ***Thank you …***

… **Matthias G.**, not only for supervising this thesis and thus having me here, but also your trust in me, backing me up in times of need, listening to problems and designing potential solutions. I thank you for giving me the chance to visit conferences and a summer school and for being open to sometimes wild suggestions. I appreciate that even when not seeing eye-to-eye, you let me speak my mind and were available for criticism and discussions, valuing opinion. I think, we can both be proud of what we achieved together. Thank you!

… **Joachim**, for the supervision and your help getting me accustomed to the clinical climate, the chance to build a laboratory and to recruit and organize staff as necessary.

… **Philipp**, for being my personal 200g dermatologist buddy! Time of day never mattered, and motivation was never lacking even when it came to write surplus TVAs, grant proposals or slicing night after night through the S.L.A.V.E.-project. We build a whole new laboratory and group together, learning to manuver, cooperate or fight our way through clinical and scientific society. I thank you for all I learned, and I am proud of what we achieved!

… **Sebastian**, my cardiologist counterpart and friend, for your vast interest in developing new technologies and approaches to visualize immunological processes of MI. It was a pleasure to travel the research road together, rapidly progressing and promoting each other towards a common goal.

… **Yu**, for this wonderful culinary exploration time in German and Chinese hot-pot cuisine. Discussing social and scientific problems with you guided me to new perspectives.

… **Sophie, Franzi and Lucas**, my (recent) fellow PhD students, taking me in and accompanying me on this journey of ours. Thanks for the discussions, the help, the evenings in the Nord, the beer brewing, the gaming evenings, the squash games and the guidance.

… **Marc, Anja and Juliane**, for your ongoing support, scientific and social advice and the patience to listen to the problems before shooting people with rockets or else :)

… **Andreas and Ricarda**, for giving me both moral support and technical advice. You were instrumental, starting with building a new laboratory from scratch to the execution of the SLN study. Without you two, this would have been a really hard time!

… **Ingo, Eva and Klaus** for your support concerning sample acquisition, project and study planning, histological insights and valuable criticism.

… **Matthias T.**, for your trust, patience and input while handling up to three PhDs in the same meeting! I appreciated your opinion and your sharing of clinical knowledge.

… **Sven**, for the cooperation and sharing your scientific opinion.

... **Uwe, Heinrich and Gernot**, for your faith in me, the chance to perform my PhD in this challenging setting, the tutoring experience and the valuable and fruitful collaboration. I look forward to working with you in the future.

… **Anthony and Alex**, for all your help and support concerning morale in front of a non-functional device, swapped filters or the detailed assessment of the intricate heart vasculature. I learned a lot from both of you!

… **Svenja,** for enduring all the science related stories and providing integral project management guidance.

… **my family**, for helping and supporting me on my labyrinthine ways here and hopefully beyond.

… **Lea**, for your unending love and support! During times of gut-wrenching conflicts and stress, you lend me an ear and gave me guidance and peace, sometimes just by listening. Apart from social support, working with you in different projects opened my eyes to your refreshing view of science, your minds' precision and your loyalty. It was and will be utmost fun to work and live by your side. *I love you.*

6.5. Curriculum vitae

Der Lebenslauf ist in der Online Verison aus Gründen des Datenschutzes nicht enthalten.

Der Lebenslauf ist in der Online Verison aus Gründen des Datenschutzes nicht enthalten.

Der Lebenslauf ist in der Online Verison aus Gründen des Datenschutzes nicht enthalten.

6.6. Declarations / Erklärungen

Hiermit erkläre ich, gem. § 7 Abs. (2) d) + f) der Promotionsordnung der Fakultät für Biologie zur Erlangung des Dr. rer. nat., dass ich die vorliegende Dissertation selbständig verfasst und mich keiner anderen als der angegebenen Hilfsmittel bedient, bei der Abfassung der Dissertation nur die angegeben Hilfsmittel benutzt und alle wörtlich oder inhaltlich übernommenen Stellen als solche gekennzeichnet habe.

Essen, den *Simon F. Merz*

Hiermit erkläre ich, gem. § 7 Abs. (2) e) + g) der Promotionsordnung der Fakultät für Biologie zur Erlangung des Dr. rer. nat., dass ich keine anderen Promotionen bzw. Promotionsversuche in der Vergangenheit durchgeführt habe und dass diese Arbeit von keiner anderen Fakultät/Fachbereich abgelehnt worden ist.

Essen, den *Simon F. Merz*

Hiermit erkläre ich, gem. § 6 Abs. (2) g) der Promotionsordnung der Fakultät für Biologie zur Erlangung der Dr. rer. nat., dass ich das Arbeitsgebiet, dem das Thema „Mesoscopic Whole Organ Imaging using Light Sheet Fluorescence Microscopy - From Experimental Systems to Clinical Application“ zuzuordnen ist, in Forschung und Lehre vertrete und den Antrag von Simon F. Merz befürworte und die Betreuung auch im Falle eines Weggangs, wenn nicht wichtige Gründe dem entgegenstehen, weiterführen werde.

Essen, den *Prof. Matthias Gunzer*